Catalytic and pseudocapacitive energy storage performance of metal (Co, Ni, Cu and Mn) ferrite nanostructures and nanocomposites

Jose-Luis Ortiz-Quiñonez [a], Sachindranath Das [b], Umapada Pal [a,*]

[a] *Instituto de Física, Benemérita Universidad Autónoma de Puebla, Apdo. Postal J-48, Puebla, Pue. 72570, Mexico*
[b] *Department of Instrumentation Science, Jadavpur University, Kolkata 700032, India*

A B S T R A C T

Metal ferrites are promising low-cost, highly-abundant metal oxides of low toxicity, which have been explored extensively during the past three decades for catalytic, energy storage, microwave screening and biomedical applications. In nanostructure forms, they have received tremendous attention during the past decade, especially for their applications in high-value organic compound synthesis and fabrication of energy storage devices. While the presence of multivalent cations is an attractive feature for catalytic and energy storage applications of metal ferrite nanostructures, the inherent magnetic nature is another attractive feature for their catalytic applications. With the current surge in the utilization of metal ferrite nanostructures in different technologies, it has become necessary to make a balanced assessment of the progress made in their design and synthesis over the past 20 years, and analyze the performance of these newly designed nanostructures in catalysis and energy storage devices. In this critical review, we highlight the progress made in the design and synthesis of some important metal ferrite nanostructures, their performance as catalysts in organic synthesis and as active electrode materials in supercapacitors (SCs). By analyzing the performances of these nanostructures in catalysis and pseudocapacitive energy storage devices, we highlight their prospects and perspectives.

1. Introduction

Growing energy demand, coupled with depleted fossil-fuel reserves and environmental pollution concerns necessitates a search for cleaner and sustainable energy resources [1–4]. While the generation of usable energy such as electricity from renewable resources is the primary concern of humanity, storage and delivery of that energy are two essential steps that need to be followed for its efficient utilization. Over the past three decades, researchers have devoted intense efforts in developing efficient devices to capture energy from renewable resources such as sunlight, wind, and water along with their transformation into electricity. However, serious attention has been paid to the development of energy storage and delivery devices only in the last two decades. Whether it is the production, storage or supply, one of the main obstacles for developing these technologies is the availability of suitable materials with desired functionalities. For example, photovoltaic cells have been developed in the mid-60s and commercialized on a large scale only in the '90s [1]. In spite of intense research for such a long period, the efficiency of photovoltaic devices remained below 30% (except for multi-

---

junction solar cells) due to improper choice or unavailability of appropriate materials [1]. Similarly, lithium-ion batteries (LIBs) and electrochemical supercapacitors (SCs) are the two leading devices utilized for electrochemical energy production and storage [1,6]. Although they have been developed and commercialized in 1978 [2], the search for efficient materials to utilize as active components of their working electrodes has intensified only recently [3]. Although material requirements in each of these devices depend on their operating mechanisms and structural configurations, it can be noticed that the materials of some particular categories have been traditionally preferred for photovoltaic cells, LIBs, and SCs, over others. To highlight this further, we can point out the intense research carried out recently on perovskite materials and their nanostructures for application in solar cells [9–12]. Likewise, nanostructures of layered $LiCoO_2$, spinel $LiMnO_2$, polyanion oxide $Li_xFe_2(SO_4)_3$, highly conductive transition metal oxides (e.g., RuO_2, $NiCo_2O_4$), and carbonaceous materials (e.g., graphene, activated carbon) have been considered as excellent electrode materials either for LIBs or for SCs [4].

In addition to the structural configuration (symmetric, asymmetric or hybrid, as discussed later), the energy storage and delivery performance of a SC depend on the nature of the electrode material and the used electrolyte [14–17]. It is also important to consider the toxicity, earth-abundance and cost of the electrode materials to make the SCs commercially viable. Currently, asymmetric and hybrid SCs have higher energy storage capacities than symmetric SCs [5]. To enhance the storage capacity, as well as potential window of SCs, different electrolytes (ionic liquid, molten salts, aqueous solutions of acid, base and salts) have been investigated. Among the aqueous electrolyte-based SCs, excellent performance has been achieved using some metal oxides such as RuO_2, MnO_2, Co_3O_4, NiO, Fe_3O_4, Nb_2O_5, V_2O_5 as electrode materials [1,19–21]. However, some of these oxides are either expensive (RuO_2, Nb_2O_5) or poor electrical conductors (Co_3O_4, NiO, MnO_2, $TiO_2(B)$, etc.), impeding SCs to achieve high specific capacitance, high rate capability, and high cycling stability [6–22]. In addition, some of these metal oxides can be used only in acidic (RuO_2) or neutral (MnO_2) media [6]. In the case of Nb_2O_5, $TiO_2(B)$, V_2O_5 and few other lithium containing metal oxides (e.g., $Li_4Ti_5O_{12}$, $LiMn_2O_4$), Li^+ ions are used in the electrolyte because these oxides work both through surface redox pseudocapacitance and Li^+-ion intercalation pseudocapacitance mechanisms [17,24–26]. However, the disadvantages of using Li^+ ion in SCs are its toxicity and elevated market price.

To address the problems highlighted above, several metal oxides with the general formula $A_xB_yO_z$ (where A and B represent transition metal ions) such as $NiCo_2O_4$, $NiMoO_4$ and metal ferrites have been tested in SCs. Multiple oxidation states of metal ions in these materials and their ability to perform multiple redox reactions have been explored [1]. Among the Li-free metal oxides, double oxides such as $NiCo_2O_4$ and $NiMoO_4$ exhibit superior supercapacitive performances. In fact, the electrochemical performance of double oxides in SCs has always been better than that of their single oxide components [2,6,27]. While the SC performance of $NiCo_2O_4$ remained the best among the double oxides owing to its lower electrical resistivity (~20 mΩ cm) [2,28], the disadvantages of using cobalt-based metal oxides are their non-eco-friendly nature and recent surge in the market price of cobalt [1,29]. The performance of metal oxide nanostructures as SC electrode materials reported in the last two decades has been summarized periodically in several review articles [2,6,16,24,30–36]. Nonetheless, they include very few results of metal ferrites.

Metal ferrites (MFe_2O_4, M = Mn, Fe, Co, Ni, Cu) and metal ferrite-based composites have demonstrated their potentials for utilization in energy storage devices such as LIBs [37–42], SCs [43–55], and generation of hydrogen either through water splitting or reforming of small organic molecules [56–58]. Utilization of metal ferrites and their composites in SCs has several advantages, such as: (i) occurrence of multiple redox reactions, (ii) wider potential windows for the operation of SCs (SCs based on MFe_2O_4 can operate at voltages as high as 1.8 V), (iii) enhanced chemical stability of the electrodes, (iv) high natural abundance and low cost of Fe and its environmental friendliness [1,47]. In fact, metal oxides and metal ferrites received special attention in the search of appropriate materials for utilization in catalysis (e.g., synthesis of heterocycles, tertiary aromatic amines, phenol esters, quinolines and vinyl-boronates) [59–63], energy harvesting, storage and delivery since the past three decades [24]. Considering the ubiquitous roles played by metal oxides and metal ferrites, especially their nanostructures in the above-mentioned applications, it is necessary to evaluate the progress made on their design, synthesis, and application during the last two decades to shed light on their prospects and associated challenges. Several excellent reviews have been published on the synthesis of metal oxide nanostructures and their SC applications over the past 20 years [1,2,19,20,26,30,32,34,36,64–66]. Also a large number of articles have been published in the literature, reporting the synthesis and SC application of metal ferrite nanostructures. However, to date, only one book chapter and one review article have been published on the use of metal ferrites in SCs [56,67], and only one review article has been published summarizing the synthesis, characterization and application of metal ferrite nanostructures in the degradation of organic pollutants, hydrogen evolution reaction (HER) and photocatalytic reduction of CO_2 [68]. Therefore, a critical review, summarizing the performance of metal ferrite nanostructures in chemical processes such as synthesis of organic molecules and energy storage is indispensable, which can help us to assess the convenience of using them in catalytic (in terms of yields, selectivity, and sustainability) and energy storage (in terms of electrochemical performance) applications.

As the performance of metal ferrite nanostructures in organic synthesis and energy storage depends critically on their size, morphology and composition [14], it seems that the secrete of successful application of these nanostructures lies on the used synthesis protocol. For SC application, once the electrode material is successfully synthesized, the next important component to look for is the electrolyte. Currently, all commercial SCs use organic electrolytes as they provide larger working potential windows. However, in most cases, metal ferrite based SCs have been tested using aqueous electrolytes. In aqueous electrolytes, H_2O decomposes into O_2 and H_2 in-between 1.4 and 2.0 V bias potential (depending on the used electrocatalyst) during charge–discharge cycles, thus limiting the working potential and the energy density (*ED*) of the SCs. The higher the overpotential, the higher the working potential that can be used during the operation of a SC. Therefore, by comparing the overpotentials of metal ferrites for oxygen evolution reaction (OER), we can have an idea on the potential windows for their utilization in SCs. In fact, both the electrochemical and chemical catalytic activities of metal ferrites strongly depend on their composition and electronic structure.

Some basic requirements for selective catalytic and pseudocapacitive energy storage applications of metal ferrite nanostructures

are highlighted in Table 1. Except for the low electrical conductivity and agglomeration, especially during successive operations, metal ferrite nanostructures meet all the requirements for catalytic and pseudocapacitive energy storage applications, provided that an appropriate synthesis method is used for obtaining them. Fortunately, the problems associated to the electrical conductivity and agglomeration of metal ferrite nanostructures can be solved through the fabrication of their nanocomposites containing conductive materials. Some additional requirements are discussed in corresponding sub-sections of this review.

In the present review, in addition of providing the structural, electronic, and energetic aspects of some common metal ferrites, we present the current status of their catalytic (which is part of their environmental aspects) and energy storage applications. This review is comprised of nine sections. In section (2), we present the structural characteristics and cation distributions in the spinel lattice of the metal ferrites to understand the origin of their chemical and electrochemical functionalities. In section (3), we discuss the general synthetic strategies for controlling the morphology, size and texture of metal ferrite nanostructures, which define the number of active sites (a key parameter for redox reactions) available on their surface and their accessibility, along with the diffusion of ions from electrolytes to the nanostructured electrodes of SCs. In section (4), we present some typical organic reactions catalyzed by metal ferrite nanostructures, which can help us to figure out how the surfaces of the ferrites and their composites interact with organic molecules. Understanding the mechanisms of interaction between metal ferrites and organic species is also helpful for understanding the redox reactions occurring at the surface of metal ferrite electrodes in SCs. Some important catalytic and photocatalytic processes assisted by metal ferrites such as the degradation of pollutants and pharmaceuticals, photoreduction of toxic gases (e.g., CO_2, NO), generation of H_2 and oxygen evolution reaction are also addressed. In section (5), the mechanisms of energy storage in supercapacitors are discussed along with a comparative analysis of the performance of SCs based on different metal ferrite nanostructures. In section (6), relative band edge positions of some important metal ferrites and a few other metal oxides are presented to highlight the convenience of fabricating metal ferrite nanocomposites and heterojunctions for improving their performance in catalysis. In section (7), we introduce supercapattery, a two-electrode electrochemical energy storage device, that uses SC material in one electrode and LIB material in the other electrode, highlighting the potential of utilizing metal ferrite nanostructures in them. Finally, the challenges associated with the fabrication of metal ferrite nanostructures with selective functionalities and their applications in catalysis and energy storage devices are presented in section (8), along with brief conclusions in section (9). The topics covered in this review are schematically presented in Fig. 1.

2. Lattice structure, cation coordination and spin alignment in metal ferrites (MFe_2O_4, M = Mn, Co, Ni, Cu)

Metal ferrites possess a spinel-type crystal structure, comprising of a distorted face-centered cubic (fcc) sub-lattice of O^{2-} anions, in which one-eighth of the tetrahedral (T_d) lattice sites and half of the octahedral (O_h) lattice sites are occupied by cations [69,70]. As can be seen in the schematic crystallographic structure presented in Fig. 2a, Co^{2+}, Ni^{2+}, and Cu^{2+} cations remain at the O_h sites of MFe_2O_4 (M = Co, Ni, Cu) lattice. On the other hand, half of the Fe^{3+} cations are located at the T_d sites and the remaining half at the O_h sites. As the M cations occupy O_h lattice sites, all these metal ferrites are inverse spinels [71]. In contrast, the Mn^{2+} cations in $MnFe_2O_4$ are located both at the T_d and O_h lattice sites, and therefore, the compound has a partially inverse spinel structure. As can be seen in Fig. 2a, all the neighboring octahedra share edges, which facilitates electron hopping between the cations at the octahedral sites. In contrast, the occupied tetrahedral sites do not share edges or corners, excluding the possibility of electron hopping among the cations at the occupied T_d sites. Another important aspect of metal ferrites is their magnetic ordering, which plays an important role in their catalytic applications. The spins of the cations at the O_h lattice sites are parallel to each other. Likewise, the spins of the cations at the T_d lattice sites are parallel, but antiparallel to the spins of cations at the O_h lattice sites. As a result, metal ferrites exhibit ferrimagnetic or superparamagnetic behavior, facilitating their use as magnetically separable catalysts.

The cation distribution among the tetrahedral and octahedral sites of a spinel lattice also depends on the octahedral site preference energies (OSPEs) of the cations. The OSPE quantifies the preference of a cation in a complex/compound to exhibit an octahedral

Table 1
Basic requirements for utilizing metal ferrite nanostructures in selective catalytic and supercapacitive energy storage applications.

| Basic requirements	Application			
	Organic synthesis	Oxygen evolution reaction, OER	Hydrogen evolution reaction, HER	Pseudocapacitor
Presence of cations exhibiting variable valence states	Desirable	Essential	_	Essential
Ability to accept an electron-pair from adsorbed molecules or an electron from a free radical	Desirable	_	_	_
Ability to accept or donate electrons from redox mediators such as $Fe(CN)_6^{3-/4-}$	_	_	_	Desirable
Reversible electrochemical behavior under an applied bias	_	Essential	_	Essential
High specific surface area	Essential	Essential	Essential	Essential
Moderate to high electrical conductivity either alone or forming a nanocomposite	_	Essential	Essential	Essential
Stable in acidic and/or basic aqueous solutions	Desirable	_	_	Essential
Wide potential window	_	_	_	Essential
Low agglomeration during successive operations	Desirable	Desirable	Desirable	Desirable
Low cost	Essential	Essential	Essential	Essential
Low toxicity (environmentally friendly)	Desirable	Desirable	Desirable	Desirable
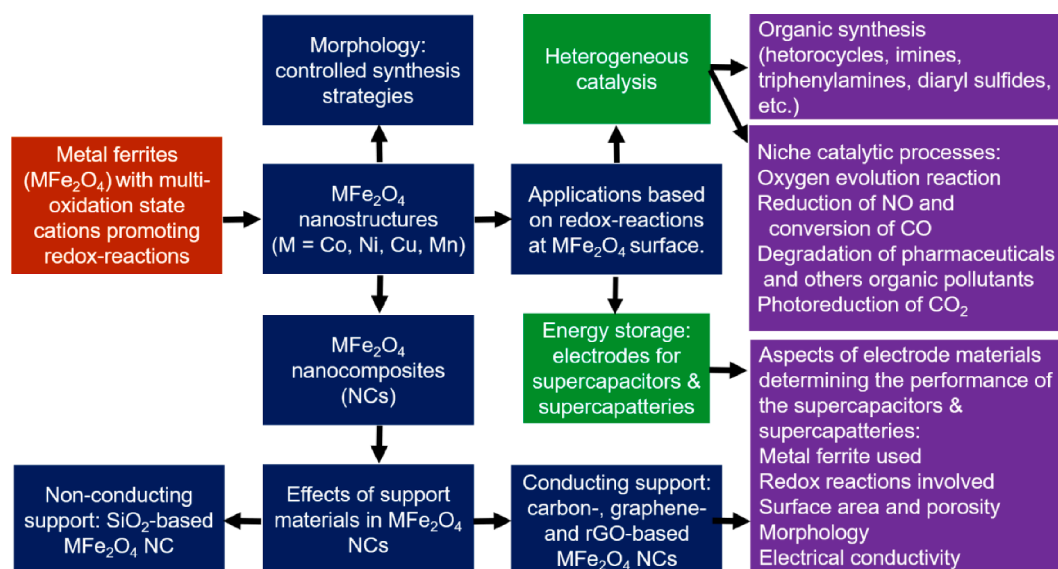
Fig. 1. Schematic summary of metal ferrite nanostructures, nanocomposites and their technological applications.

geometry over a tetrahedral geometry, and is defined as the difference in the crystal field stabilization energies for octahedral and tetrahedral coordination in terms of the d-electron configuration of the cation and the crystal field splitting energy (Δ) [72]. The OSPEs of the Fe^{3+}, Mn^{2+}, Co^{2+}, Ni^{2+} and Cu^{2+} cations are 0.0, 0.0, -31.0, -86.2 and -63.7 kJ/mol, respectively [73]. These differences in the OSPE values explain why the Mn^{2+} cations are located both at the O_h and T_d lattice sites in $MnFe_2O_4$. To some extent, the cation distribution among the O_h and T_d sites also depends on temperature. As demonstrated by Wei et al., the content of Mn^{2+} ions at the O_h sites of air-annealed $MnFe_2O_4$ nanocrystals is sensitive to the annealing history of the sample [74].

To be effective as a chemical catalyst or as an electrocatalyst in SC electrodes, a material requires high surface area as the chemical reactions and charge storage occur at their surfaces. Both crystalline and amorphous materials have been utilized for catalytic and energy storage applications [23,35]. As the cations in amorphous materials and at the outermost surface of crystalline materials frequently possess dangling bonds, they behave like transition metal complexes (i.e., metal cations bonded to ligands such as small organic or inorganic molecules, anions, etc.). Two closely related bonding theories that address the electronic structure of these complexes are the crystal field theory and ligand field theory [75]. In these theories, crystal field splitting energy (Δ) has been used as a measure of the magnitude of metal–ligand interactions [75], which is an important parameter in ligand substitution reactions. The stronger the interaction, the higher the Δ value. The Δ value of a metal complex depends on whether the cation is located at the octahedral (Δ_o) or tetrahedral (Δ_t) site. The crystal field splitting energy values of the cations at the O_h sites (Δ_o) and at T_d sites (Δ_t) are presented schematically in Fig. 2**b**. Since the Δ_o value of Fe^{3+} ions is superior to that of other cations in metal ferrites, this cation exhibits the strongest metal–ligand interaction. In fact, the metal–ligand (M−O in the present case) interaction is significantly weaker for Cu^{2+} and Mn^{2+} ions.

While the energy difference between the barycenter and the triply degenerated (t_{2g}) orbitals of cations at the octahedral sites is $= 2/5*(\Delta_o)$, the energy difference for the doubly degenerate (e_g) orbitals of the octahedral sites is $= 3/5*(\Delta_o)$. The same is true for the cations at the T_d sites, except that Δ_o is replaced by Δ_t. Among the considered cations, Cu^{2+} ions present a strong Jahn-Teller effect, causing a degeneracy breakdown of the t_{2g} and e_g orbitals (Fig. 2**b**). Therefore, in complexes containing Cu^{2+} ions, the Cu-O bonds along the z axis become slightly longer and weaker than the Cu-O bonds along the $\times$ or y axis, making them easier to be substituted by other ligands, facilitating ligand substitutional reactions [76].

On the other hand, the reported standard reduction potentials for the Fe^{3+}/Fe^{2+} and Cu^{2+}/Cu^+ couples [vs. NHE (normal hydrogen electrode)] are 0.77 and 0.16 V, respectively [77]. Therefore, from a thermodynamic point of view, Fe^{3+} and Cu^{2+} ions can accept one electron from other species (i.e., adsorbed molecules). In contrast, reported standard reduction potentials for Mn^{2+}/Mn, Fe^{2+}/Fe, Co^{2+}/Co and Ni^{2+}/Ni couples [vs. NHE] are -1.18, -0.44, -0.28 and -0.24 V [77], respectively; and hence, these four ions cannot accept electron from the adsorbed species easily. Moreover, when a Fe^{3+} or Cu^{2+} ion accepts one electron, it occupies the 3d orbital, while the two electrons received by Mn^{2+}, Fe^{2+}, Co^{2+} or Ni^{2+} ions (if at all occurs in the ferrites) occupy the 4 s orbital. The analysis presented above clearly suggests the superior catalytic activity of $CuFe_2O_4$ ferrite due to its enhanced ability to accept electrons from adsorbed organic molecules, promoting catalytic reactions.

3. Morphology and size-controlled synthesis of metal ferrite (MFe_2O_4, M = Co, Ni, Cu, Mn) nanostructures

Morphology and size are two parameters that broadly define the utility and performance of metal oxide nanostructures in chemical catalysis and energy storage applications [78–81]. While the large surface area of these nanostructures provides ample active sites for
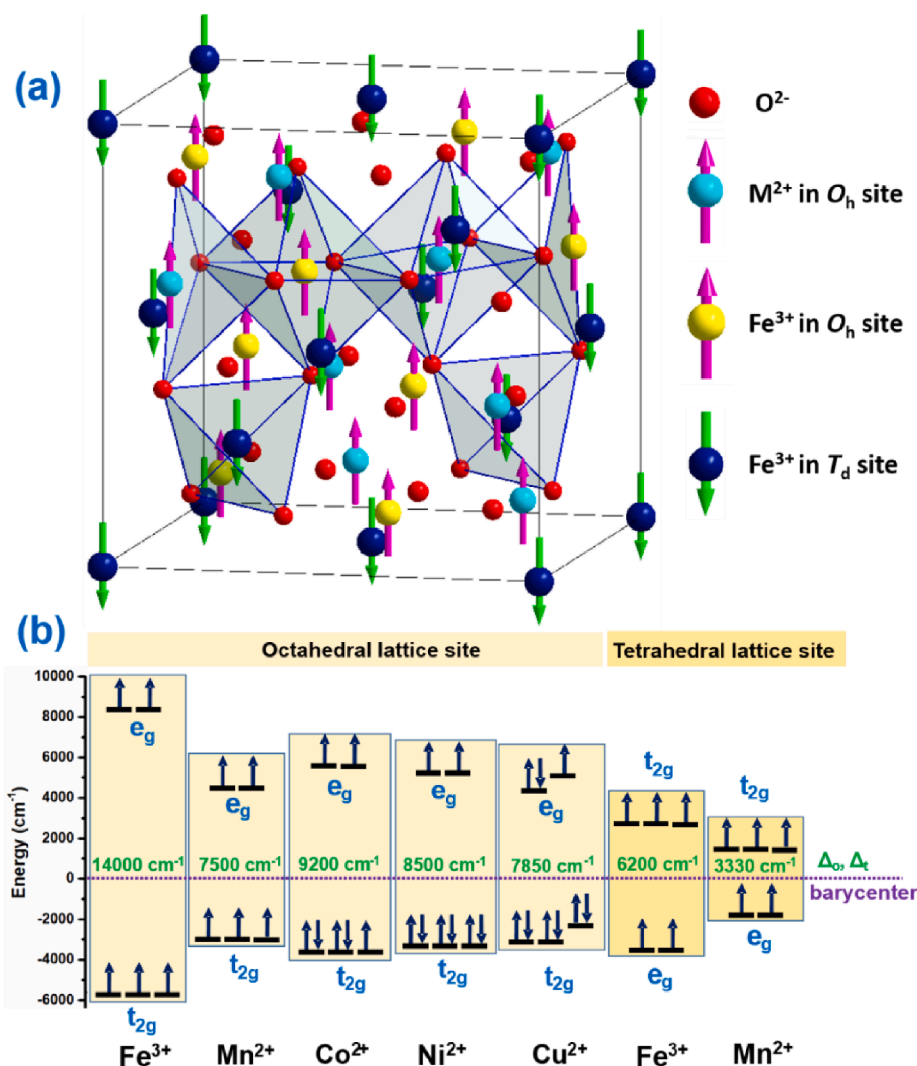
Fig. 2. Schematics of (a) crystallographic structure of spinel MFe_2O_4 (M = Co^{2+}, Ni^{2+}, Cu^{2+}, Mn^{2+}), and (b) crystal field splitting energy (Δ_o) diagram for the cations at O_h sites and T_d sites of the spinels.

catalytic reactions at their surfaces [82–83], their porous texture provides open architecture in supercapacitor electrodes, which allows faster diffusion of ions at the electrolyte–electrode interface [30]. The large surface area of metal oxide nanostructures also provides a higher number of electro-active sites along with providing a larger electrolyte–electrode contact area, leading to a higher charge–discharge capacity of SCs at high current density [32]. Among the nanostructures of different morphologies, 1D structures provide shorter path lengths for ion and electron transport, faster ion insertion/extraction (owing to the small diameter of the 1D structures), and large specific surface area, which facilitate strain relaxation during electrochemical cycling [32]. On the other hand, metal ferrite nanocomposites, especially the graphene-based nanocomposites were seen more effective for catalytic and electrocatalytic applications than the corresponding pure nanostructures. To highlight this fact, we can mention the notable work of Shi et al., who used soft-templates to fabricate composites of graphene and ultrathin MnO_2 nanosheets (thickness ≈ 2 nm) for applying them as SC electrode materials. The asymmetric SCs fabricated using these 2D graphene-MnO_2 nanocomposites exhibited high energy density (97.2 Wh kg^{-1}), with 97% capacitance retention after 10,000 charge–discharge cycles [84]. On the other hand, the superior performance of graphene-based metal ferrite nanocomposites in chemical catalysis has been nicely highlighted by Dhanda et al. [85], where they coupled two amine molecules to generate one imine molecule under solvent-free conditions utilizing a graphene-$CuFe_2O_4$ nanocomposite. Although the reaction yield for bare $CuFe_2O_4$ nanoparticles (NPs) was only 20%, excellent yields (88–95%) under mild reaction conditions were achieved for the nanocomposites. The performance of graphene-based metal ferrite nanocomposites in catalysis and energy storage applications has been observed to be closely dependent on the morphology of metal ferrite nanostructures [43]. Although we do not have sufficient information on the contribution of morphology of metal ferrite nanostructures and their composites in organic catalysis and SCs to draw a definitive conclusion, the roles of size and morphology of the nanostructures in these applications are largely accepted. Considering that the morphology of nanomaterials is a key parameter that plays an important role in

their catalytic and energy storage performance, we present some of the most relevant works dealing with the fabrication of metal ferrite nanostructures with specific morphologies. In general, two strategies have been adapted for the synthesis of metal ferrite nanostructures in bottom-up approach to tailor their morphology: using templates (soft or hard) and without using templates.
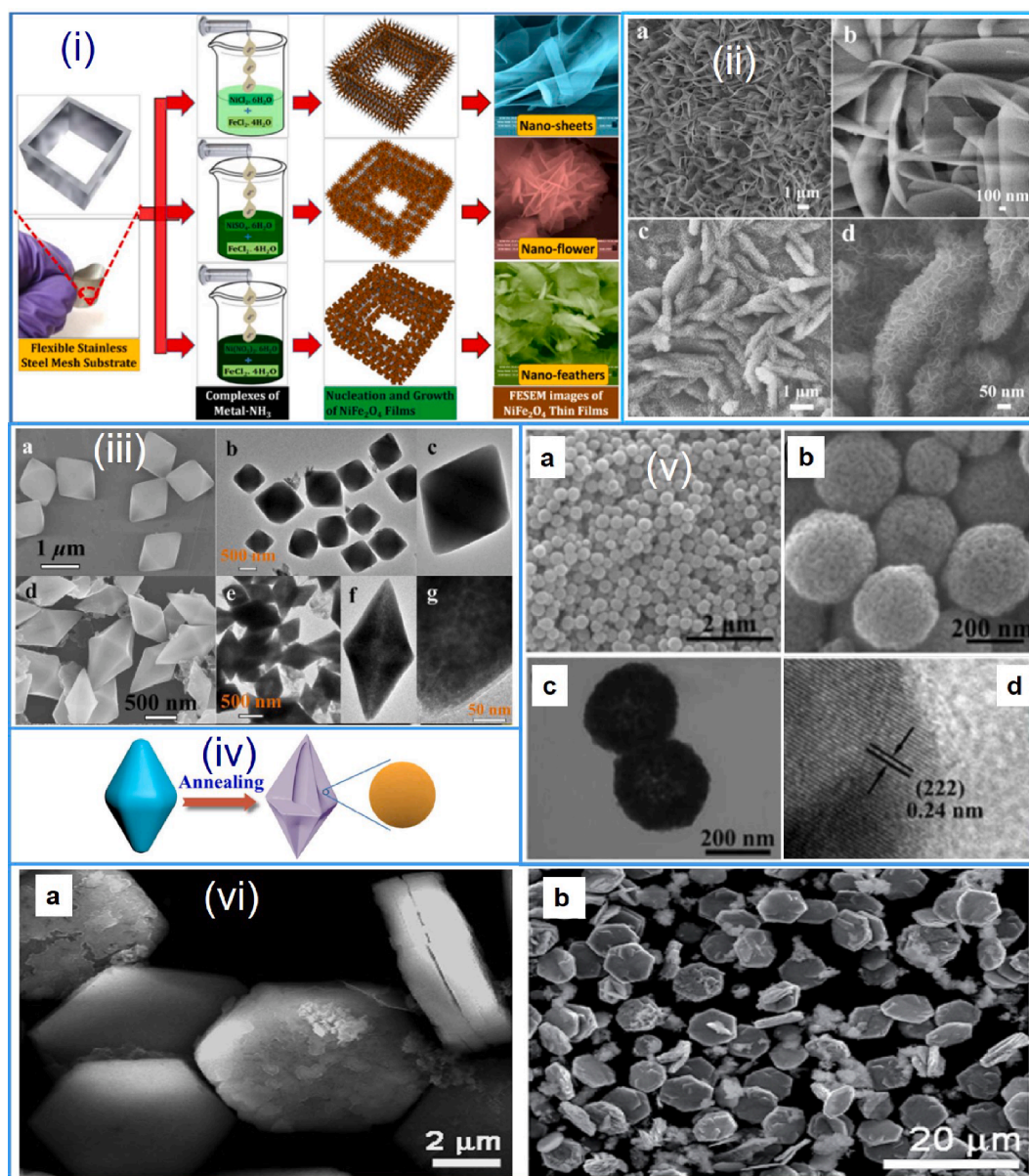

Fig. 3. SEM (scanning electron microscopy)/TEM (transmission electron microscopy) images of MFe$_2$O$_4$ (M = Ni, Co) nanostructures with interesting morphologies. (i) Schematic of the formation mechanisms of NiFe$_2$O$_4$ thin film nano-sheet, nano-flower and nano-feather morphologies through rotating chemical bath deposition [43]. Reproduced with permission from American Chemical Society, Copyright 2018. (ii) SEM images of (a,b) NiFe$_2$O$_4$ nanosheet arrays (NSAs) and (c,d) hierarchical NiFe$_2$O$_4$@MnO$_2$ NSAs grown on Ni foam synthesized by hydrothermal processes [44]. Reproduced with permission from Royal Society of Chemistry, Copyright 2018. (iii) (a) Typical FESEM (field emission scanning electron microscopy) and (b,c) TEM images of Ni/Fe-fumaric acid bimetallic MOF (metal–organic framework) precursors. (d) FESEM image and (e-g) TEM images of NiFe$_2$O$_4$ hexagonal bipyramids fabricated by solvothermal process [98]. (iv) Schematic of the preparation process of hollow NiFe$_2$O$_4$ hexagonal bipyramids [98]. Reproduced with permission from the Centre National de la Recherche Scientifique (CNRS) and Royal Society of Chemistry, Copyright 2018. (v) SEM (a,b), TEM (c) and HRTEM (high-resolution TEM) (d) images of CoFe$_2$O$_4$ nanoporous spheres synthesized through glycol-mediated solvothermal process [39]. Reproduced with permission from the Centre National de la Recherche Scientifique (CNRS) and Royal Society of Chemistry, Copyright 2017. (vi) SEM image of CoFe$_2$O$_4$ platelets synthesized by co-precipitation method [95]. Reproduced with permission from Royal Society of Chemistry, Copyright 2015.

3.1. Template-free synthesis

Although the utilization of solid templates is one of the most ancient technologies for fabricating nanostructures with well-defined morphologies, owing to difficulties associated with template removal and unavailability of templates with desired morphologies, researchers have gradually moved to template-free techniques for fabricating nanostructures with specific morphologies. Depending on the adapted process along with the used precursors, chelating agent, ligand, surfactant and other structure directing agents (SDAs), morphology control of nanostructures in template-free chemical synthesis processes is driven by the preferential adsorption of the SDA species at selected facets of the nanocrystals during their growth [86,87]. In the case of metal ferrites, pH of the reaction mixture along with the nature of precipitating agents, structure-directing agents (e.g., urea), solvents, and small organic molecules (e.g., ascorbic acid, ethylene glycol, glucose) play important roles in controlling the morphology of the nanostructures [88–90]. Recently, researchers started using solid substrates such as stainless steel meshes, nickel foams, or porous carbon particles of specific characteristics which can adsorb metal ion precursors from the reaction solution and support the growth of nanostructures over their surfaces [43,50,54,91–93]. Generally, metal hydroxides are formed at the surface of these supports, which on air annealing, transform to metal ferrites. Although a clear link has not been established, use of different pH-controlling agents (e.g., NH_4F, urea, NaOH, and ammonia solution) has been seen to produce metal ferrite nanostructures of different morphologies with good reproducibility. In some cases, the use of small organic molecules such as ethylene glycol, fumaric acid or hexamethylenetetramine has been seen helpful in controlling the morphology, probably by forming coordination compounds with the precursor cations or by binding the molecules to specific facets of the nanostructures during their growth. While metal ferrite nanostructures with hierarchical morphologies have been reported by a few research groups [44,50], some of the typical morphologies reported extensively in the literature are nanosheets, hexagonal bipyramids, nanospheres, nanorods and nanocubes. Processes involved in the synthesis of such morphology-defined nanostructures are presented below.

Nanosheets. $NiFe_2O_4$ thin films of nanosheet, nanoflower and nanofeather morphologies were fabricated by Bandgar et al. (Fig. 3 **(i)**) through rotating chemical bath deposition (R-CBD) process utilizing three different nickel salts [43]. The authors prepared three solutions by dissolving each of the $NiCl_2$, $NiSO_4$ and $Ni(NO_3)_2$ salts and $FeCl_2$ in 1:2 M ratio in water at 50 °C and adjusting their pH to 10 by dropwise addition of ammonia solution. Stainless steel meshes (3 cm × 1 cm) were immersed in each solution for 3 h. Finally, the substrates were washed, dried and air annealed at 500 °C to transform the formed hydroxides to $NiFe_2O_4$ [43]. Use of nickel chloride, nickel sulfate, and nickel nitrate salts generated $NiFe_2O_4$ nanostructures of sheet, flower, and feather-like morphologies, respectively. Niu et al. synthesized Ru-doped $NiFe_2O_4$ nanosheets over porous Ni foams by electrodeposition [94]. To obtain these nanosheets, they first grew layered $Ni_xFe_yRu_zOH_{(2x+2y+3z)}$ double hydroxide over nickel foams by potentiostatic electrodeposition and then annealed at 300 °C under Ar atmosphere [94]. On the other hand, Zhang et al. (Fig. 3**(ii)**) [44] synthesized hierarchical $NiFe_2O_4@MnO_2$ nanosheet arrays (NSAs) over Ni foams through a two-step hydrothermal process. In their synthesis, $Ni(NO_3)_2$ and urea $\{CO(NH_2)_2\}$ in a 1:16 M ratio were dissolved in deionized water (DI) and then $FeSO_4$ and NH_4F (in a 1:4 M ratio) were added to the solution. The solution and a piece of nickel foam were placed inside a polytetrafluoroethylene (PTFE) vesseled stainless steel autoclave and a hydrothermal treatment (100 °C, 2 h) was carried out. After the hydrothermal treatment, the nickel foam coated with the deposit was washed and dried. The dried nickel foam coated with the $NiFe_2O_4$ precursor was immersed in a dilute 0.05 M $KMnO_4$ solution and a second hydrothermal treatment (140 °C, 4 h) was performed. The product was isolated and air-annealed at 500 °C to generate MnO_2 on the
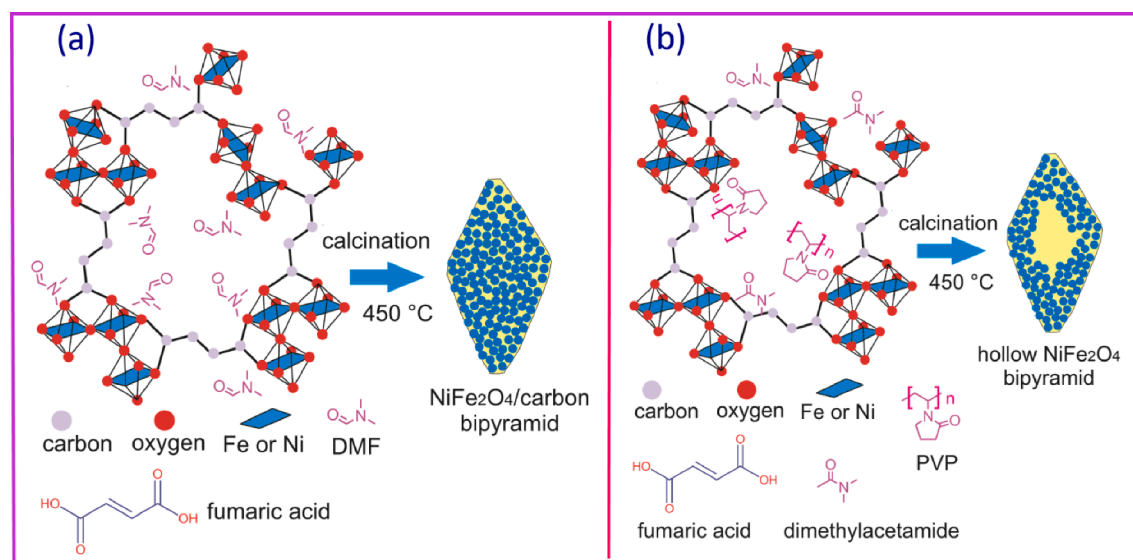

Fig. 4. Schematic representation of mixed-MOF precursor formation assisted by fumaric acid to generate $NiFe_2O_4$ (a) without and (b) with the use of PVP (polyvinylpyrrolidone). While the obtained metal ferrite bipyramids in (a) are porous, in (b) they are porous and hollow. The concept of the scheme was adapted from ref. [99], with permission from Royal Society of Chemistry, Copyright 2017.

surface of the $NiFe_2O_4$ nanosheets [44].

Holey $CuFe_2O_4$ nanosheets have been synthesized over rotating stainless-steel meshes inside a boiling (110 °C) precursor mixture containing $FeSO_4·7H_2O$, $CuSO_4·5H_2O$, urea and NH_4F under reflux for 18 h. On termination of the process, the substrate with the deposited CuFe-hydroxide was washed, dried, and annealed at 500 °C in air atmosphere [91]. In the absence of rotation, holey $CuFe_2O_4$ nanorods were grown over the substrate, instead of holey nanosheets.

On the other hand, using the co-precipitation method, Zhang et al. prepared $CoFe_2O_4$ mesoporous microplatelets (~10 μm diameter) of controlled thickness for high-performance lithium ion battery (LIB) anodes (Fig. 3(vi)) [95]. The thickness of the microplatelets was controlled by changing the concentration of hexamethylenetetramine (HMT) in the reaction solution, which acted as a precipitating agent. A slow and progressive hydrolysis of HMT makes the solution alkaline and induces homogeneous precipitation [96]. The thicker platelets (~2 μm thick) manifested better electrochemical performance than the thinner platelets. The authors found that platelet thickness has a significant impact on the specific capacity and stability of the electrodes. The LIBs fabricated with mesoporous $CoFe_2O_4$ microplatelet electrodes achieved a capacity of 580 mA h g^{-1} (at a current density of 5 A g^{-1}) after 2000 cycles. Metal ferrite nanostructures with sheet-like morphologies have also been utilized as catalysts and electrocatalysts, providing excellent performance in hydrogen evolution reactions (HER) and oxygen evolution reactions (OER), which have been discussed later [94,97].

Hexagonal bipyramids. $NiFe_2O_4$, $CoFe_2O_4$, $MnFe_2O_4$ and $ZnFe_2O_4$ nanostructures with hexagonal bipyramid shapes were synthesized by Jiang et al. [99]. The authors dissolved metal salts and fumaric acid in dimethylformamide (DMF) to create a mixed metal organic framework (mixed-MOF) under hydrothermal conditions at 100 °C. After 4 h of hydrothermal treatment, the formed mixed-MOF was separated and annealed at 450 °C (2 h) to form the corresponding metal ferrite nanostructures embedded in the carbon network (MFe$_2$O$_4$/C, M = Ni, Co, Mn, Zn) [99]. The mixed-MOF exhibited a hexagonal bipyramidal morphology (Fig. 4a). The LIBs fabricated with the nanostructures exhibited high specific capacity (787–962 mA h g^{-1} at a current scan of 200 mA g^{-1}) even after 80 cycles, owing to the (i) percolative (interconnected pores) structure of the nanostructures and their high surface area (~103 m^2 g^{-1}), which facilitate electrolyte diffusion, (ii) good morphology retention during charge–discharge cycles, and (iii) an interconnected carbon network that increases the electrical conductivity of the active materials. Good morphology retention even after 400 charge/discharge cycles in the $ZnFe_2O_4$/C nanostructures is due to the mitigation of volume fluctuations (expansion and contraction) during the lithiation-delithiation process. Owing to the highly porous nature and presence of carbon scaffold, the active material leached during the lithiation (charging) process remains in the vicinity of the electrode, which reincorporates into the electrode during delithiation (discharging).

Several MOFs have been utilized as precursors to generate porous hollow nanostructures by calcination in air under mild conditions (at relatively low temperatures). The MOFs containing bridging ligands (e.g., fumaric acid, terephthalic acid, benzene-1,3,5-tricarboxylate, imidazole, etc.) coordinate with metal centers (Fig. 4) [100,101], and get decomposed during thermal treatment to generate hollow structures. Porous hollow structures are attractive for SC applications as they provide abundant electroactive sites and interconnected channels for fast ion-transport [102]. Other approaches used to generate hollow metal oxide micro/nanostructures include surface-protected etching, Ostwald ripening, exploitation of the Kirkendall effect at nanoscale and galvanic replacement [103,104].

Nanospheres. Porous $NiFe_2O_4$ and $CoFe_2O_4$ nanospheres were fabricated through a glycol-mediated solvothermal process (180 °C, 30 min), followed by thermal treatment at 500 °C for 3 h (Fig. 3(iv)) [39]. Ethylene glycol (EG) was utilized as a solvent to dissolve the metal ion precursors. Ammonium acetate was added to the reaction mixture for a gradual release of NH_3 during heating, which promotes the deprotonation of EG. In fact, the same strategy (use of EG as solvent) has been utilized frequently for the synthesis of several other metal oxide nanostructures with spherical morphology [105,106]. When the salts of first-row transition metals (M) are dissolved in EG and the solution is heated (~180 °C), M(glycolate)$_x$ complexes are formed, which polymerize to form MO_6 polyhedrons bridged with the two oxygen atoms of the glycolate [106,107]. The M(glycolate)$_x$ complexes grow in an isotropic manner, generating spherical particles. Due to the release of gases such as CO, CO_2 and H_2O from the decomposition of organic species (e.g., metal-glycolate complex and glycolate anions), the nanostructures are porous [105]. The BET (Brunauer-Emmett-Teller) estimated specific surface areas of the $CoFe_2O_4$ and $NiFe_2O_4$ nanospheres were 22.8 m^2 g^{-1} and 17.2 m^2 g^{-1}, respectively. The specific pore volumes in the nanostructures were 0.086 cm^3 g^{-1} and 0.082 cm^3 g^{-1}, respectively [39].

Yang et al. synthesized $MnFe_2O_4$ nanospheres of about 5 nm diameter inside porous carbon polyhedrons (PCPs) obtained from a zeolitic imidazole metal–organic framework (ZIF-8) [92]. Their synthesis initiated with the dispersion of PCPs in ethanol under sonication (for 2 h). Then, $Mn(NO_3)_2$ and $Fe(NO_3)_3·9H_2O$ salts were dissolved in the solution sequentially and the pH of the mixture was adjusted between 9 and 10 by adding an ammonia solution. Subsequently, the suspension was hydrothermally treated at 180 °C for 24 h. The obtained product was centrifuged, washed and annealed at 300 °C in an Ar atmosphere for 2 h [92]. On the other hand, spherical $NiFe_2O_4$ NPs of about 17 nm diameter were synthesized by Taylor et al. by a hydrothermal process [108]. For that, $FeSO_4·7H_2O$ and $NiCl_2·6H_2O$ in stoichiometric ratio were dissolved in a water-EG mixture and sodium citrate and hydrazine hydrate were added as the surfactant and reducing agent, respectively. The solution was hydrothermally treated at 120 °C for 20 h [108]. A dimpled Ni electrode modified with these $NiFe_2O_4$ NPs exhibited reduced overpotential and a highly sustained current density for OER in comparison to unmodified dimpled Ni electrodes. As can be noticed, for fabricating spherical metal ferrite nanostructures, most of the researchers adapted hydrothermal/solvothermal technique, although the hydrothermally obtained nanostructures frequently require a post-growth thermal treatment.

Nanorods. Through hydrothermal treatment (160 °C, 10 h) of aqueous nickel nitrate and iron nitrate mixture containing a certain volume of NaOH, Shan et al. synthesized $NiFe_2O_4$ nanostructures of different morphologies by varying only the pH of the reaction mixture [89]. $NiFe_2O_4$ nanorods of ~50 nm diameter, nanooctahedrons of ~150 nm side length and nanospheres of 15–21 nm diameter were obtained by adjusting the pH of the reaction solution to 12, 13, and 7, respectively. Although the utility or performance

of these nanostructures in catalysis or in supercapacitor electrodes was not tested by the authors, they evaluated the magnetic properties of the nanostructures of all three morphologies. While the nanorods and nanospheres exhibited saturation magnetization (M_s) of ~ 40 emu g^{-1}, the M_s value for the nanooctahedrons was 55 emu g^{-1}. These magnetic assessments further confirm the inverse spinel nature of nickel ferrite discussed earlier, as the expected magnetic moment for $NiFe_2O_4$ with inverse-spinel structure is about $2\mu_B$ per formula unit, that is, M_s of ~ 50 emu g^{-1} [109]. The lower M_s values for the nanorods and nanospheres are attributed to their poor crystallinity and smaller sizes.

Yan et al. synthesized mesoporous $MnFe_2O_4$ nanorods (~40 nm diameter and 200 nm – 1 μm length) by simultaneous dropwise addition of two precursor solutions (A and B) into aqueous NH_4Cl solutions of four different concentrations (0, 0.3, 0.55, and 0.8 M) under an Ar atmosphere [110]. The solution A contained $Mn(NO_3)_2 \cdot 6H_2O$ and $Fe(NO_3)_3 \cdot 6H_2O$ salts dissolved in water, while the solution B was 1 M NaOH. Utilization of NH_4Cl in the reaction produced NH_3 (through the reaction of NH_4^+ with OH^- ions), which helped to synthesize porous structures and tailor the length of the nanorods. The resulting four solutions were aged at room temperature for 12 h, and the formed precipitates were filtered, washed and dried at 100 °C (6 h). Finally, the dried samples were annealed in Ar atmosphere at 350 °C (6 h). Interestingly, when the concentration of NH_4Cl in the reaction solution was increased from 0.3 to 0.8

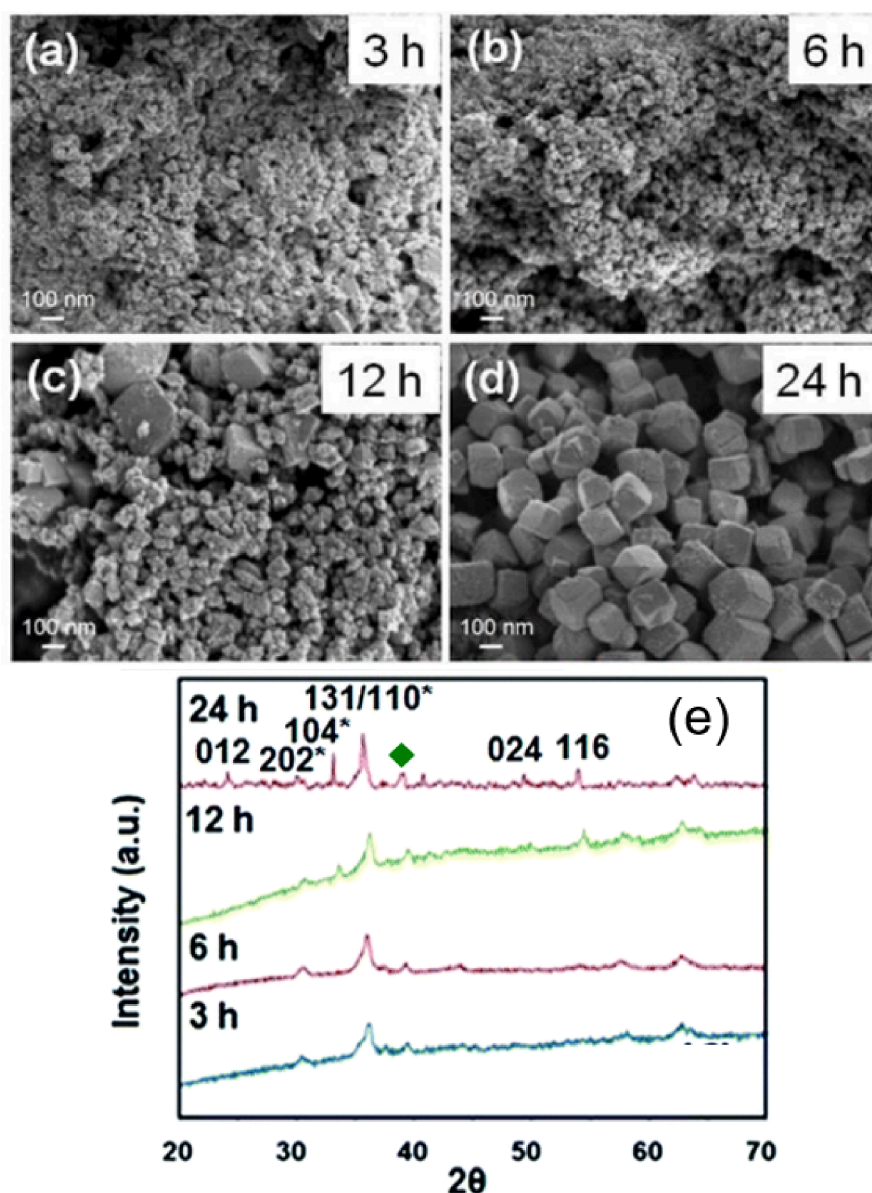**Fig. 5.** (a–d) Typical FESEM micrographs and (e) XRD patterns of $CuFe_2O_4$-Fe_2O_3 nanocomposites prepared at different reaction times [112]. The Miller indices with asterisk symbols in (e) correspond to α-Fe_2O_3 phase and the peak marked with diamond symbol corresponds to CuO phase. Reproduced from ref. [112] with permission from Royal Society of Chemistry, Copyright 2015.

M, the length and diameter of the nanorods decreased, along with the formation of $Fe(OH)_3$ as a byproduct. As NH_4Cl is an acidic salt, initial pH of the 0.3, 0.55, and 0.8 M NH_4Cl solutions were 4.89, 4.76, and 4.67, respectively. These values increased progressively on the reaction of NH_4^+ ions with added (dropwise) NaOH. While the Fe^{3+} ions precipitate at these initial pH values through the formation of $Fe(OH)_3$ [111], Mn^{2+} ions remain dissolved in the solution until the pH is increased beyond 6.0 [111], which explains the formation of the byproduct $Fe(OH)_3$. The fabricated nanorods behaved as excellent electrocatalysts for water oxidation reactions at a relatively low overpotential (~315 meV at 10.0 mA cm^{-2}). On the other hand, through a hydrothermal process, Dhiman et al. synthesized $NiFe_2O_4$ nanorods using $(NH_4)_2Fe(SO_4)_2$ and $NiSO_4·7H_2O$ as precursors, an EG-water mixture (1:3, v/v) as solvent, and oxalic acid as structure-directing agent [88]. The hydrothermal treatment was performed in a Teflon-lined stainless-steel autoclave at 120 °C for 24 h to generate a precipitate, which was washed, dried and air-annealed at 400 °C for 1 h to obtain the $NiFe_2O_4$ nanostructures. However, the obtained nanorods were not uniform in diameter or in length. The obtained $NiFe_2O_4$ nanorods exhibited excellent performance in the photocatalytic degradation of safranine-O and remazol brilliant yellow dyes under visible light in the presence of H_2O_2.

Nanocubes. While reports on the fabrication of cube-shaped metal ferrite nanostructures are relatively scarce, using solvothermal technique, Song et al. fabricated $CoFe_2O_4$ nanostructures of cube-shaped morphology over nickel foams [90]. Dissolving iron (ferrous sulfate) and nickel (nickel chloride) precursors in alcohol-water mixtures of different volumetric ratios and urea as precipitating agent, they could synthesize hollow and solid cube or box-shaped nanostructures over nickel foams. In fact, they could tune the shape of the nanostructures by using different alcohols and alcohol-water volume ratios, keeping the other conditions of hydrothermal treatment fixed (160 °C, 24 h). Using *tert*-butanol/water (75:25, v/v), ethylene glycol/water (50:50, v/v), isobutanol/water (50:50, v/v) and n-butanol/water (50:50, v/v) mixtures as solvents, $CoFe_2O_4$ nanostructures with cube-shaped hollow skeleton (~700 nm), solid nanocubes (~500 nm), porous nanocubes (~50–600 nm) and nanosheets were obtained, respectively. Specific surface area of the $CoFe_2O_4$ nanostructures varied from 51.27 to 19.33 m^2 g^{-1}. On using the nanostructures as active electrode materials in SCs, the cube-shaped hollow nanostructures, which had the highest specific surface area (51.27 m^2 g^{-1}), exhibited highest specific capacitance (848.5F g^{-1} at a scan rate of 10 mV s^{-1}). However, the cube-shaped morphology of the hollow nanostructures was progressively lost during charge–discharge cycling. After 8000 charge–discharge cycles, the specific capacitance of the device also dropped to 60 % of its initial value.

On the other hand, $CuFe_2O_4$-Fe_2O_3 nanocomposites of cube-shaped morphology were synthesized by Oh et al. [112] through co-precipitation near the boiling temperature of water (Fig. 5). For synthesizing the nanostructures, they dissolved $Cu(NO_3)_2·3H_2O$ and $Fe(NO_3)_3·9H_2O$ precursors (in 1:2 M ratio) in DI water under magnetic stirring and adjusted the pH of the reaction mixture between 10 and 11 using 6 M NaOH. The resultant solution was heated at 95 °C under vigorous stirring for different durations [112]. While the reactions of 3 and 6 h produced small (<40 nm) nanostructures of undefined shapes (Fig. 5**a–b**), a reaction of 24 h duration produced cube-shaped nanostructures with edge lengths > 100 nm (Fig. 5**d**) [112]. Formation of such larger cube-shaped composite nanostructures was considered to occur following the (i) nucleation, (ii) self-assembly and growth, and (iii) Ostwald ripening steps. X-ray diffraction (XRD) analysis of the samples through Rietveld refinement revealed that the samples synthesized by 3 and 6 h of reaction were of single $CuFe_2O_4$ phase, while the samples obtained by 12 and 24 h of reaction contained $CuFe_2O_4$ and α-Fe_2O_3 phases (Fig. 5**e**) with a $CuFe_2O_4$/α-Fe_2O_3 ratio of 2:3. From the examples presented above we can see that factors such as pH, presence of structure directing agents, pH-controlling agents (e.g., NH4F, urea, NaOH, and ammonia solution), solvent and reaction time play major roles in determining the morphology of metal ferrite nanostructures. While the post-growth annealing temperature (which is usually < 300 °C) normally does not affect the morphology of the nanostructures, it may alter their dimensions.

3.2. Template-assisted synthesis

Template-assisted growth has been the most successful strategy so far for fabricating morphology defined nanostructures. In fact, both hard and soft templates have been utilized for controlling the morphology of metal ferrite nanostructures. In the hard template strategy, porous solid templates such as porous silica and alumina have been utilized, where the morphology of the nanostructures is defined by the texture of the porous templates. In the soft template strategy, organic polymers, long-chain fatty acids, amines or macromolecules have been utilized frequently as templates. These compounds are added to the reaction mixture at specific concentrations, and the morphology control of the nanostructures is driven by inter-molecular or intra-molecular interaction forces (hydrogen bonding, chemical bonding, and electrostatic interactions). Utilizing a large variety of templates (both hard and soft), metal ferrite nanostructures with several morphologies such as nanosheets, nanospheres, nanorods and nanocubes were fabricated. Here we present some of the most important works reported on the morphology-controlled synthesis of metal ferrite nanostructures using soft and hard templates.

3.2.1. Morphology control using soft template

As stated earlier, utilization of soft templates has been more frequent than hard templates for morphology-controlled synthesis of nanostructures [98,113–117] Metal oxide nanostructures of different morphologies have been fabricated using soft templates. Below we describe the procedures adapted for synthesizing some of these morphology-defined metal ferrite nanostructures. Although the morphologies we present here might not be the most common morphologies of metal ferrite nanostructures synthesized so far, the procedures adapted to synthesize these morphologies are either unique or highly reproducible.

Hexagonal bipyramids. Utilizing PVP as soft template and fumaric acid as organic linker, Song et al. prepared a Ni/Fe-MOF precursor, which on thermal treatment produced porous $NiFe_2O_4$ hexagonal bipyramidal nanostructures with specific surface area as high as 64.78 m^2 g^{-1} (Fig. 3**(iii)–(iv)**) [98]. Adapting a similar procedure but without using PVP, Jiang et al. [99] synthesized $NiFe_2O_4$ hexagonal bipyramidal nanostructures with an even higher specific surface area (103 m^2 g^{-1}). However, utilization of PVP in

Table 2

CoFe$_2$O$_4$ and MnFe$_2$O$_4$ nanostructures of cubic and spherical morphologies synthesized by thermal decomposition of organometallic complexes.

Metal ferrite and their morphology	Method and used solvent	Surfactants (amount)	Precursors (amount)	Concentration of Fe (acac)$_3$, (mmol/liter)	Maximum temp. (°C)	Reaction time	Surfactants /Fe (acac)$_3$ $_M$ ratio	Ref.
MnFe$_2$O$_4$ nanocubes	Thermal decomposition, 20 mL benzyl ether	Oleic acid (6 mmol) and Oleylamine (6 mmol)	Fe(acac)$_3$ (2 mmol) and Mn (acac)$_2$ (1 mmol)[a]	100	295	1 h	6.0	[124]
CoFe$_2$O$_4$ nanocubes	Thermal decomposition, 20 mL dioctyl ether	Oleic acid (4.96 mmol) and Oleylamine (4.96 mmol)	Fe(acac)$_3$ (1.26 mmol) and Co(acac)$_2$ (0.63 mmol)[b]	63	295	1 h	7.9	[121]
CoFe$_2$O$_4$ nanocubes	Solvothermal, 20 mL benzyl alcohol	Oleylamine (12 mmol)	Fe(acac)$_3$ (2 mmol) and Co (acac)$_2$ (1 mmol)	100	175	48 h	6.0	[120]
CoFe$_2$O$_4$ nanospheres	Solvothermal, 20 mL benzyl alcohol	Oleic acid (12 mmol)	Fe(acac)$_3$ (2 mmol) and Co (acac)$_2$ (1 mmol)	100	175	48 h	6.0	[120]
CoFe$_2$O$_4$ nanocubes	Thermal decomposition, 20 mL benzyl alcohol	Oleic acid (7.9 mmol)	Fe(acac)$_3$ (–) and Co(acac)$_2$ (–)	–	290	30 min	–	[123]
CoFe$_2$O$_4$ nanospheres	Thermal decomposition, 40 mL benzyl ether	Oleic acid (9.45 mmol) and Oleylamine (9.11 mmol)	Fe(acac)$_3$ (–) and Co(acac)$_2$ (–)	–	290	45 min	–	[123]
CoFe$_2$O$_4$ nanohexagons	Thermal decomposition, 15 mL benzyl alcohol	Oleic acid (7.9 mmol)	Fe(acac)$_3$ (–) and Co(acac)$_2$ (–)	–	290	90 min	–	[123]
CoFe$_2$O$_4$ nanospheres	Thermal decomposition, 40 mL benzyl ether	Oleic acid (7.9 mmol)	Fe(acac)$_3$ (1.2 mmol) and Co (acac)$_2$ (0.6 mmol)	30	280	20 min	6.6	[122]
CoFe$_2$O$_4$ nanocubes	Thermal decomposition, 30 mL benzyl ether	Oleic acid (7.9 mmol)	Fe(acac)$_3$ (1.2 mmol) andCo (acac)$_2$ (0.6 mmol)	40	280	40 min	6.6	[122]
CoFe$_2$O$_4$ nanohexagons	Thermal decomposition, 20 mL benzyl ether	Oleic acid (7.9 mmol)	Fe(acac)$_3$ (1.2 mmol) and Co (acac)$_2$ (0.6 mmol)	60	280	90 min	6.6	[122]
CoFe$_2$O$_4$ nanocubes	Thermal decomposition, 20 mL 1-octadecene	Oleic acid (1.77 mmol)	(Co^{2+}Fe^{3+})-oleate complex (5 g)	–	320	120 min	–	[125]

[a] 10 mmol of 1,2-hexadecanediol (HDD) was used as an additive.

[b] 1.5 mmol of HDD was used as an additive.

Table 3

Summary of the template-assisted and template-free synthetic approaches adapted for obtaining the MFe_2O_4 (M = Ni, Co, Mn, Cu) nanostructures of different morphologies.

Morphology	Metal ferrite	Used precursors	Solvent, structure directing agent (SDA) and substrate or template	pH	Synthetic approach and temperature	Annealing temperature and atmosphere	Surface area (m^2 g^{-1})	Application	Ref.
Nanostructures synthesized using template-free methods									
Nanosheets	$NiFe_2O_4$	$NiCl_2$ $FeCl_2$	Solvent: water SDA: none Substrate: stainless steel mesh	10[c]	Rotating chemical bath deposition; 50 °C	500 °C (air)	47	SCs	[43]
Nanoflower	$NiFe_2O_4$	$NiSO_4$ $FeCl_2$	Solvent: water SDA: none Substrate: stainless steel mesh	10[c]	Rotating chemical bath deposition; 50 °C	500 °C (air)	25	SCs	[43]
Nanofeather	$NiFe_2O_4$	$Ni(NO_3)_3$ $FeCl_2$	Solvent: water SDA: none Substrate: stainless steel mesh	10[c]	Rotating chemical bath deposition; 50 °C	500 °C (air)	11	SCs	[43]
Nanosheets	Ru-doped $NiFe_2O_4$	$Ni(NO_3)_3$ $FeSO_4$	Solvent: water SDA: none- Substrate: Ni foam	–	Electrodeposition	300 °C (Ar)	–	HER	[94]
Nanosheets	$NiFe_2O_4@MnO_2$	$Ni(NO_3)_3$ $FeSO_4$, $KMnO_4$ solution	Solvent: water SDA: $CO(NH_2)_2$ & NH_4F. Substrate: Ni foam	10	Two-step hydrothermal process; 100 and 140 °C.	500 (air)	132	SCs	[44]
Holey nanosheets	$CuFe_2O_4$	$CuSO_4$ $FeSO_4$	Solvent: water SDA: $CO(NH_2)_2$ & NH_4F. Substrate: none	–	Rotating chemical bath deposition in a reflux for 18 h, 110 °C.	500 °C (air)	74	SCs	[91]
Hexagonal bipyramids	$NiFe_2O_4$, $CoFe_2O_4$, $MnFe_2O_2$, $ZnFe_2O_4$	$Ni(NO_3)_2$ $Co(NO_3)_2$ $Mn(NO_3)_2$ $Zn(NO_3)_2$ $Fe(NO_3)_3$	Solvent: DMF SDA: fumaric acid Substrate: none	–	Hydrothermal (100 °C, 4 h)	400 °C (air)	103	LIBs	[99]
Nanospheres	$NiFe_2O_4$, $CoFe_2O_4$,	$FeCl_2$ $Co(CH_3COO)_2$	Solvent: ethylene glicol SDA: ammonium acetate Substrate: none	–	Solvothermal (180 °C, 30 min)	500 °C (–)	17.2 & 22.8	LIBs	[39]
Nanospheres	$MnFe_2O_4$	$Mn(NO_3)_2$ $Fe(NO_3)_3$	Solvent: ethanol SDA: none Substrate: carbon from decomposited ZIF-8.	9–10[c]	Hydrothermal (180 °C, 24 h)	300 °C (Ar)	187	SCs	[92]
Nanospheres	$NiFe_2O_4$	$NiCl_2$ $FeSO_4$	Solvent: mixture water-ethylene glycol. SDA: sodium citrate Substrate: none	–	Hydrothermal (120 °C, 20 h)	–	–	OER	[108]
Nanorods	$NiFe_2O_4$	$Ni(NO_3)_2$ $Fe(NO_3)_3$	Solvent: water SDA: none Substrate: none	12[d]	Hydrothermal (160 °C, 10 h)	–	–	–	[89]
Nanorods	$MnFe_2O_4$	$Mn(NO_3)_2$, $Fe(NO_3)_3$	Solvent: water SDA: NH_4Cl solution Substrate: none	10[d]	Coprecipitation in argon atmosphere.	350 °C (Ar)	85	OER	[110]
Nanorods	$NiFe_2O_4$						758		[88]

(*continued on next page*)

Table 3 (*continued*)

Morphology	Metal ferrite	Used precursors	Solvent, structure directing agent (SDA) and substrate or template	pH	Synthetic approach and temperature	Annealing temperature and atmosphere	Surface area (m² g⁻¹)	Application	Ref.
		$(NH_4)_2Fe(SO_4)_2$ $NiSO_4$	Solvent: mixture water-ethylene glycol. SDA: oxalic acid Substrate: none	–	Hydrothermal (160 °C, 10 h)	400 °C (air)		Degradation of dyes	
Nanocubes	$CoFe_2O_4$	$NiCl_2$ $FeSO_4$	Solvent: mixture water-*tert*-butanol. SDA: $CO(NH_2)_2$ and NH_4F. Substrate: Ni foam	– (c)	Hydrothermal (160 °C, 24 h)	300 °C (–)	51.3(a)	SCs	[90]
Nanocubes	$CuFe_2O_4$(g)	$Cu(NO_3)_2$ $Fe(NO_3)_3$	Solvent: water SDA: none Substrate: none	10–11(d)	Coprecipitation (95 °C, 24 h)		63	Oxidation of bisphenol A	[112]
Hexagonal bipyramids	$NiFe_2O_4$	$Ni(NO_3)_2$ $Fe(NO_3)_3$	Solvent: dimethylacetamide SDA: fumaric acid Template: PVP	–	Solvothermal (100 °C, 8 h)	450 °C (air)	64.78	Sensing propanol	[98]
Nanostructures synthesized using soft templates									
Nanospheres	$NiFe_2O_4$	$Ni(NO_3)_2$ $Fe(NO_3)_3$	Solvent: ethanol SDA: none Template: pluronic F127	–	Aerosol spray pyrolysis (400 °C, -)	300 °C (air)	278	H_2 photogeneration	[113]
Nanospheres	$CuFe_2O_4$	$CuCl_2$ $FeCl_3$	Solvent: ethylene glycol SDA: sodium acetate Template: PVP	–	Hydrothermal (160 °C, 24 h)		57.7	SCs	[114]
Nanofibers	$NiFe_2O_4$	$Ni(NO_3)_2$ $FeCl_3$	Solvent: mixture water–ethanol SDA: citric acid and DMF. Template: PVP	–	electrospinning	550 °C (–)	41.7	SCs	[118]
Nanorods	$CoFe_2O_4$	$Co(NO_3)_2$ $Fe(acac)_3$	Solvent: mixture ethanol-DMF SDA: none Template: terephthalic acid	–	Hydrothermal (120 °C, 12 h)	400 °C (air)	60.4	Oxidation of bisphenol A	[119]
Nanocubes	$CoFe_2O_4$	$Co(CH_3COO)_2$; $Fe(NO_3)_3$	Solvent: isopropyl alcohol/ water mixture SDA: none- Template: CTAB	– (e)	Hydrothermal (180 °C, 24 h)	350 °C (–)	102.4	SCs	[115]
Nanostructures synthesized using hard templates									
Nanospheres	$NiFe_2O_4$	$Ni(NO_3)_2$ $Fe(NO_3)_3$	Solvent: ethanol SDA: none Template: KIT-6 mesoporous silica	–	Thermal treatment (300 °C, 2 h)	550 °C (air)	123.4	Li-O_2 batteries	[116]
Nanorods	$NiFe_2O_4$	$NiSO_4$, γ-FeOOH nanorods	Solvent: water SDA: Na_2CO_3 Template: γ-FeOOH nanorods	–	Adsorption of Ni^{2+} ions over γ-FeOOH nanorods (24 h)	900 °C (–)	–	–	[126]
Microtubes	$NiFe_2O_4$ $CoFe_2O_4$	$(NH_4)_2Fe(SO_4)_2$	Solvent: water SDA: Na_2CO_3 and	– (f)	Solvothermal (200 °C, 12 h)		54.6 47.6	HER and OER	[117]

Table 3 (*continued*)

Morphology	Metal ferrite	Used precursors	Solvent, structure directing agent (SDA) and substrate or template	pH	Synthetic approach and temperature	Annealing temperature and atmosphere	Surface area (m^2 g^{-1})	Application	Ref.
		Ni(CH$_3$COO)$_2$ Co(CH$_3$COO)$_2$	polyacrylamide Template: α-MnO$_2$ nanowires			—			

(a): The surface area value corresponds to the nanocubes along with the Ni foam. (b) Progressively increased adding NaOH solution dropwise. (c), (d), (e), (f) Solutions used to adjust or control the pH were ammonia, NaOH, ammonia-ammonium acetate, and Na$_2$CO$_3$, respectively. (f) Fe$_2$O$_3$ was obtained as impurity.

the former case helped to produce hollow nanostructures. Although both the research groups used the same organic linker to generate the MOF, Jiang et al. used DMF and Song et al. used dimethylacetamide as solvent (Fig. 4). The other difference between the nanostructures fabricated by these two groups is their carbon content. While the $NiFe_2O_4$ bipyramids grown by Jiang et al. had a high carbon content, the nanostructures prepared by Song et al. had very low carbon content. Although the porous hexagonal bipyramids fabricated by Song et al. have not been tested in catalysis or SC electrodes, they exhibited excellent n-propanol sensing performance at a relatively low operating temperature (120 °C). However, the $NiFe_2O_4$ nanostructures fabricated by Jiang et al. exhibited high specific capacity (962 mA h g^{-1} at current rate of 200 mA g^{-1}) when used as anode in LIBs.

Nanospheres. Mesoporous $NiFe_2O_4$ spheres of sub-micrometric dimensions were fabricated by spray pyrolysis of a precursor solution utilizing Pluronic F127 as a structure-directing agent [113]. The oxygen atoms of Pluronic F127 chains, [–OCH$_2$CH(CH$_3$)-]$_n$ bind with the high energy facets of the crystallites and reduce their surface energies, preventing their preferential growth along any specific crystal plane or direction. Because of the high specific surface area (121 m^2 g^{-1}) and good crystallinity of the nanospheres, they revealed substantial photocatalytic activity for H_2 evolution (0.09 μmol h^{-1}) from a water-methanol mixture under visible light (λ > 420 nm) irradiation. On the other hand, utilizing a glycol-mediated hydrothermal process, Zhu et al. synthesized $CuFe_2O_4$ nanospheres with hierarchical pore structures [114]. They dissolved $CuCl_2 \cdot 2H_2O$, $FeCl_3 \cdot 6H_2O$, CH_3COONa (sodium acetate, NaAc) and PVP in EG under magnetic stirring and treated the mixture hydrothermally at 160 °C (24 h) in a Teflon-lined autoclave. The authors found that the size of the nanospheres increases with the concentration of sodium acetate. Moreover, by replacing PVP with sodium dodecyl sulfate (SDS) and cetyltrimethylammonium bromide (CTAB), they obtained $CuFe_2O_4$ nanostructures of irregular and flower-shaped morphologies, respectively. The porous nanospheres synthesized using sodium acetate and PVP had a high specific surface area (57.7 m^2 g^{-1}) and exhibited good specific capacitance (320F g^{-1}) when utilized as electrode material for SCs.

Nanofibers and Nanorods. $NiFe_2O_4$ nanofibers (~200 nm diameter) could be produced through electrospinning using citric acid and PVP in a metal precursor solution [118]. The nanofibers were utilized to fabricate micro-supercapacitors [118]. On the other hand, utilizing a hydrothermal process, Yang et al. prepared rod-like Co/Fe-MOF nanostructures with an average length of ~ 2 μm and ~ 200 nm average diameter [119]. On air-annealing (400 °C, 1 h), the Co/Fe-MOF nanostructures converted to porous $CoFe_2O_4$ nanorods decorated with small (<40 nm) $CoFe_2O_4$ NPs. The porous 1D structures of high BET surface area (60.4 m^2 g^{-1}) were utilized successfully as catalysts for the degradation of bisphenol A, assisted by peroxymonosulfate.

Nanocubes. Fan et al. [115] synthesized porous hollow $CoFe_2O_4$ nanocubes using ferric nitrate and cobalt acetate as metal precursors and CTAB as surfactant. The precursors in stoichiometric ratio along with the surfactant were dissolved in an isopropyl alcohol/water mixture (1:1, v/v) and an ammonia-ammonium acetate buffer solution was used to adjust the pH (pH = 11) of the reaction mixture. The final mixture was hydrothermally treated at 180 °C for 24 h. The obtained solid was washed with DI water and absolute ethanol, dried at 60 °C under vacuum, and calcined at 350 °C (4 h). The morphology of the nanostructures could be tuned by adjusting the precursor-to-surfactant ratio. While for a high cobalt acetate/CTAB molar ratio (~13:1) they obtained $CoFe_2O_4$ nanospheres, for a low cobalt acetate/CTAB ratio of 10:9, nanocubes (~80 nm edge length) were obtained. The SCs fabricated using these porous hollow nanocubes exhibited a high specific capacitance (816F g^{-1} at a current density of 15 A g^{-1}) and good rate capability. The outstanding performance of the SCs has been ascribed to the high surface area (102.37 m^2 g^{-1}), small pore size (~10 nm) and hollow structure of the nanostructures, which provided good wettability and efficient charge transfer. On the other hand, through thermal dissociation of metal acetylacetonate (acac) and metal oleate precursors, several research groups synthesized $CoFe_2O_4$ and $MnFe_2O_4$ nanostructures of cubic, spherical and hexagonal morphologies. The principal synthesis parameters that induce cubic morphology (instead of spherical or hexagonal) in $CoFe_2O_4$ and $MnFe_2O_4$ nanostructures are the concentration of precursors, surfactant/Fe(acac)$_{3 M}$ ratio, temperature, and reaction time [120–125]. The reaction parameters used for the synthesis of $CoFe_2O_4$ and $MnFe_2O_4$ nanostructures in the thermal dissociation of metal(acac) and metal oleate precursors are presented in Table 2. As can be seen in the Table, for thermal dissociation synthesis of metal ferrites, metal complexes such as metal-acetylacetonate (acac) or metal-oleate were often utilized as precursors; benzyl ether, dioctyl ether, benzyl alcohol or 1-octadecene were used as solvents; and oleic acid and/or oleylamine were used as surfactants. Generally, the thermal dissociation reactions were performed under N_2 or Ar atmosphere and the reaction mixtures are heated progressively up to the boiling point of the solvent (280–320 °C) for 45–120 min. By varying the ratio of surfactant/Fe(acac)$_3$ [120,124], concentration of surfactant [121,122], or using different surfactants (e.g., oleic acid by oleylamine) [120], metal ferrite nanostructures of different morphologies could be synthesized.

As can be noted in Table 2, metal ferrite nanostructures of several morphologies can be obtained using soft templates. However, utilization of thermal decomposition technique for synthesizing cube-shaped nanostructures has some disadvantages such as the use of expensive solvents, the chemical reactions are needed to be carried out under N_2 or Ar atmosphere, and difficulty in removing the surfactant residues by water washing. Repetitive centrifugation, decantation, and resuspension of the product in water or buffer solution are often required. Moreover, a rigorous control of the experimental parameters is required for obtaining homogeneous morphology of the nanostructures. On the other hand, metal ferrite nanostructures of hexagonal bipyramid and fiber-like morphologies are easier to synthesize using solvothermal and electrospinning techniques, respectively. However, a calcination process is required to obtain pure metal ferrite nanostructures while using these techniques, which generate undesired CO and CO_2 gases in large quantities due to the thermal decomposition of organic linkers (used to prepare the MOFs) or polymers such as PVP. The examples included in this section clearly demonstrate that the presence of soft template induces the formation of hollow and/or porous metal ferrites with high specific surface area (in the range of 57.7–121 m^2 g^{-1}). In Table 3 we provide a summary of the template-assisted and template-free synthetic approaches adapted frequently.

3.2.2. Morphology control using hard template

Use of hard template is probably the most convenient way for controlling the morphology of metal, metal oxide and metal ferrite

nanostructures. Although the utilization of hard templates for morphology-controlled nanostructure synthesis is becoming obsolete due to the constraints mentioned earlier, Li et al. [116] fabricated three-dimensional ordered mesoporous $NiFe_2O_4$ nanostructures of quasispherical morphology with tunable pore size (5.0 to 25 nm) utilizing KIT-6 mesoporous silica templates. The mesoporous silica templates were impregnated with an ethanolic solution of nickel and iron nitrate salts (1:2 M ratio) under magnetic stirring and then heated at 300 °C for 2 h to evaporate the solvent after pyrolyzing the precursors inside the pore structure of the silica template. After repeating the process for 2 more times, the sample was annealed at 550 °C (5 h) and then the silica matrix was removed by NaOH (2 M) etching at 60 °C [116].

Using γ-FeOOH and α-FeOOH nanorods as hard sacrificial templates, Cao et al. synthesized $NiFe_2O_4$ nanorods through chemical precipitation-topotactic reactions [126]. For the fabrication of $NiFe_2O_4$ nanorods from γ-FeOOH and α-FeOOH, they mixed the pre-fabricated γ-FeOOH or α-FeOOH nanorods with $NiSO_4 \cdot 6H_2O$ and Na_2CO_3 in water, keeping the Ni^{2+}/Fe^{3+} ion ratio in the mixture 1:2. Then an aqueous solution of Na_2CO_3 was added to the previous solution, maintaining the Ni^{2+}/Na^+ ion ratio 1:2 in the final mixture. After 24 h of resting, the product was filtered and dried at 60 °C for 3 h. The obtained materials, which were the $NiCO_3$ layer (amorphous)-coated γ-FeOOH or α-FeOOH nanorods were considered as precursors for obtaining $NiFe_2O_4$ nanorods. The prepared precursors were calcined at 900 °C for 2 h to obtain the $NiFe_2O_4$ nanorods of several micrometer lengths (Fig. 6a). The $NiFe_2O_4$ nanorods obtained using α-FeOOH nanorods as templates were of 0.3–1.0 μm lengths (aspect ratios between 6 and 12) and the $NiFe_2O_4$ nanorods obtained using γ-FeOOH nanorods as templates were of 3–8 μm lengths (aspect ratios between 4 and 5). During calcination, at relatively lower temperature (around 350 °C), the α-FeOOH (γ-FeOOH) nanorods used as template, get dehydrated to produce α-Fe_2O_3 (γ-Fe_2O_3) and $NiCO_3$ layer decomposes to form NiO. At higher temperature (above 500 °C), the two compounds react to form $NiFe_2O_4$ nanostructures maintaining the shape of the FeOOH sacrificial templates. The authors studied the magnetic behavior of the fabricated $NiFe_2O_4$ nanorods.

Utilizing a similar strategy Yuan et al. synthesized tubular $NiFe_2O_4$, $CoFe_2O_4$ and Fe_3O_4 nanostructures using FeOOH microtubes as sacrificial templates (Fig. 6**b-f**). [117]. For preparing the FeOOH microtubes, they mixed about 45 mg (~0.517 mmol) of prefabricated (through hydrothermal synthesis) α-MnO_2 nanowires and 392 mg (1.0 mmol) of $(NH_4)_2Fe(SO_4)_2 \cdot 6H_2O$ in a mixture of 24 mL of DI water and 6 mL of EG, and refluxed inside a three-necked flask at 120 °C for 4 h. To prepare the $NiFe_2O_4$, $CoFe_2O_4$ and Fe_3O_4 nano-/microtubes, first a certain amount of polyacrylamide (PAM) was mixed with the FeOOH microtubes suspension and refluxed at 120 °C under stirring for 30 min. After cooling to room temperature, certain amounts of metal salt (i.e. ammonium iron(II) sulfate, ferrous sulfate, cobalt(II) acetate or nickel(II) acetate) and sodium acetate were added to the earlier solution and treated hydrothermally (in a Teflon-lined stainless-steel autoclave) at 200 °C for 12 h. On cooling, the product was magnetically separated and dried at 60 °C for 12 h. The roles of the polyacrylamide and sodium acetate were to increase the viscosity and adjust the pH of the reaction mixture, respectively. The tubular, porous metal-ferrite microstructures had high specific surface area (47.60 m^2g^{-1} for $CoFe_2O_4$, 54.63 m^2g^{-1} for $NiFe_2O_4$, and 39.49 m^2g^{-1} for Fe_3O_4) and rendered good performance in electrocatalytic OER and HER in 1.0 M KOH electrolyte with high (50 h) durability.
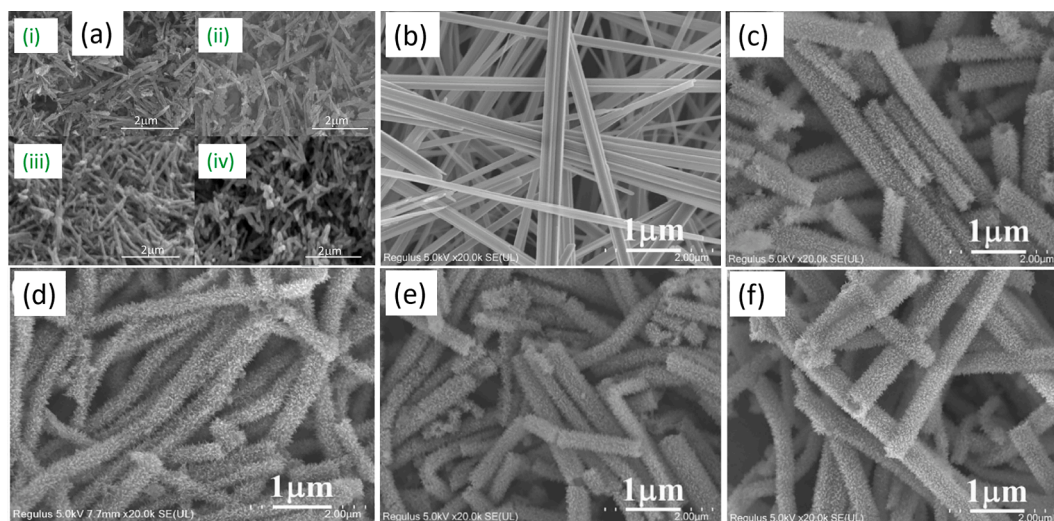

Fig. 6. (a) Typical SEM images of (i) γ-FeOOH and (ii) α-FeOOH nanorods used as sacrificial templates for the synthesis of $NiFe_2O_4$ nanorods; (iii) and (iv) correspond to $NiFe_2O_4$ nanorods obtained using γ-FeOOH and α-FeOOH nanorods as sacrificial templates, respectively. Reproduced from ref. [126] with permission from Elsevier, Copyright 2018. (b)-(f) Representative FESEM images of hard templates and the obtained metal ferrites: (b) α-MnO_2 nanowires utilized as templates, (c) FeOOH microtubes, (d) $CoFe_2O_4$ microtubes, (e) Fe_3O_4 microtubes, and (f) $NiFe_2O_4$ microtubes. Reproduced from ref. [117] with permission from Elsevier, Copyright 2019.

3.3. Metal ferrite (MFe$_2$O$_4$, M = Co, Ni, Cu) nanocomposites

Metal ferrite nanocomposites, i.e., metal ferrite nanostructures embedded or incorporated into conducting and nonconducting supports, have been fabricated by several research groups to enhance their performance in catalysis and energy storage devices. Generally, these nanocomposites perform better than bare metal ferrite nanostructures in the photoelectrochemical reduction of CO$_2$ to methanol [127], OER [58], photocatalytic oxidation of phenol [128], degradation of antibiotics and dyes [112,129,130], synthesis of coumarin-based 1,4-dihydropyridines [131], and as electrode materials in SCs and LIBs because of their enhanced electron transfer abilities through conducting supports. Growth of ultrasmall (~6 nm average size) NiFe$_2$O$_4$ NPs over graphene has been reported by Yan et al. [132]. For that, they first deposited Ni$_3$O$_2$(OH)$_4$ and Fe(OH)$_3$ on the surface of graphene by heating (80 °C for 10 h) graphene sheets in ethanol, nickel acetate, ferric acetylacetonate, water and ammonia mixture. After freeze-drying, the product was thermally treated in an electric furnace at 350 °C for 3 h under the flow of an Ar/H$_2$ mixture. The hydroxides anchored to the graphene surface were converted to NiFe alloy during annealing in inert ambient. Finally, the composite was air-annealed at 200 °C for 3 h and at 280 °C for 3 h, sequentially. The well-dispersed nanoparticles on the graphene sheets exhibited excellent electromagnetic wave (EMW) absorption properties [132]. Xiong et al. synthesized CoFe$_2$O$_4$/graphene/polyaniline hierarchical nanocomposites for high-performance supercapacitors using a hydrothermal method, followed by polyaniline coating through *in situ* polymerization of aniline [133]. Interestingly, the size of the CoFe$_2$O$_4$ nanostructure was affected by the presence of graphene, as their size increased with the increase of precursor/graphene ratio [133]. Flexible CoFe$_2$O$_4$/rGO (reduced graphene oxide) nanocomposite aerogels used as anodes in SCs were obtained by Zheng et al. [45]. For that, DI water dispersed rGO (prepared by a modified Hummers′ method) was mixed with a
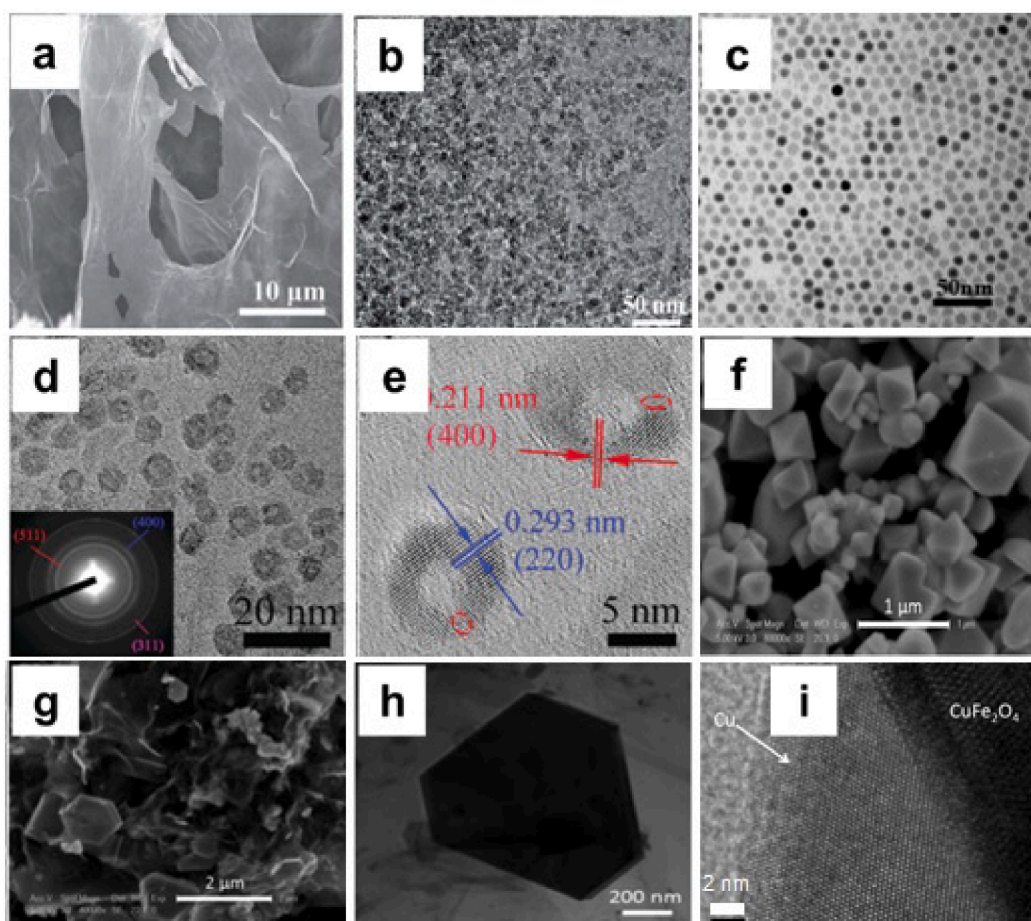

Fig. 7. Typical (a) SEM and (b) TEM images of CoFe$_2$O$_4$/rGO hybrid hydrogel [45]. Reproduced with permission from Royal Society of Chemistry, Copyright 2018. (c) TEM image of core–shell MnFe$_2$O$_4$@CoFe$_2$O$_4$ nanocrystals [134]. Reproduced with permission from American Chemical Society, Copyright 2018. (d) TEM and (e) HRTEM images of hollow CoFe$_2$O$_4$ nanoparticles grown on graphene [136]. The inset of (d) shows corresponding selected area electron diffraction (SAED) pattern. Reproduced from ref. [136] with permission from Royal Society of Chemistry, Copyright 2018. (f, g) SEM images of Cu/CuFe$_2$O$_4$ composite obtained by hydrothermal method without (f) and (g) using graphene substrate [137]. (h) TEM image of representative CuFe$_2$O$_4$ hexagonal platelet anchored on graphene [137]. (i) HRTEM image of metallic Cu attached to the edge of CuFe$_2$O$_4$ hexagonal platelet in the Cu/CuFe$_2$O$_4$/graphene composite [137]. Images in (f-i) correspond to the same sample. Reproduced with permission from Royal Society of Chemistry, Copyright 2014.

separately prepared EG solution containing $Co(NO_3)_2 \cdot 6H_2O$, $Fe(NO_3)_2 \cdot 6H_2O$ and CH_3COONa. The mixed solution was hydrothermally treated at 180 °C (12 h) in a Teflon-lined autoclave. The product was washed and freeze-dried under vacuum to obtain the $CoFe_2O_4$/ rGO hybrid hydrogel (Fig. 7**a and b**). The SCs fabricated using this hybrid hydrogel revealed enhanced capacity retention (87%) after 4000 cycles and long-term stability without obvious capacity fading at high current density (5 A g^{-1}) [45]. Song and Zhang synthesized $MnFe_2O_4$ nanocrystals of about 6 nm average size and used them to fabricate core–shell $MnFe_2O_4@CoFe_2O_4$ nanostructures with varied shell thickness (0.75, 1, 2 and 2.5 nm) (Fig. 7**c**) [134,135]. The authors also synthesized 6 nm $CoFe_2O_4$ nanocrystals and core–shell $CoFe_2O_4@MnFe_2O_4$ nanostructures with shell thicknesses of 0.5, 1, 2 and 3 nm. To prepare the $CoFe_2O_4$ core, they dissolved $Co(acac)_2$ in phenyl ether and added 1,2-hexadecanediol, oleic acid, and oleylamine. Then, the mixture was heated at 140 °C and Fe $(acac)_3$ dissolved in phenyl ether was added dropwise [134,135]. The temperature of the reaction was increased quickly to 260 °C and maintained under reflux for 30 min. The obtained $CoFe_2O_4$ nanocrystals were isolated and used as seeds for the growth of $CoFe_2O_4@MnFe_2O_4$ structures. The $MnFe_2O_4$ shells were grown over the $CoFe_2O_4$ seeds through thermal decomposition of coordination compounds (benzoylacetonate or acetylacetonate ligands coordinated to Fe(III) and Mn(II) ions) dissolved in benzyl ether, using oleylamine and oleic acid as surfactants. The obtained nanocrystals were well dispersed, with only about 10% polydispersity. Importantly, the size of the spherical NPs could be precisely controlled between 4 and 12 nm through a seed-mediated growth process by adjusting the contents of the $CoFe_2O_4$ seeds and metal precursors ($Co(acac)_2$ and $Fe(acac)_3$) in the reaction mixture [134,135]. Yan et al. synthesized 9 nm $CoFe_2O_4$ hollow nanoparticles on graphene sheets (Fig. 7**d–e**) using a solvothermal method [136]. The nanoparticles were well-dispersed over the graphene sheets, which is highly desirable for applications such as catalysis and energy storage. Using a hydrothermal method, Dong et al. grown metallic copper decorated $CuFe_2O_4$ hexagonal platelets over graphene sheets to use the composite as anode material for LIBs (Fig. 7**g–h**) [137]. The metal incorporated composite (Fig. 7**i**) performed exceptionally as LIB anode material due to the synergetic effects of metallic copper, $CuFe_2O_4$ and graphene. In the absence of graphene, the $CuFe_2O_4$ nanostructures were grown with octahedral morphology (Fig. 7**f**). The presence of graphene induced the hexagonal morphology of the $CuFe_2O_4$ nanostructures, enhanced the electron conductivity of the electrode, and maintained the structural integrity of the active material ($CuFe_2O_4$ nanostructures). The composite ($Cu-CuFe_2O_4/G$) delivered a high capacity of 672 mA h g^{-1} after 200 cycles at a current density of 1000 mA g^{-1} [137]. Zhang et al. prepared a $NiFe_2O_4$/rGO composite through hydrothermal treatment of a pH-controlled (using ammonia) aqueous solution of $Fe(NO_3)_3 \cdot 9H_2O$, $Ni(NO_3)_2 \cdot 6H_2O$, and rGO at 180 °C for 12 h [138]. On utilizing as SC electrode material, the composite exhibited high specific capacity (1129 mA·h·g^{-1} at 0.2 A·g^{-1} after ~ 300 discharge–charge cycles). The excellent performance of the nanocomposite has been associated to the uniform dispersion of ultrafine (<10 nm) $NiFe_2O_4$ nanocrystals immobilized on rGO, which prevented the stacking of the rGO sheets and thus facilitated the diffusion of Li$^+$ ions. However, the specific capacity of the SC fabricated with the nanocomposite was highly dependent on the precursor/rGO ratio used during the synthesis of the nanocomposite.

Very recently, a nanocomposite consisting of $CoFe_2O_4$ and CoOOH was fabricated by Song et al. [139] for utilizing in high-performance supercapacitors. For that, a $CoFe_2O_4$ layer (thickness of ~ 5 μm) consisting of 20–200 nm NPs was grown *in situ* on Ni sponge (NS) by a hydrothermal method, followed by a thermal deposition growth of CoOOH nanowires. Although the thermally deposited CoOOH nanowires were loosely bound to the bare NS, they were strongly attached to the NS in presence of the $CoFe_2O_4$ layers (hydrothermally grown). A supercapacitor made of this composite as active electrode material exhibited a very high specific capacity (200.3 mA h g^{-1} at 1 mA g^{-1}) and excellent cycling stability (92.7% after 2000 cycles at 1 mA g^{-1}). Furthermore, a flexible SC assembled using this nanocomposite as anode and rGO as a cathode generated an energy density of 54.1 Wh kg^{-1} at a power density of 374.9 W kg^{-1}. Moreover, the flexible supercapacitor could be charged by a mechanical generator with about 84% mechanical energy converted to electrical energy. The results presented above clearly demonstrate the advantage of incorporating conducting materials such as graphene, GO and rGO with metal ferrite nanostructures for enhancing their performance in catalytic and supercapacitor applications.

3.4. Metal ferrites grown on conducting supports

The low electronic conductivity of metal oxides, which also include metal ferrites, requires them to combine with conductive materials (additives) to improve their performance in energy storage devices [140]. For this reason, metal ferrites have been grown over or pressed with Ni foam, rGO, graphene or carbon black. Combining metal ferrites with carbon, rGO or graphene is an excellent strategy for electrode preparation as these carbonaceous materials offer high electrical conductivity and chemical stability. However, these carbonaceous materials have limited charge-storage capacities [133,141]. In the case of 2D nanomaterials, their entire surface is accessible to the electrolyte ions, enabling fast charge storage [141]. Nonetheless, restacking of 2D structures limits electrolyte penetration and ion transport [141]. In this aspect, redox-active NPs on the surface of conductive 1D and 2D materials enhance their charge storage capacity by preventing their aggregation and restacking [133,141]. Due to lower work functions of carbonaceous materials (e.g., graphene, rGO, CNTs (carbon nanotubes), carbon onions) than metal oxides, electrons are injected from the carbonaceous materials into the oxide, increasing the electrical conductivity of the latter [133,141]. The MFe_2O_4 nanostructures grown over rGO also act as spacers between the rGO sheets, preventing their restacking [46]. Furthermore, the hollow nanostructures (metal ferrites) facilitate the diffusion of the electrolyte ions into the inner region of the electrode, which accelerates electrochemical reactions [46]. The rGO-metal ferrite composites exhibit better performance in SC electrodes as the contributions in equivalent series resistance (*ESR*) and charge transfer resistance (R_{ct}) of the composites are considerably lower than the contributions imposed by rGO and metal ferrite individually [46].

Selected STEM (scanning transmission electron microscopy), SEM, TEM and HRTEM images of $MnFe_2O_4$ and $CoFe_2O_4$ nanostructures grown on rGO and other conductive materials are shown in Fig. 8. In general, the metal ferrite nanostructures are well

dispersed on the conductive materials. However, depending on the synthesis conditions and the characteristics of the support (Ni foam, rGO, carbon), their sizes are significantly different (Fig. 8**a–d, g** and **h**). Using a hydrothermal process, Makkar et al. synthesized $MnFe_2O_4$/rGO composites and utilized them as electrode materials for SCs. For synthesizing the composite, $MnCl_2 \cdot 4H_2O$, $FeCl_3 \cdot 6H_2O$, CH_3COONa and polyethylene glycol (PEG) were dissolved in EG [46]. The CH_3COONa/PEG weight ratio in the solution was maintained at 1:3.6. After adding EG dispersed rGO in this solution, the mixture was transferred to a Teflon-lined autoclave and heated at 200 °C for 22 h. The obtained precipitate was washed and dried under vacuum. A schematic of the adapted synthesis procedure is presented in Fig. 9**a**. A typical STEM image of the composite prepared using 20% rGO is shown in Fig. 8**a**. Electrochemical behaviors of this composite are discussed in the "energy storage in SCs" section. Xiong et al. also prepared the same ($CoFe_2O_4$/rGO) nanocomposite through hydrothermal process, utilizing ethanol as solvent (instead of EG) and NaOH as precipitating agent (instead of sodium acetate) [133]. For that, first they dispersed GO in ethanol by ultrasonication. Then, the dispersion was mixed with an ethanolic solution of cobalt nitrate and iron nitrate. After adding a fixed amount of aqueous NaOH solution, the mixture was treated hydrothermally at 180 °C for 20 h. The precipitated was filtered, washed and dried under vacuum. The process produced well-dispersed $CoFe_2O_4$ NPs of about 6 nm diameter over the rGO surface (Fig. 8**d**).

On the other hand, porous $CoFe_2O_4$/rGO nanocomposite with relatively larger $CoFe_2O_4$ (~89 nm) NPs attached on rGO surface were synthesized by Rahmanifar et al. [51] by solvothermal processing (180 °C, 20 h) of an EG solution of $CoCl_2 \cdot 2H_2O$, $FeCl_3 \cdot 6H_2O$, sodium acetate and PVP. The used technique generated well-dispersed $CoFe_2O_4$ NPs over rGO sheets (Fig. 8**g** and **h**). The SCs fabricated using the nanocomposite exhibited excellent performance. A similar nanocomposite with relatively smaller $CoFe_2O_4$ NPs (~10
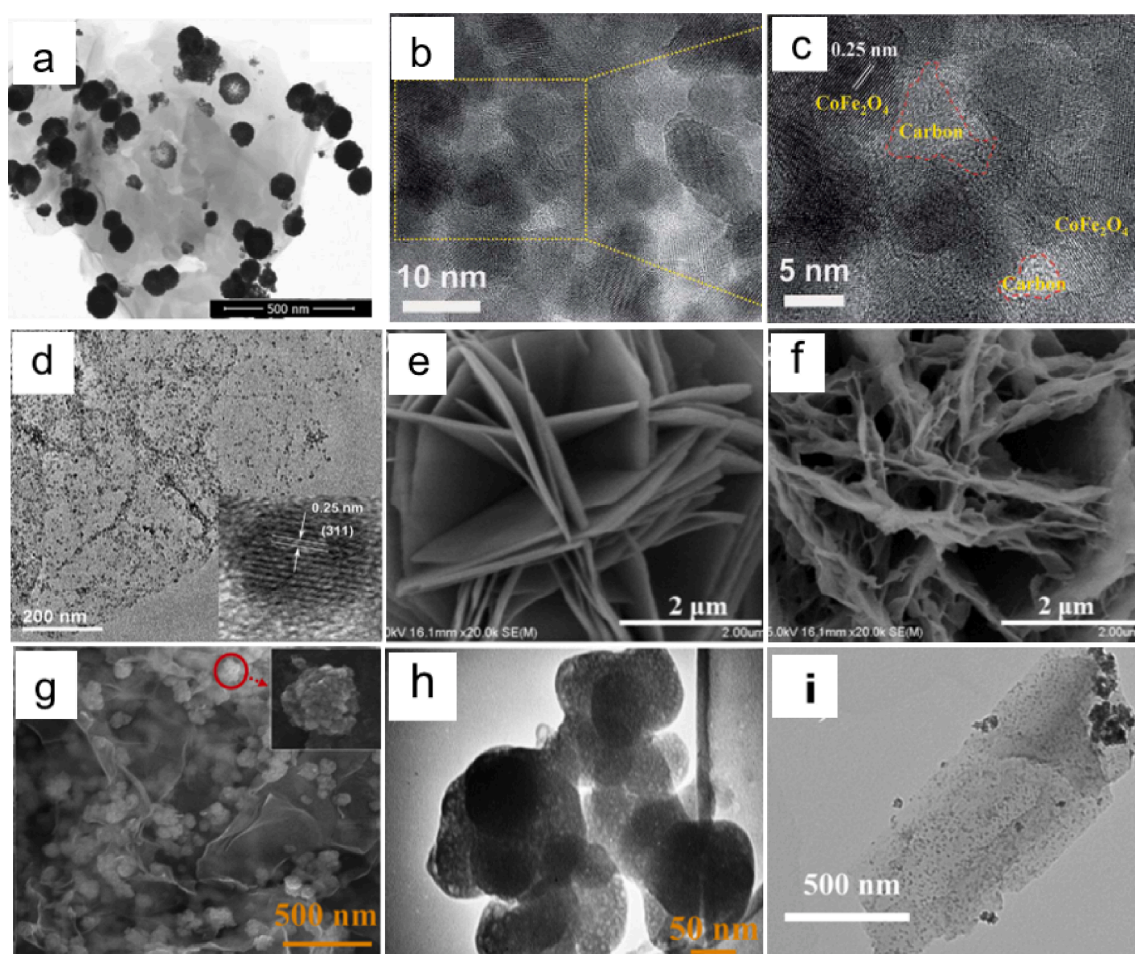

Fig. 8. Selected images highlighting the dispersion of metal ferrite nanostructures on conductive substrates. (a) STEM image of a $MnFe_2O_4$-rGO composite (20% of rGO) [46]. Reproduced with permission from American Chemical Society, Copyright 2020. (b) HRTEM image and (c) enlarged HRTEM image of a low-crystalline mesoporous $CoFe_2O_4$/carbon composite [48]. Reproduced with permission from Royal Society of Chemistry, Copyright 2017. (d) TEM image of a $CoFe_2O_4$/rGO (34.5% of cobalt ferrite) nanocomposite [133]. Reproduced with permission from Elsevier, Copyright 2014. (e) SEM image of $CoFe_2O_4$ on Ni foam [93]. (f) SEM image of $ZnO@CoFe_2O_4$ nanoplate heterostructures on Ni foam [93]. Reproduced with permission from Royal Society of Chemistry, Copyright 2018. (g) FE-SEM (with a BSE detector) and (h) TEM image of a $CoFe_2O_4$-rGO nanocomposite [51]. Reproduced with permission from Elsevier, Copyright 2019. (i) TEM image of $CoFe_2O_4@graphene$ composite (40% of graphene) [52]. Adapted with permission from American Chemical Society, Copyright 2018.
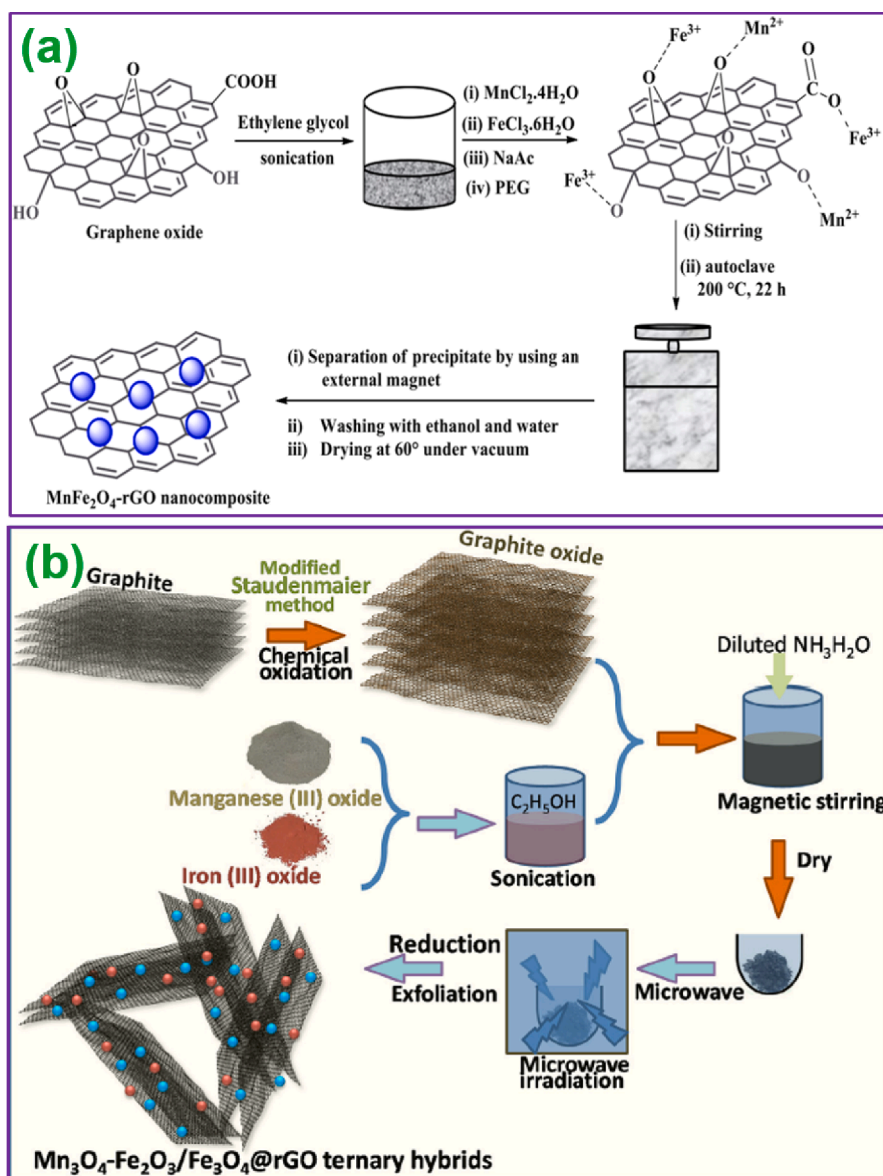
Fig. 9. (a) Schematic step-by-step presentation of a one-pot hydrothermal process utilized for the synthesis of MnFe$_2$O$_4$/rGO nanocomposite. Reproduced from ref. [46] with permission from American Chemical Society, Copyright 2020. (b) Schematic of a microwave-assisted synthesis process utilized to prepare Mn$_3$O$_4$-Fe$_2$O$_3$/Fe$_3$O$_4$@rGO ternary hybrid. Reproduced from ref. [144] with permission from Elsevier, Copyright 2020.

nm) dispersed over rGO (Fig. 8i) was synthesized by Wang et al. utilizing a very similar hydrothermal process (180 °C, 5 h) and same metal precursors (FeCl$_3$·6H$_2$O and CoCl$_2$·2H$_2$O). However, they utilized ethanol as solvent instead of EG [52]. While the specific capacitance of the electrode made of CoFe$_2$O$_4$/rGO nanocomposite (in three-electrode configuration) fabricated by Wang et al. was 579.3F g^{-1} (at 1A g^{-1} current density), the specific capacitance of the SC electrode fabricated using CoFe$_2$O$_4$/rGO nanocomposite of Rahmanifar et al. was 263F g^{-1} (at 1A g^{-1} current density), which clearly indicates the advantage of smaller CoFe$_2$O$_4$ NPs in SCs.

Synthesis of low-crystalline mesoporous CoFe$_2$O$_4$/carbon composite through citric acid-assisted sol–gel process was reported by Zhao et al. [48]. To prepare the composite, ferric nitrate and cobalt nitrate were dissolved in water along with citric acid (the citric acid/cobalt nitrate molar ratio was 3:1). The solution was heated at 90 °C for 24 h and the product was collected, dried and air-annealed at different temperatures (300, 400, and 700 °C, for 4 h) (Fig. 8b and c). The composite annealed at 300 °C had ~ 59 atom % carbon, and manifested superior electrochemical performance than the composites prepared by annealing at 400 or 700 °C.

Through a hydrothermal process, Reddy et al. synthesized CoFe$_2$O$_4$ microspheres (composed of nanoflake bundles) on nickel foam utilizing Co(NO$_3$)$_2$·6H$_2$O and FeCl$_3$·6H$_2$O as metal precursors and urea as precipitating agent [93]. NH$_4$F was utilized in the reaction solution to generate intermediates such as triammonium hexafluoroferrate(III) to avoid the formation of α-Fe$_2$O$_3$ phase [142,143]. After dissolving all the reagents in water, the solution was hydrothermally treated at 90 °C for 7 h in presence of nickel foam inside the

autoclave [93]. The nickel foam covered with the deposit was washed, dried and air-annealed at 250 °C for 2.5 h. As can be observed in the SEM image of the composite presented in Fig. 8e, a considerable volume fraction of the Ni foam does not contain any material, and hence the Ni foam/$CoFe_2O_4$ composite was not ideal for SC application. Using a similar procedure and addition of $Zn(NO_3)_2 \cdot 6H_2O$ to the reaction mixture, the same authors synthesized $ZnO@CoFe_2O_4$ nanoplate heterostructures on Ni foams (Fig. 8f). Galvanostatic charge–discharge (GCD) tests on the electrodes fabricated with $CoFe_2O_4$ and $ZnO@CoFe_2O_4$ grown on Ni foam revealed that the $ZnO@CoFe_2O_4$ composite electrode exhibits higher discharge time and higher specific capacitance than the $CoFe_2O_4$ containing electrode.
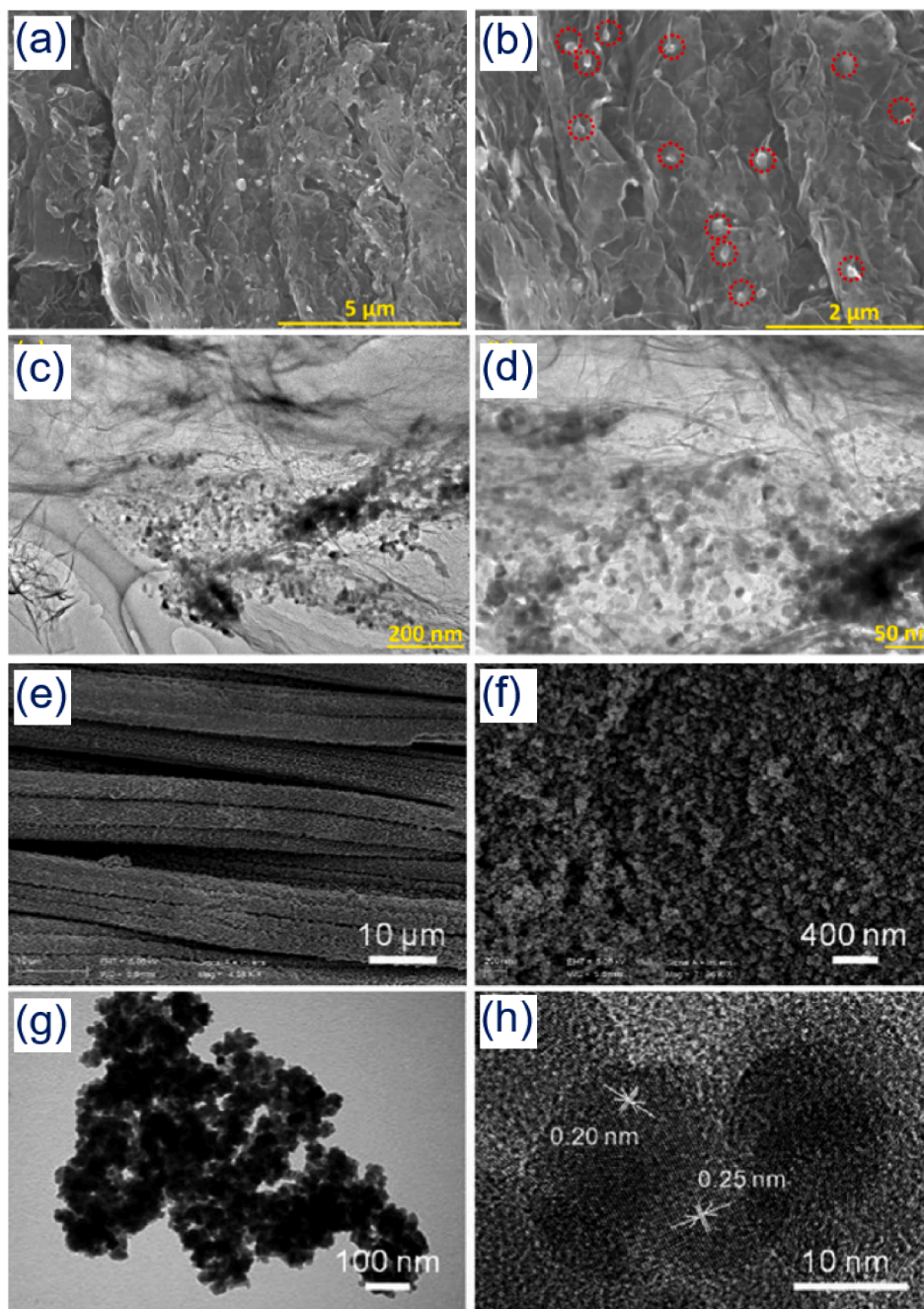

Fig. 10. (a,b) Typical SEM, and (c,d) TEM images of a Mn_3O_4-Fe_2O_3/Fe_3O_4@rGO ternary hybrid prepared by microwave-assisted synthesis. Reproduced from ref. [144] with permission from Elsevier, Copyright 2020. (e) Typical low- and (f) high magnification SEM images of a $NiFe_2O_4$/ carbon cloth composite, and the (g) TEM and (h) HRTEM images of $NiFe_2O_4$ nanoparticles extracted from it by sonication. Reproduced from ref. [145] with permission from Royal society of Chemistry, Copyright 2014.

Kumar et al. synthesized a Mn_3O_4-Fe_2O_3/Fe_3O_4@rGO ternary nanocomposite containing multivalent metal oxides as a strategy for preparing high performance electrode materials for energy storage application [144]. The authors mixed GO (0.7 g), manganese (III) oxide (50 mg) and iron (III) oxide (50 mg) in ethanol (150 mL) under magnetic stirring. Then, 1 mL of diluted ammonia solution was added to the mixture and ultrasonicated for 10 min. The mixture was dried and treated by microwave irradiation (900 W) for 30 s. The aim of the microwave irradiation was to remove oxygenated functional groups of GO. A schematic of the procedure utilized for the synthesis of the nanocomposite is presented in Fig. 9**b**. SEM images of the sample (Fig. 10**a and b**) revealed the formation of agglomerated NPs (indicated by the red circles) dispersed homogeneously over rGO sheets. On the other hand, TEM images of the sample (Fig. 10**c and d**) revealed the formation of small ($<$40 nm) composite NPs and good exfoliation of the rGO nanosheets. The BET surface area of the composite was about 322 m^2 g^{-1}. The nanocomposite was used to fabricate an electrode for SC, which exhibited a rectangular-shaped cyclic voltammetry curve, moderate specific capacitance (590.7F g^{-1} at 5 mV/s) and cyclic stability (capacitance retention of 64.5% after 1000 cycles at scan rate of 50 mV/s). On the other hand, Yu et al. synthesized $NiFe_2O_4$ NPs on carbon cloth through a surfactant (CTAB)–assisted hydrothermal process [145]. In brief, 1.0 mmol of $Ni(NO_3)_2 \cdot 6H_2O$, 2.0 mmol $Fe(NO_3)_3 \cdot 9H_2O$ and 0.55 mmol of CTAB were dissolved in 32 mL of water. Then, a piece of carbon cloth was immersed into the solution and 3.0 mL of aqueous ammonia was added drop-wise. After that, the mixture was transferred to a Teflon-lined stainless autoclave and heated at 180 °C for 12 h. The carbon cloth was washed, dried and air-annealed at 450 °C (2 h). Typical SEM images of the $NiFe_2O_4$/carbon cloth nanocomposite presented in Fig. 10**e and f** clearly demonstrate the $NiFe_2O_4$ NPs are attached to the carbon cloth fibers. The TEM and HRTEM images of $NiFe_2O_4$ NPs obtained by sonication of the nanocomposite (Fig. 10**g** and **h**) demonstrate that the $NiFe_2O_4$ NPs formed over the carbon cloth were of 14–18 nm sizes. The nanocomposite was used to fabricate an all-solid-state flexible super-capacitor using a PVA (poly(vinyl alcohol))–H_2SO_4 gel as electrolyte, which achieved a high energy density of 2.07 mW h cm^{-3} at 2 mA cm^{-2}. The results presented above clearly demonstrate that metal ferrite nanocomposites fabricated using porous conducting materials have been utilized frequently for energy storage applications and manifested good performance. Porous conducting matrices not only play a key role in the fast electron transfer through electrode materials in SCs, but also their porous texture allows an easy penetration of electrolyte ions into the electrodes during the operation of SCs, even at high scan rates [146]. From the results presented above we can see that utilization of conducting support (carbonaceous or metallic) in synthesis allows us to control the size and dispersion of metal ferrite nanostructures. Smaller metal ferrite nanostructures well-dispersed over conducting support render better performance both in catalytic and SC energy storage processes.

4. Metal ferrite catalyzed chemical reactions

Metal ferrite nanoparticles suspended in water or low-toxicity solvents have been systematically utilized as catalysts for chemical reactions (including multicomponent reactions) to produce aromatic amines, amides, esters and heterocycles. They have also been utilized for carbon–carbon coupling reactions. In this section, we summarize the main organic reactions catalyzed by metal ferrites, along with niche photocatalytic processes assisted by metal ferrites such as H_2 production, oxygen evolution reaction, reduction of NO, conversion of CO, degradation of pharmaceuticals and other organic pollutants, and CO_2 photo-reduction.

4.1. Synthesis of organic molecules

In this section, we present some outstanding works reported on the synthesis of organic molecules catalyzed by (i) $CuFe_2O_4$ nanostructures and $CuFe_2O_4$-base nanocomposites, and (ii) other MFe_2O_4 (M = Ni, Co, Mn) nanostructures. Principal reactions catalyzed by metal ferrite nanostructures and nanocomposites have been presented schematically for a clear understanding of the processes along with the interactions between the catalysts and the reagents. We present the catalytic performance of metal ferrites in three sub-sections, as there are many organic reactions that are catalyzed only by $CuFe_2O_4$. However, this number is considerably lower for other metal ferrites. Similarly, the catalytic performance of $CuFe_2O_4$ nanocomposites has been presented in a separate sub-section, because in these cases, the catalytic processes could occur in multiple steps where one step could be attributed to the ferrite nanostructures and the other step is catalyzed by the support. The unique and superior catalytic activities of $CuFe_2O_4$ nanostructures and nanocomposites are probably associated with the weaker Cu-O bonds in $CuFe_2O_4$ than the Mn-O, Fe-O, Ni-O, and Co-O bonds in corresponding metal ferrites. The Cu-O bonds at the surface of the ferrite can be broken by solvents under heating, and the Cu^{2+} cations can be easily reduced. Before discussing the catalytic activities of the metal ferrites in selective organic synthesis, we need to understand their Gibbs free energy of reduction (ΔG_{red}) because the more negative this value is, the easier it is to break these M−O bonds and reduce the M^{2+} cation to M^{1+} or M^0.

4.1.1. Gibbs free energy of reduction (ΔG_{red}) of selected oxides and hydroxides

To understand why $MO(OH)_x$, $M(OH)_x$, MO_x and M^0 species are generated in supercapacitor electrodes made of MFe_2O_4 during charge–discharge cycles, we first need to know the chemical stability of metal ferrites under the reducing atmosphere of the SC electrolyte caused by the applied bias. These species are also generated during chemical reactions catalyzed by the ferrites, especially in reactions performed at high temperatures. The stability issue is also important in the cases where some of the species generated in metal-ferrite-catalyzed chemical reactions work as catalysts. In the absence of extensive research on the stability of MFe_2O_4 (M = Mn, Co, Ni, Cu) in organic and aqueous solvents, their stabilities can be approximated to those of their oxides (M_xO_y, M = Mn, Co, Ni, Cu), assuming that the energies of the M−O chemical bonds in M_xO_y are similar to those in MFe_2O_4. The reported bond dissociation energies for the M−O bonds are in the following order: Fe-O (409 kJ/mol) > Mn-O (402 kJ/mol) > Ni-O (391.6 kJ/mol) > Co-O (368 kJ/mol) > Cu-O (343 kJ/mol) [147]. These values suggest that $CuFe_2O_4$ and $MnFe_2O_4$ are the least and most stable metal ferrites, respectively.

The stability of M_xO_y oxides can be evaluated by considering their reactions with EG at 200 °C, as EG is a moderate reducing agent when heated at its boiling point (200 °C) or at temperatures close to it. Metal oxides used as electrode materials in SCs or as chemical catalysts are usually exposed to reducing agents and solvents. As we will see in the next paragraph, while the oxides and hydroxides of iron and manganese cannot be reduced with EG at 200 °C, the oxides and hydroxides of nickel, cobalt and copper can be reduced. This observation is consistent with the fact that the Fe-O and Mn-O bonds have higher bond dissociation energies than the Ni-O, Co-O and Cu-O bonds.

Larcher and Patrice calculated the ΔG_{red} of selected metal oxides and hydroxides utilizing their reactions with EG at 200 °C (Fig. 11) [148]. The reactions of hot EG with metal oxides and metal hydroxides can be expressed by equations (rx 1) and (rx 2), which have been used for calculating ΔG_{red}, assuming a total oxidation of EG (to CO_2 and H_2O) in both the cases [148]. The ΔG_{red} values for the oxides and hydroxides were estimated using the relations (1) and (2), where $\Delta G_f(H_2O)$, $\Delta G_f(CO_2)$ and $\Delta G_f(EG)$ were −53, −94 and −62 kcal/mol, respectively, and the ΔG_f (Gibbs free energy of formation) values for the oxides were taken from the literature [148]. The oxides and hydroxides containing $Cu^{1+,2+}$, Ni^{2+} and $Co^{2+,3+}$ ions have negative ΔG_{red} values and are reduced easily by EG at 200 °C. On the contrary, oxides and hydroxides containing Mn^{2+} and Fe^{3+} ions have positive ΔG_{red} values {except for $Fe(OH)_3$} and are
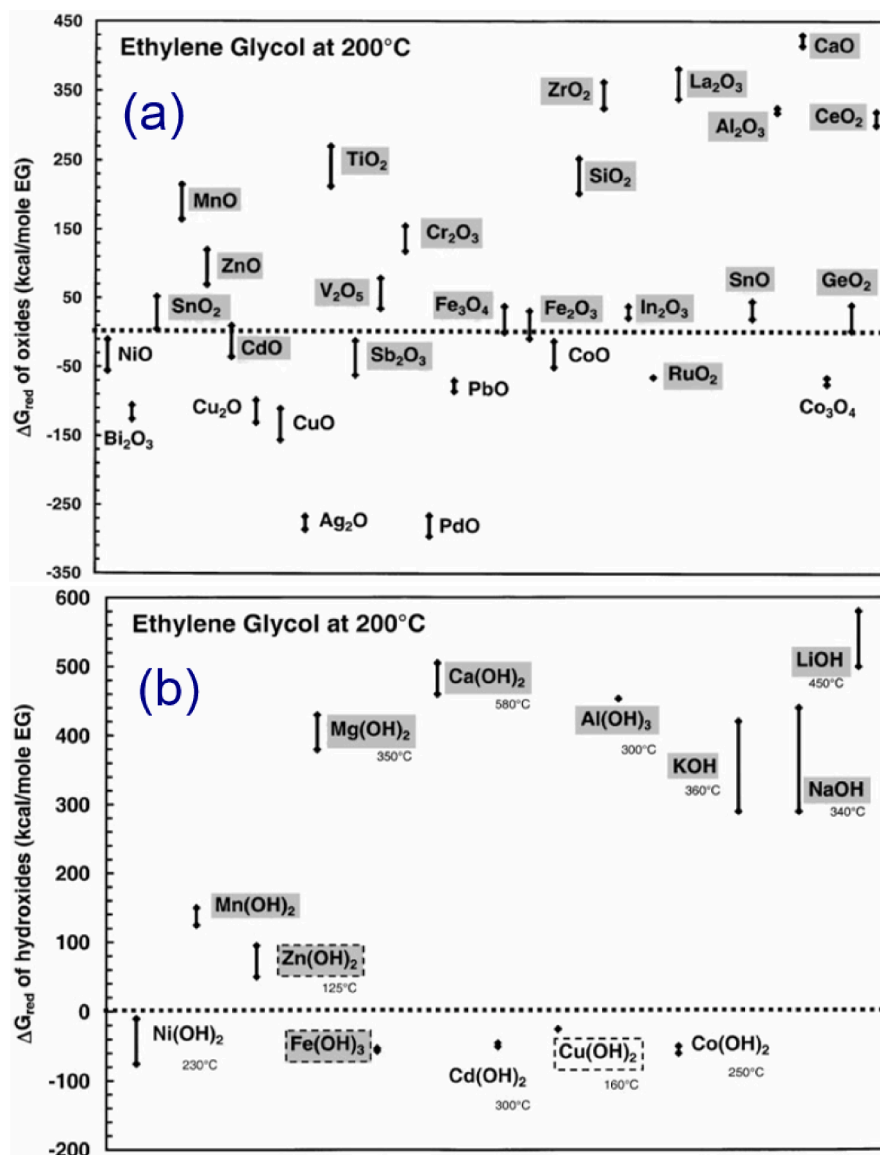

Fig. 11. ΔG_{red} values of various metal (a) oxides and (b) hydroxides estimated from their reduction by ethylene glycol at 200 °C, assuming a total oxidation of the alcohol and formation of metal according to the reactions (rx 1) and (rx 2). The non-shadowed (shadowed) labels indicate that the oxides/hydroxides are experimentally reduced (non-reduced) to M^0 reacting with EG at 200 °C [148]. When well-documented, the dehydration temperatures for the hydroxides are indicated in (b). Reproduced from ref. [148] with permission from Elsevier, Copyright 2000.
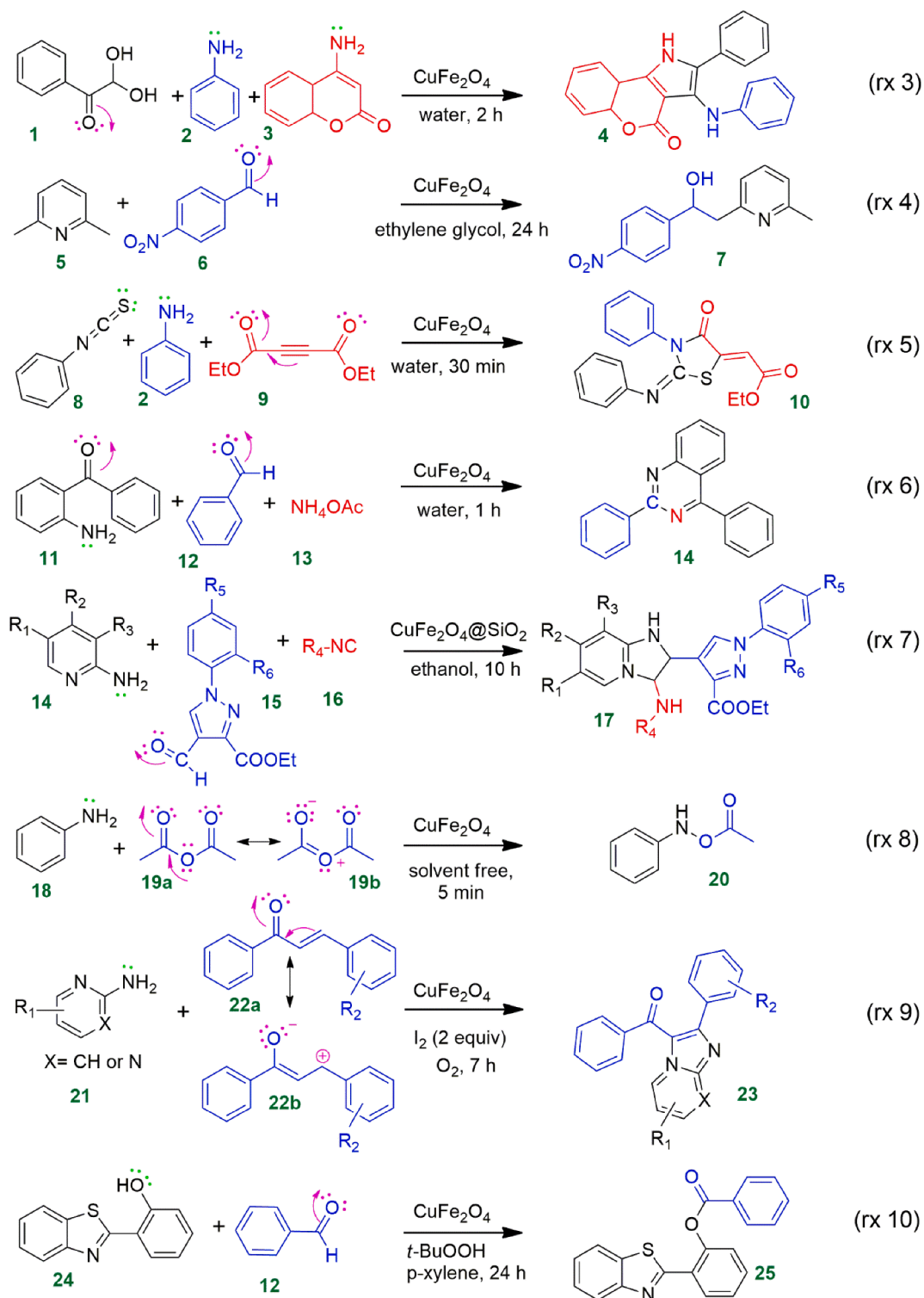
Scheme 1. Selected organic reactions catalyzed by CuFe$_2$O$_4$ nanoparticles. Lone-pair electrons presented in pink color around oxygen atoms are used by the molecule to be adsorbed at the cation sites of CuFe$_2$O$_4$ surface. Lone-pair electrons presented in green color are the electron used by the molecules for nucleophilic attacks. Pink arrows indicate the temporarily movement of electrons from the π bonds towards the oxygen atom, facilitating the adsorption of the molecules at Fe^{3+}/Cu^{2+} cation sites of CuFe$_2$O$_4$.
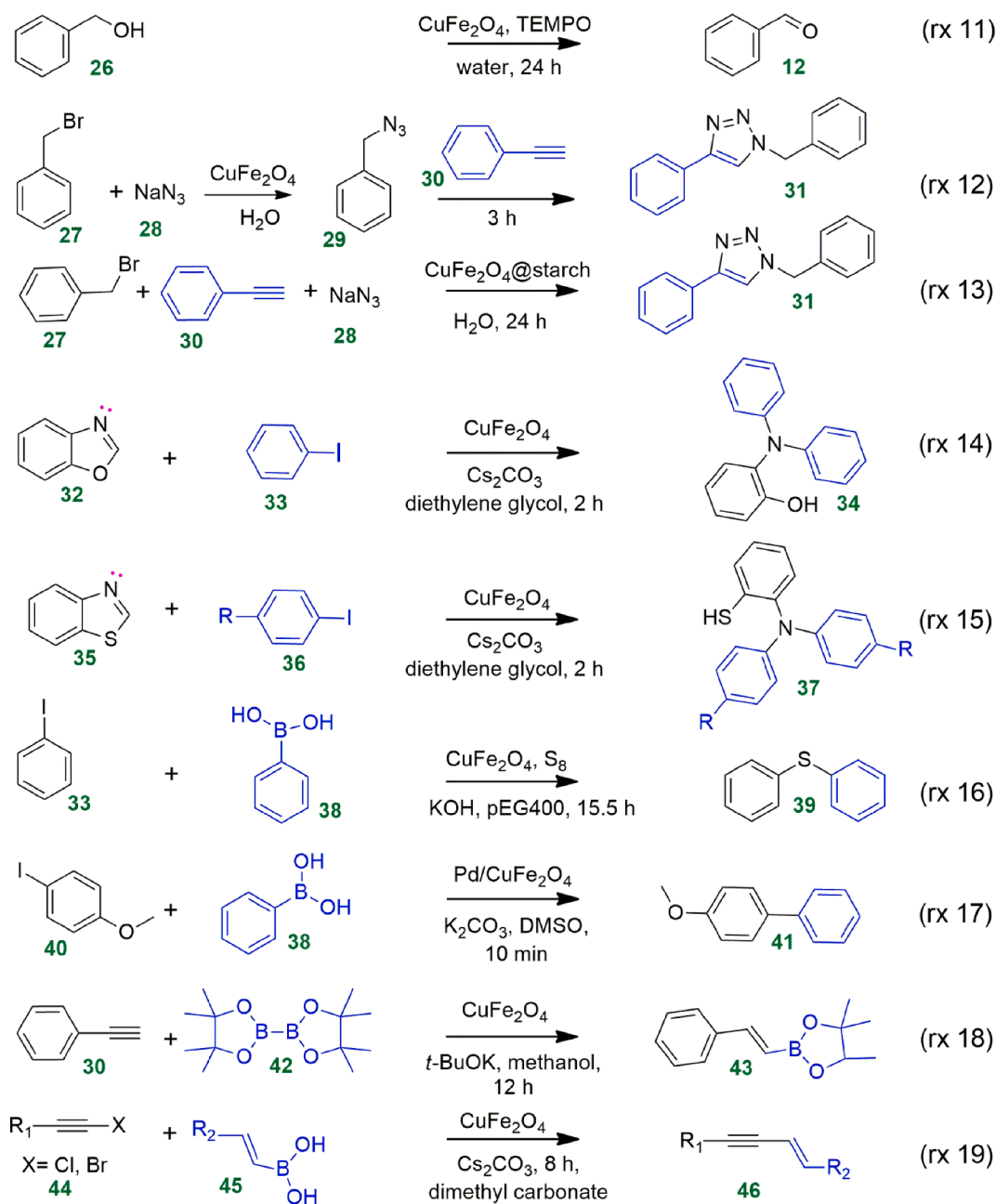
Scheme 1. (*continued*).

not reduced by hot EG. Among the metal oxides of $Cu^{1+,2+}$, Ni^{2+} and $Co^{2+,3+}$ ions, Cu_2O and CuO have larger negative ΔG_{red} values compared to the same of nickel and cobalt oxides. The estimated ΔG_{red} values of these metal oxides suggest that among $CuFe_2O_4$, $NiFe_2O_4$, $CoFe_2O_4$ and $MnFe_2O_4$, the copper ferrite surface is more prone to a partial reduction (specifically, the Cu^{2+} ions may be reduced to Cu^+, or even to Cu^0) during chemical and electrochemical reactions (e.g., electrodes in supercapacitors). The variation of ΔG_{red} values in metal oxides can be better understood by considering the effective nuclear charge and its effect on each of the valence electrons of the corresponding metal ions. The calculated effective nuclear charges (Z_{eff}) acting on an electron in the 3d orbitals of Mn, Fe, Co, Ni and Cu atoms are 5.60, 6.25, 6.90, 7.55 and 8.20, respectively [149]. Higher Z_{eff} values for Co, Ni and Cu are consistent with the observed negative ΔG_{red} values of their oxides and hydroxides. The argument presented above clearly explains why in the hydrothermal synthesis of $CuFe_2O_4$ using EG or a water-hydrazine hydrate mixture solvent researchers obtained metallic copper NPs as the byproduct [112,137].

$$CH_2OHCH_2OH_{(l)} + 5/x\ MO_{x\ (s)} \xrightarrow{\Delta} 5/x\ M^o_{(s)} + 2CO_{2(g)} + 3H_2O_{(g)} \qquad (rx\ 1)$$

$$CH_2OHCH_2OH_{(l)} + 10/x\ M(OH)_{x\ (s)} \xrightarrow{\Delta} 10/x\ M^o_{(s)} + 2CO_{2(g)} + 8H_2O_{(g)} \qquad (rx\ 2)$$

$$\Delta G_{red} = 2\Delta G_f(CO_2) + 3\Delta G_f(H_2O) - (5/x)\Delta G_f(MO_x) - \Delta G_f(EG) \qquad (1)$$

$$\Delta G_{red} = 2\Delta G_f(CO_2) + 8\Delta G_f(H_2O) - (10/x)\Delta G_f(M(OH)_x) - \Delta G_f(EG) \qquad (2)$$

4.1.2. Synthesis of organic molecules catalyzed by CuFe$_2$O$_4$

Catalytic organic synthesis processes suffer from one or more disadvantages, such as the multistep approach, use of toxic organic reagents and solvents, lower yields, difficulty in recovering the catalyst and high cost of some of the metals such as Pd, Pt and Rh [59]. CuFe$_2$O$_4$ has been used as a catalyst for several chemical reactions to partially solve some of the above-mentioned problems. Some important chemical reactions (rx) catalyzed by CuFe$_2$O$_4$ NPs are presented in Scheme 1, and corresponding reaction conditions and product yields are listed in Table 4. In general, copper ferrite is a valuable catalyst for the synthesis of heterocycles [60,150], 1,2,3-triazoles [151,152], tertiary aromatic amines [61], aromatic disulfides [153], phenol esters [62], coumarin fused pyrrole derivatives [154], thiazolidinone derivatives [155], quinoline and quinazoline derivatives [59], vinylboronates [63,156], and many others. These molecules are highly demanding for many practical applications such as in pharmaceuticals, agrochemicals, dye-sensitized solar cells, fluorescence sensors, photo-electrochemical sensors, and synthesis of photofunctional polymers [61]. They also act as valuable synthetic building blocks for organic semiconductors and drugs [156].

Copper ferrite also catalyzes some carbon–carbon coupling reactions [157], avoiding the use of expensive catalysts such as Pd. Moreover, in the synthesis of many of the above-mentioned organic compounds utilizing copper ferrite as catalyst, the used solvent is water, and the yields are above 85% (Table 4). Interestingly, when some of the chemical reactions presented in Scheme 1 were carried out in the presence of Fe$_2$O$_3$ or CuO instead of CuFe$_2$O$_4$, in some cases the reaction yields were very low (<45%) [154,158], and in some other cases the products were not formed [154,155]. Moreover, when the copper ferrite was replaced by ZnO [154,155], SiO$_2$ [154], Al$_2$O$_3$ [154,155], I$_2$ [154], p-toluenesulfonic acid [154], or acetic acid [154,155] in some of the reactions of Scheme 1, expected products were not formed.

CuFe$_2$O$_4$ nanostructures can catalyze organic reactions involving one, two or three components (e.g., Scheme 1, organic molecules on the left side). To understand the interaction mechanism of these molecules with the CuFe$_2$O$_4$ catalyst, we should look at some of

Table 4
Selected organic reactions catalyzed by CuFe$_2$O$_4$ nanoparticles, and corresponding reaction conditions.

Reactions in schemes 1 and 3	Catalyst	Particle size of the catalyst (nm)	Solvent and additives	Tempe-rature (°C)	Reaction time	Yield (%)	Ref.
rx 3	CuFe$_2$O$_4$	15–18	H$_2$O	70	2 h	92	[154]
rx 4	CuFe$_2$O$_4$	–	ethylene glycol	100	24 h	67	[158]
rx 5	CuFe$_2$O$_4$	15–18	H$_2$O	r.t.	30 min	94	[155]
rx 6	CuFe$_2$O$_4$	5–15	H$_2$O	80	32 min	95	[59]
rx 7	CuFe$_2$O$_4$@SiO$_2$[a]	40–60	ethanol	78	10 h	96	[60]
rx 8	CuFe$_2$O$_4$	8.8	solvent free	r.t.	5 min	98	[163]
rx 9	CuFe$_2$O$_4$	–	1,4-dioxane	140	7 h	84	[164]
rx 10	CuFe$_2$O$_4$	~15–80	p-xylene, t-BuOOH in H$_2$O	80	24 h	89	[62]
rx 11	CuFe$_2$O$_4$, TEMPO	–	H$_2$O	100	24 h	95	[165]
rx 12	CuFe$_2$O$_4$	15	H$_2$O	90	3 h	90	[151]
rx 13	CuFe$_2$O$_4$@starch	20	H$_2$O	30	24 h	92	[152]
rx 14	CuFe$_2$O$_4$	–	diethylene glycol K$_2$CO$_3$	140	2 h	95	[61]
rx 15	CuFe$_2$O$_4$	–	diethylene glycol and K$_2$CO$_3$	140	16 h	79	[61]
rx 16	CuFe$_2$O$_4$	22.5	PEG400 or glycerol or DMF	80	15.5 h	100	[153]
rx 17	Pd/CuFe$_2$O$_4$		K$_2$CO$_3$, DMSO,	120	10 min	98	[157]
rx 18	CuFe$_2$O$_4$	–	methanol and t-BuOK or KOH or K$_2$CO$_3$	50	12 h	90	[63]
rx 19	CuFe$_2$O$_4$	–	dimethyl carbonate, Cs$_2$CO$_3$	100	8 h	> 81	[166]
rx 20	CuFe$_2$O$_4$/HNTs		H$_2$O		2 h	92	[167]
rx 21	CuFe$_2$O$_4$/rGO (30% of rGO)	12 ± 2	solvent free	60	8–10 h	87–95	[85]

r.t. = room temperature. HNTs = halloysite nanotubes.

[a] Sulfonic acid functionalized silica-coated CuFe$_2$O$_4$. TEMPO = 2,2,6,6-tetramethylpiperidine N-oxide; an aminoxyl radical. DMSO = dimethyl sulfoxide.

their common structural features. As can be noticed in reactions (rx 3) - (rx 10), at least one of the reacting molecules in each of these reactions contains C=O group. The C=O group behaves as a dipole, with a negative charge (δ^-) located at the more electronegative oxygen atom, which is used to coordinate the molecule at the surface of copper ferrite. Once the molecule is coordinated with the catalyst, the π electrons in the C=O double bond migrate temporarily to the 3d orbitals of the cations in the catalyst, as indicated by the pink arrows in Scheme 1. As a result, the carbon atom in the C=O group becomes highly active to form: (i) a C-N chemical bond with the amino group of molecules **2, 11, 14, 18** and **21**; (ii) a C-C chemical bond with the benzylic carbon present in molecule **5**, and (iii) a C-O chemical bond with the free radical generated in molecule **24** (the radical is formed by the reaction of molecule **24** with *tert*-butyl hydroperoxide solution). In process (i), the reactions take place through a nucleophilic attack of the amino group (–NH$_2$) on the carbonyl group (C=O) of ketone **1** (rx 3), ester **9** (rx 5) or aldehydes **12, 15** (rx 6, rx 7). In process (ii), the reactions occur through a three-step mechanism. First, a Lewis acid or Brønsted acid accepts electrons from the nitrogen atom of an azaarene (e.g., 2,6-dimethyl-pyridine in (rx 4)) **5**, then a cleavage of the benzylic C-H bond occurs to generate a C=C bond. Finally, the π electrons of this C=C bond makes nucleophilic attack on the C=O group of nitrobenzaldehyde **6** to generate the C-C bond, as depicted in (rx 4) [158]. Other azaarenes such as 2-methylpyrazine, 2-methylbenzothiazole and 2-methylquinoline can also be functionalized under the same conditions (rx 4) [158]. This mechanism of functionalization of azaarenes using Lewis acids, such as I$_2$, or Brønsted acids or Pd as catalysts has been proposed by several researchers [159–162]. To achieve the functionalization of azaarenes, they must have a CH$_3$, CH$_2$ or CH group attached to the aromatic ring at the carbon 2 position. The C-C bond formation shown in (rx 4) is important because it potentially provides a new synthetic tool for obtaining bioactive compounds by functionalization of azaarenes, i.e., nitrogen-containing aromatic heterocycles [159].

Some of the organic molecules have two C=O groups, and both of them can interact electrostatically with the cations of CuFe$_2$O$_4$ surface. This is the case for diethyl acetylenedicarboxylate **9** shown in (rx 5). CuFe$_2$O$_4$ NPs not only provide the necessary surface active metal centers for the adsorption of these molecules, but also the Fe^{3+} cations at the surface of the catalyst can accept π electrons from the C=O and C=N groups [154]. It is worth recalling that, while the outer-shell electron configuration of Fe^{3+} is [Ar]3d^5, the configuration for Cu^{2+} is [Ar]4s^{0}3d^9. Consequently, the number of electrons that can be accepted inside the 3d orbitals of Fe^{3+} and Cu^{2+} ions at the surface of CuFe$_2$O$_4$ NPs are 5 and 1, respectively. Therefore, most of the reacting organic molecules are adsorbed at the Fe^{3+} cation sites of the CuFe$_2$O$_4$ surface.

The reaction between aniline **18** and acetic anhydride **19** catalyzed by CuFe$_2$O$_4$ in the absence of a solvent is shown in (rx 8) [163]. Note that, two resonance structures are presented for acetic anhydride **19a** and **19b**. While the negative charge on the oxygen atom in **19b** can be stabilized by the Fe^{3+} and Cu^{2+} cations of the catalyst surface, the oxygen atom, temporarily bearing a positive charge, binds to the aniline. The cyclization of 2-aminopyrimidine **21** and *trans*-chalcone **22a** is presented in (rx 9) [164]. Again, two resonance structures (**22a** and **22b**) are presented for the *trans*-chalcone (an α,β-unsaturated ketone). In this case, while the oxygen atom in molecule **22b**, bearing a negative charge, interacts with the Fe^{3+}/Cu^{2+} ions at the surface of CuFe$_2$O$_4$, the carbon atom, bearing a positive charge (a carbocation), forms a chemical bond with the amine group of the 2-aminopyrimidine. However, I$_2$ must be added in the reaction mixture to enhance the stability of the carbocation **22b**.

The common structural feature of the organic molecules participating in reactions (rx 3) - (rx 10) has been discussed in the earlier paragraphs. On the other hand, the common feature of the molecules participating in (rx 10) and (rx 11) is that both bear a C-OH group. Both the molecules **24** and **26** are converted to free radicals by the oxidant species (i.e., *tert*-butylhydroperoxide (*t*-BuOOH) or TEMPO). To carry out (rx 10) and (rx 11), it is necessary to use both copper ferrite and an oxidant species (*t*-BuOOH or TEMPO). These two model reactions clearly highlight the necessity of an efficient catalyst such as CuFe$_2$O$_4$ and a strong oxidant for the coupling of phenols **24** with benzaldehyde **12** and oxidation of alcohols **26** [62,165]. The yield of (rx 10) without using copper ferrite or *t*-BuOOH was only 3 and 0%, respectively [62]. To determine the role of Fe^{3+}/Cu^{2+} cations in (rx 10), Nguyen et al. used several copper and iron salts as catalysts instead of CuFe$_2$O$_4$ [62]. The yields of the reaction they obtained using CuI, CuBr, CuCl, CuBr$_2$, Cu(OA$_C$)$_2$, FeCl$_2$, FeCl$_3$, Fe(OAc)$_2$ as catalyst were 67, 61, 77, 72, 78, 26, 11 and 34% respectively. Likewise, the yields of (rx 10) using nanoparticles of Fe$_2$O$_3$, Fe$_3$O$_4$, NiFe$_2$O$_4$, CoFe$_2$O$_4$, CuO, Cu$_2$O, and CuFe$_2$O$_4$ were 5, 7, 4, 39, 68, 61, and 89%, respectively. The results clearly demonstrate that the Cu^{2+} ions in CuFe$_2$O$_4$ and other Cu coordinating compounds play a key role in reactions involving free radicals generated by oxidants such as *t*-BuOOH. More importantly, these results highlight that the activity of Fe^{3+}/Cu^{2+} ions in chemical reactions is highly sensitive to their chemical coordination environment.

The common feature between the molecules involved in the (rx 12) - (rx 17) and (rx 19) is their C-X (X = Cl, Br) bond, which breaks up during azide−alkyne cycloaddition reactions, reactions of benzoxazoles with iodoarenes, cross-coupling reactions of phenylboronic acid with aryl/heteroaryl/benzyl halides in the presence of S$_8$, and some Suzuki coupling reactions. CuFe$_2$O$_4$ NPs are also good catalysts for synthesizing 1,2,3-triazoles **31** via Huisgen azide-alkyne cycloaddition (AAC) reactions as shown in (rx 12) and (rx 13) [151,152,168]. Reagents used in (rx 12) were benzyl bromide **27**, sodium azide (NaN$_3$) and alkyne phenylacetylene **30**. However, when the CuFe$_2$O$_4$ NPs were replaced by Fe$_2$O$_3$ NPs, no reaction occurred [168]. Huisgen cycloaddition reactions carried out at low temperature must be catalyzed by Cu^{1+} ion containing salts or Cu^{1+} coordination compounds [169,170]. However, the salts or co-ordination compounds containing divalent Cu^{2+} ions do not catalyze these cycloaddition reactions [169]. This fact suggests that at least some of the Cu ions at the surface of CuFe$_2$O$_4$ NPs remain in Cu^{1+} state. In fact, through XPS (X-ray photoelectron spectroscopy) analysis, Feng et al. recently demonstrated that copper ferrite NPs prepared using oleylamine (a mild reducing agent) at high temperature (300 °C) have a considerable amount of Cu^{1+} ions at their surfaces [171]. Furthermore, when benzyl bromide **27** in (rx 12) is replaced by boronic acid R-B(OH)$_2$, a similar triazole was obtained. All the facts presented above demonstrate the important role played by copper cations in AAC reactions.

Nguyen et al. demonstrated that CuFe$_2$O$_4$ catalyzes the ring-opening reaction of benzoxazoles **32** and benzothiazoles **35** with iodoarenes **33, 36** to generate triarylamines **34, 37**, as shown in (rx 14) and (rx 15), respectively [61]. The authors proposed that the

solvent (diethylene glycol) reduces the Cu^{2+} ions to Cu^{1+}. Triarylamines were also obtained by He et al. using the same reagents (**32** and **33**), however, using different copper and iron-based catalysts {CuCl, CuCN, CuBr, CuI, $CuSO_4$, $CuCl_2 \cdot 2H_2O$, $Cu(OAc)_2 \cdot 2H_2O$, CuO and $FeSO_4 \cdot H_2O$} instead of copper ferrite [172]. The highest yield (84%) was obtained using CuCN catalyst [172], However, this yield is lower than the yield of the reaction (95%) obtained using $CuFe_2O_4$ as the catalyst. In addition, while the reaction time for the CuCN catalyst was 18 h [172], it was only 2 h for the $CuFe_2O_4$ NPs catalyst [61]. In fact, $CuFe_2O_4$ NPs and other copper-based catalysts were seen to be more active in ring-opening reactions than nanostructured $NiFe_2O_4$, $CoFe_2O_4$, and Fe_2O_3 catalysts. Given the toxicity of cyanide ions (CN^-) in humans and the environment [173], $CuFe_2O_4$ NPs should be used as a catalyst instead of CuCN whenever possible. The role played by cesium carbonate in reactions (rx 14) and (rx 15) was considered to remove the acidic proton attached to the C2 carbons of the azoles by carbonate anions [174].

Another important reaction catalyzed by $CuFe_2O_4$ is the C-S bond formation reaction. While the C-S bond formation reactions are of great demand in general organic synthesis, in pharmaceutical industries and material science [175], frequently expensive palladium-based catalysts are needed to form the C-S bonds with high yields [175]. Other Cu compounds are also seen effective as catalysts for C-S bond formation [175]. For example, in presence of a base, CuO and Cu_2O are good catalysts for C-S cross-coupling reactions between thiols and aryl halides (I^-, Br^-) [176,177]. Panova et al. demonstrated that the catalytically active species in these reactions are the copper thiolate complexes, such as $[Cu(SPh)_2]^-$ and $[CuI(SPh)]^-$ formed by leaching of Cu ions from the metal oxide surface [176]. The Cu-based catalysts are not only cheaper and more earth abundant than Pd-based catalysts, but also in some cases superior in terms of efficiency and functional group tolerance [175,176]. $CuFe_2O_4$ NPs also catalyze efficiently the one-pot C–S–C bond formation reactions to generate diaryl sulfides (rx 16). For example, utilizing $CuFe_2O_4$ NPs as catalyst, aryl/heteroaryl/benzyl halides such as **33**, phenylboronic acid **38** and sulfur powder, Amiri et al. synthesized several compounds with C–S–C bonds in high yields [153]. This method is attractive because it does not use volatile and foul-smelling thiols which can lead to serious safety and environmental problems [153]. It seems that the catalytically-active species such as $[Cu(SPh)_2]^-$ and $[CuI(SPh)]^-$ complexes were not generated in these cases through the leaching of copper ions from $CuFe_2O_4$ NP surface, as the ICP-OES (inductively coupled plasma-optical emission spectrometry) estimated Fe and Cu ions leached into the reaction solution (after>20 h of reaction) were < 1 ppm. The main disadvantages of this method are: (i) it requires 11 to 40 h to complete the reaction, and (ii) after six recycling of the catalyst, the reaction yield drops to ~ 50% of initial yield. $CuFe_2O_4$ nanostructures are also useful for supporting expensive metal catalysts such as Pd utilized in Suzuki coupling reactions to generate C-C bonds (rx 17) [157]. To highlight this point, we can mention the work of
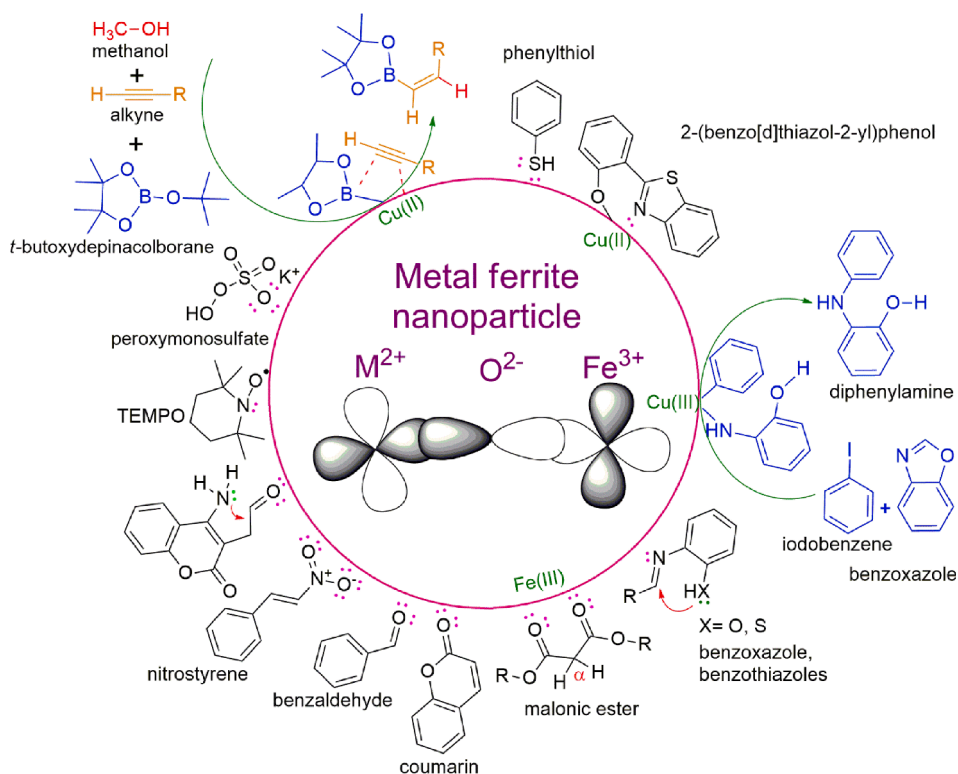
Scheme 2. Schematic presentation of adsorption of organic molecules and free radicals on the surface of metal ferrite nanoparticles. The adsorption occurs through the non-bonding lone-pair electrons (indicated by pink dots) in polar functional groups such as carbonyl (C=O), nitro (–NO_2), amino (-NHR, -NR_2) and thiol (RS-H). The adsorption enhances the intra-molecular nucleophilic attacks in some adsorbed molecules, as indicated by red arrows. Simultaneous adsorption of two reagents on the same (or near) binding site are sometimes needed to achieve the catalytic processes; for example, in the formation of diphenylamines and alkenes bonded to pinacolborane (green arrows). Partially-filled 3d orbitals in metal ferrites serve as a temporary electron sink to activate the adsorbed organic molecules. Further details are given in refs. [61–63,131,178,179].

Lakshminarayana et al., [157] who utilized $CuFe_2O_4$ nanorods to support Pd NP catalyst for the reaction of phenylboronic acid **38** with 4-methoxyiodobenzene **40** to produce 4-methoxybiphenyls **41**. Utilization of magnetic support solved the problems related to the recovery and recyclability of the metal catalyst.

$CuFe_2O_4$ NPs have been successfully utilized as catalyst in the synthesis of vinylboronates regioselectively through hydroboration of alkynes **30** using bis(pinacoloto)diboron **42**, as shown in (rx 18) [63]. Most of the vinylboronate synthesis reactions (e.g., **43**) are homogeneous catalytic reactions. When copper-based coordination compounds are used as catalyst, these reactions require a high amount of catalyst loading, ligands (some of them are toxic, e.g., phosphines) and a long reaction time to furnish high yield and good selectivity [63]. All these requirements could be avoided using $CuFe_2O_4$ NPs as catalyst [63]. Synthesis of vinylboronates with 90% yield was achieved using $CuFe_2O_4$ catalyst and methanol as solvent [63]. Nonetheless, the yields were lower than 27% for acetonitrile, toluene, tetrahydrofuran or dimethyl sulfoxide solvents. Further experiments with deuterated methanol demonstrated that a hydrogen atom of the methanol molecule was used to generate vinylboronate **43,** which explains the strong dependence of the product yield on the nature of the solvent. On using CuO and Cu_2O nanostructures as catalysts instead of $CuFe_2O_4$, the yields decreased to 77 and 80%, respectively [63], supporting our claim that the catalytic activity of Cu ions depends on their chemical environment as discussed earlier. In fact, such a synergetic effect of Cu ions and their chemical environments has been detected experimentally by Zeng et al., who found that the reaction (rx 18) occurs at a shorter time (8 h) and lower temperature (22 °C) even with higher yield on utilizing Cu/$CuFe_2O_4$ nanocomposite instead of just copper ferrite or Cu nanoparticles as catalysts [156]. In fact, under similar experimental conditions (rx 18), utilizing both aliphatic and aromatic alkynes, the authors synthesized more than 25 vinylboronates with high yields and good regioselectivity [156].

Synthesis of conjugated 1,3-(*E*)-enynes **46** catalyzed by copper ferrite is depicted in (rx 19) [166]. According to the mechanism proposed by the authors, the alkenyl moiety in **45** interacts with the coordination sphere of the tetrahedrally substituted Cu(II) towards nucleophilic activation in presence of a strong base such as Cs_2CO_3. Then the Fe(III) center of the metal ferrite activates the C-X (X = Br, Cl) bond in **44** and makes the C(sp) center electrophilic. The 1,3-(*E*)-enyne is obtained by copper- and iron-assisted nucleophilic displacement of the halide atom through a six-membered intermediate [166]. Importantly, when CuO or Fe(III) oxide NPs were used, the product was not formed. Therefore, both Fe(III) and Cu(II) moieties are needed to be present in the catalyst for the successful synthesis of 1,3-(*E*)-enynes. Nonsymmetrical 1,3-dyines were also obtained under similar reaction conditions.

A common feature of several reactions presented in Scheme 1 is that the Fe(III) centers on the surface of $CuFe_2O_4$ NPs accept electrons from the carbonyl groups (C=O) present in ketones, aldehydes, anhydrides, etc. Once the organic molecules are adsorbed on the surface of the metal ferrite, the nucleophilic attacks of the amines (–NH_2), isocyanide (R-NC), phenols (Ar-OH) and ammonia (NH_3) groups toward the carbonyl groups are enhanced. Some molecules in the reactions presented in Scheme 1 behave as electric dipole with negative charge located at the lone-pair electrons. These lone pairs are adsorbed on the surface of metal ferrites (Scheme 2). In addition, the Fe(III) centers at the ferrite surface adsorb I^-, Br^- and Cl^- ions coming from aryl halides (e.g., iodobenzene). In this way, copper ferrite promotes the reactions depicted in Scheme 1. On the other hand, there are several organic reactions catalyzed by Cu(I) salts or Cu(I)-coordination compounds which do not occur when Cu(II) salts or Cu(II)-coordination compounds are utilized. However, these reactions do occur when $CuFe_2O_4$ NPs are utilized as catalyst [151,152,168]. As it is improbable that the Cu(II) centers in $CuFe_2O_4$ NPs catalyze these reactions, the experimental results suggest that the Cu(II) centers in $CuFe_2O_4$ NPs transform to Cu(I) in the reducing atmosphere of the reaction. The results presented above highlight the advantage of utilizing $CuFe_2O_4$ catalyst in coupling reactions as it provides necessary redox active surface centers for the adsorption and activation of electroactive species [58]. It is worth mentioning that the formation of diphenylamine occurs in the presence of $CuFe_2O_4$ but not in presence of $NiFe_2O_4$, $CoFe_2O_4$, and Fe_2O_3 catalysts. Therefore, presence of Cu(I) ions at the catalyst surface is the key to the successful formation of diphenylamine (Scheme 2).

The regioselective hydroboration of alkynes shown at the top of Scheme 2 has been reported to occur in high yields on using nanostructured $CuFe_2O_4$ (90%) and copper oxide (CuO and Cu_2O, 80 %) catalysts [63]. Interestingly, copper ferrite promotes selective ring-opening of benzoxazoles or benzothiazoles in the presence of aryl halides such as iodobenzene (shown at the right of Scheme 2). In addition, $CuFe_2O_4$ nanoparticles act as catalysts for the synthesis of substituted benzoxazoles, benzothiazoles and benzimidazoles in toluene solvent under oxygen ambient [178]. A key step for the formation of benzoxazoles and benzothiazoles is shown at the bottom of Scheme 2, in which the o-aminophenol or 2-aminobenzenethiol is adsorbed over MFe_2O_4 surface through the lone-pair electrons of
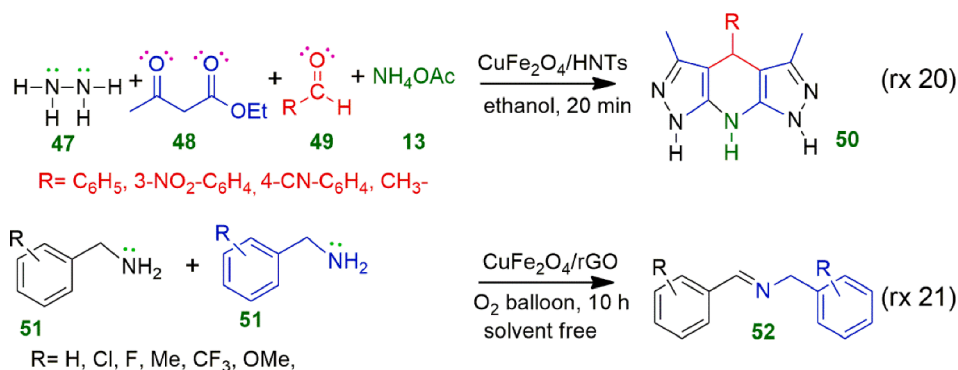
Scheme 3. Selected organic reactions catalyzed by $CuFe_2O_4$ based nanocomposites.

Table 5

Some important metal ferrite nanocomposites and their catalytic performances.

Composite	Particle size and surface area	Catalytic process and features	Temp., time, yield	Ref.
$CuFe_2O_4/\alpha\text{-}Fe_2O_3$ thin films deposited over FTO coated glass	– –	Photoelectrochemical water splitting. The thin films were tested as anode material. Highest photoconversion efficiency was achieved for $CuFe_2O_4$:α-Fe_2O_3 = 1:1.	r.t., – 2.87%	[184]
$CuFe_2O_4/\alpha\text{-}Fe_2O_3$ nanocomposite	100–200 nm, 63 $m^2\,g^{-1}$	Degradation (oxidation) of bisphenol A by activation of peroxymonosulfate. Performance of the catalyst was better at pH 9 than at pH 5.	25 °C 10 min 100%	[112]
$CuFe_2O_4$ impregnated graphene oxide	45–65 nm, –	Photoelectrochemical reduction of CO_2 to methanol. GO incorporation reduced the e^-/h^+ recombination in the hybrid catalyst. Methanol yield was 28.8 $\mu mol\,L^{-1}\,cm^{-2}$ at 20.5% quantum efficiency.	r.t., 240 min –	[127]
$CuFe_2O_4/$ MWCNTs nanocomposite	– 84.3 $m^2\,g^{-1}$	Degradation (oxidation) of trimethoprim antibiotic. Peroxymonosulfate was used to generate free radicals.	27 °C, 24 min 90%	[129]
$(NiFe_2O_4@Cu)SO_2$ montmorillonite	16 nm, 14.8 $m^2\,g^{-1}$	One-pot synthesis of coumarin-based 1,4-dihydropyridines by three-component condensation reaction of 4-hydroxycoumarin, aromatic aldehydes and ammonia. The composite shows better efficiency than acid catalysts such as silica gel and acidic alumina.	60 °C 20 min 90%	[131]
Ni/$NiFe_2O_4$ Nanocomposite	17 ± 3 nm, –	OER. The $NiFe_2O_4$-modified electrodes exhibited reduced overpotentials and higher sustained current densities for the OER when compared to pure Ni electrodes.	– – –	[108]
NiO/$NiFe_2O_4$	– 18 $m^2\,g^{-1}$	OER. The best electrochemical oxygen evolution activity was obtained for a Fe/(Fe + Ni) molar ratio 1:10. *In situ* EXAFS experiments demonstrated that under OER conditions some of the Fe^{3+} ions change their coordination from tetrahedral to octahedral.	– – –	[185]
$FeNi_3$ foam/ $NiFe_2O_4$ nanocomposite	110 nm width and 180 nm long, –	OER. Superior OER activity and remarkable durability achieved due to large active surface area, high hydrophilicity and enhanced electronic conductivity.	– – –	[186]
$NiFe_2O_4$ NP (7 mol%) incorporated MgH_2	~20 nm –	Improving the hydrogen storage properties of MgH_2. At 300 °C and 4 MPa of H_2 pressure, the composite can absorb 4.50 wt% H_2. Desorption of H_2 from the composite takes place at temperatures below 300 °C.	300 °C 66 min –	[187]
$TiO_2@NiFe_2O_4$ nanocomposite	52–57 nm 22–52 $m^2\,g^{-1}$ [b]	The sol–gel grown core–shell composite was used for N,4-diphenylbutyramide synthesis in a radiofrequency-heated continuous flow reactor.	150 °C – 60%	[188]
$NiFe_2O_4$/rGO nanocomposite	11 nm 178 $m^2\,g^{-1}$ [b]	Degradation of methylene blue under visible-light illumination. When *tert*-butanol was used as a scavenger for the hydroxyl ($^\cdot$OH) radical, the degradation diminished considerably. The composite was synthesized by mechanical ball-milling.	60 °C 180 min 99 %	[130]
$CoFe_2O_4$/CoO, $CoFe_2O_4$/ZrO_2, $CoFe_2O_4$/Al_2O_3 nanocomposites	– –	Two-step thermochemical CO_2 splitting to generate CO. $CoFe_2O_4$/CoO composite produced a significantly higher amount of CO (8.5 mL g^{-1}) than the other two composites.	1000 °C 30 min –	[189]
$CoFe_2O_4$/SiO_2 nanocomposite	25–35 nm 91.8 $m^2\,g^{-1}$	Oxidation of cyclohexane to cyclohexanone and cyclohexanol. Catalytic activities of $CoFe_2O_4$/SiO_2 composite was much higher than pristine $CoFe_2O_4$ NPs. The oxidant used was O_2.	160 °C 6 h 95.4%	[190]
$CoFe_2O_4$/TiO_2 nanocomposite	5 nm, 69.7 $m^2\,g^{-1}$	Photocatalytic oxidation of phenol in air-saturated aqueous suspension. Photo-generated electrons of TiO_2 were transferred to $CoFe_2O_4$, followed by O_2 reduction. $CoFe_2O_4$ supported on TiO_2 acts as a bifunctional cocatalyst for reduction of O_2 to H_2O_2 and oxidation of phenol.	25 °C 90 min ~90%	[128]
$CoFe_2O_4$@graphene aerogel	35 ± 8 nm, 69.7 $m^2\,g^{-1}$	Degradation (oxidation) of norfloxacin, phenol, indigo carmine, methyl orange, orange II and malachite green in presence of peroxymonosulfate. Cobalt ferrite activated the peroxymonosulfate to generate $SO_4^{\bullet-}$ free radicals responsible for the oxidation.	r.t., 7–12 min –	[191]
$CoFe_2O_4$NRs/SWCNTs Nanocomposite[a]	~45 nm [c] –	OER and HER. Worked at low overpotentials (310 mV for OER and 262 mV for HER). R_{ct} of the composite was only 8.835 Ω.	– – –	[58]

OER = oxygen evolution reaction, HER = hydrogen evolution reaction,

[a] SWCNTs = single-walled carbon nanotubes, NR_S = nanorods.

[b] Value corresponds to the surface area of the composite.

[c] Value corresponds to average diameter of the nanorods.
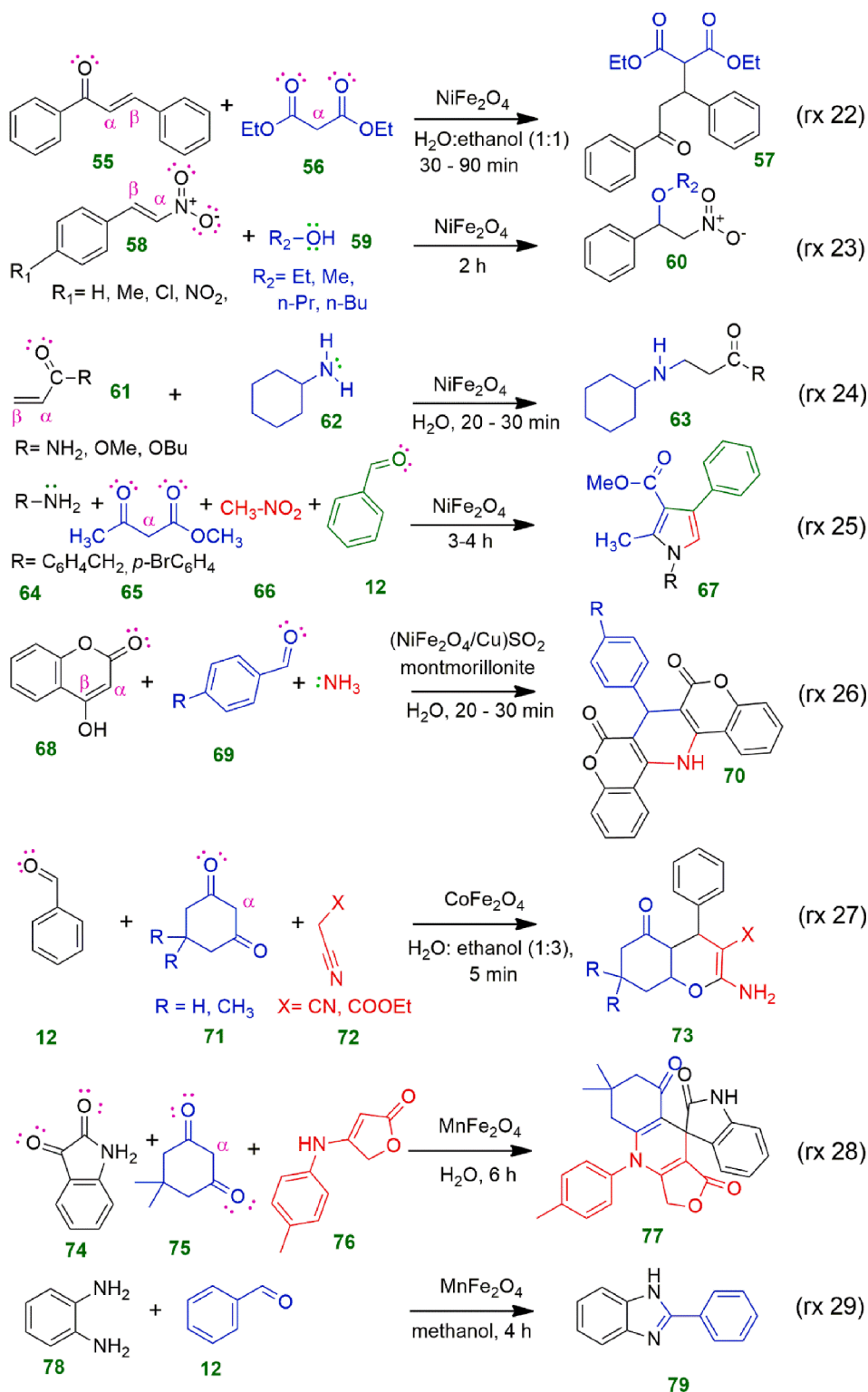
Scheme 4. Selected organic reactions catalyzed by NiFe₂O₄, CoFe₂O₄ and MnFe₂O₄ nanoparticles.

nitrogen to activate the carbon atom of the C=N double bond (an imine group). Then, the hydroxyl or sulfhydryl (-SH) group of the phenol or thiol makes a bond with the activated carbon atom through intra-molecular attraction.

4.1.3. Synthesis of organic molecules catalyzed by CuFe2O4 based nanocomposites

Utilization of copper ferrite-based nanocomposites in the synthesis of organic molecules is desmonstrated trhough two examples presented in Scheme 3. In the first example, (rx 20), pyrazolopyridine derivatives **50** were synthesized at room temperature using CuFe$_2$O$_4$ supported on halloysite nanotubes (HNTs) [167]. These derivatives were obtained through a multicomponent reaction using hydrazine **47**, ethyl acetoacetate **48**, aromatic aldehydes **49** and ammonium acetate **13** as reagents [167]. Being a Lewis acid, CuFe$_2$O$_4$@HNTs nanocomposite participates in several steps of the reaction and accelerates the multicomponent process. A Hantzsch-type mechanism was proposed for the formation of pyrazolopyridine derivatives [180]. The yields of reaction (rx 20) using HNTs, CuFe$_2$O$_4$ NPs and CuFe$_2$O$_4$@HNTs nanocomposite as catalysts were 28, 53 and 96%, respectively, evidencing the advantage of using the CuFe$_2$O$_4$@HNTs composite over bare CuFe$_2$O$_4$ nanostructures. Even after eight reusability tests, the nanocomposite produced 88% reaction yield. Synthesis of pyrazolopyridine derivatives with high yield is highly desirable considering their utility in antileishmanial, antimicrobial and antiviral applications [167].

In the second example, imine **52** was generated by coupling two amines **51** (rx 21) [85]. Utilization of CuFe$_2$O$_4$ NPs, Fe$_2$O$_3$/rGO, CuO$_2$/rGO and CuFe$_2$O$_4$/rGO composites as catalysts produced 23, 18, 56 and 90% yields, respectively [85]. The efficiency of the coupling reaction is also affected by the reaction atmosphere. For example, the reactions performed with CuFe$_2$O$_4$/rGO composite catalyst in O$_2$ and N$_2$ atmospheres revealed 90 and 16% yields, respectively; which suggests the formation of superoxide (O$_2$·$^-$) species at the surface of the CuFe$_2$O$_4$/rGO composite. The π–π stacking and electrostatic interactions between aromatic amines and rGO sheets increase the adsorption of the reactant molecules on the catalyst surface [85].

Faungnawakij et al. fabricated CuFe$_2$O$_4$/γ-Al$_2$O$_3$ composite for producing H$_2$ through steam reformation of dimethyl ether [57]. While the role of γ-Al$_2$O$_3$ was to generate methanol from dimethyl ether, the role of copper ferrite was to transform methanol and H$_2$O vapors into H$_2$ and CO$_2$. About 85% conversion of dimethyl ether was achieved by this process. Interestingly, when the composite was exposed to H$_2$ (10% H$_2$ in N$_2$) at 350 °C for 3 h, the copper ferrite was reduced, generating Cu$^+$ and Cu^0 species at the surface of the composite [57]. The presence of Cu$^+$ ions at the surface of the composite was associated with its high catalytic activity. Utilization of bare CuFe$_2$O$_4$ nanoparticles in the programmed temperature reduction experiment under Ar + H$_2$ (5%) gas flow (150–350 °C) was seen to generate Cu^0 and Fe$_3$O$_4$ [57]. This observation indicates an electron transfer process between the support and the ferrite nanostructures is in vogue, which determines the valence state of the ionic species at the surface of the composite [181–183]. Although several other copper ferrite based nanocomposites have been prepared by different research groups for water splitting [184], reduction of CO$_2$ [127], and degradation of antibiotics and pollutants [112,129], only a very few works have been reported on the utilization of these nanocomposites in organic molecule synthesis.

Hussain et al. fabricated CuFe$_2$O$_4$/α-Fe$_2$O$_3$ composite thin films deposited on FTO (fluorine doped tin oxide) coated glass substrates for photoelectrochemical (PEC) water splitting [184]. The photogenerated charge carriers could be separated effectively at the interface of n-type α-Fe$_2$O$_3$ and p-type CuFe$_2$O$_4$, and the photoexcited electrons could be transferred from the conduction band (CB) of α-Fe$_2$O$_3$ to the valence band (VB) of CuFe$_2$O$_4$ [184]. The electrons at the VB of CuFe$_2$O$_4$ are photoexcited to its conduction band, and migrate to the outer circuit [184]. The holes generated in the VB of α-Fe$_2$O$_3$ are responsible for PEC water oxidation to generate O$_2$. The highest PEC activity was obtained for a CuFe$_2$O$_4$/α-Fe$_2$O$_3$ ratio of 1:1. On the other hand, copper ferrite nanocomposites have been utilized for the photoelectrochemical reduction of CO$_2$ (to produce methanol, CO, etc.) [127], degradation of antibiotics (e.g., trimethoprim) [129] and phenols (e.g. bisphenol A) [112]. Utilization of copper ferrite nanocomposites in different catalytic and photocatalytic processes has been highlighted in Table 5.

4.1.4. Synthesis of organic molecules catalyzed by NiFe2O4, CoFe2O4 and MnFe2O4 NPs and their nanocomposites

Organic synthesis catalyzed by NiFe2O4 nanoparticles and nanocomposites. Michael addition is an important chemical reaction frequently used in organic synthesis to generate C-C bonds. NiFe$_2$O$_4$ nanoparticles have been utilized to catalyze nucleophilic addition (Michael addition) of several active methylene groups, along with aromatic/aliphatic amines, alcohols and thiols with conjugated alkenes. For example, the reactions (rx 22)- (rx 24) presented in Scheme 4 were performed by Payra et al. [179] at 20–100 °C utilizing NiFe$_2$O$_4$ NPs (~15 nm diameter) as catalyst, obtaining product yields in-between 88 and 98%. The classical Michael addition occurs when a nucleophilic enolate ion reacts with an α,β-unsaturated carbonyl compound. The nucleophilic enolate ion is formed by removing an acidic α proton from β-dicarbonyl compound, such as diethylmalonate **56** in presence of a strong base (usually NaOCH$_2$CH$_3$ or KOH). In the example (rx 22), the enolate ion generated from **56** binds to the β carbon of 1,3-diphenyl-prop-2-ene-1-one **55** [179]. One example of an oxa-Michael addition of alcohols to conjugated alkenes is shown in (rx 23), in which alcohol **59** binds to the β carbon of an α,β-unsaturated nitrocompound (β-nitrovinyl benzene, **58**) [179]. In the Aza-Michael addition reaction of aliphatic amines with α,β-unsaturated carbonyl compounds presented in (rx 24), the amine bind to the β carbons of the carbonyl compounds **61** [179]. The organic molecules (α,β-unsaturated ketones and nitrocompounds) participating in (rx 22) - (rx 24) are adsorbed on the surface of NiFe$_2$O$_4$ nanoparticles through their lone-pair electrons over oxygen atom (drawn in pink color, Scheme 4), thereby making the β carbon in **55**, **58** and **61** more active to be accepted by the nucleophiles (i.e., enolate anion of **56**, alcohol **59**, amine **62**). Moreover, the presence of nickel ferrite catalyst in the Michael addition reactions avoids the use of a strong base needed to remove acidic protons from the α and β carbons of the carbonyl compounds. These protons become more acidic (i.e., weaker C-H bonds) once the compounds are adsorbed over NiFe$_2$O$_4$ surface (a Lewis acid), thus avoiding the requirement of a base in the reaction [192]. In fact, other Lewis acids such as Zn(OTf)$_2$, Cu(OTf)$_2$, Sc(OTf)$_2$, In(OTf)$_2$ and FeCl$_3$·6H$_2$O have also been used to catalyze the Michael addition between 2-cyclopentenon and β-dicarbonyl compounds [192]. As shown in Scheme 2, two oxygen atoms of

β-dicarbonyl compound coordinate simultaneously with the Fe(III) ion of the metal ferrite surface, removing a proton from α carbon [192]. The analysis presented above supports the fact that $NiFe_2O_4$ NPs behave as Lewis acid catalysts in Michael reactions.

On the other hand, pyrroles are among the most prominent organic frameworks with important pharmaceutical and biological activities [193]. Moghaddam et al. reported a one-pot four-component synthesis of substituted pyrroles **67**, with high to excellent yields (70–96%) in the presence of $NiFe_2O_4$ nanoparticles (rx 25) [193]. To highlight their success, we must recall that these four-component reactions are some of the most difficult reactions to achieve with high yield without utilization of an efficient catalyst. The usefulness of nickel ferrite nanostructures in Hantzsch reactions is highlighted in (rx 26). Utilizing copper-immobilized nickel ferrite@sulfate-activated montmorillonite ($NiFe_2O_4$@Cu)SO$_2$(montmorillonite) nanocomposite, Zeynizadeh et al. synthesized coumarin-based 1,4-dihydropyridines **70**, exploiting the Hantzsch reaction as presented in (rx 26) [131]. The yields of this reaction with and without catalyst were 98 and 5%, respectively.

Organic synthesis catalyzed by $CoFe_2O_4$ nanoparticles and nanocomposites. 2–8 nm $CoFe_2O_4$ nanoparticles with a specific surface area of 141 $m^2 g^{-1}$ were used as catalyst in a multicomponent reaction to obtain 2-amino-4-(phenyl)-5,6,7,8-tetrahydro-7,7-dimethyl-5-oxo-4H-chromene-3-carbonitrile derivatives **73**, (rx 27) [194]. When × corresponds to the CN group in (rx 27), the reaction yield was 89%. When the benzaldehyde in (rx 27) was replaced with other aromatic aldehydes, the reaction yield varied between 60 and 96%. The merits of this reaction pointed out by the authors are high efficiency, clean reaction, simplicity, short reaction time (<20 min), versatility and high yield [194]. Although several other catalysts such as alumina, MgO and Ni also produced ∼ high yield (90%) in reactions similar to (rx 27), utilization of $CoFe_2O_4$ nanostructures in such reactions is advantageous as it needs smaller catalyst loading and shorter reaction time to produce a comparable reaction yield.

Organic synthesis catalyzed by $MnFe_2O_4$ nanoparticles and nanocomposites. An important chemical process catalyzed by MFe_2O_4 (M = Ni, Zn, Mn, Co) nanostructures is the conversion of methanol to C6–C21 hydrocarbons as demonstrated by Lai et al. [195]. The reactions were carried out at 280 °C for 180 min inside an autoclave in two steps: (i) catalytic reforming of methanol to H_2 and CO, and (ii) subsequent conversion of syngas to hydrocarbons via Fischer–Tropsch synthesis (FTS) [195]. The efficiency of liquid C6–C21 hydrocarbon production for the metal ferrite catalysts was in the order $ZnFe_2O_4 > MnFe_2O_4 > CoFe_2O_4 \gg NiFe_2O_4$. Some liquid ketones, alcohols and methyl esters were also obtained in small quantities. In addition, the authors analyzed the composition of gases (i.e., H_2, CH_4, C_2H_2, C_2H_6, C_3H_6, C_3H_8, CO_2, etc.) generated during the reaction. While the principal gaseous product of the reaction catalyzed by $ZnFe_2O_4$ and $MnFe_2O_4$ ferrites was H_2, for the $CoFe_2O_4$ and $NiFe_2O_4$ ferrites the principal product was methane [195].

Among the metal ferrite nanostructures, $MnFe_2O_4$ NPs have been used as Lewis acid catalysts for the oxidation of 5-hydroxymethylfurfural to generate 2,5-furandicarboxylic acid in presence of *tert*-butyl hydroperoxide [196], in the synthesis of spirooxindoles [197] and synthesis of 2-substituted benzimidazoles [198]. A representative Lewis acid reaction catalyzed by $MnFe_2O_4$ NPs for the synthesis of spirooxindole **77** is shown in (rx 28) [197]. The synthesis was carried out through condensation of isatin **74**, dimedone **75** and 4-(p-tolylamino)furan-2(5H)-one **76**, using water as the solvent. The reaction performed at 90 °C for 6 h in presence of $MnFe_2O_4$ NPs produced 88% yield. Adsorption of isatin and dimedone on the surface of the catalyst activated the carbonyl groups of the molecules and weakened the C-H bond at the α-carbon of the dimedone molecule, enhancing the reaction yield. On the other hand, 2-substituted benzimidazoles have been synthesized with high yield using $MnFe_2O_4$ NPs. For example, 2-phenylbenzimidazole **79** has been synthesized with 92% yield by mixing o-phenylenediamine **78** and benzaldehyde **12** in methanol at room temperature in the presence of $MnFe_2O_4$ NPs, as shown in (rx 29) [198]. On replacing benzaldehyde with benzyl (diphenylethanedione), the reaction generated 2,3-diphenylquinoxaline with high yield. Utilization of $MnFe_2O_4$ catalyst in the reaction allowed it to occur at room temperature, with high selectivity, even under air atmosphere. The presence of O_2 is indispensable for the synthesis of 2-substituted
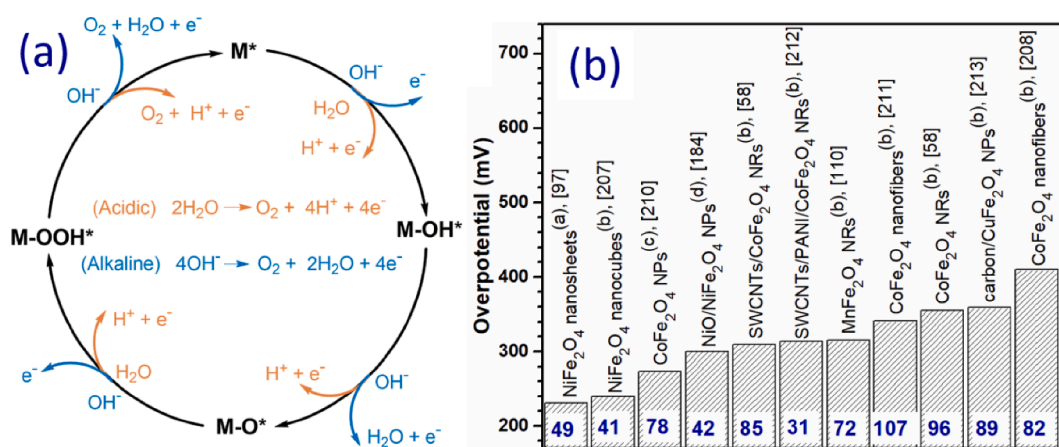

Fig. 12. (a) OER elementary reactions under acidic and alkaline media, where M represent a transition metal. M* refers to the adsorption site on catalyst surface. Reproduced from ref. [210] with permission from Wiley-VCH GmbH, Copyright 2020. (b) Overpotential of nickel, cobalt, manganese and copper ferrites used as electrocatalysts for OER at 10 mA cm^{-2} in alkaline media. Values inside the bars correspond Tafel slopes (mV dec^{-1}) for the electrocatalysts. Values inside brackets correspond to the references. $NiFe_2O_4$ nanosheets were functionalized with $H_2PO_3^-$ and PO_3^- ions. Electrodes were prepared in (a) carbon cloth, (b) glassy carbon, (c) Ni foam and (d) carbon paper substrates.

benzimidazoles as O_2 molecules remove hydrogen atoms from the C-H and N-H bonds of the intermediate 2-phenyl-2,3-dihydro-1H-benzo[d]imidazole, allowing the formation of the desired product, as demonstrated by Xue and Long [199].

4.1.5. Niche catalytic processes assisted by metal ferrites

4.1.5.1. H_2 production and oxygen evolution reaction (OER). The production and storage of H_2 are two important aspects of current alternative energy drives. Metal ferrite nanostructures and nanocomposites have been successfully utilized for both hydrogen production and OER. While nanoparticles of noble metals such as Pd and Pt have been frequently utilized as electrocatalysts for hydrogen production, some transition metal oxides such as TiO_2 have been utilized as effective catalysts for photocatalytic hydrogen generation. On the other hand, RuO_x and IrO_x are the two best performing electrocatalysts for OER [200,201]. While the noble metals such as Pd and Pt bear high cost and limited earth abundance, TiO_2 has a large bandgap (3.0–3.2 eV at room temperature) with low visible light absorption capacity, limiting its utilization in visible-light photocatalytic OER [202]. To overcome these problems, transition metal oxides and layered double hydroxides (LHDs) based on cobalt, nickel, iron, etc. have been extensively explored and some of them have achieved noticeable efficiencies [201,203–205]. While electrocatalytic water splitting is the most common procedure for H_2 generation (apart from the steam reforming process, which is utilized for commercial hydrogen production [206]), the efficiency of this process is limited by the OER, which occurs simultaneously [185]. To address the problem of low efficiency, several research groups have used $NiFe_2O_4$ and $CoFe_2O_4$ nanostructures as active electrode materials [58,97,185,207–209]. In fact, finding low-cost electrocatalysts with low overpotential, low Tafel slope, and high stability under acidic or alkaline conditions was the main focus of OER and H_2 production research.

Although electrochemical OER can occur both in acidic and alkaline media, OER tests are usually performed in 0.1 M or 1.0 M KOH solutions because of the better stability and performance of the electrocatalyst in alkaline media. The OER consists of four elementary steps, in which four electrons are generated along with an O_2 molecule per cycle (Fig. 12**a**). In alkaline media, an OH^- ion binds to the metal ion (M*) on the surface of the oxide to generate M−OH moiety. By reaction with another OH^- ion, the hydrogen atom of the M−OH moiety is removed, producing MO* moiety, which acts as an adsorption site. Another OH^- ion binds to the oxygen atom of MO* to form M−OOH. Once the M−OOH peroxide is formed, the M−O bond is needed to be broken to release O_2. As can be seen in Fig. 12**a**, each of the above-mentioned steps produces one electron. As these electrons travel through the electrocatalyst and other components of the electrode, a low charge-transfer resistance (R_{ct}) is required. For this reason, high resistive metal ferrites are frequently functionalized or mixed with conducting materials to reduce the R_{ct} of the metal ferrite containing electrodes, diminishing their overpotentials and Tafel slopes in the OER tests. For example, Chen et al. fabricated nickel ferrite nanosheets on carbon cloth through a solvothermal method and annealed them at 500 °C (1 h) under N_2 atmosphere in presence of $NaH_2PO_2 \cdot H_2O$. The phosphate-ion-functionalized $NiFe_2O_4$ nanostructures revealed excellent performance in electrocatalytic OER [97]. The phosphating process changed the Fe^{2+}/Fe^{3+} ratio on the surface of the ferrite due to the reduction of Fe^{3+} ions to Fe^{2+} [97]. The R_{ct} of the phosphate-ion-functionalized $NiFe_2O_4$ electrode (0.3 Ω) was significantly smaller than the pristine $NiFe_2O_4$ electrode (17.5 Ω) [97]. Due to low R_{ct} and presence of phosphate ions ($H_2PO_3^-$ and PO_3^-), the composite had enhanced charge transfer rate and higher number of active catalytic sites [97]. Relatively low overpotential (231 mV at 10 mA cm^{-2}) and smaller Tafel slope (49 mV dec^{-1}) for the phosphate functionalized metal ferrite indicate its superior electrocatalytic activity for the target reaction [97,207]. To highlight the performance of metal ferrite nanostructures and nanocomposites in electrochemical OER, reported overpotential values for the electrodes made of some of them are presented in Fig. 12**b**. As can be seen in Fig. 12**b**, the phosphated $NiFe_2O_4$ has the lowest overpotential among the values reported for metal ferrite nanostructures and nanocomposites. Qiao et al. fabricated mesoporous $NiFe_2O_4$ nanocubes (60 nm edge length) with a high surface area (125 m^2 g^{-1}) and utilized them in OER by depositing over glassy carbon disc electrodes. As the $NiFe_2O_4$ nanocubes were not combined with any other material to form a conducting composite, the R_{ct} of the fabricated electrode was as high as 42 Ω. The electrodes exhibited a low overpotential (240 mV) and a small Tafel slope (41 mV dec^{-1}) at a current density of 10 mA cm^{-2} [208]. Similarly, Li et al. fabricated MFe_2O_4 nanofibers deposited on glassy carbon electrodes for application in OER. The overpotentials of the fabricated electrodes for OER at 5 mA cm^{-2} were in the order of $CoFe_2O_4$ (410 mV) < $CuFe_2O_4$ (450 mV) < $NiFe_2O_4$ (467 mV) < $MnFe_2O_4$ nanofibers (520 mV) [209]. As the authors did not prepare any nanocomposite of the MFe_2O_4 nanofibers by combining with a conductive material and the diameter of the nanofibers were large enough (between 100 and 300 nm), the reported R_{ct} values for the fabricated electrodes were higher than 1700 Ω. Estimated R_{ct} values of the four electrodes were in commensurate with their OER performance, clearly demonstrating the role of R_{ct} on the electrocatalytic activity of the metal ferrite nanostructures.

To accelerate the sluggish HER/OER kinetics of transition metal oxide nanostructures, some researchers have synthesized hierarchical metal oxide nano-/microstructures over hollow conducting templates to used them as conductive networks, surface modifiers, or structural stabilizers [214,215]. Utilization of such conductive hollow templates as host material not only improves the electronic conductivity of the composite electrocatalysts, but also prevents the aggregation the supported nano-/microstructures during electrocatalytic reactions [214]. Additional advantages of such hollow nano-/micro structures in HER/OER are their abundant exposed active sites, high contact area between catalysts and electrolyte, and shortened mass/charge transport length [214]. Moreover, these hollow hierarchical nano-/microstructures preserve their morphology and structural characteristics even after prolonged catalytic cycles. For example, Ni-Fe LDH hollow prisms demonstrated their excellent OER activity with high stability over 1000 cycles [206].

Apart from the number of accessible active sites, the electrocatalytic activities of OER electrocatalysts depend largely on the stability of adsorbed intermediates (OH*, O*, OOH*) on their surface (* denotes the surface adsorbed specie) [215]. In others words, tuning the binding energy of M−O within the intermediates (M−O, M−OH, and M−OOH; where M is the surface metal cation) is

critical for enhancing the OER performance of the electrocatalyst [216]. In the case of Fe-, Co-, Ni- and Mn-based catalysts, there occur some compositional changes at their surface during catalysis, especially during OER process. M−O, M−OH and M−OOH - type intermediates are usually formed at the surface of the catalysts under alkaline conditions due to the electron transfer process occurring in OER [216,217]. At the surface of the Fe-, Co-, Ni- and Mn-based metal oxides electrocatalysts (such as metal ferrites), some hydroxides and oxihydroxides (called intermediates) can be formed during OER (e.g. α-FeOOH, β-FeOOH, γ-FeOOH, α-Ni(OH)$_2$, β-NiOOH, γ-NiOOH, CoOOH and MnOOH) [216]. The local structures of these hydroxides and oxyhydroxides also depend on the applied bias potential and the nature of used electrolyte [216]. In the case of Ni- and Co-based oxyhydroxides, the OER activity can be significantly improved if iron is incorporated into the oxyhydroxides as impurity [218]. The OER activity trend for the oxyhydroxide thin films grown on conductive Au substrate is seen to be Ni(Fe)O$_x$H$_y$ > Co(Fe)O$_x$H$_y$ > FeO$_x$H$_y$ > CoO$_x$H$_y$ > NiO$_x$H$_y$ > MnO$_x$H$_y$ [216,218]. These intermediates can be progressively transformed into another polymorph during the OER cycles. For example, during prolonged cycling (about 100 cyclic voltammetry), α-Ni(OH)$_2$ is seen to transform into an electroactive species γ-NiOOH [215]. According to Feng et al. mixed Ni − Fe compounds are the most promising Earth-abundant OER electrocatalysts in alkaline electrolytes [216]. Indeed, as we can see in Fig. 12b, NiFe$_2$O$_4$ nanostructures render the best performance in OER in comparison with the performance of other metal ferrite nanostructures.

On the other hand, metal ferrite composites of a large variety such as CoFe$_2$O$_4$ NRs/SWCNTs [58], NiO/NiFe$_2$O$_4$ [185], and FeNi$_3$ foam/ NiFe$_2$O$_4$ [186] have been utilized in H$_2$ production and OER, aiming to reduce the overpotential and Tafel slope, increase the stability of the electrodes in alkaline media and increase the long-term durability of the catalyst. Although bare metal ferrite nanostructures have been utilized for H$_2$ production through photocatalytic water splitting, their efficiencies are relatively low [202,211]. On the other hand, metal ferrite nanocomposites fabricated by coupling metal ferrite nanostructures with conducting materials such as metals, carbonaceous materials and selective semiconducting materials with adequate conduction band positions (e.g., g-C$_3$N$_4$) produced H$_2$ with much higher efficiencies. A notable example of such an approach is the work reported by Zeng et al., [211] who prepared Au/g-C$_3$N$_4$/NiFe$_2$O$_4$ nanocomposite with approximately 1.0 wt% Au NP loading and utilized it in photocatalytic water splitting to generate H$_2$. The nanocomposite produced H$_2$ gas from water at a rate of 1.607 mmol g^{-1}h^{-1} under visible light illumination upon the utilization of triethanolamine (10%, v/v) as a hole scavenger. The plasmonic Au NPs in the composite served in two counts: (i) to enhance the visible-light absorption and generate more photoelectrons and (ii) to utilize the photoelectrons at the conduction band of g-C$_3$N$_4$ for reducing the H$^+$ ions to produce H$_2$. Another notable example of utilizing metal ferrite nanocomposites is the work reported by Dhanalaxmi et al., where the authors utilized a MnFe$_2$O$_4$/benzene-benzylamine-1 nanocomposite as photocatalyst for H$_2$ generation through photocatalytic water splitting, achieving an efficiency around 6.1 mmol g^{-1}h^{-1} [202]. In addition to high efficiency, the advantages of using this organic–inorganic nanocomposite were to avoid the use of precious noble metal co-catalysts and use of sacrificial agents. Ding et al. fabricated CoFe$_2$O$_4$/SWCNT composites by wrapping CoFe$_2$O$_4$ nanorods with SWCNTs and used them for electrocatalytic OER and HER [58]. Lower overpotentials for OER (310 mV at a current density of 10 mA cm^{-2}) and HER (263 mV at 10 mA cm^{-2}) were obtained for the nanocomposite in 1.0 M KOH electrolyte in comparison to the pristine CoFe$_2$O$_4$ nanorods (355 mV at a current density of 10 mA cm^{-2}) owing to good charge transfer between CoFe$_2$O$_4$ and SWCNTs. This also effectively boosted the OER and HER performance of the CoFe$_2$O$_4$ nanostructures [58]. Liu et al. grew small (<11 nm), well-dispersed CoFe$_2$O$_4$ NPs over PANI (polyaniline) functionalized SWCNTs and utilized them for oxygen evolution reaction [212]. The PANI provided enough active sites over the SWCNTs for the nucleation of CoFe$_2$O$_4$ NPs uniformly. Moreover, the formed metal ferrite NPs remained tightly attached to the SWCNTs even after 1000 cycles of OER. The electrodes prepared by depositing the CoFe$_2$O$_4$/ PANI/SWCNTs composite over glassy carbon achieved an overpotential of 314 mV at 10 mA cm^{-2} and a low Tafel slope of 30.69 mV dec^{-1}, indicating the nanocomposite is a promising alternative to RuO$_2$ and IrO$_2$ for OER. Li at al. synthesized CuFe$_2$O$_4$ nanocrystals embedded in 3D hierarchical porous carbon nanowires and utilized for electrochemical OER by depositing on rotating disk electrodes [213]. The fabricated electrodes exhibited lower overpotential (359 mV) and lower Tafel slope (89.4 mV dec^{-1}) in comparison to the overpotential (474 mV) and Tafel slope (164.6 mV dec^{-1}) of the bare CuFe$_2$O$_4$ electrodes. The R_{ct} of the nanocomposite electrode was much lower than that of the electrode made of bare CuFe$_2$O$_4$, clearly demonstrating the advantage of using a conductive support and small NPs. The Tafel slope of the nanocomposite (~89.43 mV dec^{-1}) was slightly higher than the corresponding values obtained for commercial RuO$_2$ (~78.36 mV dec^{-1}) [213], which is one of the best electrocatalysts for OER.

Many studies have been published recently on the utilization of metal ferrite nanostructures and nanocomposites in OERs and HERs (Tables 5 and 6) [58,108,110,113,185,186,219–221]. While the performance of CuFe$_2$O$_4$ spinel nanostructures in H$_2$ evolution reactions has been reported to be considerably better [222,223] than NiFe$_2$O$_4$, CoFe$_2$O$_4$, and MnFe$_2$O$_4$ nanostructures [222], NiFe$_2$O$_4$ nanostructures demonstrated superior performance in oxygen evolution reactions. It must be noted that while several research groups utilized CuFe$_2$O$_4$ nanostructures and their nanocomposites for HER [223–227], very few works have been reported on their utilization in OERs [209,213,228]. Moreover, reported overpotential values for CuFe$_2$O$_4$ nanostructures in OERs varied significantly from one group to the other.

Among the metal ferrite nanocomposites, Cu/CuFe$_2$O$_4$ (1.2% of Cu) exhibited superior performance (2.26 mmol g^{-1}h^{-1}) in hydrogen evolution reactions [225]. However, the disadvantage of using Cu/CuFe$_2$O$_4$ nanocomposite in HER is that the synthesis of the Cu NPs is needed to be carried out under vacuum or through the utilization of organic surfactants to avoid the oxidation of copper. On the other hand, CuFe$_2$O$_4$/ZnO (3% of ZnO) nanocomposite exhibited reasonably good HER performance (441 μmol g^{-1}h^{-1}) under normal reaction conditions, requiring no sacrificial agent or vacuum ambient [224]. As for OER, NiO/NiFe$_2$O$_4$ and CoFe$_2$O$_4$/PANI/ SWCNTs nanocomposites exhibited superior performance in terms of low overpotential and low Tafel slope (Fig. 12b). While a higher crystallinity is an important aspect for the good performance of metal ferrite nanostructures in OERs [113,220], creating heterojunctions of metal ferrite and other semiconductors (e.g., g-C$_3$N$_4$ and α-Fe$_2$O$_3$) to diminish the recombination rate of photogenerated electrons and holes is an efficient strategy for improving the HER performance of metal ferrite nanostructures [184,211].

4.1.5.2. Reduction of NO and conversion of CO. Although there are very few literature reports, metal ferrite nanostructures can be utilized to catalyze both the reduction and oxidation reactions of common toxic gases such as NO and CO. While the toxic NO reduces to non-toxic N_2, CO can either be oxidized to less-toxic CO_2 or reduced to carbon. For these reactions, we take advantage of some of the specific features of metal ferrites, such as: (i) the presence of multivalent cations, (ii) moderate-to-high thermal stability, and (iii) the possibility of incorporating highly active metal ions (e.g., Pt^{2+}). For example, $NiFe_2O_4$ NPs catalyze the reduction of NO in the presence of C_3H_6, CO and O_2 at moderate temperatures (e.g., 325 °C) [238]. In this reaction, the propene molecules adsorbed on the surface of the nickel ferrite catalyst oxidize to form acetate (CH_3COO^-) ions, which react with NO to generate the intermediate NCO^- ion and finally N_2 and CO_2, as demonstrated by Ueda et al. through operando Fourier transform infrared (FTIR) spectroscopy [238]. The major disadvantages of this process are that it occurs at elevated temperatures (depending on the used catalysts) and generates carbon

Table 6
Selected catalytic processes assisted by metal ferrites (MFe_2O_4, M = Co, Ni, Cu, Mn).

Catalyst	Size and surface area	Catalytic process	Reaction conditions and features	Ref.
$NiFe_2O_4$ NPs	5–45 nm –	Electrocatalytic oxidation of glucose	The catalyst was mixed with carbon (50 wt%). The oxidation potential was 0.76 V (vs SCE, saturated calomel electrode).	[229]
$NiFe_2O_4$ nanosheets	~2 nm thick 154 $m^2\,g^{-1}$	Degradation of tetracycline hydrochloride (TCH) antibiotic	Degradation of TCH occurs within 15 min with ~ 90% efficiency by microwave heating of a 50 mL aqueous solution containing TCH (10 mg L^{-1}) and $NiFe_2O_4$ (50 mg).	[230]
$NiFe_2O_4$ NPs	< 50 nm 85.7 $m^2\,g^{-1}$	Selective hydrogenation of eight aldehydes to generate alcohols without using H_2	2-propanol was used as H-donor and solvent. The amount of aldehyde, $NiFe_2O_4$ and 2-propanol used were 1 mmol, 60 mg and 10 mL, respectively. High yields (>74%) for reactions in 180–200 °C temperature range. Negligible yields for no catalyst. The process takes place through the MPV[a] reduction mechanism.	[231]
$NiFe_2O_4$ –	– 85.7 $m^2\,g^{-1}$	Reduction of NO to N_2, and oxidation C_3H_6 and CO to CO_2 and H_2O	As NO, CO and C_3H_6 gases are commonly present in gasoline vehicle exhausts, the conversion of these gases carried out in-between 300 and 500 °C is interesting for using as low-cost catalyst in vehicle exhausts. Efficiency of NO reduction decreased in presence of water vapor.	[232]
Mesoporous $NiFe_2O_4$ NPs	> 100 nm 121 $m^2\,g^{-1}$	Photocatalytic water splitting for H_2 generation	The reaction was performed under photo-irradiation (λ > 420 nm) of a mixed suspension of H_2O (4.0 mL) and methanol (1.0 mL) with $NiFe_2O_4$ (2 mg) catalyst. H_2 evolution rate was 0.09 μmol h^{-1}. $NiFe_2O_4$ NPs with higher crystallinity exhibited better performance.	[113]
$Cu_xNi_{1-x}Fe_2O_4$ NPs	20 nm 92.28 $m^2\,g^{-1}$	Electrocatalytic oxidation of acetaldehyde	$Cu_xNi_{1-x}Fe_2O_4$ NPs achieved a considerably higher current densities in the cyclic voltammetry curves compared with $NiFe_2O_4$. The electrode made of $Cu_xNi_{1-x}Fe_2O_4$ NPs exhibited lower R_{ct} than the electrode fabricated with $NiFe_2O_4$ NPs. The oxidation was carried out using KOH solution as electrolyte.	[233]
$NiFe_2O_4$ NPs	– 48 $m^2\,g^{-1}$	Photocatalytic OER	2 mL of an aqueous buffer solution (pH 8.0) containing the catalyst (0.50 g L^{-1}), $Na_2S_2O_8$ (5.0 mM) and $[Ru(bpy)_3]^{2+}$ (0.25 mM) was exposed to UV light (λ > 420 nm). The O_2 evolution rate was 5.3 ± 0.2 μmol $s^{-1}\,g^{-1}$. $Na_2S_2O_8$ was used as sacrificial agent and $[Ru(bpy)_3]^{2+}$ as a photosensitizer.	[221]
$CoFe_2O_4$ particles	– 14 $m^2\,g^{-1}$	Degradation of herbicide 2,4-dichloro-phenoxyacetic acid (2,4-D)	A dispersion containing 2,4-D (20 mg L^{-1}), H_2O_2 (9 mM) and the catalyst (1 g L^{-1}) were exposed to UV light (254 nm) for 180 min at pH 6.0. Above 90 % of total organic carbon could be removed (mineralized).	[234]
$CoFe_2O_4$ NPs	18 nm 39 $m^2\,g^{-1}$	Degradation of methylene blue	The reaction mixture consisted 17.0 mL of the dye solution (4.8 mg L^{-1}), 8.0 mL of H_2O_2 (3 vol%) and 30 mg of $CoFe_2O_4$. The pH was adjusted to 3. Efficiency of degradation under UV irradiation was 87% in 420 min.	[235]
$CoFe_2O_4$ NPs grown on nickel foam (NF)	111 nm –	Electrochemical OER	The catalyst exhibits excellent electrocatalytic performance with an overpotential of 273 mV at a current density of 10 mA cm^{-2}. The Tafel slope was 78 mV dec^{-1}.	[219]
$CoFe_2O_4$ nanofibers	> 3 μm length and 92 ± 30 nm diameter –	Electrochemical OER	The electro-spinned nanofibers exhibited an overpotential of 341 mV at 10 mA cm^{-2} current density. The Tafel slope was 107 mV dec^{-1}. Electrochemical impedance spectroscopy (EIS) determined R_{ct} of the $CoFe_2O_4$ electrode under OER conditions was 44.8 Ω.[b]	[220]
$CoFe_2O_4$ NPs	12 nm 69 $m^2\,g^{-1}$	Chemical loop reforming of ethanol to produce H_2	Good H_2 production yield at 450 °C. CO, CO_2, H_2O, ethylene, ethane, acetaldehyde, ethyl acetate, coke, and acetone were obtained as byproducts.	[236]

[a] MPV = Meerwein-Ponndorf-Verley [237].

[b] R_{ct} = charge transfer resistance.

dioxide. However, Pt doped nickel ferrite ($NiFe_{1.95}Pt_{0.05}O_4$) nanoparticles (50–100 nm) exhibited high catalytic activity (96% efficiency) for the reduction of NO at a lower temperature (60 °C) in the presence of both H_2 and O_2 [239]. The presence of both Pt^{2+} and Pt^{4+} ions at the T_d and O_h sites in the spinel lattice, which enhances the chemisorption of NO at the catalyst surface, has been considered to be the main reason for its high catalytic activity. However, only a small fraction of Pt ions can be incorporated into the nickel ferrite lattice and the doped spinel nanoparticles lose their catalytic activity considerably above 120 °C because of the reaction of H_2 with O_2.

4.1.5.3. Degradation of pharmaceuticals and other organic pollutants. Metal ferrite nanostructures are useful catalysts for the degradation of organic pollutants such as dyes and expired pharmaceuticals [240]. For example, porous $CuFe_2O_4$ cubes (of edge length ~ 492 nm) were used for the photodegradation of rhodamine-B (RhB) with 90% efficiency after 200 min of reaction under visible light in the presence of H_2O_2 [241]. On the other hand, $CoMn_{0.2}Fe_{1.8}O_4$ NPs have been seen to be very active for the degradation of orange II dye in the presence of $NaHSO_3$ [242]. In fact, these manganese-containing metal ferrite NPs showed much higher degradation efficiency (85.4% in 2 h) than $CoFe_2O_4$ NPs (42.5% in 2 h). However, the degradation efficiency of $CoMn_{0.2}Fe_{1.8}O_4$ NPs was greatly suppressed by the addition of pyrophosphoric acid, which binds with Mn(III) ions at the surface of the ferrite. These two facts clearly demonstrate the beneficial effect of Mn^{3+} ion incorporation in the lattice of ferrite nanostructures on their dye degradation abilities.

Metal ferrites are excellent activators of common oxidants such as potassium peroxymonosulfate and hydrogen peroxide (H_2O_2). H_2O_2 can be activated by metal ferrites to generate highly active $^\bullet OH$ radicals to oxidize organic pollutant molecules. Likewise, in the presence of metal ferrites, the peroxymonosulfate ions (HSO_5^-) transform into more active sulfate radicals ($SO_4^{\bullet -}$) with superior oxidizing power [191].

On the other hand, metal ferrite-based nanocomposites have also been used for the degradation of organic pollutants and pharmaceuticals. For example, $Ni/NiFe_2O_4$ and $Co_3O_4/CoFe_2O_4$ nanocomposites have been used as catalysts for the degradation of 4-nitrophenol to 4-aminophenol in presence of $NaBH_4$ [243,244]. Interestingly, in the case of the $Ni/NiFe_2O_4$ nanocomposite, while the efficiency of nitrophenol degradation in the first cycle was only ~ 60 % in 160 min, in the subsequent reusability cycle, the efficiency of the catalyst increased up to 95% in 60 min only [243]. The reduction activity of the catalyst remained same in the subsequent four reusability cycles. Such an enhancement of degradation efficiency in reusability cycles was attributed to the removal of NiO shells formed around the nickel NPs by $NaBH_4$, which hindered the charge transfer between the nitrophenolate ion and the nickel NPs. Huang et al. used an $Ag_3PO_4@CoFe_2O_4$ nanocomposite for the photodegradation of methyl orange under visible light, achieving a degradation efficiency of 98% in 30 min [245]. However, the efficiency decreased considerably on performing the experiment in Ar atmosphere instead of oxygen or on utilizing a hole scavenger (triethanolamine) in the reaction solution, indicating that photogenerated holes and $O_2\bullet-$ are the dominant reactive species. Bai et al. used rGO supported metal ferrites (MFe_2O_4, M = Mn, Zn, Co and Ni) for the photocatalytic degradation of RhB and methylene blue (MB) dyes under visible light irradiation [246], revealing their photocatalytic activities in the order: $CoFe_2O_4/rGO > ZnFe_2O_4/rGO > MnFe_2O_4/rGO > NiFe_2O_4/rGO$. Over 85% degradation was achieved in 180 min using the $CoFe_2O_4/rGO$ nanocomposite. The improved photocatalytic performance of the composite has been associated with the π–π stacking of the rGO layers with planar aromatic rings in the dyes, which facilitates the adsorption of dye molecules on rGO surface. Adsorption of the dye molecules over rGO also improved due to the electrostatic interactions between the positively charged dye molecules and negatively charged functional groups at the rGO surface. Apart from enhanced dye adsorption, slow recombination of photo-generated charge carriers at MFe_2O_4/rGO interface is also responsible for the enhanced photocatalytic activity of the nanocomposites.

$CoFe_2O_4@$graphene aerogel nanocomposite has been utilized in presence of peroxymonosulfate ions for the degradation of Norfloxacin, a common antibiotic drug with bacteriostatic effect [191]. The nanocomposite exhibited remarkable catalytic performance with long-term stability toward degradation of organic contaminants and antibiotics, even at a high flow rate (120 mL h^{-1}) of the probing solutions. For example, complete degradation of Norfloxacin in aqueous solution (20 ppm) occurred within 10 min. To achieve such high catalytic performance, the $CoFe_2O_4@$graphene sheets in the aerogel needed to be aligned (through directional freezing and subsequent freeze-drying of the hybrid aerogel) to allow a high fluid flux through the interlayers of the aligned graphene sheets. On the other hand, $CuFe_2O_4/MWCNTs$ (multi-walled carbon nanotubes) nanocomposite has been utilized as a heterogeneous activator of HSO_5^- ions to generate $SO_4^{\bullet-}$ radicals and dissociate the antibiotic trimethoprim (89 % efficiency in 24 min) in aqueous solution [127]. However, for the successful dissociation of the antibiotic, the pH of the reaction mixture should be maintained either neutral (pH = 7) or basic (e.g., pH = 11). At low pH conditions, the adsorption of trimethoprim molecules at the composite surface decreased due to the protonation of amino groups of trimethoprim at the $CuFe_2O_4$ NP surface. The protonated amine groups and $CuFe_2O_4$ NPs repel each other, decreasing the degradation of trimethoprim. On the other hand, at higher pH values, the presence of OH^- ions at high concentration in the solution accelerates the decomposition of HSO_5^- ions to form $OH^\bullet$ radicals [247], which oxidize trimethoprim molecules.

$CoFe_2O_4$ nanostructures along with $CuFe_2O_4/\alpha-Fe_2O_3$ and $Cu/CuFe_2O_4$ nanocomposites have been used for the degradation (oxidation) of bisphenol A by activating peroxymonosulfate ions at the surface of these catalysts [112]. Again, the efficiency of the catalysts in the degradation of bisphenol A from its aqueous solution decreases with the reduction of solution pH, for the same reason as discussed above. The bisphenol A degradation performance of the catalysts followed the order $CuFe_2O_4/\alpha-Fe_2O_3 > Cu/CuFe_2O_4 > CoFe_2O_4$. $CoFe_2O_4$ nanostructures have been successfully utilized for the degradation of highly toxic 2,4-dichlorophenoxyacetic acid (2,4-D), a herbicide, in the presence of H_2O_2 under UV light (λ = 254 nm) [234]. The 2,4-D could be completely degraded within 180 min of reaction, producing oxalic acid, formic acid and acetic acid [234]. Such outstanding 2,4-D degradation performance of $CoFe_2O_4$ nanostructures is attributed to the formation of ample $O_2^{\bullet -}$ and $^\bullet OH$ radicals near the catalyst surface induced by the photogenerated

electrons and holes at the conduction and valence bands of cobalt ferrite, respectively. Although $MgFe_2O_4$ NPs have also been tested for the photocatalytic mineralization of 2,4-D, their performance is inferior to that of $CoFe_2O_4$ NPs. The photocatalytic mineralization of 2,4-D was about 93% in 180 min for $CoFe_2O_4$ NPs, whereas it was only about 52% for $MgFe_2O_4$ NPs. The presence of Co^{2+} ions and efficient regeneration of surface Fe^{3+} and Co^{2+} species are responsible for the high photocatalytic activity of the former nanostructures [234]. Co^{2+} ions in cobalt ferrite promote the generation of hydroxyl ($^•OH$) radicals necessary for the degradation of the herbicide. Performances of metal ferrite nanostructures and nanocomposites in the degradation of organic dyes and residual pharmaceuticals in aqueous media along with their relevant features are listed in Tables 3 and 4.

4.1.5.4. Photoreduction of CO₂ catalyzed by metal ferrites. Photoreduction of CO_2 is an interesting field of research, pretending not only to find a way for reducing the emission of this greenhouse gas to the atmosphere, but also to generate value-added molecules such as CO, HCOOH, HCOH, CH_3OH, CH_4, etc. Researchers working in this field are thriving to find suitable low-cost catalysts for the efficient photocatalytic and photoelectrocatalytic reduction of CO_2 to generate value-added chemicals selectively. Recently, several metals, metal oxides and their composites have been tested for the photoreduction and photoelectrochemical reduction of CO_2 [248–250]. For example, copper-based oxides have been explored for producing methanol selectively through CO_2 reduction. Exploiting the high surface energy of specific crystalline planes, Wu et al. fabricated sub-micrometric (0.5–1 μm) Cu_2O crystallites with exposed (1 1 0) facets and applied them to generate methanol by photoreduction of CO_2 in water [251]. The crystal facet engineered Cu_2O nanostructures could generate methanol at 1.2 mol $g^{-1}h^{-1}$ rate.

To achieve the photoreduction of CO_2, the conduction band edge of the semiconductor must lie at a potential that is more negative than the proton-assisted multi-electron reduction potentials of CO_2 [248]. The valence and conduction band positions of some typical semiconductors along with the thermodynamic reduction potentials needed to generate solar fuels at pH = 0 are presented in Fig. 13a. The reduction potentials of CO_2 for generating different hydrocarbons at pH = 7 are presented in Fig. 13b [252]. Among metal ferrites, $CoFe_2O_4$ has been rarely utilized for the photoelectrochemical reduction of CO_2. Only one study has been published on the utilization of $Co_3O_4/CoFe_2O_4$ nanocomposite in the photoelectrochemical reduction of CO_2 [253]. In the case of the photoreduction of CO_2 using the $Co_3O_4/CoFe_2O_4$ nanocomposite (Co_3O_4 nanocubes of 370 mm average size covered with $CoFe_2O_4$ nanosheets), $[Ru(bpy)_3]$
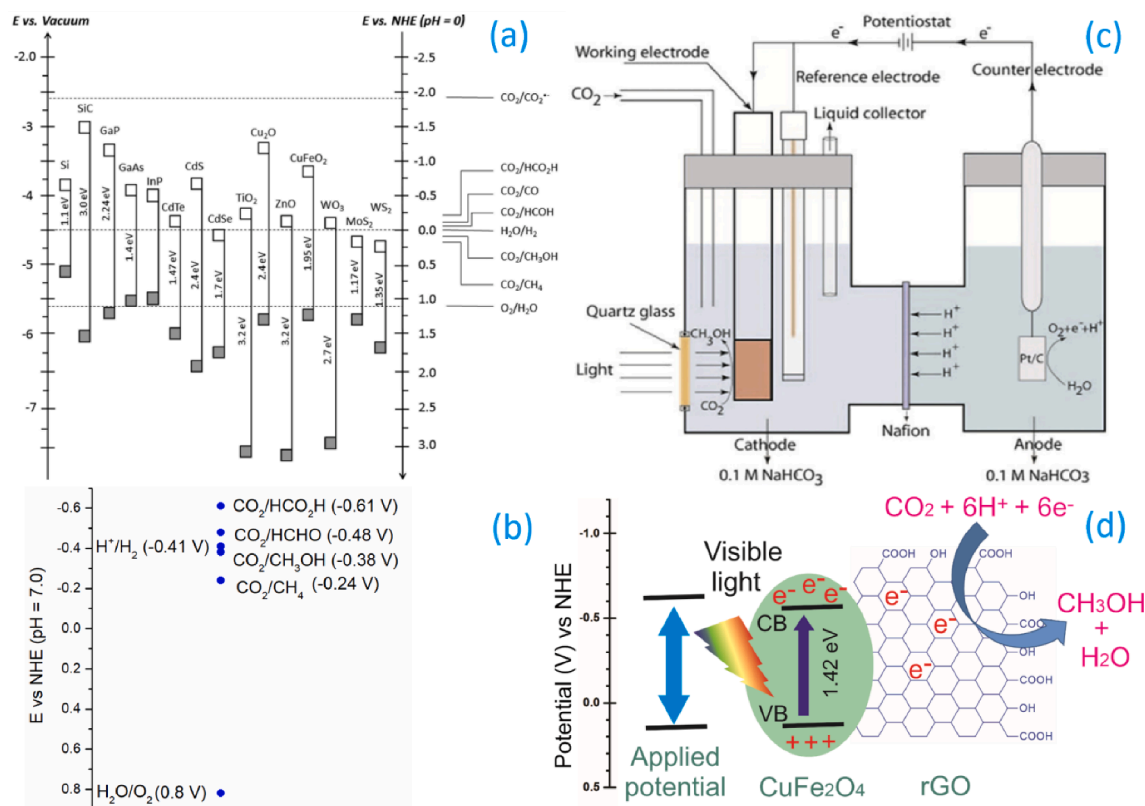

Fig. 13. (a) Conduction band (white squares) and valence band (gray squares) potentials of some commonly used semiconductors along with the potentials of several CO_2 and water redox couples at pH 0, plotted versus vacuum and NHE. Adapted from ref. [248] with permission from American Chemical Society, Copyright 2015. (b) Potentials of some redox pairs in CO_2 reduction reactions at pH = 7 [252]. (c) A typical double-chamber cell reactor equipped with quartz window utilized for photoelectrolytic CO_2 reduction. Reproduced from ref. [255] with permission from Elsevier, Copyright 2018. (d) Mechanism of photoelectrocatalytic CO_2 reduction in $CuFe_2O_4/GO$ composite electrode surface. Adapted from ref. [127] with permission from American Chemical Society, Copyright 2019.

Cl$_2$·6H$_2$O was added to a H$_2$O/triethanolamine (TEOA)/acetonitrile (1:1:3) solution along with the nanocomposite. The solution was then exposed to UV–vis light. The principal product was CO, along with a small quantity of CH$_4$. On the other hand, copper ferrite has been utilized as a catalyst in the photoelectrochemical reduction of CO$_2$, generating methanol as the principal reduction product. Uddin et al. performed photocatalytic reduction of CO$_2$ in water using CuFe$_2$O$_4$ and CuFe$_2$O$_4$/TiO$_2$ composite as catalysts, obtaining methanol with 220 and 651 μmol g^{-1} L^{-1} yields, respectively, after 8 h of reaction [254]. The enhanced photoactivity of the CuFe$_2$O$_4$/TiO$_2$ composite was attributed to interfacial transfer of photogenerated charges, which inhibited the aforementioned recombination. By utilizing CuFe$_2$O$_4$ NP (45–65 nm) impregnated carbon paper as photocathode (~1 cm^2 active area), Karim et al. performed electrochemical reduction of CO$_2$ at −0.5 V (vs. NHE) bias potential, under visible light, using the double-chamber cell reactor depicted in (Fig. 13c) [255]. As can be seen in Fig. 13c, the protons (H$^+$) needed for the photoreduction of CO$_2$ are generated at the anode compartment of the cell and pass through the Nafion membrane, separating the two compartments (anode and cathode compartments), to reach the cathode. While the required potential was adjusted by a potentiostat, the pH of the electrolyte was regulated by adding NaHCO$_3$. The catalyst produced methanol as the principal reduction product at 20.23 μmol L^{-1} cm^{-2} with a quantum efficiency of about 14.4 %. Later, to enhance the efficiency of the process, the authors utilized CuFe$_2$O$_4$/GO nanocomposites as electrocatalysts instead of bare CuFe$_2$O$_4$ NPs [127]. In Fig. 13d a scheme of this nanocomposite, highlighting the role of GO as an electron acceptor (electron scavenger) of the electrons present in the conduction band of the CuFe$_2$O$_4$ is presented. The electrons in GO are transferred to the catalytic sites in conjugation with the protons (H$^+$) (proton-coordinated electron transfer) and reduce CO$_2$ adsorbed over the catalyst surface. Utilization of CuFe$_2$O$_4$/GO composites under the same electrochemical conditions and visible light produced methanol at 28.8 μmol L^{-1} cm^{-2} with 20.5% quantum efficiency. Moreover, on utilizing the nanocomposite, the required bias potential decreased from −0.5 V to −0.4 V (vs. NHE) [127]. Coupling GO with the CuFe$_2$O$_4$ nanostructures reduced the e$^-$/h$^+$ recombination in the hybrid catalyst by trapping the photo-excited electrons from CuFe$_2$O$_4$ NPs. In fact, GO is a well-known electron scavenger used to modify the photo-carrier recombination rate in several composite materials [256,257]. As can be noticed in the examples highlighted above, metal ferrite nanostructures exhibit better CO$_2$ reduction performance (photocatalytic or photo-electrocatalytic) only when they are coupled with Co$_3$O$_4$, TiO$_2$, GO, etc. which generate heterojunctions of Z-scheme band structures, improving charge separation through interface junction potential. However, the performance of metal ferrite nanostructures (bare nanostructures or nanocomposites) in CO$_2$ reduction (photocatalytic or photo-electrocatalytic) even in composite form remained fairly low [127,253–255] in comparison to other advanced electrocatalysts such as CdS and Cu$_2$O [248–250,258,259]. This is probably the main reason why metal ferrites have been utilized mainly in the thermocatalytic reduction of CO$_2$ to produce methane and CO [260–264], which are performed at elevated temperatures and pressures [265,266].

5. Energy storage in supercapacitors

Supercapacitors (SCs) are electrochemical devices, used for storing energy and distinguished by their high power density, low charging and discharging times (1–10 s) and enhanced cyclic stability (>3000 cycles) [8]. Applications of supercapacitors include back-up power supplies to provide protection against power disruption [17,267], energy storage and delivery in hybrid/electric vehicles (the charging of the SCs is via an alternator during vehicle braking steps) [267], portable electronic devices, power systems that require high-power throughput, military applications (e.g., guided missile and highly sensitive naval warheads) [8], electric buses [17,267], emergency doors in airplanes [268], and high power energy sources for heavy loading trucks or cranes [7]. To highlight the advantage of utilizing SCs as energy storage systems in place of conventional energy storage devices such as LIBs and other electrochemical power packs (e.g., fuel cells), we can mention the case of hybrid diesel/electric rubber-tired gantry crane, where the utilization of DLCAP^{TM} (a commercial double-layer supercapacitor) electrochemical capacitor is seen to be about 40% fuel saving [7].

The key components of a SC are the electrodes, electrolyte and separator (Fig. 14a). The device consists of two conducting electrodes coated with electrochemically active materials separated by a porous membrane (separator), and an electrolyte, containing mobile ionic species [21]. The electronically insulating separator prevents a short circuit between the electrodes while permitting the electrolyte ions to pass through. The electrodes in an assembled SC store electric charge by non-faradaic (reversible adsorption of ions on the electric double layer) or faradaic (redox reactions at the electrode/electrolyte interface) processes. The electrodes must be highly porous with highest possible specific surface area, low electrical resistivity and high chemical stability [269]. Therefore, choosing a proper material with adequate microstructure and texture parameters is the key for developing efficient SCs. On applying a potential difference between the electrodes, electric charges are stored at their surfaces either through the accumulation of ions (formation of a double layer) at electrode/electrolyte interfaces or by redox reactions and/or intercalation of ions at the active sites of the electrode materials. For electric double layer (EDL) type materials (where there is no redox reaction), the electrostatic attraction between the ions in the electrolyte and the charge present at the electrode surface generates the EDL at each electrode [21]. These two layers (which have opposite charges) in an EDL are separated by a few angstroms and there is no ion exchange between the layers. For a pseudocapacitive material, redox reactions occur between the electrode materials and the ions in the electrolyte during charge–discharge cycles. During charging, the charge separation occurs due to redox reactions, while these charges flow between the two electrodes through the external circuit at the time of discharge (Fig. 14a). As discussed in the following section, the chemical composition of electrodes also plays a vital role in the performance of SCs.

5.1. Classifications of supercapacitors (SCs) and mechanism of energy storage

SCs can be classified into three categories based on their charge storage mechanism: i) electric double layer capacitors (EDLCs), ii) pseudocapacitors, and iii) hybrid capacitors (Fig. 14b) [93]. Depending on its configuration, a SC can be symmetric (having two

equivalent electrodes), asymmetric (having two different electrodes operating with same charge storage mechanism) or hybrid (having two different electrodes operating with different charge storage mechanisms) [269]. In EDLCs, the energy is stored through ion adsorption at the electrolyte/electrode interface (non-faradaic process), while in pseudocapacitors, the energy is stored through faradaic processes (i.e., through fast surface redox reactions between the electrode material and the electrolyte) [8,93]. On the other hand, in hybrid capacitors, both non-faradaic and faradaic processes are involved. The electrons produced by redox reactions at the electrode/electrolyte interface decrease (increase) the oxidation state of cations in metal oxide electrodes during charging (discharging) of the pseudocapacitor. Carbon based electrodes (e.g., activated carbon, graphene, rGO, CNTs, carbon cloth and nitrogen-doped carbon) are used in commercial SCs, which store the charge through double layer mechanism. Carbon based materials are preferred for commercial SCs because of their rapid response, good electrical conductivity, high chemical stability, non-toxicity, high abundance and high specific surface area ($1000–3500 \ m^2 \ g^{-1}$). Normally, the double-layer SCs have high cycle lives as charge storage occurs through a physical process. However, their specific capacitances (capacitance per unit volume or unit mass) are relatively small. To address this issue, researchers have used redox active materials such as transition metal oxides and conducting polymers in pseudocapacitor electrodes, which store charges through fast faradaic reactions. In the case of transition metal oxides, multivalent cations exposed at the electrode/electrolyte interface participate in redox reactions [270]. In the case of conducting polymers, electron insertion into the conduction band via *n*-doping (reduction) and/or removing an electron from the valence band via *p*-doping (oxidation) increases the charge carrier concentration and hence increases the electrochemical capacitance [271].

Although metal oxides demonstrated high charge storage capability, high resistivity of these redox active materials enhances the internal resistance of the fabricated devices, which hampers power delivery of the fabricated devices. To address this concern, different carbonaceous materials have been blended with these oxides to fabricate their composites. These composite materials can store charges through both physical double layer formation and fast faradaic reactions, resulting in a large storage capacity of the fabricated device. The SCs made of carbonaceous redox-active composites have charge storage capacities higher than EDLCs and pseudocapacitors, with the added benefit of a long cycle life. On the other hand, in the case of hybrid capacitors, charge storage in the two electrodes occurs through two different mechanisms: capacitive in one and battery-type faradaic in the other [6]. Moreover, devices consisting of a faradaic electrode (such as $Ni(OH)_2$ or Co_3O_4) and a carbonaceous electrode represent a typical hybrid type capacitor [6]. On the other hand, some transition metal oxides and electron conducting polymers such as poly(pyrrole), poly(thiophene), poly(aniline) or PEDOT:PSS {poly(3,4-ethylenedioxythiophene)-poly(styrenesulfonate)} are used as electrode materials for pseudocapacitors (Fig. 14b). Some monometallic oxides extensively studied in pseudocapacitors are RuO_2, NiO, MnO_2, MoO_3, Co_3O_4, VO_2 and V_2O_5 [272,273]. Because of the presence of multi-valent cations, different binary metal oxides including MCo_2O_4, (M = Ni, Mn, Zn), $MMoO_4$ (M = Ni, Co), MFe_2O_4 (M = Ni, Co, Sn, Mn), $MSnO_3$ (M = Ni, Co), and $NiMn_2O_4$ have also been used in pseudocapacitors [272,274]. These metal oxides often possess high theoretical capacitance and low resistance compared to the single metal oxides [275]. Frequently, these metal oxides are grown on or deposited over carbon nanotubes, graphene sheets, rGO films, carbon textile and other micro/mesoporous carbonaceous materials, which work as support matrix of high surface area and high electrical conductivity, providing a faster electron transport through the electrodes [46]. Therefore, in the electrode materials made of metal oxide grown on carbonaceous materials, both pseudocapacitive and EDL charge storage mechanisms contribute to the specific capacitance of the
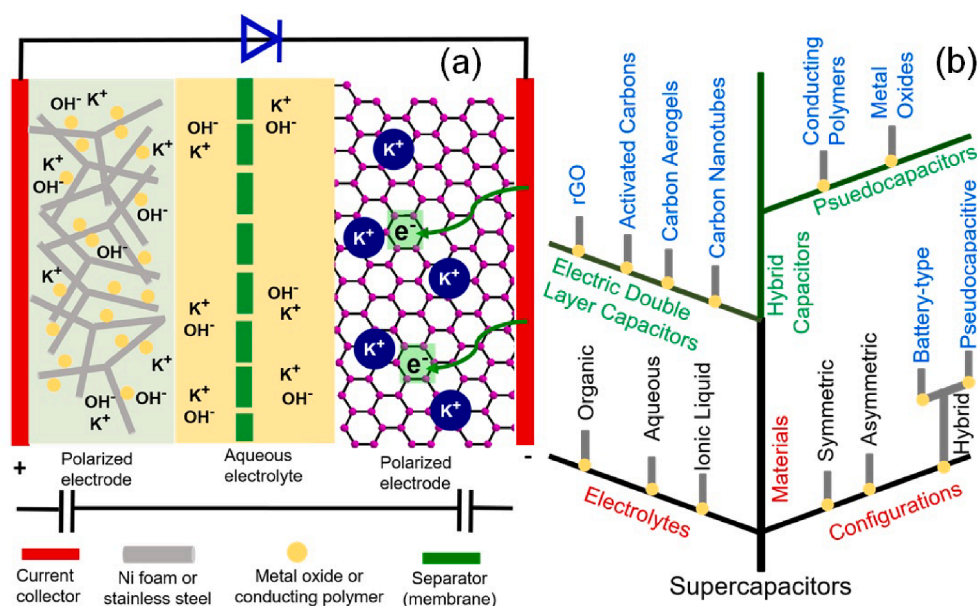

Fig. 14. (a) Components and basic operation mechanism of a typical SC. The negative electrode is made of graphene, which facilitates the electronic conductivity and the adsorption of ions from the electrolyte. (b) An overview of the taxonomical classification of supercapacitors. Adapted from ref. [269] with permission from Royal Society of Chemistry, Copyright 2020.
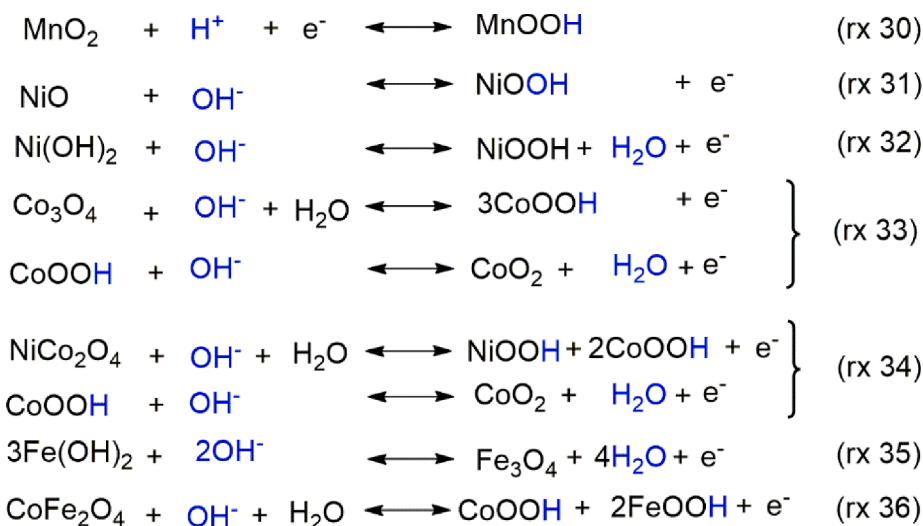
electrode.

Some representative redox reactions that occur at the interfaces of electrolytes and Mn, Ni, Co and Fe based metal oxide (hydroxide) electrodes are shown in the (rx 30–36) of Scheme 5. While the use of MnO_2 and RuO_2 requires acidic electrolytes (e.g., diluted H_2SO_4) because of their instability in basic media, for the majority of other metal oxide electrodes, basic electrolytes (KOH or NaOH) are utilized. In general, the specific capacitances of metal ferrite-based electrodes in aqueous electrolytes such as Na_2SO_4 and H_2SO_4 solutions are quite low ($<450F\ g^{-1}$) [47,74,276–278], probably due to their lower reactivity (Scheme 5) in neutral and acidic media. The redox reaction occurring at the electrolyte/metal ferrite electrode interface under an applied bias potential is presented in (rx 36), illustrating the specific case of $CoFe_2O_4$. Interestingly, as the utilization of metal ferrite electrodes involves a faradaic process, it leads to the formation of metal oxyhydroxides at their surfaces. At higher bias potentials (i.e., under highly oxidizing conditions), the formed CoOOH oxyhydroxide further reacts with the OH^- ions of the electrolyte to produce CoO_2 (rx 33–34). For example, Moysiadou et al. found that CoOOH is oxidized to CoO_2 only when a potential of 1.5 V (vs. RHE, reversible hydrogen electrode) or higher is applied [279]. The authors used cyclic voltammetry of CoOOH in 0.1 M Fe-free KOH electrolyte to study the oxidation process. A similar oxidation of FeOOH to FeO_2 has also been suggested by Makkar et al. and other researchers [46,280,281], although the formation of this metal oxide through redox reactions at electrolyte/electrode interface has not yet been confirmed experimentally. Utilization of [57]Fe Mössbauer spectroscopy might shed some light on this issue.

The iron oxyhydroxide (FeOOH) generated in the reaction (rx 36) turned out to be a good electrode material for SCs, as demonstrated by Owusu et al. [3]. The SCs fabricated using low-crystalline FeOOH as electrode material revealed capacitance values as high as $1,066F\ g^{-1}$ ($1\ A\ g^{-1}$). However, during electrochemical cycling in a -1.2 to 0.0 V potential window (vs. SCE), the FeOOH NPs partially reduce to form $Fe(OH)_2$, which allows FeOOH to be used as anode (i.e., negative electrode) material in SCs with high performance and good rate capability. For example, in a SC assembled using FeOOH NPs and $NiMoO_4$ nanowires as anode and cathode materials, respectively, a 91% of cycling stability after 10,000 cycles at $1\ A\ g^{-1}$ and 74.6% of capacitance retention at $30\ A\ g^{-1}$ was achieved [3].

The electrochemical processes occurring in supercapacitors include the adsorption of electrolyte ions at electrode surface and the formation of electric double layer at electrode–electrolyte interface. Therefore, the specific surface area of the electrode material plays a vital role in the performance of the device [8]. The pore size and pore size distribution in electrode materials also influence the charge storage capacity of SCs. As has been demonstrated experimentally by Largeot et al. [285], SCs fabricated with carbon based microporous materials with $\sim$ 0.7 nm average pore size generate highest capacitance in ethyl-methylimmidazolium-bis(trifluoro-methane-sulfonyl)imide ionic liquid (EMI-TFSI) electrolyte due to an easy flow of ions in their micropores [8]. We should remember that a microporous material has a higher specific surface area in comparison with its mesoporous counterpart. Therefore, a correct matching between the pore size in the electrodes and the size of the electrolyte ions is necessary for obtaining the optimal capacitance of an electrochemical supercapacitor [15,146].

The performance of a SC is measured by its specific capacitance (normalized by electrode mass, volume, or area), energy density (*ED*), power density, rate capability (retained capacitance at a high current loading) and cycling stability [272]. As has been pointed out by Chen et al. [1], to improve the specific capacitance (C_{sp}) and *ED* of a SC, ideal electrode materials should posse a high specific surface area (which governs the C_{sp}), controlled porosity (which affects the C_{sp} and rate capability) and high electronic conductivity (which is crucial for enhancing the rate capability and power density of SCs). There are a few ways for tuning the electronic conductivity of electrode materials; of which, the formation of composites with carbonaceous materials and fabrication of electrode materials with ordered morphology are the most common ones. Nanostructures with fiber-like morphology produce interconnected

$$MnO_2 \ + \ H^+ \ + \ e^- \ \longleftrightarrow \ MnOOH \qquad\qquad (rx\ 30)$$

$$NiO \ + \ OH^- \ \longleftrightarrow \ NiOOH \ + \ e^- \qquad\qquad (rx\ 31)$$

$$Ni(OH)_2 \ + \ OH^- \ \longleftrightarrow \ NiOOH + \ H_2O + e^- \qquad\qquad (rx\ 32)$$

$$Co_3O_4 \ + \ OH^- \ + \ H_2O \ \longleftrightarrow \ 3CoOOH \ + \ e^-$$
$$CoOOH \ + \ OH^- \ \longleftrightarrow \ CoO_2 + \ H_2O + e^- \qquad\qquad (rx\ 33)$$

$$NiCo_2O_4 \ + \ OH^- \ + \ H_2O \ \longleftrightarrow \ NiOOH + 2CoOOH \ + \ e^-$$
$$CoOOH \ + \ OH^- \ \longleftrightarrow \ CoO_2 + \ H_2O + e^- \qquad\qquad (rx\ 34)$$

$$3Fe(OH)_2 \ + \ 2OH^- \ \longleftrightarrow \ Fe_3O_4 + 4H_2O + e^- \qquad\qquad (rx\ 35)$$

$$CoFe_2O_4 \ + \ OH^- \ + \ H_2O \ \longleftrightarrow \ CoOOH \ + \ 2FeOOH + e^- \qquad\qquad (rx\ 36)$$

Scheme 5. A few typical redox reactions that occur at the interface of electrolyte and Mn, Ni, Co and Fe based metal oxide (hydroxide) electrodes [48,282–284].

redox active sites, which can reduce the bulk resistance of the material [286]. For example, Agyemang et al. synthesized porous $ZnFe_2O_4$-based nanofibers through electrospinning [286]. By electrospinning a mixture of precursor salts and PVP, nanofibers with a diameter of ~ 1 μm were fabricated. An annealing treatment (500 °C, 1 h) was performed to generate pores in the fibers. During annealing, the diameter of the fibers decreased from 1060 ± 100 nm to 542 ± 80 nm, and the fibers exhibited excellent charge storage performance due to their high porosity and moderate specific surface area (21.4 $m^2\,g^{-1}$). A C_{sp} of 450F g^{-1} was reported for the porous nanofibers at a scan rate of 5 mV s^{-1} [286]. On the other hand, Wang et al. reported the fabrication of $NiFe_2O_4@CoFe_2O_4$ core–shell nanofibers for using them as an electrode material for SCs. The SCs fabricated using such nanofibers revealed non-rectangular voltammograms, which are typical of charge storage through faradaic reactions. A maximum C_{sp} of 480F g^{-1} was obtained for a current density of 1.0 A g^{-1}. Most importantly, the electrode material retained 87% of C_{sp} after 5000 GCD cycles, suggesting a high structural stability of the nanofibers [287].

The capacitance of metal oxide-based electrodes can be calculated theoretically using equation (3), where n is the mean number of electrons transferred in the redox reaction, F is the Faraday constant (96,485C/mol), M is the molar mass of the metal oxide and V is the operating voltage window [272]. The amount of stored electrochemical energy (E) is determined by integrating the charge stored on the electrode (equation (4)) over the electrostatic potential difference (ΔV) [284]. The specific energy density (ED) refers to the energy stored per unit mass of the electrode, and is defined by equation (5), where C_{sp} is the specific capacitance of the electrode or the SC, and p is a constant, the value of which depends on the used unit of current density [284,288]. In equation (5), when the unit of C_{sp} is F g^{-1} and ED is expressed in Wh kg^{-1}, p takes the value of 7.2. When the unit of C_{sp} is F g^{-1} and ED is expressed in W s g^{-1}, p takes a value of 2.

The maximum power density can be estimated using equation (6), where I_{max} is the maximum current passing through the electrodes and ΔV_{max} is the maximum working potential range [288]. Alternatively, the maximum power density is given by the expression $P_{max} = V^2/4R_s$, where V is the operating voltage and R_s is the equivalent series resistance (ESR) in Ohms [16,17,272,289]. The components that contribute to the ESR are: (i) intrinsic electronic resistances of the active material and the current collectors (conductive materials in the electrodes connected to the external circuit), (ii) contact resistance between the active materials and current collectors, (iii) ionic resistance of the electrolyte, and (iv) the diffusion resistance of the electrolyte ions into the porous electrode [6,290,291]. However, depending on the configuration of the SC, the relations for estimating C and ED can be slightly different [46,93,284,288].

$$C = \frac{n \times F}{M \times V} \tag{3}$$

$$E = \frac{C \times (\Delta V)^2}{p} \tag{4}$$

$$ED = \frac{1}{p} \times C_{sp} \times (\Delta V)^2 \tag{5}$$

$$\text{Power density} = \frac{I_{max} \times \Delta V_{max}}{m} \tag{6}$$

While the C_{sp}, rate capability and cyclic stability of electrode materials can be probed in a three-electrode system, for estimating the energy density, power density and cycling durability of an assembled SC, we must use a two-electrode system [65]. The C_{sp}, ED and other electrochemical parameters of SCs are usually obtained from cyclic voltammetry (CV) or galvanostatic charge–discharge (GCD) curves. The C_{sp} can be estimated from CV curve using equation (7):

$$C_{sp} = \frac{\int I dV}{v \times m \times \Delta V} \tag{7}$$

where I (A) is the current density, ΔV (V) is the potential window, v is the potential scan rate (mV s^{-1}), and m (g) is the mass of the electroactive material in each electrode [93,276]. The C_{sp} can be estimated from the GCD curve using equation (8):

$$C_{sp} = \frac{I \times t}{m \times \Delta V} \tag{8}$$

where I (A) is the discharge current, t (s) is the discharge time, m (g) is the mass of the active material in the electrode and ΔV (V) is the potential window. The C_{sp} values obtained from GCD curves are more accurate than those obtained from CV curves. Some authors used equation (9) to calculate the C_{sp} of the device [49], where I is the current density and dV/dt is the slope of the linear part of the GCD curve.

$$C_{sp} = \frac{I}{dV/dt} \tag{9}$$

To estimate the C_{sp} values of SCs, some authors used equation (10), where C_1 and C_2 stand for the specific capacitance of the electrodes [292].

$$C_{sp} = \frac{C_1 \times C_2}{C_1 + C_2} \tag{10}$$

However, as has been pointed out by Shao et al. [6] and Zhang et al. [293], for nonlinear GCD curves, the *ED* values must be calculated using equation (11) instead of equation (4), to avoid an overestimation or underestimation of the charge-storage capability of SCs.

$$ED = \int_{t_1}^{t_2} IV_t dt \tag{11}$$

In equation (11), I is the constant current applied to the supercapacitor, V_t is the nonlinear change in voltage, t_1 is the time after the initial voltage drop, and t_2 is the moment at which the discharge is completed [6].

The energy density and power density of SCs are commonly presented through Ragone plot, as the energy density of a SC depends on its discharge power density. Two Ragone plots that summarize the performances of different types of batteries and SCs are presented in Fig. 15. It can be seen that SCs exhibit higher power density (also referred as specific density) but lower energy density (also referred as specific energy) than batteries. It is worth mentioning that although asymmetric SCs have high power density, an improvement in energy density is required (Fig. 15b) to complement LIBs and make them commercially attractive. The highest C_{sp} values reported for pseudocapacitors fabricated using transition metal oxides are based on $NiCo_2O_4$ [274]. Among the electrode materials that have a spinel structure, $NiCo_2O_4$ has been the most investigated material because of its relatively low electrical resistivity and good electrochemical performance [50]. However, the voltage window of $NiCo_2O_4$-based electrodes is low (0.35–0.6 V), which limits their practical application [50]. Composite materials are currently the best choices for electrode materials in SCs [8]. Efforts devoted to enhance the capacitance of SCs through electrode engineering are: (i) developing nanoporous materials or hierarchical micro- and nano-structures with a large effective surface area, (ii) improving the wettability of the electrode surface exposed to the electrolyte, and (iii) the use of innovative active materials that allow high mass transportation [8].

As shown in equations (5)-(6), the energy density and power density of a SC are proportional to the potential window. Most commercial supercapacitors use tetraethylammonium tetrafluoroborate $(C_2H_5)_4N^+BF_4^-$ as the electrolyte salt, and acetonitrile (CH_3CN) or propylene carbonate $(C_4H_6O_3)$ as the solvent [295]. In fact, utilization of organic electrolytes in SCs is advantageous as they provide wider operating potential windows (2.5–2.8 V) [15,284]. Although organic electrolyte-based SCs are currently dominating the market, they have been least studied in academic research [284].

5.2. Metal ferrites (MFe₂O₄, M = Co, Ni, Cu, Mn) as electrode materials in supercapacitors

There are ample literature reports on the utilization of metal ferrites as active materials for supercapacitor electrodes. In fact, utilization of metal ferrites or metal ferrite nanocomposites has been seen to enhance the C_{sp} and *ED* of carbonaceous material based SCs. For example, utilizing $CoFe_2O_4/rGO$ nanocomposite in three-electrode system, the C_{sp} of rGO electrodes increased from 218.7F g^{-1} to 254.5F g^{-1} [133]. On the other hand, SCs fabricated using $CuCo_2O_4/rGO$ and activated carbon as positive and negative electrodes, respectively, manifested an *ED* of 53.8 Wh kg^{-1} at a specific power of 840 W kg^{-1} [51]. On replacing the activated carbon
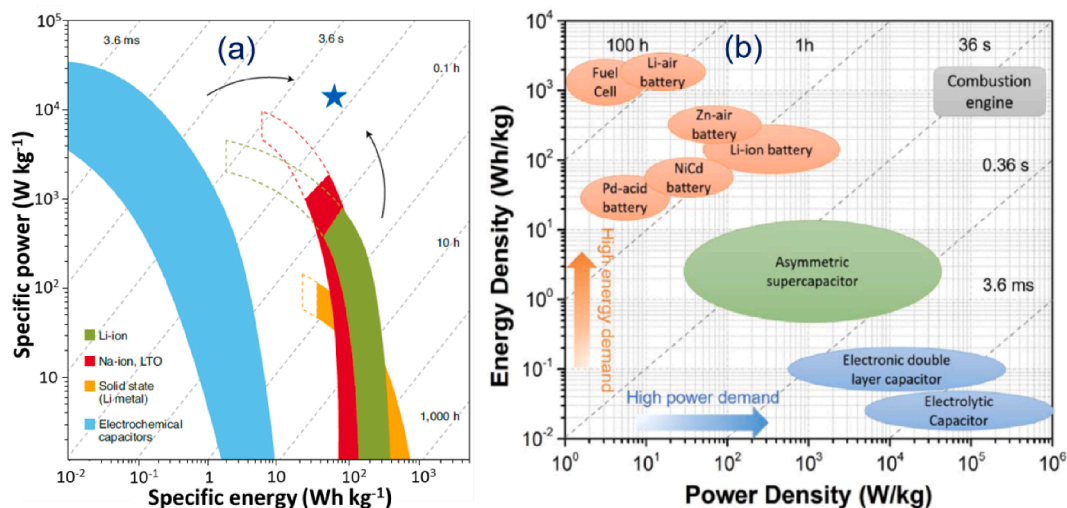

Fig. 15. (a) Ragone plot showing the trends towards greater specific power for batteries and specific energy for electrochemical capacitors (arrows), blurring the boundaries between the two as the trends approach the star. Dashed lines represent zones where the cyclability of the device is altered in the case of symmetric cycling (same charging and discharging rate at 100% depth of discharge). For Li-ion batteries, Li plating at the negative electrode is mainly responsible for the decrease in cycle life and the limitation of charging rate. The diagonal dotted lines and timescales represent characteristic operation timescales, obtained by dividing the energy by the power. LTO, lithium titanium oxide ($Li_4Ti_5O_{12}$). Reproduced from ref. [294] with permission from Springer Nature, Copyright 2020. (b) Ragone plot illustrating the performances of specific power vs. specific energy for different electrical energy-storage technologies. Times shown in the plot are the discharge time obtained by dividing the energy density by the power density. Reproduced from ref. [6] with permission from American Chemical Society, Copyright 2018.

negative electrode by $CoFe_2O_4/rGO$, the *ED* of the device increased considerably (77.2 Wh kg^{-1} at a specific power of 953.0 W kg^{-1}) [51]. The enhanced *ED* of the SC made of $CuCo_2O_4/rGO$ and $CoFe_2O_4/rGO$ composites as positive and negative electrode, respectively, is due to the combination of moderate operating window (1.5 V) and high charge storage capability of both the electrodes through redox reactions. The high surface area (50.9 m^2 g^{-1}) of the $CoFe_2O_4/rGO$ composite along with homogeneous dispersion of $CoFe_2O_4$ NPs over rGO layers generates ample active sites for these redox reactions, increasing the C_{sp} of the SC. Typical FE-SEM and TEM images of the $CoFe_2O_4/rGO$ nanocomposite are shown in Fig. 7**g** and **h**, respectively. A summary of C_{sp}, *ED*, capacitance retention (C_R) and other relevant parameters for the electrode materials and SCs based on metal ferrites is provided in Table 7.

The capacitance of an electrode is governed due to the accumulation of ions at its surface via Faradaic process across the electrolyte–electrode interface. On the other hand, pseudocapacitance is developed through redox reactions between the active material and the electrolyte. The theoretical specific capacitance of a pseudocapacitor is calculated on the basis of some crucial assumptions: (i) the whole surface area contributes to the charge storage, (ii) the charge transfer process is very fast, and (iii) the electrode material possesses high electronic conductivity. The estimation of the theoretical specific capacitance of an active electrode is done using the equation (3) [296]. To estimate the theoretical specific capacitance value of metal ferrites, we can consider the general equations (rx 37 & rx 38) for the electrode operating in alkaline solution/electrolyte:

$$MFe_2O_4 + H_2O + OH^- \rightleftharpoons MOOH + 2FeOOH + e^- \quad (rx\ 37)$$
$$MOOH + OH^- \rightleftharpoons MO_2 + H_2O + e^- \quad (rx\ 38)$$

where, M stands for Co, Ni, Mn, or Cu. The theoretical specific capacitance of $CoFe_2O_4$, $NiFe_2O_4$, $MnFe_2O_4$, and $CuFe_2O_4$ with potential window 0.8 V are 1028, 1029, 1046, and 1008 Fg^{-1}, respectively. Although theoretical values of specific pseudocapacitance are very high for metal ferrites, it is challenging to reach these values experimentally. A major obstacle for attaining these values experimentally is the low electrical conductivity of metal ferrites. Moreover, the performance of metal ferrites in supercapacitors depends on their morphology, porosity, wettability, the value of dead mass, and interconnectivity among the redox-active sites. Thus, the selection of appropriate material (metal-ferrite), calcination temperature, and modification of electrical conductivity (through the formation of a nanocomposite with a conducting material) greatly affect the energy storage capability of these ferrite materials.

The high C_{sp} values obtained in the works presented in Table 7 were attributed to the presence of MFe_2O_4 nanostructures in the electrodes. It should be noted that MFe_2O_4 nanostructures are generally used in positive electrodes of SCs. While the entries 1–4 and 19 of Table 7 correspond to symmetric SCs, the entries 6, 7, 12–18 and 20 correspond to asymmetric SCs. Furthermore, the authors of entries 5, 8–11 and 21 did not fabricate any SC. The maximum operating voltages for the symmetric and asymmetric SCs were in-between 1.0 and 1.2 V and 1.3–1.8 V, respectively, unless the lithium-based electrolytes are used (entry 1). While the entries 1 and 2 correspond to all-solid-state SCs, $LiClO_4$ dissolved in CH_3CN was used as electrolyte in the work presented in entry 3. All the remaining SCs were fabricated using aqueous electrolytes. As can be seen in entry 18 of the table, the asymmetric SC made of positive and negative electrodes containing $MnFe_2O_4/rGO$ and MnO_2/carbon nanotubes operating with aqueous Na_2SO_4 electrolyte had the maximum operating voltage (1.8 V). Although the theoretical limit of water decomposition voltage is 1.23 V, the H_2 evolution overpotential and OH^- ion generation potential are high in neutral electrolytes such as aqueous Na_2SO_4, which allowed the SC (in entry 18) to operate at such high voltage [6].

While the data from cyclic voltammetry curves and equation (7) were used to calculate the C_{sp} values of the electrode and/or the SC in entries 1, 4, 8, 9 and 18 of Table 7, data from galvanostatic charge–discharge (GCD) curves and equation (8) were used to estimate the C_{sp} values in entries 2, 5, 6, 7, 10–14 and 20. The GCD curves and equation (9) were utilized to estimate C_{sp} in the work presented in entry 3. On the other hand, the authors of entries 13 and 19 used equation (8) for estimating C_{sp} of asymmetric (entry 13) and symmetric SCs (entry 19), although both multiplied the current term at the right-hand side of equation (8) by 4 for some unknown reason. Finally, only one research group (entry 6) calculated the C_{sp} values of their SCs using equation (10). Stoller and Ruoff recommended the use of equation (9) to calculate the C_{sp} of SCs, as galvanostatic discharge is a well-accepted measurement method for determining the capacitance of packaged ultracapacitors in industries [297].

Among the metal ferrite based (metal ferrite nanostructures and nanocomposites) electrode materials assessed using three-electrode configuration (see Table 7), the $ZnO@CoFe_2O_4$ nanocomposite exhibited the highest C_{sp} value [93]. The CV curves of the electrodes containing this nanocomposite recorded at different scan rates and GCD curves recorded at different current densities are presented in Fig. 16. A considerable change in area under the CV curves with the variation of scan rate is evident in Fig. 16**a and b**. A larger discharge time of the electrode made of $ZnO/CoFe_2O_4$ composite compared with the electrode made of $CoFe_2O_4$ nanoparticles is evident in the GCD curves recorded at the same current density (Fig. 16**c and d**), which demonstrates a higher C_{sp} for the nanocomposite (Fig. 16**e**).

The specific capacitances reported for electrodes containing $CoFe_2O_4$ nanostructures are compiled in entries 8–17 of Table 7. Although not all the researchers fabricated SCs, the highest C_{sp} value (~4050F g^{-1} measured at 10 mA cm^{-2}) was achieved for $CoFe_2O_4$ microspheres grown on Ni foam (entry 11). On the other hand, the $CoFe_2O_4@graphene$ composite has been utilized as an electrode material (entry 17) for enhancing the C_{sp} of SCs. However, the SCs made of the $CoFe_2O_4@graphene$ composite electrode revealed pseudocapacitive characteristics with a pair of well-defined redox peaks in the potential window of 0.0 – 0.6 V.

On the other hand, $NiFe_2O_4$ thin films grown on stainless steel foils with nanosheet, nanoflower and nanofeather morphologies have been utilized as electrodes for SCs by Bandgar et al. (Fig. 3**(i)**) [43]. The C_{sp} values of the electrodes (measured at 5 mA cm^{-2}) were 1139, 677 and 435F g^{-1}, respectively. The C_{sp} values were proportional to the specific surface area of the respective nanostructures [43]. The advantages of using $NiFe_2O_4$ as an electrode material are its low cost and environmental friendliness. However, it

Table 7

Comparative electrochemical performance of metal ferrite (MFe_2O_4, M = Co, Ni, Cu, Mn) nanostructures used as electrode materials in supercapacitors (SCs). Specific capacitance (C_{sp}), energy density (*ED*) and capacitance retention (C_R) at the end of n charge–discharge cycles of the SCs are presented.

Entry	Working electrode material	Synthesis technique (structure directing agent, SDA)	Counter electrode	Electrolyte	Specific surface area, $m^2 g^{-1}$, (pore size, Å)	C_{sp} of the electrode, F g^{-1} (scan rate)	C_{sp} of the SC, F g^{-1} (scan rate)	Max. operating voltage (V)	Energy density (Wh kg^{-1})	Power density (W kg^{-1})	Capacitance retention C_R, (number of cycles)	Ref.
1	$NiFe_2O_4$ nanocones grown on carbon textile substrate.	Hydrothermal (CTAB, urea)	same as anode	LiCl-PVA gel[i]	593.6 (139)	697 (5 mV s^{-1})	86 (5 mV s^{-1})	1.6	54.9	300	93.57% (10 000)	[50]
2	$NiFe_2O_4$ nano-sheet grown on stainless steel.	Coprecipitation followed by air annealing at 500 °C. (Cl^- anions, NH_3 solution)	same as anode	PVA-KOH gel[j]	47 (18)	1139 (5 mA cm^{-2})	236 (2 mA cm^{-2})	1.2	47.0	333	98% (7000)	[43]
3	$NiFe_2O_4$ NPs/PEDOT composite pressed on stainless steel.[a,b]	Sol-gel followed by air annealing at 400 °C, 24 h. (ethylene glycol)	same as anode	$LiClO_4$ in CH_3CN, 1 M	110 (45)	—	251 (1 mA cm^{-2})	1.0	34.86	—	(84%) 500	[49]
4	$NiFe_2O_4$ NPs (<10 nm) incorporated hierarchical porous carbon nanofibrous membrane.	Electrospinning of a solution containing DMF, $NiFe_2O_4$ precursors and polyacrylonitrile, followed by N_2 annealing at 850 °C, 2 h. (acetylacetonate ions + DMF solvent + polyacrylonitrile)	same as anode	1 M H_2SO_4 aqueous solution	493 (21–33)	–	343 (10 mV s^{-1})	—	27.0	2000	97.4% (10 000)	[53]
5	$NiFe_2O_4$ NPs deposited on Ni foam.[g]	Hydrothemal (CTAB, NH_3 solution)	—	2 M KOH aqueous solution	15.6 (10.7)	720F g^{-1} (2 A g^{-1})	—	—	—	—	—	[292]
6	$NiFe_2O_4$ NPs grown on graphene capsules deposited on Ni foam.[c,d]	Hydrothermal (CTAB, NH_3 solution)	activated carbon	2 M KOH aqueous solution	43.6 (7.6)	1028 (2 A g^{-1})	86F g^{-1}	–	—	—	—	[292]
7	$NiFe_2O_4$@MnO_2 core–shell nanosheet arrays over Ni foam	Two-step hydrothermal method followed by air annealing at 500 °C, 3 h. (SO_4^{2-} anions, urea, NH_4F)	activated carbon	2 M KOH aqueous solution	132.4 (40-145)	1391 (2 mA cm^{-2})	(– – –)	1.5	45.2	174	92.5% (3000)	[44]

Table 7 (*continued*)

Entry	Working electrode material	Synthesis technique (structure directing agent, SDA)	Counter electrode	Electrolyte	Specific surface area, m² g⁻¹, (pore size, Å)	C_{sp} of the electrode, F g⁻¹ (scan rate)	C_{sp} of the SC, F g⁻¹ (scan rate)	Max. operating voltage (V)	Energy density (Wh kg⁻¹)	Power density (W kg⁻¹)	Capacitance retention C_R, (number of cycles)	Ref.
8	CoFe₂O₄ nanorods (0.4 μm width) was pressed onto nickel grid.[g]	Hydrothermal (Cl⁻ anions, PVP, DMF, N₂H₄)	—	1 M KOH aqueous solution	8.5 (– – –)	99F g⁻¹ (10 mV s⁻¹)	—	—	—	—	—	[301]
9	CoFe₂O₄ nanorings (0.3 μm width) pressed onto nickel grid.[g]	Hydrothermal (Cl⁻ anions, DMF, N₂H₄)	—	1 M KOH aqueous solution	21.5 (– – –)	195F g⁻¹ (10 mV s⁻¹)	—	—	—	—	—	[301]
10	CoFe₂O₄ microspheres (11.2 μm) grown on Ni foam.	Hydrothermal (urea and NH₄F)	—	3 M KOH aqueous solution	— (– – –)	3499.9F g⁻¹ (10 mA cm⁻²)	—	—	—	—	—	[93]
11	ZnO@CoFe₂O₄ microspheres (11.2 μm) grown on Ni foam.	Hydrothermal (urea and NH₄F)	—	3 M KOH aqueous solution	— (– – –)	4050.4F g⁻¹ (10 mA cm⁻²)	—	—	—	—	—	[93]
12	Hierarchically porous CoFe₂O₄ nanosheets grown over Ni foam.	Hydrothermal method followed by calcination at 400 °C for 2 h (urea)	activated carbon	3 M KOH aqueous solution	68.3 (20-40)	503 (2 A g⁻¹)	73.12F g⁻¹ (1.2 A g⁻¹)	1.5	22.85	900	98% (5000)	[54]
13	Low-crystalline CoFe₂O₄/C nanocomposite coated over Ni foam.	Citric acid assisted sol–gel, calcinated at 300 °C for 4 h. (citric acid)	activated carbon	2 M KOH aqueous solution	131 54.3	600F g⁻¹ (1 A g⁻¹) (h)	100F g⁻¹ (1 A g⁻¹)	1.6	14.38	720	76% (800)	[48]
14	CoFe₂O₄/rGO composite hydrogel pressed onto Ni foam .	Hydrothermal, (CH₃COONa and ethylene glycol mixed solvent)	rGO	6 M KOH aqueous solution	614.4 (30-40)	356F g⁻¹ (0.5 A g⁻¹)	76F g⁻¹ (1 A g⁻¹)	1.3	17.84	650	87% (4000)	[45]
15	CoFe₂O₄ NPs (10 nm) deposited on stainless steel.[c]	Solution combustion, (glycine + PEG)	rGO	1 M KOH aqueous solution	— —	125F g⁻¹ (0.5 A g⁻¹). 195F g⁻¹ (1 mV s⁻¹)	38F g⁻¹ (3 mA cm⁻²)	1.5	12.14	643	67% (3000)	[55]
16	CoFe₂O₄ NPs (89 nm) grown over rGO (used as negative electrode)	Hydrothermal, (CH₃COONa + PVP + PEG mixture)	CuCo₂O₄/rGO pressed onto Ni foam	6 M KOH aqueous solution	50.9 (35)		247F g⁻¹ (1 A g⁻¹)	1.5	72.2	953	96% (5000)	[51]
17	CoFe₂O₄ NPs (10 nm) grown on graphene (40%		Fe₃O₄/rGO	1 M KOH aqueous	158 (20-70)	579F g⁻¹ (1 A g⁻¹)		1.7	45.5	840	91% (5000)	[52]

Table 7 (*continued*)

Entry	Working electrode material	Synthesis technique (structure directing agent, SDA)	Counter electrode	Electrolyte	Specific surface area, $m^2 g^{-1}$, (pore size, Å)	C_{sp} of the electrode, F g^{-1} (scan rate)	C_{sp} of the SC, F g^{-1} (scan rate)	Max. operating voltage (V)	Energy density (Wh kg^{-1})	Power density (W kg^{-1})	Capacitance retention C_R, (number of cycles)	Ref.
	of graphene in the composite) was pressed onto Ni foam.[b]	Hydrothermal (NH$_3$ solution)	pressed onto Ni foam	solution			114F g^{-1} (1 A g^{-1})					
18	MnFe$_2$O$_4$ NPs (10 nm) grown on rGO.[c]	Hydrothermal (without SDA)	MnO$_2$/ carbon nanotube	3 M Na$_2$SO$_4$ aqueous solution	—	221F g^{-1} (50 mV s^{-1})	60 (10 mV s^{-1})	1.8	25.9	225	90% (4500)	[47]
19	MnFe$_2$O$_4$ hollow spheres grown on rGO, deposited over Ni foam.[d]	Hydrothermal (CH$_3$COONa + ethylene glycol + PEG).	same as anode	3 M KOH + 0.1 M K$_4$[Fe (CN)$_6$] aqueous solution	— (~38)	768F g^{-1} (8 A g^{-1})	468F g^{-1} (3 A g^{-1})	1.0	16.25	1500	80% (4000)	[46]
20	MnFe$_2$O$_4$ hollow spheres grown on rGO, deposited over Ni foam.[d]	Hydrothermal (CH$_3$COONa + ethylene glycol + PEG).	rGO	3 M KOH + 0.1 M K$_4$[Fe (CN)$_6$] aqueous solution	— (~38)	768F g^{-1} (8 A g^{-1})	90F g^{-1} (1 A g^{-1})	1.5	28.12	750	95% (4000)	[46]
21	CuFe$_2$O$_4$ NPs (100 nm) grown on rGO.	Hydrothermal (PVP)	—	3 M KOH aqueous solution	35 (– – –)	576F g^{-1} (1 A g^{-1})	—	–	—	—	—	[302]

[a] PEDOT = poly(3,4-ethylenedioxythiophene).
[b] 10 wt% acetylene black and 5 wt% polytetrafluoroethylene (PTFE) were used to form a thick paste to assemble the electrode.
[c] Approximately 10 wt% carbon black was added to the composite.
[d] A slurry prepared by mixing the composite, polyvinylidene difluoride (PVDF) and N-methyl-2-pyrrolidine was used to deposit the material on the substrate. The electrode was dried at 120 °C (12 h) under vacuum. Finally, the electrode was pressed under 4 MPa pressure. [e]A three-electrode cell with a platinum foil counter electrode and an Ag/AgCl reference electrode was used to obtain the C_{sp} of the electrode. [f]The specific surface area of the CuFe$_2$O$_4$ NPs was 22 $m^2 g^{-1}$.
[g] 10-15 wt% acetylene black and 5 wt% PTFE were used to form a thick paste to assemble the electrode.
[i] A 6 M LiCl aqueous solution was used to assess the C_{sp} of the electrode.
[j] A 6 M kOH aqueous solution was used to assess the C_{sp} of the electrode.

exhibits high electrical resistivity (4.85×10^6 Ω cm) [298], low energy density, and poor cycling performance [273]. Jadev et al. recorded the CV curves of an electrode consisting of $NiFe_2O_4$ nanostructures deposited on a carbon textile, using 6 M LiCl aqueous electrolyte [50]. The voltage window used to measure the CV curves was from -0.2 to 0.7 V. The C_{sp} of the electrode was 697F g^{-1} when measured at 5 mV s^{-1}. However, XRD analysis performed on the electrode after 50 cycles of operation revealed the formation of Ni^0, Fe^0 and Li_2O species.

The *ED* values for the best performing SCs fabricated using metal ferrite nanostructures are listed in Table 7. In the case of nickel ferrite electrodes, most of the researchers calculated *ED* values using equation (5) and determined the C_{sp} values as described earlier, however, with different values for p (p = 2 for entries 3, 14, 16 and 20; p = 7.2 for entries 1–3, 5–7 and 12; and p = 8 for entries 13 and 19). The works presented in entries 4, 15, 17 and 18 (Table 7) did not report which equation they used to estimate the *ED* values. The highest energy density (54.9 Wh kg^{-1} at 300 W kg^{-1}) value obtained for $NiFe_2O_4$ nanostructure-based SCs (entries 1–4) was reported for the nanostructures of nanocone morphology, grown on carbon textile [50]. $NiFe_2O_4$ nanosheets grown on stainless steel also exhibited high *ED* values (e.g., 47 Wh kg^{-1} at 333 W kg^{-1}) [43]. The *ED* values reported in the above two works are comparable to the energy density value (50.6 Wh kg^{-1}) reported for an asymmetric SC consisting of a $Ni(OH)_2$ nanoflake/CNT composite grown on Ni foam as the anode and activated carbon as the cathode [299]. The performance of $NiFe_2O_4$ nanostructures in SCs is comparable to that of one of the most extensively studied hydroxides ($Ni(OH)_2$) as an electrode material for SCs [66,300]. SCs constructed using core-shell $NiFe_2O_4@MnO_2$ nanosheets arrays (Fig. 3(ii)) as electrode also exhibited high energy density (45.2 Wh kg^{-1}), although this value was obtained at lower power density (entry 7) [44]. The good performance of the SCs was attributed to the high specific surface area and good electric conductivity of the assembled nanosheets, which provided abundant active sites for electrochemical reactions, short ion-diffusion path and fast charge transfer during charging and discharging [44].

Although $MnFe_2O_4$ nanostructures were not sufficiently probed in supercapacitors, it seems the performance of $MnFe_2O_4$ nanostructure-based electrodes in aqueous electrolyte supercapacitors depends strongly on their morphology and size. Wang et al. synthesized spherical $MnFe_2O_4$ NPs of about 160 nm average size and prepared working electrodes by pressing (1 MPa) them over nickel foam. The electrodes exhibited relatively low C_{sp} values (152.5F g^{-1} at a current density of 0.1 A g^{-1}) in aqueous 6 M KOH electrolyte [303]. On the other hand, through a combined chemical co-precipitation and hydrothermal technique, Fei et al. grew $MnFe_2O_4$ nanosheets (10–20 nm thick and 1–2 μm wide) over Ni foam. The electrode exhibited high areal capacity (302.6 mC cm^{-2}) at 1 mA cm^{-2} current density [304]. As different research groups presented the C_{sp} values of their fabricated electrodes in different units and at different current densities, it is quite impossible to compare their performances quantitatively. However, the asymmetric SC
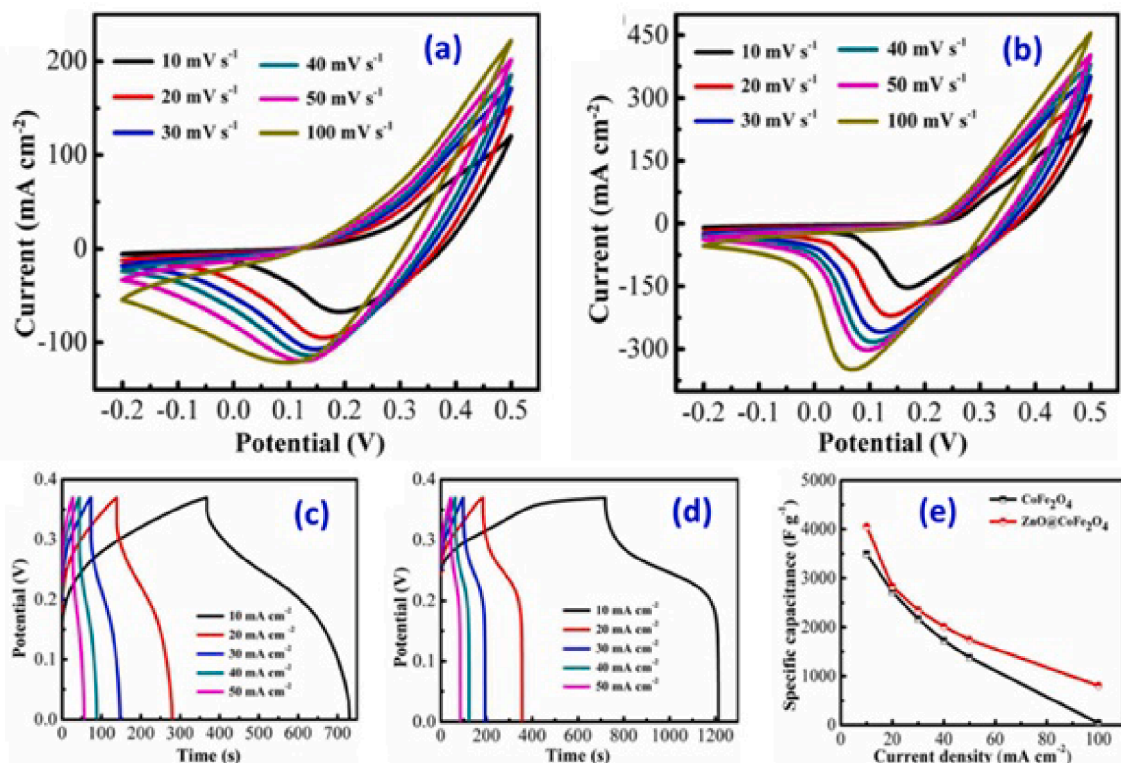

Fig. 16. (a) CV curves of nanostructured $CoFe_2O_4$ and (b) $ZnO@CoFe_2O_4$ electrodes measured using 3 M KOH electrolyte at different scan rates from 10 to 100 mV s^{-1}. Charge-discharge curves of (c) $CoFe_2O_4$ and (d) $ZnO@CoFe_2O_4$ electrodes at different current densities (10 – 100 mA cm^{-2}) in 3 M KOH solution. (e) Estimated specific capacitance as a function of current density. Reproduced from ref. [93] with permission from Royal Society of Chemistry, Copyright 2018.

fabricated using $MnFe_2O_4$ nanosheet based electrode as cathode and activated carbon as anode revealed high energy density (68.7 mWh cm^{-2} at 587 mW cm^{-2}) and high cyclic stability [304].

To overcome the common problems of low electronic conductivity and poor cycling stability of metal ferrite electrodes, researchers have also fabricated nanocomposites of $MnFe_2O_4$ with conductive materials. For example, Nilmoung et al. fabricated a $MnFe_2O_4$/carbonized polyacrylonitrile composite, which exhibited a moderate C_{sp} (292F g^{-1} at 5 A g^{-1}) when used as an electrode material [305]. The capacitance retention of the electrode after 1000 cycles at a scan rate of 100 mV s^{-1} was 80%. On the other hand, Sankar and Selvan used a $MnFe_2O_4$/graphene/polyaniline nanocomposite as an active material for SC electrodes [297]. As the $MnFe_2O_4$ NPs were first synthesized and then attached to the graphene sheets through a hydrothermal method, the NPs were not well dispersed over the support (as noted in their TEM images). The electrode exhibited a C_{sp} of 241F g^{-1} at 0.5 mA cm^{-2} current density. A SC assembled with this nanocomposite as the negative electrode and activated carbon as the positive electrode achieved a relatively low *ED* (17 Wh kg^{-1} at 100 W kg^{-1}) [306]. An electrode made of $MnFe_2O_4$ hollow spheres/rGO composite pressed on Ni foam exhibited a C_{sp} of 129.6F g^{-1} at 8 A g^{-1} in 3 M KOH electrolyte [46]. A significant enhancement in the C_{sp} (592F g^{-1} at a current density of 8 A g^{-1}) of the electrode material was achieved by adding a small amount of redox-active $K_4[Fe(CN)_6]$ additive to the electrolyte. Moreover, on using the $MnFe_2O_4$ hollow spheres/rGO composite as the positive electrode and rGO as the negative electrode, along with $K_4[Fe(CN)_6]$ additive in the electrolyte, a high energy density (28.12 Wh kg^{-1} at 750 W kg^{-1}) was achieved for the SC [46]. In fact, a substantial enhancement in C_{sp} values for several other metal oxide nanostructures (e.g., MnO_2 nanowire, $BiFeO_3$ nanowires/rGO composite) has been observed using $K_4[Fe(CN)_6]$ as an electrolyte additive [307,308]. A fast electron exchange process between the $[Fe(CN)_6]^{4-}/[Fe(CN)_6]^{3-}$ species and the surface of the composite electrode is responsible for the higher C_{sp} and *ED* values of the device upon the addition of $K_4[Fe(CN)_6]$ in aqueous electrolyte. While the $[Fe(CN)_6]^{4-}$ ions are generated in the electrolyte from the dissolution of $K_4[Fe(CN)_6]$, the $[Fe(CN)_6]^{3-}$ ions are produced through oxidation during the discharge of the SC.

According to the reported molecular orbital diagrams of $[Fe(CN)_6]^{3-}$ and $[Fe(CN)_6]^{4-}$ [309], these metal complexes have low-spin $(t_{2g})^5(e_g)^0$ and $(t_{2g})^6(e_g)^0$ configurations, respectively. In addition, as the CN$^-$ anion is a π acceptor ligand, there occurs metal back-bonding [309]. The back-bonding between the Fe cation and the cyanide anion (CN$^-$) is represented by the blue arrows in Scheme 6a. In $[Fe(CN)_6]^{3-/4-}$ complexes, electrons can move from the ligand to the cation (red arrow in Scheme 6a) through the sigma bond, and vice versa (i.e., from the cation to the ligand, blue arrows in Scheme 6a) through the π bond. In this way, the Fe ion can change its oxidation state from Fe^{3+} to Fe^{2+} very quickly in the $[Fe(CN)_6]^{3-/4-}$ species, which enables fast charge–discharge of the device. On the other hand, the OH$^-$ anion is a π donor ligand (as indicated by the curved arrows in Scheme 6b) as well as a σ donor (as indicated by the straight arrows in the scheme); hence the redox behavior of the OH$^-$ ligand present in the electrolyte (aqueous) is significantly different from the redox behavior of the $[Fe(CN)_6]^{3-/4-}$ ion. Different interactions between the ligands (OH$^-$ and CN$^-$) and transition metal cations can be noted in the spectrochemical series presented in scheme 6c. In this series, the ligands are arranged according to the extent of energy level splitting of 3d orbitals of the transition metal cations caused by the ligands, i.e., their crystal field splitting energies (Δs). A large Δ value signifies that the interaction between the transition metal cation and the ligand is strong, as is the case for the CN$^-$ ligand. Such a strong interaction between the CN$^-$ ligand and the $Fe^{2+/3+}$ cation in $[Fe(CN)_6]^{3-/4-}$ species makes this complex
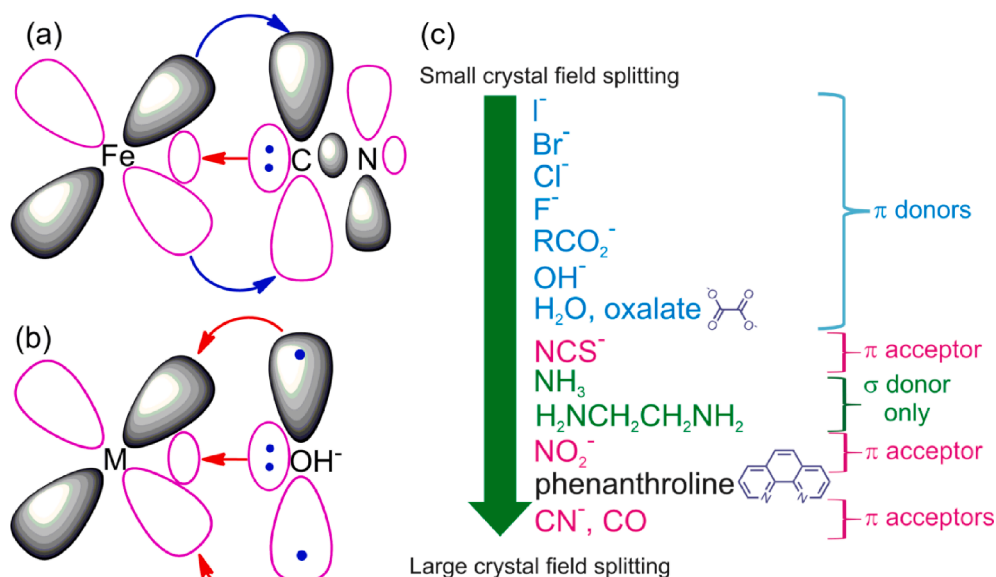
Scheme 6. (a) Interactions between the 3d orbitals of Fe ion and CN$^-$ ligand (a π acceptor) in $[Fe(CN)_6]^{4-}/[Fe(CN)_6]^{3-}$ red-ox couple. (b) Expected interactions between the 3d orbitals of cations in metal ferrites and OH$^-$ ligands (a π donor) in aqueous electrolyte. Linear arrows represent σ interactions and curved arrows represent π interactions. Pink and grey colors in the lobules (both in (a) and (b)) represent different phases (+or -) of the wavefunctions. Sketch adapted from ref [310]. (c) Spectrochemical series of some common ligands highlighting the large crystal field splitting caused by the CN$^-$ ligand on the 3d orbital of transition metal cations. Classification of the ligands as π donors or acceptors is also included.
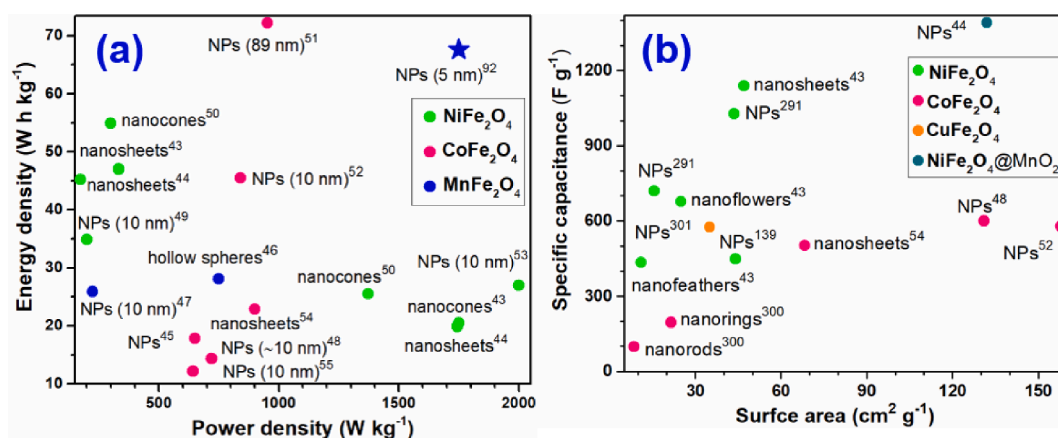
Fig. 17. (a) Ragone plot for SCs fabricated with metal ferrites nanostructures of different morphologies. (b) Specific capacitance for some electrodes as a function of the surface area. The numbers presented as superscipts correspond to the reference from which the value was taken. The star in (a) indicates that the SCs used an ionic liquid in the electrolyte (1-ethyl-3-methylimidazolium tetrafluoroborate, EMIMBF$_4$).

stable even under an applied bias in a SC.

Normally, the performance of an energy storage device is expressed through a Ragone plot, i.e., energy density vs. power density plot. A Ragone plot for SCs made of selective metal ferrite nanostructures of different morphologies is presented in Fig. 17a. The highest *ED* value (72.5 Wh kg) was obtained for a SC consisting of a CoFe$_2$O$_4$/rGO composite as the negative electrode and CuCo$_2$O$_4$/ rGO as the positive electrode [51]. Among the SCs containing cobalt ferrite nanostructures, the second highest *ED* value (45.5 Wh kg^{-1}) was achieved for a SC fabricated using CoFe$_2$O$_4$/rGO as the positive electrode and Fe$_3$O$_4$ as the negative electrode. In fact, use of oxide/ferrite nanostructures containing transition metals in both electrodes is seen to produce high *ED* in SCs. As can be noticed in Fig. 17a, the remaining SCs constructed with either of the electrodes (positive or negative) containing CoFe$_2$O$_4$ or MnFe$_2$O$_4$ nanostructures produced considerably lower *ED* values. Among the SCs fabricated using nickel ferrite nanostructures, the best and second-best performances corresponded to NiFe$_2$O$_4$ nanostructures of nanosheet and hierarchical nanocone morphologies, when they were utilized in both electrodes. However, the *ED* values for the SCs containing NiFe$_2$O$_4$ decreased rapidly with the increase of power density [43,50,52].

For SC applications, most of the studies used metal ferrite nanostructures of small (<10 nm average size) sizes (Fig. 17a), probably due to their high specific surface areas, which facilitated electron transfer toward the conductive material (i.e., rGO, activated carbon or Ni foam) in the electrodes. However, the principal drawbacks of utilizing nanostructures of small dimensions are their agglomeration affinities and low mass density of their composites [141]. For example, CoFe$_2$O$_4$ NPs are prone to aggregate during their synthesis and during the charge–discharge process of SCs, causing a substantial reduction in the electrochemical activity and stability of the electrodes [52,311]. Among the works reported on SCs fabricated using metal ferrites as electrode materials, only one used ionic liquid (IL) as the electrolyte (the IL used was 1-ethyl-3-methylimidazolium tetrafluoroborate, EMIMBF$_4$) [92]. Importantly, a high *ED* value (67.6 Wh kg^{-1} at a power density of 1750 kW kg^{-1}) was obtained for this SC (indicated by the star symbol in Fig. 17a). In this SC, MnFe$_2$O$_4$ NPs of about 5 nm average size, grown on porous carbon polyhedra, were used as the active material in the negative electrode and activated carbon in the positive electrode. Both electrodes were prepared by pressing the electroactive nanostructures on graphite paper. The SC worked in a wide potential window (from 0.0 to 3.5 V) without degradation of metal oxide inside the porous carbon, and exhibited a capacity retention of 93.2% after 10,000 cycles at 10 mA/cm^2 current density. It should be recalled that during charge–discharge cycling at high voltage, metal ferrite nanostructures in SC electrodes operating in aqueous electrolytes decompose to form α-Fe$_2$O$_3$ and metal oxides (hydroxides) of complementary metals [46,48,284,312,313]. However, the decomposition of metal ferrites in ILs has not been observed.

The specific capacitances for some of the best performing electrode materials as function of their surface area are shown in Fig. 17b. The highest *C$_{sp}$* (1391F g^{-1}) in this figure corresponds to the NiFe$_2$O$_4$@MnO$_2$ core@shell nanostructures. Importantly, this *C$_{sp}$* value is higher than the reported value for MnO$_2$ [314]. As can be noticed in Fig. 17b, in general, metal ferrite nanostructures with higher specific surface areas exhibit higher *C$_{sp}$* values (irrespective of their morphology). To provide a specific example, we can mention the work of Deng et al., who synthesized CoFe$_2$O$_4$ nanorods and nanorings of 8.5 m^2/g and 21.5 m^2/g specific surface area, respectively [301]. *C$_{sp}$* value of the electrode fabricated using CoFe$_2$O$_4$ nanoring was about two times higher than the electrode fabricated using CoFe$_2$O$_4$ nanorods. A similar trend was found by Bandgar et al. for the NiFe$_2$O$_4$ nanostructures with nanosheet, nanoflower and nanofeather morphologies, as shown in Fig. 17b [43].

As can be noticed, most of the metal ferrite nanocomposites prepared for SC applications are either graphene/rGO-based or nickel foam-based, to overcome the problem of low electronic conductivity of metal ferrite nanostructures. However, the performance of such composite electrode materials depends on the weight ratio of the active material and the support, i.e., the ferrite and graphene or rGO. For example, Wang et al. found that the *C$_{sp}$* of a CoFe$_2$O$_4$/graphene electrode can be enhanced up to 579F g^{-1} at 1 A g^{-1} by adjusting the CoFe$_2$O$_4$ and graphene ratio to 3:2 in the composite [52]. On the other hand, Rahmanifar and co-workers found the optimum

CoFe$_2$O$_4$ and rGO contents in a CoFe$_2$O$_4$/rGO nanocomposite is ~ 70% and ~ 30%, respectively [51]. Xiong et al. evaluated the electrochemical performance of a multi-component organic–inorganic composite such as CoFe$_2$O$_4$/rGO/PANI with different rGO contents for SC application [133]. By measuring the C_{sp} value of the nanocomposite in a three-electrode system, they found that the C_{sp} value is maximum for 34.5 wt% rGO content in the composite. The presence of conducting polymer PANI in the composite also increased its C_{sp} value from 254.5 to 1133.5F g^{-1} [133]. In another study, the highest C_{sp} value was achieved for the MnFe$_2$O$_4$ and rGO
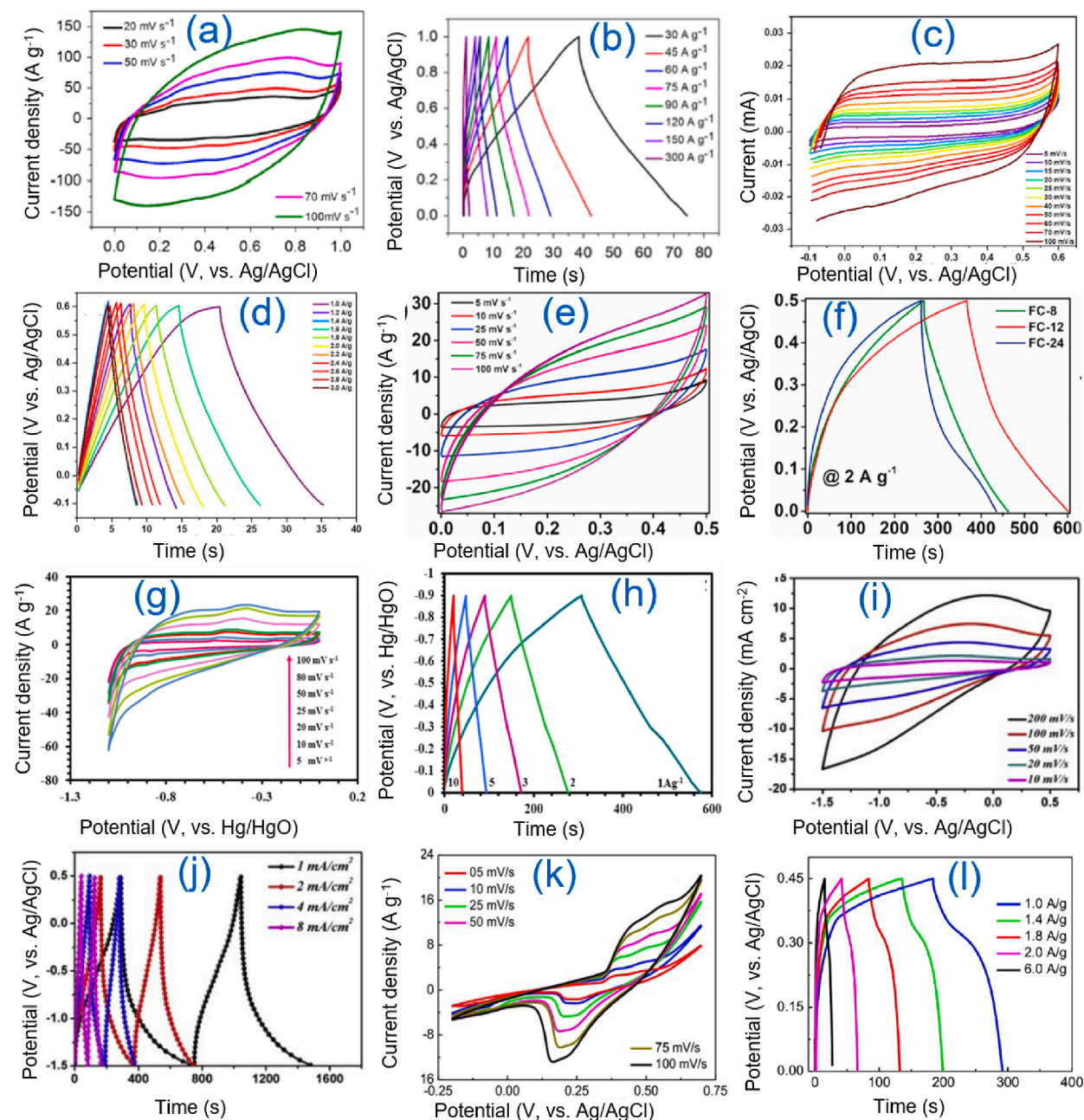
Fig. 18. CV and GCD curves for selected electrode materials based on metal oxides, measured in three-electrode setups. (a) CV and (b) GCD curves of a RuO$_2$/rGO electrode (1 M H$_2$SO$_4$ aqueous electrolyte). Reproduced from ref. [320] with permission from Elsevier, Copyright 2015. (c) CV and (d) GCD curves of a Mn$_3$O$_4$-Fe$_2$O$_3$/Fe$_3$O$_4$@rGO electrode (1 M KOH aqueous electrolyte). Reproduced from ref. [144] with permission from Elsevier, Copyright 2020. (e) CV and (f) GCD curves of a FeCo$_2$O$_4$/graphite electrode (3 M KOH aqueous electrolyte). Reproduced from ref. [324] with permission from Elsevier, Copyright 2019. (g) CV and (h) GCD curves of a CoFe$_2$O$_4$/rGO electrode (6 M KOH aqueous electrolyte). Reproduced from ref. [51] with permission from Elsevier, Copyright 2019. (i) CV and (j) GCD curves of MnFe$_2$O$_4$ quantum dots confined in porous carbon electrode (EMIMBF$_4$ ionic liquid). Reproduced from ref. [92] with permission from Elsevier, Copyright 2020. (k) CV and (l) GCD curves of a NiFe$_2$O$_4$/carbon textile electrode (1 M LiCl aqueous electrolyte). Reproduced from ref. [50] with permission from the Royal Society of Chemistry, Copyright 2016.

contents in MnFe$_2$O$_4$/rGO composite 80 and 20 wt%, respectively [46]. All these studies indicate that for SC application, the content of rGO or graphene in metal ferrite nanocomposites should be maintained in-between 20 and 40 wt%.

The C_{sp} values for electrodes made of NiFe$_2$O$_4$ and CoFe$_2$O$_4$ NPs in neutral electrolytes (e.g., 1 M Na$_2$SO$_4$) are relatively low [74,315]. For this reason, in most of the SCs fabricated with NiFe$_2$O$_4$ and CoFe$_2$O$_4$ NPs (Table 7) basic (e.g., 1 M KOH solution) or acidic (e.g., 1 M H$_2$SO$_4$) electrolytes are utilized [53]. However, for MnFe$_2$O$_4$ NPs and nanocomposite-based electrodes, acidic (H$_2$SO$_4$) [313,316], neutral (Na$_2$SO$_4$) [47,317] or basic (KOH) [46,318], aqueous electrolytes can be utilized. In fact, this has been confirmed by Wei et al. [74] who used a neutral (1 M Na$_2$SO$_4$) electrolyte to evaluate the performance of electrodes made of MnFe$_2$O$_4$, NiFe$_2$O$_4$ and CoFe$_2$O$_4$ NPs. They found that the C_{sp} value for the electrode made of MnFe$_2$O$_4$ NPs is considerably higher than that of the electrodes made of NiFe$_2$O$_4$ and CoFe$_2$O$_4$ NPs.

Ghadimi et al. fabricated a symmetric SC using a MnFe$_2$O$_4$/PANI nanocomposite annealed at 800 °C (4 h in Ar atmosphere) and 1 M H$_2$SO$_4$ as the electrolyte [313]. On thermal annealing, the PANI transformed into nitrogen doped carbon. The SC exhibited a high C_{sp} (246F g^{-1} at 1 A g^{-1}), excellent cycling stability (97% retention of C_{sp} after 10,000 cycles), low ESR (0.26 Ω) and low R_{ct} (0.88 Ω); which demonstrates the suitability of acidic electrolytes in SCs made of MnFe$_2$O$_4$/nitrogen-doped carbon. The same authors reported a similar C_{sp} value (250F g^{-1} at 1 A g^{-1}) for a symmetric SC based on MnFe$_2$O$_4$/rGO nanocomposite using a basic electrolyte (6 M KOH) [319]. Su et al. also fabricated a symmetric SC using MnFe$_2$O$_4$/nitrogen-doped graphene nanocomposite electrode and a basic electrolyte (6 M KOH), which exhibited a high C_{sp} (110F g^{-1} at 1 A g^{-1}) and outstanding long-term cycling stability (83% of C_{sp} retention after 65,000 cycles) [318]. Although both Su et al. and Ghadimi et al. used equation (8) to estimate the C_{sp} of their SCs, in the latter case, the electrical current (I) was multiplied by 4. To make a fair comparison, we made corresponding adjustment to the value reported by Ghadimi et al., which resulted in a higher C_{sp} value for the SC fabricated by Su et al. than that reported by Ghadimi et al.
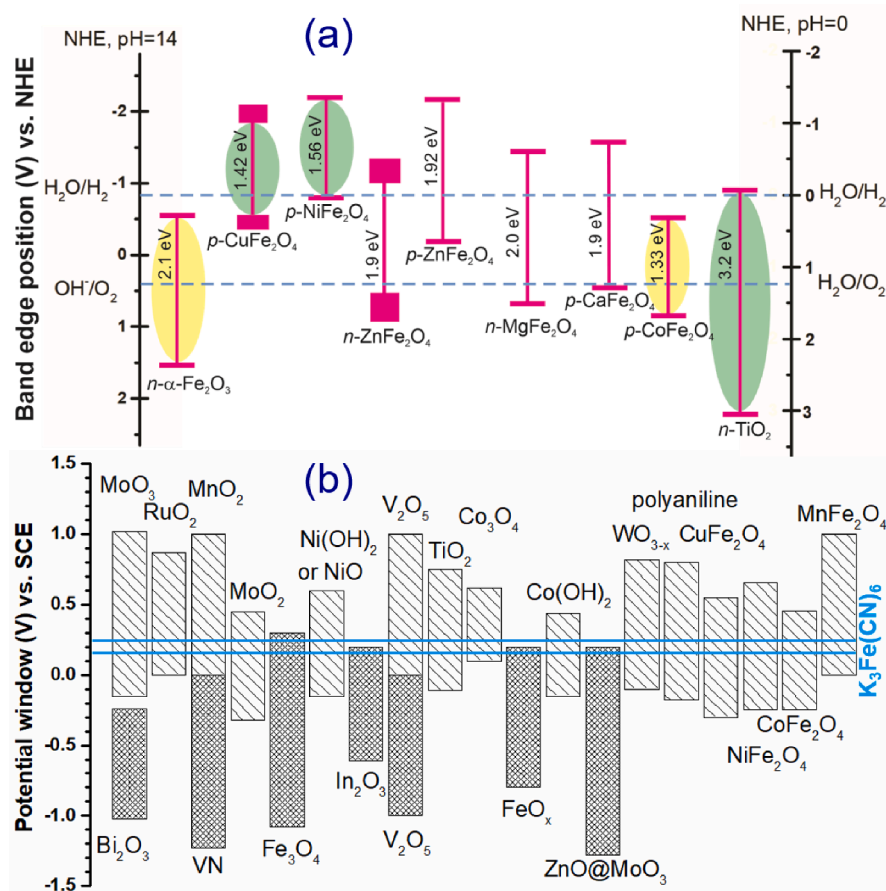

Fig. 19. (a) Band positions {valence band (E$_{CB}$) and conduction band (E$_{VB}$)} of spinel ferrites in contact with aqueous electrolyte solution referenced with NHE (left pH = 14 and right pH = 0) relative to the standard potentials for the reduction and oxidation of water [327]. The E$_{CB}$ and E$_{VB}$ of CoFe$_2$O$_4$ are estimated to be 0.34 and 1.67 V vs. NHE, respectively, as reported in ref. [128]. Adapted from ref. [327] with permission from SPIE, Copyright 2017. (b) Working potential windows of various pseudocapacitive-type materials in aqueous electrolyte. The dense bars correspond to materials used as negative electrodes. Potential window for NiFe$_2$O$_4$, CoFe$_2$O$_4$, CuFe$_2$O$_4$ and MnFe$_2$O$_4$ were taken from refs. [50,93,302,319]. Blue lines correspond to the anodic and cathodic peaks in the CV curves in the electrolyte containing K$_3$Fe(CN)$_6$ additive. Adapted from ref. [334] with permission from Wiley-VCH, Copyright 2011. (For interpretation of the references to color in this figure legend, the reader is referred to the web version of this article.)

Probably, the small size of the $MnFe_2O_4$ NPs (average size ~ 4.8 nm) combined with their good dispersion on the graphene substrate provided a larger number of redox-active sites, enhancing the performance of the SC fabricated by Su et al. [318].

On the other hand, the shapes of CV and GCD curves exhibited by electrode materials measured in three-electrode set-ups provide relevant information about their charge storage mechanism and performance. As stated earlier, RuO_2 and MnO_2 are two metal oxides that rendered outstanding performance as electrode materials in SCs. To enhance their performance in SCs further, researchers fabricated their composites by growing or depositing them over carbonaceous supports. The common electrochemical features of these carbonaceous metal oxide (RuO_2 and MnO_2) composites are that their CV and GCD curves have nearly rectangular and triangular shapes, respectively (Fig. 18**a and b**) [320,321]. While the CV and GCD curves of Mn_3O_4-Fe_2O_3/Fe_3O_4@rGO and $FeCo_2O_4$/graphite composites have similar shapes as that of RuO_2/rGO composite (Fig. 18**c–f**), the potential windows and current densities in their GCD curves are significantly lower than those reported for RuO_2/rGO composites [320,322]. As a result, the C_{sp} values for these electrode materials were smaller. In the case of metal ferrites grown on carbonaceous materials, redox peaks superimposed on capacitive current frequently appear in their voltammograms, which correspond to a cooperative contribution from the pseudocapacitive behavior of metal ferrites and the EDL capacitance provided by the carbonaceous (e.g., graphene, activated carbon, GO or rGO) support. For example, the CV curves for the $CoFe_2O_4$/rGO composite electrode presented in Fig. 18**g** exhibited small redox peaks around −0.9 and −0.4 V (vs Hg/HgO) bias potential. As the GCD curves of the electrode have triangular shape (Fig. 18**h**), the energy storage mechanism in the device is mainly capacitive.

On the other hand, the electrochemical behaviors of metal ferrites depend strongly on the nature of the used electrolyte. Electrolytes of different nature (e.g., acidic, basic or neutral; aqueous or non-aqueous) have different interactions or reactions with the metal ferrites present in SC electrodes, which define the shape of their CV and GCD curves. Typical CV and GCD curves obtained for the $MnFe_2O_4$ NPs embedded in porous carbon electrodes in ionic liquid electrolyte are presented in Fig. 18**i** and **j**, respectively [92]. As can be noted, there appeared no redox peak in the CV curve, which indicates the ions of the ionic liquid electrolyte are adsorbed on the $MnFe_2O_4$ surface without causing redox reaction. In fact, the redox peaks do not appear for the metal ferrite-based electrodes when their CV curves are recorded under neutral electrolytes such as aqueous Na_2SO_4 [47,74,315,317], aqueous NaCl [306], and $LiClO_4$ dissolved acetonitrile [49]. In contrast, when aqueous KOH [43–46,48,52,55,93,292,301,302,304,323], aqueous H_2SO_4 [313,316], or aqueous LiCl [50] are used as electrolytes, which are basic or acidic in nature, well-defined redox peaks appear in the CV curves along with shoulder peaks in the GCD curves of the electrodes, as exemplified in Fig. 18**k** and **l**. Appearance of such shoulder peaks in the GCD curves indicates that the charge storage in the electrodes is pseudocapacitive.

In summary, although MFe_2O_4 (M = Co, Ni, Mn) spinels have low electrical conductivity, their nanostructures have a great potential for utilization as electrode materials in high performance SCs. To achieve this, these metal ferrites must be grown or deposited on conductive supports such as carbonaceous materials or nickel foam. The optimum content of rGO or graphene in metal ferrite nanocomposites should be maintained in-between 20 and 40 wt%. As a high surface area is needed to achieve high C_{sp} and ED in SCs, the metal ferrite nanostructures must have a small size and remain well dispersed over the conducting support. Hierarchical metal ferrite nanostructures that allow easy diffusion of electrolyte ions are beneficial for enhancing the electrochemical performance of SCs. Among the aqueous electrolytes, aqueous KOH and aqueous H_2SO_4 solutions of concentrations in between 1.0 and 6.0 M are seen to be good electrolytes for high performance SCs. Although the use of ionic liquids in SCs is very rare, the ionic liquid $EMIMBF_4$ was seen to exhibit better performance than aqueous electrolytes. Incorporation of redox-active additives such as $K_4[Fe(CN)_6]$ in aqueous KOH electrolytes has been seen to enhance the performance of metal ferrite based and metal oxide based supercapacitor electrodes. Asymmetric SCs fabricated using transition metal oxides (including MFe_2O_4) in both the positive and negative electrodes generated outstanding energy density.

6. Energetic aspects: Relative band edge positions and potential windows for metal ferrite electrodes

For a better understanding of the catalytic performance of metal ferrites, an important aspect to consider is the relative position of their valence and conduction bands, especially when they form nanocomposites with other transition metal oxides. In Fig. 19**a**, we present the band edge positions for several metal ferrites with respect to the standard OER and HER reaction potentials. It can be noted from the diagram that the semiconductors α-Fe_2O_3 (hematite) and $CuFe_2O_4$ form a Z scheme, which facilitates some of the catalytic and photocatalytic reactions presented in Table 5. In the case of $NiFe_2O_4$, the position of conduction band minimum (CBM) is located above the H_2O/H_2 potential, which is favorable for generating H_2 through water splitting [325]. The reported conduction band energy (E_{CB}) and valence band energy (E_{VB}) values for $NiFe_2O_4$ at pH = 0 are −0.06 and −1.62 V (vs. NHE), respectively [325]. On the other hand, estimated E_{CB} and E_{VB} values for $CoFe_2O_4$ are 0.34 and 1.67 V (vs. NHE), respectively [128]. Therefore, cobalt ferrite is not suitable for the photoreduction of water to generate H_2. However, the position of its VB is suitable for oxidation reactions through photogenerated holes. Although the band gap for $MnFe_2O_4$ was reported to be 1.6 eV [326], to the best of our knowledge, there have been no reports on its E_{CB} and E_{VB} position values.

As mentioned in **Section 5**, the working potential window of an electrode material is one of the key parameters that determines its performance in SC. The wider the potential window, the higher the C_{sp} and ED values of the electrode or SC. Working potential window of an active material is determined through cyclic voltammetry. This window is the range of potential scan in a CV curve utilized to evaluate the electrochemical behavior of an electrode material, avoiding its degradation or occurrence of undesired reactions. The potential window for a SC can be obtained by starting with a lower voltage applied to the cell, and then slowly increasing the voltage until a spike appears at the boundary of the window [293]. As several oxide, oxyhydroxide and hydroxide species such as MnOOH, NiO, $Ni(OH)_2$, NiOOH, Co_3O_4, CoOOH, $Co(OH)_2$, FeO, FeOOH and $Fe(OH)_2$ are formed at the surface of metal ferrite electrodes during charge–discharge cycles of SCs (Scheme 5) [43,45,46,48,54,93], they can modify the potential windows for the operation of metal

ferrite based electrodes in SCs.

Considering that metal ferrites are being used in SCs as cheaper alternatives to conventional metal oxides, it is worth comparing the potential windows of metal ferrites with some metal oxides frequently used as electrode materials for SCs. In Fig. 19b, we present the potential windows for several oxides and hydroxides along with the metal ferrites of the current discussion [327]. As can be noted, the potential windows of oxides and hydroxides of nickel and cobalt are relatively smaller than those of other metal oxides and hydroxides. Different research groups have reported different potential window values for a particular metal ferrite. However, most frequent
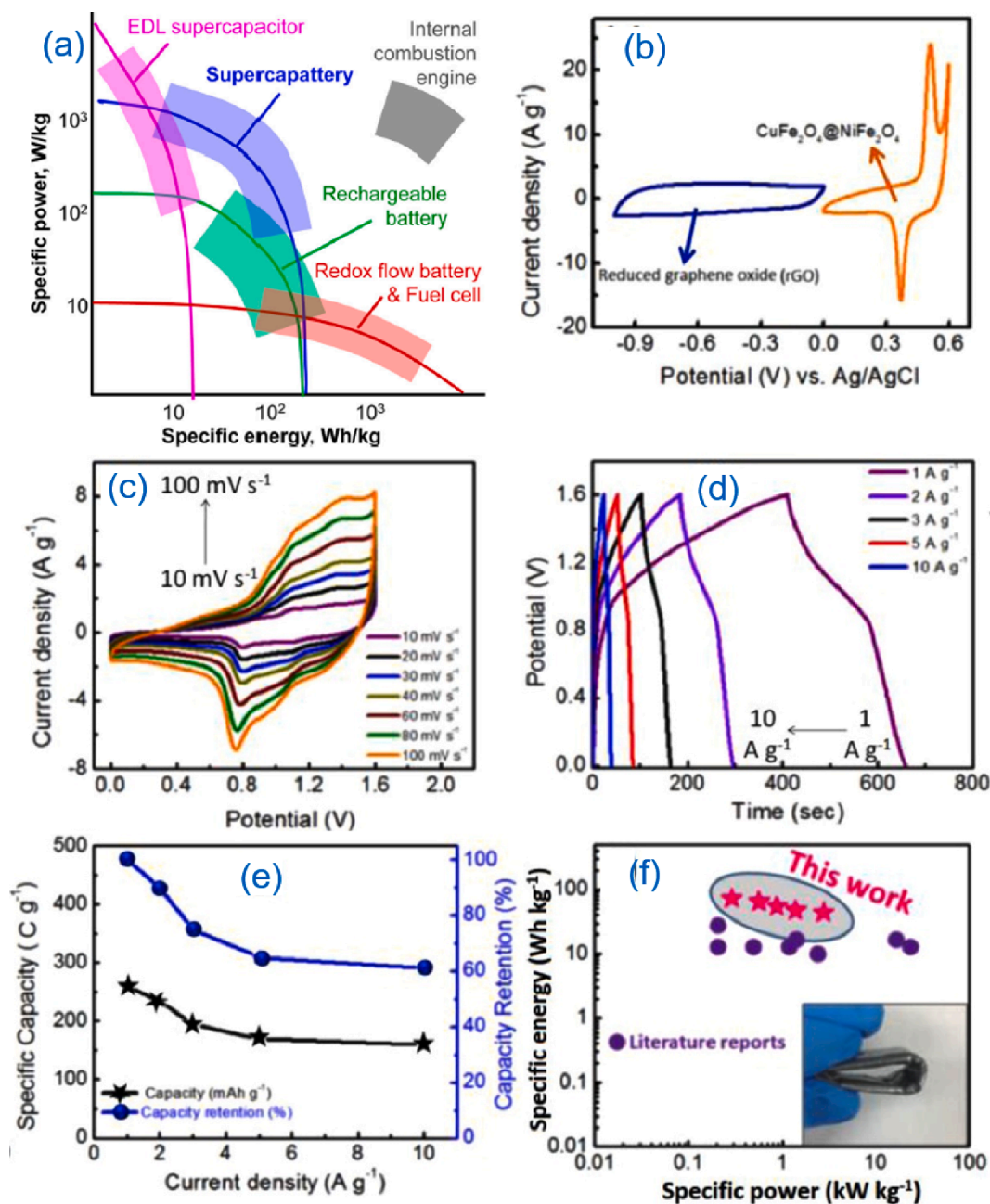
Fig. 20. Ragone plot of different energy storage devices and the position of hybrid supercapattery devices. Reproduced from ref. [339] with permission from Taylor & Francis Group, Copyright 2017. Electrochemical characterization of a supercapattery fabricated using rGO and $CuFe_2O_4$/ $NiFe_2O_4$ nanocomposite as negative and positive electrode, respectively. (b) Three electrode-based CVs at 50 mV s^{-1} for the negative and positive electrode; (c) CV profiles of the supercapattery at different scan rates operated from 0 to 1.6 V, (d) GCD profiles of the supercapattery at different current densities (1 to 10 A g^{-1}); (e) specific capacity and capacity retention plots of the supercapattery; (f) specific energy vs. specific power plot (i. e., Ragone plot) for the supercapattery in comparison with literature data of supercapacitor devices. The inset of Fig. 20f shows an actual photograph of the device in a bending state. Reproduced from ref. [343] with permission from Elsevier, Copyright 2021.

potential windows reported for $CoFe_2O_4$ and $NiFe_2O_4$ are of 0.5 V (0.0 – 0.5 V, vs. SCE) and 1.0 V (0. 0 – 1.0 V, vs. SCE), respectively [45,48–50,52,54,93,301]. In the case of $MnFe_2O_4$ nanostructures, the reported potential windows are 0.55 V (0. 0 – 0.55 V, vs. SCE) [46], 1.0 V (-1.0 – 0.0 V, vs. Hg/HgO) [318], and 1.0 V (0.0 – 1.0 V, vs. SCE) [319]. In the case of $CuFe_2O_4$, the reported potential window is 0.5 V (-0.1 – 0.4 V), although the authors did not report with respect to which reference electrode the potentials were expressed [302,328]. From the potential window values presented above, it is clear that in general, $MnFe_2O_4$ and $NiFe_2O_4$ nanostructures exhibit higher working potential windows than that of $CuFe_2O_4$ and $CoFe_2O_4$.

As mentioned earlier, the working potential window of an electrode material in aqueous electrolytes is constrained by the decomposition of water. However, the potential windows of SC electrodes in aqueous electrolytes can be extended substantially by utilizing strategies such as the addition of redox–active additives, pH regulation of electrolytes, utilization of water–in–salt electrolytes (ultra–concentrated aqueous electrolytes) and the selection of highly stable electrolyte salts [329]. For example, a wide potential window (3.0 V) was achieved by using a water-in-salt electrolyte (5 M lithium bistrifluoromethanesulfonimide, LiTFSI) in an asymmetric SC, using porous carbon as the negative electrode and MnO_2@carbon dendrites as the positive electrode [330]. The main drawback of using aqueous electrolytes based on LiTFSI is its high cost [331]. On the other hand, the utilization of redox-active additives in electrolytes sometimes causes a severe self-discharge of SCs [331].

It has been reported that the incorporation of metal ions in MnO and MnO_2 through partial substitution can generate oxides with ultra-wide potential windows. For example, incorporation of Ni ions into MnO generated $Ni_{0.25}Mn_{0.75}O$ phase, which exhibited a wide potential window (from 0.0 to 1.4 V, vs. SEC) in aqueous LiCl electrolyte when utilized as electrode material of SCs [332]. During electrochemical cycling, the $Ni_{0.25}Mn_{0.75}O$ phase was converted into low-crystalline $LiNi_{0.5}Mn_{1.5}O_4$, which suppresses the oxygen
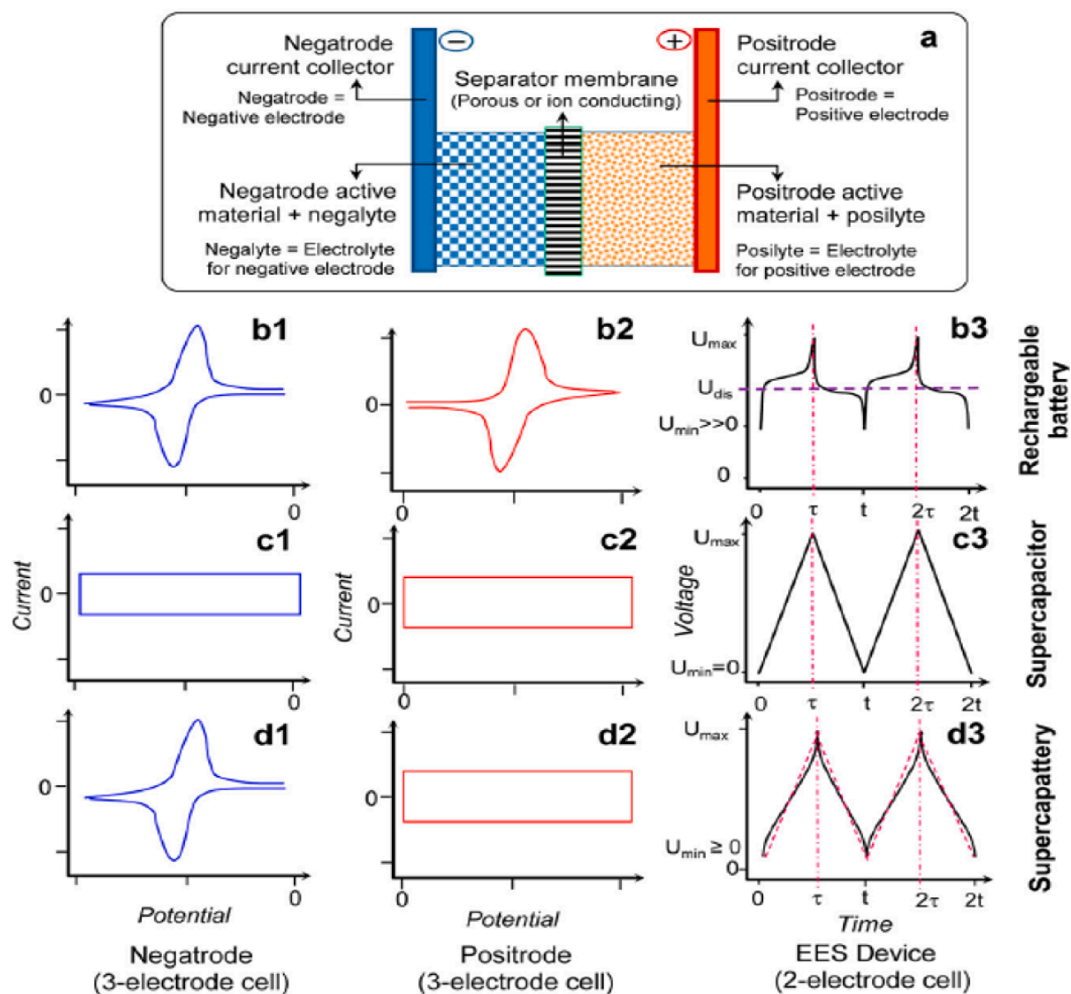

Fig. 21. Schematic illustrations of (a) a single cell of typical EES devices. (1,2) CVs of positrode and negatrode in a three-electrode cell, and (3) GCDs of the two-electrode cell of (b) rechargeable battery, (c) supercapacitor, and (d) supercapattery. U_{max} and U_{min}: maximum and minimum cell voltages that can be reached during charging and discharging, respectively, without causing irreversible changes in the cell. U_{dis}: average discharging voltage. τ and t: end times of the first charging and discharging cycle, $\tau \geq (t - \tau)$. 2τ and $2t$: end times of the second charging and discharging cycle, but not necessarily twice of τ and t. Reproduced from ref. [339] with permission from Taylor & Francis Group, Copyright 2017.

evolution from the aqueous electrolyte, and thus extends the electrode potential window. As another example, the potential window of a SC could be significantly extended (2.4 V) by utilizing $Na_{0.25}MnO_2$/carbon cloth, activated carbon and aqueous 1 M Na_2SO_4 solution as the cathode, anode and electrolyte, respectively. When Na^+ ions are inserted in MnO_2 to form the $Na_{0.5}MnO_2$ phase, the mean oxidation state of Mn decreases, reducing the work function of MnO_2, resulting in an expansion of potential window of the SC [333]. The potential window for the $Na_{0.5}MnO_2$/carbon cloth composite in aqueous Na_2SO_4 electrolyte is significantly wide (0.0–1.3 V, vs. Ag/AgCl). Consequently, the operating voltage window of an asymmetric SC fabricated using $Na_{0.5}MnO_2$/carbon cloth and Fe_3O_4@carbon as the positive and negative electrode was 2.6 V [333]. As the ionic radius of Li^+ ion (0.76 Å) is similar to that of Mn^{2+} (0.83 Å), Co^{2+} (0.745 Å) and Ni^{2+} (0.69 Å) ions, there is a good possibility of incorporating lithium ions at O_h sites in MFe_2O_4 lattice to induce a wider potential window in the MFe_2O_4 - based electrodes. Unfortunately, the ionic radius of Na^+ ion is too large (1.02 Å) to be incorporated at T_d or O_h sites in MFe_2O_4 lattice.

7. Metal ferrites as supercapattery material

All modern supercapacitors possess high power densities and long cycle lives. However, they have low energy densities. On the other hand, rechargeable batteries have high energy densities but low power densities (owing to the faradaic charge storage mechanism). Therefore, none of these two devices can meet all the requirements of an ideal electrochemical energy storage (EES) device individually. Recently, by combining the merits of rechargeable batteries and supercapacitors into one device, innovative hybrid EES devices such as supercapatteries have been fabricated to fulfill commercial expectations by bridging their performance gap (Fig. 20a). While such a class of hybrid devices has been designated as battery–supercapacitor hybrids, redox capacitors, hybrid electrochemical capacitors, etc. by different research groups, the name supercapattery was initially proposed by George Zheng Chen and co-workers by combining the phrases "supercapa" of supercapacitor and "ttery" of battery [335]. A supercapattery is basically a two-electrode device like a supercapacitor. According to the charge storage mechanism in each of the electrodes, there can be four different types of supercapatteries. The two-electrode device can have (1) capacitive faradaic electrode + capacitive non-faradaic electrode, (2) capacitive faradaic electrode + capacitive faradaic electrode, (3) capacitive non-faradaic electrode + non-capacitive faradaic electrode, or (4) capacitive faradaic electrode + non-capacitive faradaic electrode [336].

The term 'supercapattery' can be used to describe all the devices consisting of a battery electrode and a capacitive electrode such as Li-ion capacitors, Na-ion capacitors and other hybrid EES devices that combine the merits of both capacitive and non-capacitive faradaic charge storage mechanisms. While the fundamentals of supercapatteries have been nicely described by Linpo Yu and George Zheng Chen in their recent review article [337], progress made on the development of electrode materials, electrolytes along with supercapattery engineering have been critically reviewed by several authors [335,338–342] in the past 4 years. A typical CV curve for a metal ferrite nanocomposite ($CuFe_2O_4$/$NiFe_2O_4$) electrode used to fabricate a supercapattery is presented in Fig. 20b in comparison with the typical CV curve of a rGO electrode. The CV and GCD profiles of the supercapattery fabricated using $CuFe_2O_4$/$NiFe_2O_4$ nanocomposite and rGO as the positive and negative electrodes, respectively, are presented in Fig. 20c and d. The shapes of these profiles and other electrochemical characteristics of the supercapattery are discussed later.

All the EES devices are composed of a positive electrode, a negative electrode and a separator soaked in an electrolyte, as illustrated in Fig. 21(a). Generally, the electrodes are made of materials with good electronic conductivity such as various transition metal oxides, activated carbon, conducting polymers and their composites. In aqueous electrolyte devices, carbon and its derivatives are usually preferred as negative electrodes because they impose a high overpotential for hydrogen evolution and thereby maximize the potential window of the fabricated device. On the other hand, different transition metal oxides are usually used as positive electrodes. Although the concept of combining two different electrodes appears simple, in practice, their performance should match to maintain two essential conditions: i) the charges passing through the capacitive (Q_{cap}) and Nernstian (Q_{bat}) electrodes must be equal and ii) an equal current should flow through both electrodes at any time. When combining two capacitive electrodes, it is important to establish the capacitive potential range (CPR) of the electrode/electrolyte interface (EEI). CPR is the maximum potential range beyond which a non-capacitive faradaic (or Nernstian) process occurs, and the electrode and/or electrolyte decompose. During the fabrication of an asymmetric device such as supercapattery with capacitive electrode material, the charge conservation relation, i.e., $Q = C_P U_P = C_N U_N$ (where C_P and U_P are the capacitance and CPR of the positrode, and C_N and U_N are the capacitance and CPR of the negatrode, respectively) should be maintained, which can lead to an unequal capacitance in the electrodes (positrode and negatrode). There can be a large difference between the capacities of the positive and negative electrodes, and we need to engineer the electrodes and electrolyte suitably to eliminate this difference. As the electrodes made of carbonaceous materials have considerably smaller capacities than those made of transition metal oxides or battery-type materials, the mass of the carbonaceous materials in the electrodes should be adjusted to satisfy the charge conservation condition.

Hu et al. reported that an addition of 4-hydroxy-2,2,6,6-tetramethylpiperidinyloxyl (4-OH-TEMPO) to aqueous electrolyte can effectively balance the capacity mismatch between the two electrodes [344]. 4-OH-TEMPO is a stable neutral free radical with one unpaired electron, which can be oxidized to 4-OH-TEMPO$^+$ or reduced to 4-OH-TEMPO$^-$ depending on the applied bias potential. The authors fabricated a supercapattery (although they defined it as an asymmetric supercapacitor) and demonstrated that addition of 4-OH-TEMPO in mildly acidic electrolyte (composed of 0.5 M $ZnSO_4$, 0.5 M Li_2SO_4, and 5×10^{-3} M H_2SO_4) enhances the charge storage capacity of activated carbon when used as a positive electrode (Zn as the negative electrode). When the supercapattery was fabricated using activated carbon as the negative electrode and $Ni(OH)_2$ as the positive electrode in a strong alkaline electrolyte, the capacity of the activated carbon electrode was also enhanced substantially on the addition of 4-OH-TEMPO to the 3 M KOH electrolyte. Their results clearly demonstrate that the charge storage capacity of capacitive electrode materials (activated carbon and other carbonaceous materials) used either in positive or negative electrode can be enhanced by the addition of 4-OH-TEMPO to electrolyte to achieve the

necessary capacity balance between the electrodes of the device. Supercapatteries can store charges via three different mechanisms: i) the EDL process, ii) Nernstian or non-capacitive faradaic process, and iii) pseudocapacitive or capacitive faradaic process. In the case of battery-type materials used either in positive or negative electrodes, the CV curves measured individually in three-electrode systems are not symmetric. One or more spikes appear in the CV curves, indicating the occurrence of reversible red-ox reactions during voltage sweep. In the GCD curves of these electrodes, a sharp increase in potential can be observed during charging process, which is followed by a plateau region. On the other hand, during discharging, there appear two sharp falls separated by an intermediate plateau region. Fig. 21(b1–b3) shows typical CV and GCD profiles for battery type electrode materials. Such electrochemical behavior of battery type materials is largely responsible for relatively low power density of batteries. In contrast, for an ideal supercapacitor material, both the negative and positive electrodes exhibit rectangular CV curves and typical GCD profiles are linear in both the charging and discharging regions (Fig. 21(c1–c3)). The electrochemical behaviors of an ideal supercapattery are illustrated in Fig. 21(d1–d3), in which the positive electrode behaves as an ideal battery-type electrode and the negative electrode behaves as an ideal supercapacitor-type electrode. The energy density of these EES devices could also be improved by using a mixed electrolyte, $KI + VOSO_4$, which induces pseudocapacitance to the negatrode (through the redox reactions involving VO^{2+}/VO_2^+ redox couple) and positrode (through the redox reactions involving I^-/I_3^- redox couple) [345,346]. Owing to the presence of these double redox species at EEI, the charge/discharge processes do not involve solid-state reactions or solid-state diffusion [345]. Moreover, the polarized electrodes in the charged cell retard the diffusion of the oppositely charged redox-active ions to mitigate self-discharge, and hence the cell does not need
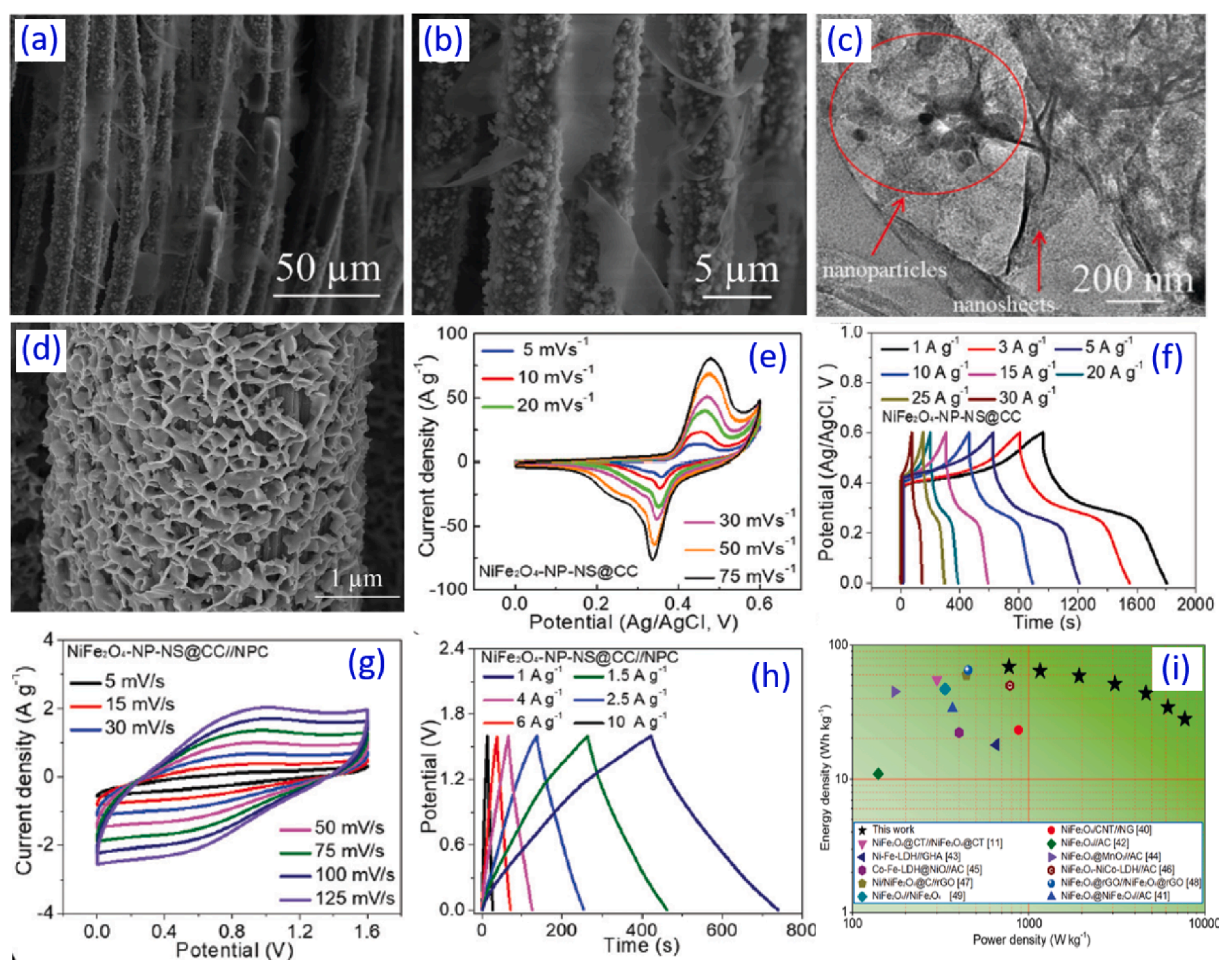

Fig. 22. Typical (a,b) SEM and (c) TEM images of $NiFe_2O_4$ nanostructures grown over carbon cloth fibers ($NiFe_2O_4$/CCF) prepared by hydrothermal process and used as positive electrode of supercapattery. The $NiFe_2O_4$ nanostructures have particle and sheet-like morphologies. A typical (d) SEM image of bimetallic MOF derived N-doped carbon nanosheets grown over carbon cloth fibers utilized as negative electrode of supercapattery. Electrochemical performance of the positive electrode in the three-electrode system under 6 M KOH electrolyte: (e) CV curves for the $NiFe_2O_4$ nanostructures at different scan rates, and (f) GCD curves for the $NiFe_2O_4$ nanostructures at different current densities. Electrochemical performance of supercapattery fabricated using $NiFe_2O_4$/CCF nanocomposite as positive electrode and N-doped carbon nanosheets/CCF as negative electrode: (g) CV curves at different scan rates, (h) GCD curves at different current densities, and (i) Ragone plot for energy and powder densities of the supercapattery along with a comparison of previously reported similar works. Reproduced from ref. [323] with permission from Royal Society of Chemistry, Copyright 2021.

an ion-selective membrane as a separator for short-time-scale energy storage. Considering the low (1.23 V) thermodynamic decomposition potential of water, it is difficult to fabricate aqueous electrolyte-based supercapacitors with wide potential windows, even using materials with high specific capacitance. Nevertheless, through a suitable combination of electrode materials such as lithium metal as the negative electrode and activated carbon as the positive electrode, a supercapattery with wide potential window can be fabricated.

Recently, researchers have attempted to apply different iron-based metal oxides to fabricate positive electrodes for supercapattery. For example, Lalwani et al. [347] fabricated nanocaterpillars of sulphur-doped iron cobalt oxide (FeCo$_2$O$_4$) through a hydrothermal technique and utilized them in supercapattery electrodes. A maximum C_{sp} value of 1809F g^{-1} was obtained for the electrodes in alkaline electrolyte. The nanocaterpillars also showed an ultrahigh stability of C_{sp} retention of ~ 138% after 15,000 cycles, suggesting an increase in the activity after electrochemical testing. Supercapatteries made of undoped FeCo$_2$O$_4$ negatrode and sulfur-doped FeCo$_2$O$_4$ positrode also performed very well in aqueous KOH electrolyte (3 mol L^{-1}). An ultrahigh energy density of 140 Wh kg^{-1} at 1434 W kg^{-1} power density was obtained for the asymmetric two electrode device [347]. However, there are only a few literature reports on the utilization of metal ferrite nano- or microstructures in supercapattery fabrication. Moreover, the CV and GCD characteristics of the supercapatteries made with metal ferrite nanostructures so far are far from ideal. Athika et al. prepared nickel/nickel ferrite/carbon (Ni/NiFe$_2$O$_4$-C) nanocomposite by a solution combustion process and utilized to fabricate supercapattery [348]. The electrode fabricated using the nanocomposite exhibited a specific capacity of 1710C g^{-1} at a current density of 2 A g^{-1} and a capacity retention of 90 % after 2000 cycles [348]. A supercapattery was also fabricated using the Ni/NiFe$_2$O$_4$-C nanocomposite as positive electrode and rGO as the negative electrode, which operated in 1.2 V potential window and revealed a maximum ED of 62 Wh kg^{-1} at a power density of 3440 W kg^{-1} and a maximum power density of 8000 W kg^{-1} at an energy density of 22 Wh kg^{-1} [348]. Very recently, Bandgar et al. [343] synthesized hierarchical core–shell nanostructures of copper ferrite nanorods and nickel ferrite nanosheets (CuFe$_2$O$_4$–NR@NiFe$_2$O$_4$–NS) via a two-step wet chemical technique and utilized them as a positive electrode (rGO being the negative electrode) of a supercapattery. In aqueous KOH (6 M) solution, the as-synthesized CuFe$_2$O$_4$–NR@NiFe$_2$O$_4$–NS electrode demonstrated superior electrochemical behavior with a specific capacity of 1366C g^{-1} at a current density of 1 A g^{-1}, and 94% capacity retention over 10,000 cycles. A flexible supercapattery device assembled using the core–shell composite electrode (as a positive electrode) with a PVA-KOH semi-solid electrolyte exhibited an enhanced specific energy of 72 Wh kg^{-1} at a specific power of 0.287 kW kg^{-1} with outstanding cycle life (~97% retention over 10,000 cycles at 1 A g^{-1}), as shown in Fig. 20e and f. The high specific capacity, superior capacity retention, and excellent cycling life of the supercapattery made of metal ferrite nanostructures containing multiple redox couples (Cu^{2+}, Fe^{3+}, and Ni^{2+}) clearly demonstrates the tremendous potential for utilizing suitably designed metal ferrite nanostructures as electrode materials in next generation energy storage devices. On the other hand, Xi et al. grew NiFe$_2$O$_4$ nanostructures on carbon cloth fibers and used them as positive electrode for high performance supercapattery [323]. The NiFe$_2$O$_4$ nanostructures grown over carbon cloth fibers had particle and sheet-like morphologies (Fig. 22a–c). The electrode fabricated using the NiFe$_2$O$_4$/carbon cloth fiber nanocomposite exhibited an excellent specific capacity (965C g^{-1} at 5 mV s^{-1} scan rate) and capacity retention (94% after 5000 cycles). The negative electrode used for fabricating the supercapattery was nitrogen-doped porous carbon nanosheets grown on carbon cloth fibers by calcinating bimetallic MOF ZIF-8/ZIF-67 (50/50) in N$_2$ atmosphere at 800 °C (Fig. 22d). A PVA/KOH gel was used as the electrolyte. While the shapes of the CV and GCD curves of the positive electrode measured in a three-electrode system were very similar to the CV and GCD curves of a battery electrode (Fig. 22e and f), the shapes of the CV and GCD of the two-electrode device were similar to those of a supercapattery (Fig. 22g and h). The EES device exhibited an outstanding ED of 69 W h kg^{-1} at a power density of 771 W kg^{-1} (Fig. 22i), which is higher than the ED values obtained for the SCs based on NiFe$_2$O$_4$ nanocones (one of the best performing SC materials among the metal ferrites) presented in the Ragone plot in Fig. 17a.

Among the metal ferrite based SCs and supercapatteries reported so far, most supercapaterries exhibit higher ED values than SCs. Nevertheless, these values are lower (~50 %) than the reported ED values for supercapatteries based on transition metal oxides such as FeCo$_2$O$_4$, for which a maximum ED value of 140 Wh kg^{-1} was achieved [347]. The advantages of utilizing metal ferrites in supercapatteries are their reasonably good electrochemical performance, low cost, low toxicity, and high abundance of their constituent elements in the earth's crust.

8. Challenges and outlook

Before addressing the challenges for utilizing metal ferrite nanostructures in catalytic and electrochemical energy storage applications, let us summarize their advantages and disadvantages. The specific advantages of the metal ferrites for utilizing in organic synthesis, OER, HER and supercapacitive energy storage are: (i) the presence of cations exhibiting two or more valence states, which allows the occurrence of redox reactions that need a fast charge–discharge of pseudocapacitors; (ii) their ability to accept an electron pair from adsorbed organic molecules or an electron from free radicals in the empty 3d orbitals of the Fe, Cu, Mn, Ni or Co cations, i.e., the ferrites act as Lewis catalysts; (iii) their ability to accept/donate electrons from redox mediators such as Fe(CN)$_6^{3-/4-}$, which is beneficial for a faster charge–discharge process at high current densities; (iv) reversible electrochemical behaviors under an applied bias, which is necessary to achieve good capacity retention of the pseudocapacitors; (v) metal ferrites are stable under basic and slightly acidic conditions, which allow their use in aqueous electrolytes such as NaOH or H$_2$SO$_4$, frequently used in pseudocapacitors; (vi) the potential window of a supercapacitor (asymmetric) made of metal ferrite electrode could be as high as 1.8 V in aqueous solutions. Additional advantages of metal ferrites are their relatively low cost and low toxicity (except CoFe$_2$O$_4$) along with the possibility of being used as magnetically-separable catalysts with high cycling stability.

On the other hand, the disadvantages associated to their applications in the above-mentioned fields are their high electrical resistivity and their proneness for aggregation due to ferromagnetic nature, which diminishes their effective surface area. To obtain

nanostructured metal ferrites with high surface area and low electrical resistivity, it is essential to synthesize them with smaller sizes with convenient morphologies, well-dispersed in a conductive material to promote the electron transfer between the active material and the conductive material.

Although metal ferrite nanostructures and nanocomposites of different morphologies, compositions, and architectures have been utilized as catalysts in several important organic and inorganic reactions with varied success, the principal hurdle for their utilization in chemical catalysis lies in their synthesis with adequate dispersion, maintaining a high surface area. While this issue has been partially resolved by growing metal ferrite nanostructures over metal foams (e.g., Ni foam) and layered carbonaceous supports such as CNTs, graphene, GO and rGO, the techniques used for such synthesis require further fine tuning to produce well-dispersed metal ferrite nanostructures of specific morphologies with good reproducibility, avoiding their agglomeration. As the durability of a catalyst depends on its chemical stability under extreme environments (e.g., highly basic or acidic media, presence of strong oxidants, etc.) of chemical reactions, *in situ* surface characterization of MFe_2O_4 (M = Cu, Ni, Co) nanocatalysts is necessary to monitor the formation of $M(OH)_2$, $Fe(OH)_3$, and MO_x species on their surface during these chemical processes.

From the catalytic point of view, metal ferrites are fairly stable under chemical and thermal fluctuations. However, to maximize the product yield of a metal ferrite catalyzed chemical reaction, ferrite nanostructures of specific metals with convenient sizes, morphologies and porosity should be selected. For example, $CuFe_2O_4$ is the best catalyst for some organic reactions. $CuFe_2O_4/TiO_2$ and $CuFe_2O_4/GO$ nanocomposites exhibit excellent performance in the photoreduction of CO_2. On the other hand, carbonaceous composites of $NiFe_2O_4$ exhibit superior performance in OER, and platinum-dope $NiFe_2O_4$ nanostructures have excellent activities in the reduction of toxic NO gas. Moreover, nickel and copper ferrite nanocomposites exhibited superior performances in the photodegradation of organic pollutants such as dyes, pharmaceuticals, and herbicides, by activating HSO_5^- ions to $SO_4^{\bullet-}$ radicals in aqueous media.

One of the drawbacks of current SCs is their high power delivery cost. Utilization of metal ferrite nanostructures containing low-cost first-row transition metals might be a good option for electrode materials to reduce the per-watt power delivery cost of SCs. Barring a couple of works, in all metal ferrite based SCs fabricated so far, researchers have used aqueous electrolytes. Although the utilization of aqueous electrolytes in laboratory-scale testing is convenient as it can avoid the use of expensive and toxic organic solvents or ionic liquids, it possesses a restriction for testing redox-active additives in the electrolyte under wide potential windows (>2.0 V), apart from the possibility of O_2 generation through OER. Sen et al. [49] used an acetonitrile based 1 M $LiClO_4$ solution (entry 3 in Table 7) and Yang et al. [92] used an ionogel (prepared with an ionic liquid, poly(vinylidene fluoride-hexafluoropropylene) and acetone) as electrolytes for their SCs. Those SCs could be operated in wide potential windows and exhibited high *EDs*. These results clearly demonstrate that metal ferrite electrodes and ionic liquids or organic solvents as electrolytes are promising combinations for obtaining high performance SCs. However, there are only a few materials that exhibit high pseudocapacitance in non-aqueous electrolytes [349]. Therefore, it is challenging to fabricate SCs containing both MFe_2O_4 nanostructures and non-aqueous electrolytes that exhibit pseudocapacitance within wide operating potential windows and have high energy densities. In non-aqueous electrolytes, the content of H_2O should be maintained below 3 ppm as the SCs operating at 1.5 V or higher potentials generate O_2 from water, which promotes the corrosion of current collectors, and increases the internal resistance of the SCs [350]. As discussed in section 4.1.5.1, metal ferrites are good electrocatalysts that generate O_2 (through OER) around this voltage. Moreover, water traces in organic electrolytes promote the self-discharge of SCs [294].

For enhancing the electrochemical performance of metal ferrite based SCs, they should be fabricated as asymmetric devices with electrolytes containing redox-active additives such as $K_4[Fe(CN)_6]$ or lithium ions for increasing their C_{sp} (through the added pseudocapacitance of intercalation). Among the metal ferrites, $NiFe_2O_4$ has revealed the best electrochemical performance in all-solid-state SCs (entries 1 and 2 in Table 7) [43,50]. One efficient strategy to increase the energy density in metal-ferrite based SCs is to increase the potential window width utilizing a convenient negative electrode material. The $Zn/Zn_4SO_4(OH)_6 \cdot 4H_2O$ composite grown on microporous carbon [351] seems to be a promising negative electrode material for SCs, as it can operate over a wide (from −1.3 to 0 V (vs. SCE)) potential window in neutral electrolytes [351]. Therefore, the SCs made of this composite as the negative electrode and metal ferrite as the positive electrode could be an interesting option that needs to be explored in the present context.

Considering the diversity of the techniques utilized for synthesizing metal ferrite nanostructures and procedures adapted for assessing their electrochemical parameters, it is almost impossible to compare the performance of metal ferrite nanostructures and nanocomposites in SCs quantitatively. Moreover, the use of different electrolytes (aqueous, organic, ionic liquid, salts containing Li^+ ions) with different solution strengths made the task even more complicated. However, by analyzing the electrochemical results reported so far, it is clear that for energy storage applications, the metal ferrite nanostructures should have a small size (5–10 nm) with a high specific surface area; they should be grown over highly conducting supports (e.g., Ni foam, graphene, GO, rGO, CNT); and they should be highly porous. The electrodes fabricated using them should have a small thickness. In the case of $NiFe_2O_4$ and $CoFe_2O_4$ nanostructures, SCs should be assembled using alkaline electrolytes, although both alkaline and neutral electrolytes can be used for $MnFe_2O_4$ nanostructures. Incorporation of a redox-active additive such as $K_4[Fe(CN)_6]$ in electrolyte enhances the power delivery efficiency of the EES device, especially at high scan rates. Use of a negative electrode made of metal oxide nanostructures (e.g., Fe_3O_4, FeOOH, $CuCO_2O_4$) while using MFe_2O_4 as a positive electrode might enhance the potential window width of a SC and hence its C_{sp} and *ED*.

Although most metal ferrite nanostructures suffer from poor electrical conductivity and moderate electrochemical cycling stability, $NiFe_2O_4$, $CoFe_2O_4$ and $MnFe_2O_4$ nanostructures of small sizes combined with carbonaceous material or Ni foam have great potential for using in asymmetric SCs. Furthermore, $MnFe_2O_4$ NPs exhibit high C_{sp} values in ionic liquids and tolerate high bias potentials (e.g., 3.5 V in asymmetric SCs based on $EMIMBF_4$ ionic liquid as electrolyte), which are two essential requirements for fabricating high energy density supercapacitors.

Finally, the performances of metal ferrite nanostructures reported so far are not as encouraging as some metal oxides and hydroxides such as nickel–cobalt binary hydroxide [352] MnO_2 [341] or $FeCo_2O_4$ [347]. However, utilization of metal ferrite nanostructures in supercapattery is very recent (past 3 years only). Informations available in the literature indicate that metal ferrite-based nanocomposites are better supercapattery materials than pure metal ferrite nanostructures. Further research is needed not only for designing suitable metal ferrite nanocomposites but also for finding adequate electrolytes for the development of efficient metal ferrite-based supercapatteries.

9. Conclusions

Research results published during the past 2 decades present a clear idea on the utility of metal ferrite MFe_2O_4 (M = Co, Ni, Cu, Mn) nanostructures as catalysts for organic reactions, oxygen evolution reaction, degradation of organic pollutants, and conversion of some toxic gases such as NO and CO. Among all the metal ferrites, $CuFe_2O_4$ is the most frequently used catalyst for some specific organic reactions such as carbon–carbon coupling, aldol condensation, azide − alkyne cycloaddition, hydroboration of alkynes, and the C-N and C-S bond formation in organic compounds. Many coupling (between the amine group and the carbonyl group of organic molecules) reactions are catalyzed by $CuFe_2O_4$ nanoparticles, which cannot be carried out in high yields using other metal oxides. The metal ferrite catalyst activates the carbonyl group of organic molecules (aldehydes, ketones, esters and acid anhydrides) to facilitate nucleophilic attack by the amine groups. In addition, using $CuFe_2O_4$ nanoparticles as catalysts, several heterocycles can be synthesized in high yields. Although the oxidation state of copper ions in $CuFe_2O_4$ is 2+, copper ferrite catalyzes many organic reactions that are usually achieved by utilizing coordination compounds containing either Cu^{1+} or Cu^{2+} ions. Nanocomposites containing MFe_2O_4 (M = Co, Ni, Cu, Mn) and some metal oxides, carbon nanotubes, graphene or rGO are useful for the synthesis of small organic molecules, OER, degradation of pollutants, and reduction of CO_2 to CO or methanol. The specific chemical reactions showcased in this review occur in higher yields when catalyzed by $CuFe_2O_4$ rather than CuO, Cu_2O or α-Fe_2O_3.

Controlling morphology, size, and texture of metal ferrite nanostructures is essential to define the number of active sites (a key parameter for redox reactions) available on their surface and their accessibility, along with the diffusion of ions from electrolytes to the nanostructured electrodes of SCs. For example, ultrathin 2D nanostructures with hierarchical arrangement provide large number of active sites, adequate accessibility of electrolyte and allow good ion diffusion, improving the performance of metal ferrite nanostructures in catalytic and SC applications.

Pseudocapacitors fabricated using metal ferrite nanostructures grown over or deposited on graphene, rGO, carbon nanofibers and Ni foams manifest quite attractive electrochemical performance. While the potential windows for metal ferrite nanocomposite-based electrodes are comparable or slightly wider than conventional pseudocapacitor materials such as Co_3O_4, $Ni(OH)_2$ and $NiCo_2O_4$, owing to the small atomic masses of Fe and M, MFe_2O_4-based electrodes have a high specific capacitance.

$NiFe_2O_4$ nanosheets and nanocones are promising nanomaterials for fabricating all-solid state SCs with high *ED* ($\geq$47 Wh kg^{-1}). The combination of $CoFe_2O_4$/rGO and $CuCo_2O_4$/rGO nanocomposites as negative and positive electrode materials, respectively, in asymmetric SCs exhibits superior performance (*ED* $\sim$ 72 Wh kg^{-1} at 953 W kg^{-1}). Use of binary redox-active metal oxides in both electrodes provides a great opportunity to enhance the specific capacitance and energy density of SCs considerably. While $CuFe_2O_4$ is a better chemical catalyst for synthesizing organic molecules, $NiFe_2O_4$ and $CoFe_2O_4$ nanostructures, especially their carbonaceous composites, are better electrocatalysts for supercapacitor applications.

Declaration of Competing Interest

The authors declare that they have no known competing financial interests or personal relationships that could have appeared to influence the work reported in this paper.

Acknowledgements

References

[1] Chen D, Wang Q, Wang R, Shenb G. Ternary oxide nanostructured materials for supercapacitors: a review. J Mater Chem A 2015;3:10158–73. https://doi.org/10.1039/C4TA06923D.
[2] Dubal DP, Gomez-Romero P, Sankapal BR, Holze R. Nickel cobaltite as an emerging material for supercapacitors: An overview. Nano Energy 2015;11:377–99. https://doi.org/10.1016/j.nanoen.2014.11.013.
[3] Owusu KA, Qu L, Li J, Wang Z, Zhao K, Yang C, et al. Low-crystalline iron oxide hydroxide nanoparticle anode for high-performance supercapacitors. Nat Commun 2017;8(1). https://doi.org/10.1038/ncomms14264.
[4] Fraas LM. Low-Cost Solar Electric Power. 1st ed. Heidelberg: Springer International Publishing; 2014.
[5] National Renewable Energy Laboratory. Best Research-Cell Efficiency Chart. https://www.nrel.gov/pv/cell-efficiency.html [accessed: 2022-05-01].
[6] Shao Y, El-Kady MF, Sun J, Li Y, Zhang Q, Zhu M, et al. Design and mechanisms of asymmetric supercapacitors. Chem Rev 2018;118(18):9233–80.
[7] Miller JR, Simon P. Electrochemical capacitors for energy management. Science 2008;321:651–2. https://doi.org/10.1126/science.1158736.
[8] Raza W, Ali F, Raza N, Luo Y, Kim K-H, Yang J, et al. Recent advancements in supercapacitor technology. Nano Energy 2018;52:441–73.
[9] Giustino F, Snaith HJ. Toward lead-free perovskite solar cells. ACS Energy Lett 2016;1:1233–40. https://doi.org/10.1021/acsenergylett.6b00499.
[10] Fan Z, Sun K, Wang J. Perovskites for photovoltaics: a combined review of organic–inorganic halide perovskites and ferroelectric oxide perovskites. J Mater Chem A 2015;3:18809–28. https://doi.org/10.1039/C5TA04235F.

[11] Jena AK, Kulkarni A, Miyasaka T. Halide perovskite photovoltaics: Background, status, and future prospects. Chem Rev 2019;119:3036–103. https://doi.org/10.1021/acs.chemrev.8b00539.

[12] Faheem MB, Khan B, Feng C, Farooq MU, Raziq F, Xiao Y, et al. All-inorganic perovskite solar cells: Energetics, key challenges, and strategies toward commercialization. ACS Energy Lett 2020;5(1):290–320.

[13] Manthiram A. A reflection on lithium-ion battery cathode chemistry. Nat Commun 2020;11:1550. https://doi.org/10.1038/s41467-020-15355-0.

[14] Wang Q, Liu B, Wang X, Ran S, Wang L, Chen Di, et al. Morphology evolution of urchin-like $NiCo_2O_4$ nanostructures and their applications as psuedocapacitors and photoelectrochemical cells. J Mater Chem 2012;22(40):21647.

[15] Zhong C, Deng Y, Hu W, Qiao J, Zhang L, Zhang J. A review of electrolyte materials and compositions for electrochemical supercapacitors. Chem Soc Rev 2015; 44:7484–539. https://doi.org/10.1039/c5cs00303b.

[16] Wang G, Zhang L, Zhang J. A review of electrode materials for electrochemical supercapacitors. Chem Soc Rev 2012;41:797–828. https://doi.org/10.1039/c1cs15060j.

[17] Wang Y, Song Y, Xia Y. Electrochemical capacitors: mechanism, materials, systems, characterization and applications. Chem Soc Rev 2016;45:5925–50. https://doi.org/10.1039/C5CS00580A.

[18] Noori A, El-kady MF, Rahmanifar MS, Kaner RB, Mousavi MF. Towards establishing standard performance metrics for batteries, supercapacitors and beyond. Chem Soc Rev 2019;48:1272–341. https://doi.org/10.1039/c8cs00581h.

[19] Kate RS, Khalate SA, Deokate RJ. Overview of nanostructured metal oxides and pure nickel oxide (NiO) electrodes for supercapacitors: A review. J Alloys Compd 2018;734:89–111. https://doi.org/10.1016/j.jallcom.2017.10.262.

[20] González A, Goikolea E, Barrena JA, Mysyk R. Review on supercapacitors: Technologies and materials. Renew Sustain Energy Rev 2016;58:1189–206. https://doi.org/10.1016/j.rser.2015.12.249.

[21] Salanne M, Rotenberg B, Naoi K, Kaneko K, Taberna P-L, Grey CP, et al. Efficient storage mechanisms for building better supercapacitors. Nat Energy 2016;1 (6). https://doi.org/10.1038/nenergy.2016.70.

[22] Ghodbane O, Pascal JL, Favier F. Microstructural effects on charge-storage properties in MnO_2-based electrochemical supercapacitors. ACS Appl Mater Interfaces 2009;1:1130–9. https://doi.org/10.1021/am900094e.

[23] Lee HY, Goodenough JB. Supercapacitor behavior with KCl electrolyte. J Solid State Chem 1999;144:220–3. https://doi.org/10.1006/jssc.1998.8128.

[24] Fleischmann S, Mitchell JB, Wang R, Zhan C, Jiang D-e, Presser V, et al. Pseudocapacitance: From fundamental understanding to high power energy storage materials. Chem Rev 2020;120(14):6738–82.

[25] Augustyn V, Come J, Lowe MA, Kim JW, Taberna P-L, Tolbert SH, et al. High-rate electrochemical energy storage through Li^+ intercalation pseudocapacitance. Nat Mater 2013;12(6):518–22.

[26] Liu H, Liu X, Wang S, Liu HK, Li L. Transition metal based battery-type electrodes in hybrid supercapacitors: A review. Energy Storage Mater 2020;28:122–45. https://doi.org/10.1016/j.ensm.2020.03.003.

[27] Peng S, Li L, Wu HB, Madhavi S, Wen X, Lou D. Controlled growth of $NiMoO_4$ nanosheet and nanorod arrays on various conductive substrates as advanced electrodes for asymmetric supercapacitors. Adv Energy Mater 2015;5:1401172. https://doi.org/10.1002/aenm.201401172.

[28] Zhen C, Zhang XiaoZhe, Wei W, Guo W, Pant A, Xu X, et al. Nanostructural origin of semiconductivity and large magnetoresistance in epitaxial $NiCo_2O_4/Al_2O_3$ thin films. J Phys D: Appl Phys 2018;51(14):145308.

[29] LME cobalt prices. https://www.lme.com/en-GB/Metals/Minor-metals/Cobalt#tabIndex=0 [accessed: 2022-05-01].

[30] Veerakumar P, Sangili A, Manavalan S, Thanasekaran P, Lin KC. Research progress on porous arbon supported metal/metal oxide nanomaterials for supercapacitor electrode applications. Ind Eng Chem Res 2020;59:6347–74. https://doi.org/10.1021/acs.iecr.9b06010.

[31] Kumar KS, Choudhary N, Jung Y, Thomas J. Recent advances in two-dimensional nanomaterials for supercapacitor electrode applications. ACS Energy Lett 2018;3:482–95. https://doi.org/10.1021/acsenergylett.7b01169.

[32] Zhang G, Xiao X, Li B, Gu P, Xue H, Pang H. Transition metal oxides with one-dimensional/one-dimensional-analogue nanostructures for advanced supercapacitors. J Mater Chem A 2017;5:8155–86. https://doi.org/10.1039/c7ta02454a.

[33] Wang F, Wu X, Yuan X, Liu Z, Zhang Yi, Fu L, et al. Latest advances in supercapacitors: From new electrode materials to novel device designs. Chem Soc Rev 2017;46(22):6816–54.

[34] Guo X, Zhang G, Li Q, Xue H, Pang H. Non-noble metal-transition metal oxide materials for electrochemical energy storage. Energy Storage Mater 2018;15: 171–201. https://doi.org/10.1016/j.ensm.2018.04.002.

[35] Li Q, Xu Y, Zheng S, Guo X, Xue H, Pang H. Recent progress in some amorphous materials for supercapacitors. Small 2018;14:1800426. https://doi.org/10.1002/smll.201800426.

[36] Poonam, Sharma K, Arora A, Tripathi SK. Review of supercapacitors: Materials and devices. J Energy Storage 2019;21:801–25.

[37] Yuvaraj S, Selvan RK, Lee YS. An overview of AB_2O_4- and A_2BO_4-structured negative electrodes for advanced Li-ion batteries. RSC Adv 2016;6:21448–74. https://doi.org/10.1039/c5ra23503k.

[38] Cherian CT, Sundaramurthy J, Reddy MV, Suresh Kumar P, Mani K, Pliszka D, et al. Morphologically robust $NiFe_2O_4$ nanofibers as high capacity Li-Ion battery anode material. ACS Appl Mater Interfaces 2013;5(20):9957–63.

[39] Li D, Li G, Ge H, Zhang J, Meng X. Fabrication of $CoFe_2O_4$ and $NiFe_2O_4$ nanoporous spheres as promising anodes for high performance lithium-ion batteries. New J Chem 2017;41:15501–7. https://doi.org/10.1039/c7nj03324a.

[40] Kumar PR, Mitra S. Nickel ferrite as a stable, high capacity and high rate anode for Li-ion battery applications. RSC Adv 2013;3:25058–64. https://doi.org/10.1039/c3ra44001j.

[41] Islam M, Ali G, Jeong MG, Choi W, Chung KY, Jung HG. Study on the electrochemical reaction mechanism of $NiFe_2O_4$ as a high-performance anode for Li-ion batteries. ACS Appl Mater Interfaces 2017;9:14833–43. https://doi.org/10.1021/acsami.7b01892.

[42] Fu Y, Chen Q, He M, Wan Y, Sun X, Xia H, et al. Copper ferrite-graphene hybrid: A multifunctional heteroarchitecture for photocatalysis and energy storage. Ind Eng Chem Res 2012;51(36):11700–9.

[43] Bandgar SB, Vadiyar MM, Ling Y-C, Chang J-Y, Han S-H, Ghule AV, et al. Metal precursor dependent synthesis of $NiFe_2O_4$ thin films for high-performance flexible symmetric supercapacitor. ACS Appl Energy Mater 2018;1(2):638–48.

[44] Zhang X, Zhang Z, Sun S, Sun Q, Liu X. Hierarchical 3D $NiFe_2O_4@MnO_2$ core-shell nanosheet arrays on Ni foam for high-performance asymmetric supercapacitors. Dalt Trans 2018;47:2266–73. https://doi.org/10.1039/c7dt04127f.

[45] Zheng L, Guan L, Yang G, Chen S, Zheng H. One-pot synthesis of $CoFe_2O_4/rGO$ hybrid hydrogels with 3D networks for high capacity electrochemical energy storage devices. RSC Adv 2018;8:8607–14. https://doi.org/10.1039/c8ra00285a.

[46] Makkar P, Ghosh NN. A Facile synthesis of $MnFe_2O_4$ hollow sphere-reduced graphene oxide nanocomposite as electrode material for all-solid-state flexible high-performance asymmetric supercapacitor. ACS Appl Energy Mater 2020;3:2653–64. https://doi.org/10.1021/acsaem.9b02360.

[47] Li B, Fu Y, Xia H, Wang X. High-performance asymmetric supercapacitors based on $MnFe_2O_4/graphene$ nanocomposite as anode material. Mater Lett 2014; 122:193–6. https://doi.org/10.1016/j.matlet.2014.02.046.

[48] Zhao Y, Xu Y, Zeng J, Kong B, Geng X, Li D, et al. Low-crystalline mesoporous $CoFe_2O_4/C$ composite with oxygen vacancies for high energy density asymmetric supercapacitors. RSC Adv 2017;7(87):55513–22.

[49] Sen P, De A. Electrochemical performances of poly(3,4-ethylenedioxythiophene)–$NiFe_2O_4$ nanocomposite as electrode for supercapacitor. Electrochim Acta 2010;55:4677–84. https://doi.org/10.1016/j.electacta.2010.03.077.

[50] Javed MS, Zhang C, Chen L, Xi Y, Hu C. Hierarchical mesoporous $NiFe_2O_4$ nanocone forest directly growing on carbon textile for high performance flexible supercapacitors. J Mater Chem A 2016;4:8851–9. https://doi.org/10.1039/c6ta01893a.

[51] Rahmanifar MS, Hemmati M, Noori A, El-kady MF, Mousavi MF, Kaner RB. Asymmetric supercapacitors: An alternative to activated carbon negative electrodes based on earth abundant elements. Mater Today Energy 2019;12:26–36. https://doi.org/10.1016/j.mtener.2018.12.006.

[52] Wang H, Song Y, Ye X, Wang H, Liu W, Yan L. Asymmetric supercapacitors assembled by dual spinel ferrites@graphene nanocomposites as electrodes. ACS Appl Energy Mater 2018;1:3206–15. https://doi.org/10.1021/acsaem.8b00433.

[53] Ge J, Fan G, Si Y, He J, Kim H-Y, Ding B, et al. Elastic and hierarchical porous carbon nanofibrous membranes incorporated with NiFe$_2$O$_4$ nanocrystals for highly efficient capacitive energy storage. Nanoscale 2016;8(4):2195–204.

[54] Gao H, Xiang J, Cao Y. Hierarchically porous CoFe$_2$O$_4$ nanosheets supported on Ni foam with excellent electrochemical properties for asymmetric supercapacitors. Appl Surf Sci 2017;413:351–9. https://doi.org/10.1016/j.apsusc.2017.04.067.

[55] Sankar KV, Selvan RK, Meyrick D. Electrochemical performances of CoFe$_2$O$_4$ nanoparticles and a rGO based asymmetric supercapacitor. RSC Adv 2015;5: 99959–67. https://doi.org/10.1039/c5ra14938j.

[56] Shinde PV, Shinde NM, Mane RS, Kim KH. Ferrites for electrochemical supercapacitors. In: Mane RS, Jadhav V, editors. Spinel ferrite nanostructures for energy storage devices. 1st ed.,. Elsevier Inc.; 2020.

[57] Faungnawakij K, Shimoda N, Fukunaga T, Kikuchi R, Eguchi K. Crystal structure and surface species of CuFe$_2$O$_4$ spinel catalysts in steam reforming of dimethyl ether. Appl Catal B: Environ 2009;92:341–50. https://doi.org/10.1016/j.apcatb.2009.08.013.

[58] Ding Yu, Zhao J, Zhang W, Zhang J, Chen X, Yang F, et al. Single-walled carbon nanotubes wrapped CoFe$_2$O$_4$ nanorods with enriched oxygen vacancies for efficient overall water splitting. ACS Appl Energy Mater 2019;2(2):1026–32.

[59] Baghbanian SM, Farhang M. CuFe$_2$O$_4$ nanoparticles: A magnetically recoverable and reusable catalyst for the synthesis of quinoline and quinazoline derivatives in aqueous media. RSC Adv 2014;4:11624–33. https://doi.org/10.1039/c3ra46119j.

[60] Swami S, Agarwala A, Shrivastava R. Sulfonic acid functionalized silica-coated CuFe$_2$O$_4$ core-shell nanoparticles: An efficient and magnetically separable heterogeneous catalyst for the synthesis of 2-pyrazole-3-amino-imidazo-fused polyheterocycles. New J Chem 2016;40:9788–94. https://doi.org/10.1039/c6nj02264b.

[61] Nguyen OTK, Nguyen LT, Truong NK, Nguyen VD, Nguyen AT, Le NTH, et al. Synthesis of triphenylamines via ligand-free selective ring-opening of benzoxazoles or benzothiazoles under superparamagnetic nanoparticle catalysis. RSC Adv 2017;7(65):40929–39.

[62] Nguyen CK, Vu HH, Dang HV, Nguyen NN, Le NTH, Phan NTS. Superparamagnetic nanoparticles as a recyclable catalyst: A new access to phenol esters via cross dehydrogenative coupling reactions. RSC Adv 2017;7:55756–66. https://doi.org/10.1039/c7ra11706j.

[63] Mohan B, Park KH. Superparamagnetic copper ferrite nanoparticles catalyzed aerobic, ligand-free, regioselective hydroboration of alkynes: Influence of synergistic effect. Appl Catal A: Gen 2016;519:78–84. https://doi.org/10.1016/j.apcata.2016.03.019.

[64] Zhao X, Mao L, Cheng Q, Li J, Liao F, Yang G, et al. Recent advances in two-dimensional spinel structured Co-based materials for high performance supercapacitors: A critical review. Chem Eng J 2020;387:124081.

[65] Zhao X, Mao L, Cheng Q, Li J, Liao F, Yang G, et al. Two-dimensional spinel structured Co-based materials for high performance supercapacitors: A critical review. Chem Eng J 2020;387:124081.

[66] Zhang L, Shi D, Liu T, Jaroniec M, Yu J. Nickel-based materials for supercapacitors. Mater Today 2019;25:35–65.

[67] Malaie K, Reza GM. Spinel nano-ferrites for aqueous supercapacitors; linking abundant resources and low-cost processes for sustainable energy storage. J Energy Storage 2020;33:102097. https://doi.org/10.1016/j.est.2020.102097.

[68] Ismael M. Ferrites as solar photocatalytic materials and their activities in solar energy conversion and environmental protection: A review. Sol Energy Mater Sol Cells 2021;219:110786. https://doi.org/10.1016/j.solmat.2020.110786.

[69] De Santis M, Bailly A, Coates I, Grenier S, Heckmann O, Hricovini K, et al. Epitaxial growth and structure of cobalt ferrite thin films with large inversion parameter on Ag (001). Acta Crystallogr, Sect B Struct Sci, Cryst Eng Mater 2019;75(1):8–17.

[70] Pullar RC. Hexagonal ferrites: A review of the synthesis, properties and applications of hexaferrite ceramics. Prog Mater Sci 2012;57:1191–334. https://doi.org/10.1016/j.pmatsci.2012.04.001.

[71] Reddy DHK, Yun YS. Spinel ferrite magnetic adsorbents: Alternative future materials for water purification? Coord Chem Rev 2016;315:90–111. https://doi.org/10.1016/j.ccr.2016.01.012.

[72] Burdett JK, Price SL, Price GD. Role of the crystal-field theory in determining the structures of spinels. J Am Chem Soc 1982;104:92–5. https://doi.org/10.1021/ja00365a019.

[73] Zhao Q, Yan Z, Chen C, Chen J. Spinels: Controlled preparation, oxygen reduction/evolution reaction application, and beyond. Chem Rev 2017;117: 10121–211. https://doi.org/10.1021/acs.chemrev.7b00051.

[74] Wei C, Feng Z, Baisariyev M, Yu L, Zeng Li, Wu T, et al. Valence change ability and geometrical occupation of substitution cations determine the pseudocapacitance of spinel ferrite XFe$_2$O$_4$(X = Mn Co, Ni, Fe). Chem Mater 2016;28(12):4129–33.

[75] Miessler GL, Fisher PJ, Tarr DA. Inorganic Chemistry. 5th ed. Boston: Pearson Education, Inc.; 2014.

[76] Lee SH, Sullivan I, Larson DM, Liu G, Toma FM, Xiang C, et al. Correlating oxidation state and surface area to activity from operando studies of copper CO electroreduction catalysts in a gas-fed device. ACS Catal 2020;10(14):8000–11.

[77] Harris DC. Quantitative Chemical Analysis. 9th ed. New York: W. H. Freeman and Company; 2016.

[78] Li W, Liu J, Zhao D. Mesoporous materials for energy conversion and storage devices. Nat Rev Mater 2016;1:16023. https://doi.org/10.1038/natrevmats.2016.23.

[79] Peng X, Peng L, Wu C, Xie Y. Two dimensional nanomaterials for flexible supercapacitors. Chem Soc Rev 2014;43:3303–23. https://doi.org/10.1039/c3cs60407a.

[80] Lin T, Yu L, Sun M, Cheng G, Lan B, Fu Z. Mesoporous α-MnO$_2$ microspheres with high specific surface area: Controlled synthesis and catalytic activities. Chem Eng J 2016;286:114–21. https://doi.org/10.1016/j.cej.2015.09.024.

[81] Binitha G, Soumya MS, Madhavan AA, Praveen P, Balakrishnan A, Subramanian KRV, et al. Electrospun α-Fe$_2$O$_3$ nanostructures for supercapacitor applications. J Mater Chem A 2013;1(38):11698.

[82] Li GJ, Zhang XH, Kawi S. Relationships between sensitivity, catalytic activity, and surface areas of SnO$_2$ gas sensors. Sensors Actuators B: Chem 1999;60: 64–70. https://doi.org/10.1016/S0925-4005(99)00245-2.

[83] Chan D, Tischer S, Heck J, Diehm C, Deutschmann O. Correlation between catalytic activity and catalytic surface area of a Pt/Al$_2$O$_3$ DOC: An experimental and microkinetic modeling study. Appl Catal B: Environ 2014;156–157:153–65. https://doi.org/10.1016/j.apcatb.2014.03.009.

[84] Shi S, Xu C, Yang C, Chen Y, Liu J, Kang F. Flexible asymmetric supercapacitors based on ultrathin two-dimensional nanosheets with outstanding electrochemical performance and aesthetic property. Sci Rep 2013;3:2598. https://doi.org/10.1038/srep02598.

[85] Dhanda R, Kidwai M. Magnetically separable CuFe$_2$O$_4$/reduced graphene oxide nanocomposites: as a highly active catalyst for solvent free oxidative coupling of amines to imines. RSC Adv 2016;6:53430–7. https://doi.org/10.1039/c6ra08868f.

[86] Aksoy M, Yanalak G, Aslan E, Patır İH, Metin Ö. Visible light-driven hydrogen evolution by using mesoporous carbon nitride-metal ferrite (MFe$_2$O$_4$/mpg-CN; M: Mn, Fe, Co and Ni) nanocomposites as catalysts. Int J Hydrogen Energy 2020;45(33):16509–18.

[87] Tan P, Li G, Fang R, Chen L, Luque R, Li Y, et al. Controlled growth of monodisperse ferrite octahedral nanocrystals for biomass-derived catalytic applications. ACS Catal 2017;7:2948–55. https://doi.org/10.1021/acscatal.6b02853.

[88] Dhiman M, Goyal A, Kumar V, Singhal S. Designing different morphologies of NiFe$_2$O$_4$ for tuning of structural, optical and magnetic properties for catalytic advancements. New J Chem 2016;40:10418–31. https://doi.org/10.1039/C6NJ03209E.

[89] Shan A, Wu X, Lu J, Chen C, Wang R. Phase formations and magnetic properties of single crystal nickel ferrite (NiFe$_2$O$_4$) with different morphologies. CrystEngComm 2015;17:1603–8. https://doi.org/10.1039/c4ce02139h.

[90] Song K, Yang R, Wang X, Zhang B, Wang J, Chen X. Solvent ratio controlled synthesis of CoFe$_2$O$_4$ hollow skeleton nanobox electrode for high-performance supercapacitor. Appl Surf Sci 2020;533:147433. https://doi.org/10.1016/j.apsusc.2020.147433.

[91] Bandgar SB, Vadiyar MM, Suryawanshi UP, Jambhale CL, Kim JH, Kolekar SS. Rotational reflux chemistry approach derived flat holey CuFe$_2$O$_4$ nanosheets for supercapacitors application. Mater Lett 2020;279:128514. https://doi.org/10.1016/j.matlet.2020.128514.

[92] Yang C, Shi M, Nuli Y, Song X, Zhao L, Liu J, et al. Interfacial electrochemical investigation of 3D space-confined MnFe$_2$O$_4$ for high-performance ionic liquid-based supercapacitors. Electrochim Acta 2020;331:135386.

[93] Reddy AE, Anitha T, Muralee Gopi VVC, Rao SS, Naresh B, Kim H-J. Construction of novel nanocomposite ZnO@CoFe$_2$O$_4$ microspheres grown on nickel foam for high performance electrochemical supercapacitors. Anal Methods 2018;10:223–9. https://doi.org/10.1039/c7ay02176c.

[94] Niu S, Li S, Hu J, Li Y, Du Y, Han X, et al. Fabrication of uniform Ru-doped NiFe$_2$O$_4$ nanosheets as an efficient hydrogen evolution electrocatalyst. Chem Commun 2019;55(97):14649–52.

[95] Zhang Z, Li W, Zou R, Kang W, San Chui Y, Yuen MF, et al. Layer-stacked cobalt ferrite (CoFe$_2$O$_4$) mesoporous platelets for high-performance lithium ion battery anodes. J Mater Chem A 2015;3(13):6990–7.

[96] Ma R, Liu Z, Takada K, Iyi N, Bando Y. Synthesis and Exfoliation of Co^{2+} - Fe^{3+} layered double hydroxides: An innovative topochemical approach. J Am Chem Soc 2007;129:5257–63. https://doi.org/10.1021/ja0693035.

[97] Chen Q, Wang R, Lu F, Kuang X, Tong Y, Lu X. Boosting the oxygen evolution reaction activity of NiFe$_2$O$_4$ nanosheets by phosphate ion functionalization. ACS Omega 2019;4:3493–9. https://doi.org/10.1021/acsomega.8b03081.

[98] Song XZ, Meng YL, Chen X, Sun KM, Wang XF. Hollow NiFe$_2$O$_4$ hexagonal biyramids for high-performance n-propanol sensing at low temperature. New J Chem 2018;42:14071–4. https://doi.org/10.1039/c8nj02438c.

[99] Jiang ZJ, Cheng S, Rong H, Jiang Z, Huang J. General synthesis of MFe2O4/carbon (M = Zn, Mn Co, Ni) spindles from mixed metal organic frameworks as high performance anodes for lithium ion batteries. J Mater Chem A 2017;5:23641–50. https://doi.org/10.1039/c7ta07097g.

[100] Zhang X, Qin W, Li D, Yan D, Hu B, Sun Z, et al. Metal-organic framework derived porous CuO/Cu$_2$O composite hollow octahedrons as high performance anode materials for sodium ion batteries. Chem Commun 2015;51(91):16413–6.

[101] Yang H, Kruger PE, Telfer SG. Metal-organic framework nanocrystals as sacrificial templates for hollow and exceptionally porous titania and composite materials. Inorg Chem 2015;54:9483–90. https://doi.org/10.1021/acs.inorgchem.5b01352.

[102] Liu D, Wan J, Pang G, Tang Z. Hollow metal–organic-framework micro/nanostructures and their derivatives: Emerging multifunctional materials. Adv Mater 2019;31:1803291. https://doi.org/10.1002/adma.201803291.

[103] Cai Z-X, Wang ZL, Kim J, Yamauchi Y. Hollow functional materials derived from metal–organic frameworks: Synthetic strategies, conversion mechanisms, and electrochemical applications. Adv Mater 2019;31:1804903. https://doi.org/10.1002/adma.201804903.

[104] Wang X, Feng J, Bai Y, Zhang Q, Yin Y. Synthesis, properties, and applications of hollow micro-/nanostructures. Chem Rev 2016;116:10983–1060. https://doi.org/10.1021/acs.chemrev.5b00731.

[105] Zhang G, Yu Le, Wu HB, Hoster HE, Lou XWD. Formation of ZnMn$_2$O$_4$ ball-in-ball hollow microspheres as a high-performance anode for lithium-ion batteries. Adv Mater 2012;24(34):4609–13.

[106] Zhao J, Yipu Liu A, Fan M, Yuan L, Zou X. From solid-state metal alkoxides to nanostructured oxides: a precursor-directed synthetic route to functional inorganic nanomaterials. Inorg Chem Front 2015;2:198–212. https://doi.org/10.1039/C4QI00191E.

[107] Takatoshi Matsumoto KT, Kitagishi K, Shinoda K, Huaman JLC, Piquemal JY, Jeyadeva B. Dissolution and reduction of cobalt ions in polyol process using ethylene glycol: Identification of the active species and its role. New J Chem 2015;39:5008–18. https://doi.org/10.1039/C5NJ00669D.

[108] Taylor AK, Andreu I, Louie M, Gates BD. Electrochemically aged Ni electrodes supporting NiFe$_2$O$_4$ nanoparticles for the oxygen evolution reaction. ACS Appl Energy Mater 2020;3:387–400. https://doi.org/10.1021/acsaem.9b01644.

[109] Perron H, Mellier T, Domain C, Roques J, Simoni E, Drot R, et al. Structural investigation and electronic properties of the nickel ferrite NiFe$_2$O$_4$: a periodic density functional theory approach. J Phys Condens Matter 2007;19(34):346219.

[110] Yan K, Lu Y, Jin W. Facile synthesis of mesoporous manganese-iron nanorod arrays efficient for water oxidation. ACS Sustain Chem Eng 2016;4:5398–403. https://doi.org/10.1021/acssuschemeng.6b00685.

[111] Wulfsberg G. Inorganic Chemistry. 1st ed. Sausalito: Science, University Books; 2000.

[112] Oh WD, Dong Z, Hu ZT, Lim TT. A novel quasi-cubic CuFe$_2$O$_4$-Fe$_2$O$_3$ catalyst prepared at low temperature for enhanced oxidation of bisphenol A via peroxymonosulfate activation. J Mater Chem A 2015;3:22208–17. https://doi.org/10.1039/c5ta06563a.

[113] Hong D, Yamada Y, Sheehan M, Shikano S, Kuo C-H, Tian M, et al. Mesoporous nickel ferrites with spinel structure prepared by an aerosol spray pyrolysis method for photocatalytic hydrogen evolution. ACS Sustain Chem Eng 2014;2(11):2588–94.

[114] Zhu M, Meng D, Wang C, Diao G. Facile fabrication of hierarchically porous CuFe$_2$O$_4$ nanospheres with enhanced capacitance property. ACS Appl Mater Interfaces 2013;5:6030–7. https://doi.org/10.1021/am4007353.

[115] Fan S, Wang W, Ke H, Zhou Y. Facile synthesis of morphology controllable CoFe$_2$O$_4$ particles as high-performance electrode materials. Part Part Syst Charact 2018;35:1800223. https://doi.org/10.1002/ppsc.201800223.

[116] Li Y, Guo K, Li J, Dong X, Yuan T, Li X, et al. Controllable synthesis of ordered mesoporous NiFe$_2$O$_4$ with tunable pore structure as a bifunctional catalyst for Li-O$_2$ batteries. ACS Appl Mater Interfaces 2014;6(23):20949–57.

[117] Yuan F, Cheng X, Wang M, Ni Y. Controlled synthesis of tubular ferrite MFe2O2 (M = Fe Co, Ni) microstructures with efficiently electrocatalytic activity for water splitting. Electrochim Acta 2019;324:134883. https://doi.org/10.1016/j.electacta.2019.134883.

[118] Li L, Lou Z, Han W, Shen G. Flexible in-plane microsupercapacitors with electrospun NiFe$_2$O$_4$ nanofibers for portable sensing applications. Nanoscale 2016;8:14986–91. https://doi.org/10.1039/c6nr04945a.

[119] Yang S, Qiu X, Jin P, Dzakpasu M, Wang XC, Zhang Q, et al. MOF-templated synthesis of CoFe$_2$O$_4$ nanocrystals and its coupling with peroxymonosulfate for degradation of bisphenol A. Chem Eng J 2018;353:329–39.

[120] De Medeiros F, Madigou V, Lopes-moriyama AL, Pereira de Souza C, Leroux C. Synthesis of CoFe$_2$O$_4$ nanocubes. Nano-Structures & Nano-Objects 2020;21 (100422). https://doi.org/10.1016/j.nanoso.2019.100422.

[121] Lu LT, Dung NT, Tung LD, Thanh CT, Quy OK, Chuc NV, et al. Synthesis of magnetic cobalt ferrite nanoparticles with controlled morphology, monodispersity and composition: the influence of solvent, surfactant, reductant and synthetic conditions. Nanoscale 2015;7(46):19596–610.

[122] Kumar Y, Sharma A, Shirage PM. Shape-controlled CoFe$_2$O$_4$ nanoparticles as an excellent material for humidity sensing. RSC Adv 2017;7:55778–85. https://doi.org/10.1039/C7RA11072C.

[123] Eom Y, Abbas M, Noh HY, Kim CG. Morphology-controlled synthesis of highly crystalline Fe$_3$O$_4$ and CoFe$_2$O$_4$ nanoparticles using a facile thermal decomposition method. RSC Adv 2016;6:15861–7. https://doi.org/10.1039/c5ra27649g.

[124] Zeng H, Rice PM, Wang SX, Sun S. Shape-controlled synthesis and shape-induced texture of MnFe$_2$O$_4$ nanoparticles. J Am Chem Soc 2004;126:11458–9. https://doi.org/10.1021/ja045911d.

[125] Bao N, Shen L, An W, Padhan P, Turner CH, Gupta A. Formation mechanism and shape control of monodisperse magnetic CoFe$_2$O$_4$ nanocrystals. Chem Mater 2009;21:3458–68. https://doi.org/10.1021/cm901033m.

[126] Cao X, Meng J, Meng Q, Dong H, Zhang J. Investigation of synthesis and magnetic property of rod-shaped NiFe$_2$O$_2$ via chemical precipitation-topotactic reaction employing needle-like γ-FeOOH and α-FeOOH as templates. Mater Lett 2018;228:356–9. https://doi.org/10.1016/j.matlet.2018.06.044.

[127] Rezaul Karim KM, Tarek M, Ong HR, Abdullah H, Yousuf A, Cheng CK, et al. Photoelectrocatalytic reduction of carbon dioxide to methanol using CuFe$_2$O$_4$ modified with graphene oxide under visible light irradiation. Ind Eng Chem Res 2019;58(2):563–72.

[128] Chen M, Xu Y. Trace Amount CoFe$_2$O$_4$ anchored on a TiO$_2$ photocatalyst efficiently catalyzing O$_2$ reduction and phenol oxidation. Langmuir 2019;35:9334–42. https://doi.org/10.1021/acs.langmuir.9b00291.

[129] Kong J, Li R, Wang F, Chen P, Liu H, Liu G, et al. Sulfate radical-induced transformation of trimethoprim with CuFe$_2$O$_4$/MWCNTs as a heterogeneous catalyst of peroxymonosulfate: mechanisms and reaction pathways. RSC Adv 2018;8(44):24787–95.

[130] Liang J, Wei Y, Zhang J, Yao Y, He G, Tang Bo, et al. Scalable green method to fabricate magnetically separable NiFe$_2$O$_4$-reduced graphene oxide nanocomposites with enhanced photocatalytic performance driven by visible light. Ind Eng Chem Res 2018;57(12):4311–9.

[131] Zeynizadeh B, Rahmani S. Sulfonyl-bridged (copper-immobilized nickel ferrite) with activated montmorillonite, [(NiFe$_2$O$_4$@Cu)SO$_2$(MMT)]: a new class of magnetically separable clay nanocomposite systems towards Hantzsch synthesis of coumarin-based 1,4. RSC Adv 2019;9:8002–15. https://doi.org/10.1039/c9ra00177h.

[132] Yan F, Guo D, Zhang S, Li C, Zhu C, Zhang X, et al. An ultra-small NiFe$_2$O$_4$ hollow particle/graphene hybrid: Fabrication and electromagnetic wave absorption property. Nanoscale 2018;10(6):2697–703.

[133] Xiong P, Huang H, Wang X. Design and synthesis of ternary cobalt ferrite/graphene/polyaniline hierarchical nanocomposites for high-performance supercapacitors. J Power Sources 2014;245:937–46. https://doi.org/10.1016/j.jpowsour.2013.07.064.

[134] Song Q, Zhang ZJ. Controlled synthesis and magnetic properties of bimagnetic spinel ferrite CoFe$_2$O$_4$ and MnFe$_2$O$_4$ nanocrystals with core−shell architecture. J Am Chem Soc 2012;134:10182–90. https://doi.org/10.1021/ja302856z.

[135] Song Q, Zhang ZJ. Shape control and associated magnetic properties of spinel cobalt ferrite nanocrystals. J Am Chem Soc 2004;126:6164–8. https://doi.org/10.1021/ja049931r.

[136] Yan F, Zhang S, Zhang X, Li C, Zhu C, Zhang X, et al. Growth of CoFe$_2$O$_4$ hollow nanoparticles on graphene sheets for high-performance electromagnetic wave absorbers. J Mater Chem C 2018;6(47):12781–7.

[137] Dong Y, Chui Y-S, Ma R, Cao C, Cheng H, Li YY, et al. One-pot scalable synthesis of Cu-CuFe$_2$O$_4$/graphene composites as anode materials for lithium-ion batteries with enhanced lithium storage properties. J Mater Chem A 2014;2(34):13892.

[138] Zhang Y, Cao W, Cai Y, Shu J, Cao M. Rational design of NiFe$_2$O$_4$-rGO by tuning the compositional chemistry and its enhanced performance for a Li-ion battery anode. Inorg Chem Front 2019;6:961–8. https://doi.org/10.1039/c9qi00055k.

[139] Song K, Wang X, Li J, Zhang B, Yang R, Liu P, et al. 3D hierarchical CoFe$_2$O$_4$/CoOOH nanowire arrays on Ni-sponge for high-performance flexible supercapacitors. Electrochim Acta 2020;340:135892.

[140] Pomerantseva E, Gogotsi Y. Two-dimensional heterostructures for energy storage. Nat Energy 2017;2:17089. https://doi.org/10.1038/nenergy.2017.89.

[141] Pomerantseva E, Bonaccorso F, Feng X, Cui Y, Gogotsi Y. Energy storage: The future enabled by nanomaterials. Science 2019;366:969. https://doi.org/10.1126/science.aan8285.

[142] Gallagher KJ, Ottaway MR. Action of ammonium fluoride solutions on "iron (III) hydroxide" gel. J Chem Soc Dalt Trans 1974:2347–50. https://doi.org/10.1039/DT9740002347.

[143] Soli AL, Byrne RH. The hydrolysis and fluoride complexation behavior of Fe(III) at 25 ~ and 0.68 molal ionic strength. J Solution Chem 1996;25(773–85). https://doi.org/10.1007/BF00973784.

[144] Kumar R, Youssry SM, Ya KZ, Tan WK, Kawamura G, Matsuda A. Microwave-assisted synthesis of Mn$_3$O$_4$-Fe$_2$O$_3$/Fe$_3$O$_4$@rGO ternary hybrids and electrochemical performance for supercapacitor electrode. Diam Relat Mater 2020;101:107622. https://doi.org/10.1016/j.diamond.2019.107622.

[145] Yu Z, Chen L, Yu S. Growth of NiFe$_2$O$_4$ nanoparticles on carbon cloth for high performance flexible supercapacitors. J Mater Chem A 2014;2:10889–94. https://doi.org/10.1039/c4ta00492b.

[146] Li Z, Gadipelli S, Li H, Howard CA, Brett DJL, Shearing PR, et al. Tuning the interlayer spacing of graphene laminate films for efficient pore utilization towards compact capacitive energy storage. Nat Energy 2020;5(2):160–8.

[147] Dean JA. Langes's Handbook of Chemistry. 15th ed. New York: McGrawHill; 1999.

[148] Larcher D, Patrice R. Preparation of metallic powders and alloys in polyol media: A thermodynamic approach. J Solid State Chem 2000;154:405–11. https://doi.org/10.1006/jssc.2000.8802.

[149] Tudela D. Slater's rules and electron configurations. J Chem Educ 1993;70:956. https://doi.org/10.1021/ed070p956.

[150] Kazemi M. Based on MFe$_2$O$_4$ (M=Co, Cu, and Ni): Magnetically recoverable nanocatalysts in synthesis of heterocyclic structural scaffolds. Synth Commun 2020;50:1899–935. https://doi.org/10.1080/00397911.2020.1723109.

[151] Mondal B, Kundu M, Mandal SP, Saha R, Roy UK, Roychowdhury A, et al. Sonochemically synthesized spin-canted CuFe$_2$O$_4$ nanoparticles for heterogeneous green catalytic click chemistry. ACS Omega 2019;4(9):13845–52.

[152] Bonyasi R, Gholinejad M, Saadati F, Nájera C. Copper ferrite nanoparticle modified starch as a highly recoverable catalyst for room temperature click chemistry: Multicomponent synthesis of 1,2,3-triazoles in water. New J Chem 2018;42:3078–86. https://doi.org/10.1039/c7nj03284f.

[153] Amiri K, Rostami A, Rostami A. CuFe$_2$O$_4$ magnetic nanoparticle catalyzed odorless synthesis of sulfides using phenylboronic acid and aryl halides in the presence of S$_8$. New J Chem 2016;40:7522–8. https://doi.org/10.1039/c6nj01434h.

[154] Saha M, Pradhan K, Das AR. Facile and eco-friendly synthesis of chromeno[4,3-b]pyrrol-4(1H)-one derivatives applying magnetically recoverable nano crystalline CuFe$_2$O$_4$ involving a domino three-component reaction in aqueous media. RSC Adv 2016;6:55033–8. https://doi.org/10.1039/c6ra06979g.

[155] Pal G, Paul S, Das AR. A facile and efficient synthesis of functionalized 4-oxo-2-(phenylimino) thiazolidin-5-ylideneacetate derivatives via a CuFe$_2$O$_4$ magnetic nanoparticles catalyzed regioselective pathway. New J Chem 2014;38:2787–91. https://doi.org/10.1039/c3nj01608k.

[156] Zeng X, Gong C, Guo H, Xu H, Zhang J, Xie J. Efficient heterogeneous hydroboration of alkynes: enhancing the catalytic activity by Cu(0) incorporated CuFe$_2$O$_4$ nanoparticles. New J Chem 2018;42:17346–50. https://doi.org/10.1039/c8nj03708f.

[157] Lakshminarayana B, Chakraborty J, Satyanarayana G, Subrahmanyam C. Recyclable Pd/CuFe$_2$O$_4$ nanowires: A highly active catalyst for C-C couplings and synthesis of benzofuran derivatives. RSC Adv 2018;8:21030–9. https://doi.org/10.1039/c8ra03697g.

[158] Wang ZL. Magnetically separable CuFe$_2$O$_4$ nanoparticles as a recoverable catalyst for the addition reaction of C(sp^3)-H bond of azaarenes to aldehydes. RSC Adv 2015;5:5563–6. https://doi.org/10.1039/c4ra14486d.

[159] Yavari I, Naeimabadi M. Synthesis of 3-(quinolin-2-yl)indolizines through iodine-mediated sp^{3}C–H functionalization of azaarenes. Synth Commun 2018;48:632–7. https://doi.org/10.1080/00397911.2017.1362436.

[160] Gao X, Zhang F, Deng G, Yang L. Brønsted acid catalyzed benzylic C-H bond functionalization of azaarenes: Nucleophilic addition to nitroso compounds. Org Lett 2014;16:3664–7. https://doi.org/10.1021/ol501422k.

[161] Das J, Vellakkaran M, Sk M, Banerjee D. Iron-catalyzed coupling of methyl N-heteroarenes with primary alcohols: Direct access to E-selective olefins. Org Lett 2019;21:7514–8. https://doi.org/10.1021/acs.orglett.9b02793.

[162] Qian Bo, Guo S, Shao J, Zhu Q, Yang L, Xia C, et al. Palladium-catalyzed benzylic addition of 2-methyl azaarenes to N-sulfonyl aldimines via C-H bond activation. J Am Chem Soc 2010;132(11):3650–1.

[163] Chutia R, Chetia B. Biogenic CuFe$_2$O$_4$ magnetic nanoparticles as a green, reusable and excellent nanocatalyst for acetylation reactions under solvent-free conditions. New J Chem 2018;42:15200–6. https://doi.org/10.1039/c8nj02685h.

[164] Nguyen OTK, Ha PT, Dang Ha V, Vo YH, Nguyen TT, Le NTH, et al. Superparamagnetic nanoparticle-catalyzed coupling of 2-amino pyridines/pyrimidines with trans-chalcones. RSC Adv 2019;9(10):5501–11.

[165] Zhu X, Yang D, Wei W, Jiang M, Li L, Zhu X, et al. Magnetic copper ferrite nanoparticles/TEMPO catalyzed selective oxidation of activated alcohols to aldehydes under ligand- and base-free conditions in water. RSC Adv 2014;4(110):64930–5.

[166] Ahammed S, Kundu D, Ranu BC. Cu-catalyzed Fe-driven C$_{sp}$−C$_{sp}$ and C$_{sp}$−C$_{sp2}$ cross-coupling: An access to 1,3-diynes and 1,3-enynes. J Org Chem 2014;79:7391–8. https://doi.org/10.1021/jo5011069.

[167] Maleki A, Hajizadeh Z, Salehi P. Mesoporous halloysite nanotubes modified by CuFe$_2$O$_4$ spinel ferrite nanoparticles and study of its application as a novel and efficient heterogeneous catalyst in the synthesis of pyrazolopyridine derivatives. Sci Rep 2019;9:5552 |. https://doi.org/10.1038/s41598-019-42126-9.

[168] Amini M, Kafshdouzsani MH, Akbari A, Gautam S, Shim C-H, Chae KH. Spinel copper ferrite nanoparticles: Preparation, characterization and catalytic activity. Appl Organomet Chem 2018;32:1–8. https://doi.org/10.1002/aoc.4470.

[169] Meldal M, Tornøe CW. Cu-catalyzed azide-alkyne cycloaddition. Chem Rev 2008;108:2952–3015. https://doi.org/10.1021/cr0783479.

[170] Worrell BT, Malik JA, Fokin VV. Direct evidence of a dinuclear copper intermediate in Cu(I)-catalyzed azide-alkyne cycloadditions. Science 2014;340:457–60. https://doi.org/10.1126/science.1229506.

[171] Feng Y, Lu C, Wang H, Meng M, Zhang Y, Rao D, et al. Spinel copper–iron-oxide magnetic nanoparticles with cooperative Cu(I) and Cu(II) sites for enhancing the catalytic transformation of 1,2-propanediol to lactic acid under anaerobic conditions. Catal Sci Technol 2020;10:8094–107. https://doi.org/10.1039/d0cy01733g.

[172] He Y, Mao J, Rong G, Yan H, Zhang G. Ligand-free, Cu- and Fe-catalyzed selective ring-opening arylations of benzoxazoles with aryl iodides. Chem - An Asian J 2016;11:1672–6. https://doi.org/10.1002/asia.201600252.

[173] Toxicological profile for cyanide. ATSDR Agency Toxic Subst Dis Regist 2006. https://www.atsdr.cdc.gov/toxprofiles/tp.asp?id=72&tid=19 [accessed: 2022-05-01].

[174] Yao L, Zhou Q, Han W, Wei S. Copper powder catalyzed direct ring-opening arylation of benzazoles with aryl iodides in polyethylene glycol. European J Org Chem 2012;2012:6856–60. https://doi.org/10.1002/ejoc.201201166.

[175] Beletskaya IP, Ananikov VP. Transition-metal-catalyzed C-S, C-Se, and C-Te bond formation via cross-coupling and atom-economic addition reactions. Chem Rev 2011;111:1596–636. https://doi.org/10.1021/cr100347k.

[176] Panova YS, Kashin AS, Vorobev MG, Degtyareva ES, Ananikov VP. Nature of the copper-oxide-mediated C-S cross-coupling reaction: Leaching of catalytically active species from the metal oxide surface. ACS Catal 2016;6:3637–43. https://doi.org/10.1021/acscatal.6b00337.

[177] Rout L, Sen TK, Punniyamurthy T. Efficient CuO-nanoparticle-catalyzed C-S cross-coupling of thiols with iodobenzene. Angew Chemie - Int Ed 2007;46:5583–6. https://doi.org/10.1002/anie.200701282.

[178] Yang D, Zhu X, Wei W, Sun N, Yuan Li, Jiang M, et al. Magnetically recoverable and reusable CuFe₂O₄ nanoparticle-catalyzed synthesis of benzoxazoles, benzothiazoles and benzimidazoles using dioxygen as oxidant. RSC Adv 2014;4(34):17832–9.

[179] Payra S, Saha A, Banerjee S. On-water magnetic NiFe₂O₄ nanoparticle-catalyzed Michael additions of active methylene compounds, aromatic/aliphatic amines, alcohols and thiols to conjugated alkenes. RSC Adv 2016;6:95951–6. https://doi.org/10.1039/c6ra21160g.

[180] Gupta R, Gupta R, Paul S, Loupy A. Covalently anchored sulfonic acid on silica gel as an efficient and reusable heterogeneous catalyst for the one-pot synthesis of Hantzsch 1,4-dihydropyridines under solvent-free conditions. Synthesis (Stuttg) 2007;18:2835–8. https://doi.org/10.1055/s-2007-983839.

[181] Corro G, Flores JA, Pacheco-Aguirre F, Pal U, Bañuelos F, Torralba F, et al. Effect of the electronic state of Cu, Ag, and Au on diesel soot abatement: performance of Cu/ZnO, Ag/ZnO, and Au/ZnO catalysts. ACS Omega 2019;4(3):5795–804.

[182] Corro G, Vidal E, Cebada S, Pal U, Bañuelos F, Vargas D, et al. Electronic state of silver in Ag/SiO₂ and Ag/ZnO catalysts and its effect on diesel particulate matter oxidation: An XPS study. Appl Catal B: Environ 2017;216:1–10.

[183] Torralba R, Corro G, Rosales F, Bañuelos F, Pal U, Olivares-xometl O, et al. Total oxidation of methane over sulfur poisoning resistant Pt/ZrO₁₂ catalyst: Effect of - Pt²⁺–Pt⁴⁺ and - Pt²⁺–Zr⁴⁺ dipoles at metal - support interface. Catal Letters 2021;151:1592–603. https://doi.org/10.1007/s10562-020-03411-9.

[184] Hussain S, Hussain S, Waleed A, Tavakoli MM, Wang Z, Yang S, et al. Fabrication of CuFe₂O₄/α-Fe₂O₃ composite thin films on FTO coated glass and 3-D nanospike structures for efficient photoelectrochemical water splitting. ACS Appl Mater Interfaces 2016;8(51):35315–22.

[185] Landon J, Demeter E, İnoğlu N, Keturakis C, Wachs IE, Vasić R, et al. Spectroscopic characterization of mixed Fe-Ni oxide electrocatalysts for the oxygen evolution reaction in alkaline electrolytes. ACS Catal 2012;2(8):1793–801.

[186] Liu J, Yuan H, Wang Z, Li J, Yang M, Cao L, et al. Self-supported nickel iron oxide nanospindles with high hydrophilicity for efficient oxygen evolution. Chem Commun 2019;55(73):10860–3.

[187] Wan Q, Li P, Shan J, Zhai F, Li Z, Qu X. Superior catalytic effect of nickel ferrite nanoparticles in improving hydrogen storage properties of MgH₂. J Phys Chem C 2015;119:2925–34. https://doi.org/10.1021/jp508528k.

[188] Liu Y, Gao P, Cherkasov N, Rebrov EV. Direct amide synthesis over core-shell TiO₂@NiFe₂O₄ catalysts in a continuous flow radiofrequency-heated reactor. RSC Adv 2016;6:100997–1007. https://doi.org/10.1039/c6ra22659k.

[189] Huang J, Fu Y, Li S, Kong W, Zhang J, Sun Y. Cobalt-based ferrites as efficient redox materials for thermochemical two-step CO₂-splitting: enhanced performance due to cation diffusion. Sustain Energy Fuels 2019;3:975–84. https://doi.org/10.1039/c8se00611c.

[190] Tong J, Bo L, Cai X, Wang H, Zhang Q, Su L. Aerobic oxidation of cyclohexane effectively catalyzed by simply synthesized silica-supported cobalt ferrite magnetic nanocrystal. Ind Eng Chem Res 2014;53:10294–300. https://doi.org/10.1021/ie5008213.

[191] Yu X-J, Qu J, Yuan Z, Min P, Hao S-M, Zhu Z-S, et al. Anisotropic CoFe₂O₄@graphene hybrid aerogels with high flux and excellent stability as building blocks for rapid catalytic degradation of organic contaminants in a flow-type setup. ACS Appl Mater Interfaces 2019;11(37):34222–31.

[192] Mekonnen A, Carlson R. Lewis acid catalyzed conjugate addition and the formation of heterocycles using Michael acceptors under solvent-free conditions. European J Org Chem 2006;2006:2005–13. https://doi.org/10.1002/ejoc.200500923.

[193] Moghaddam FM, Foroushani BK, Rezvani HR. Nickel ferrite nanoparticles: An efficient and reusable nanocatalyst for a neat, one-pot and four-component synthesis of pyrroles. RSC Adv 2015;5:18092–6. https://doi.org/10.1039/c4ra09348h.

[194] Rajput JK, Kaur G. Synthesis and applications of CoFe₂O₄ nanoparticles for multicomponent reactions. Catal Sci Technol 2014;4:142–51. https://doi.org/10.1039/c3cy00594a.

[195] Lai H, Zhang Z, Gu F, Yi Z, Zhong Z, Su F. One-pot catalytic conversion of methanol to C6–C21 hydrocarbons over bi-functional MFe₂O₄ (M = Ni, Zn, Mn, Co) catalysts. RSC Adv 2015;5:13374–84. https://doi.org/10.1039/c4ra14509g.

[196] Gawade AB, Nakhate AV, Yadav GD. Selective synthesis of 2,5-furandicarboxylic acid by oxidation of 5- hydroxymethylfurfural over MnFe₂O₄ catalyst. Catal Today 2018;309:119–25. https://doi.org/10.1016/j.cattod.2017.08.061.

[197] Ghahremanzadeh R, Rashid Z, Zarnani AH, Naeimi H. Synthesis of novel spirooxindoles in water by using MnFe₂O₄ nanoparticles as an efficient magnetically recoverable and reusable catalyst. Appl Catal A-General 2013;467:270–8. https://doi.org/10.1016/j.apcata.2013.07.029.

[198] Brahmachari G, Laskar S, Barik P. Magnetically separable MnFe₂O₄ nano-material: an efficient and reusable heterogeneous catalyst for the synthesis of 2-substituted benzimidazoles and the extended synthesis of quinoxalines at room temperature under aerobic conditions. RSC Adv 2013;3:14245–53. https://doi.org/10.1039/c3ra41457d.

[199] Xue D, Long Y. Metal-free TEMPO-promoted C(sp³)−H amination to afford multisubstituted benzimidazoles. J Org Chem 2014;79:4727–34. https://doi.org/10.1021/jo5005179.

[200] Jiang K, Luo M, Peng M, Yu Y, Lu Y-R, Chan T-S, et al. Dynamic active-site generation of atomic iridium stabilized on nanoporous metal phosphides for water oxidation. Nat Commun 2020;11(1). https://doi.org/10.1038/s41467-020-16558-1.

[201] Eftekhari A. Tuning the electrocatalysts for oxygen evolution reaction. Mater Today Energy 2017;5:37–57. https://doi.org/10.1016/j.mtener.2017.05.002.

[202] Dhanalaxmi K, Yadav R, Kumar S, Amoli V, Sinha AK, Reddy BM. Designed architecture of porous organic polymer wrapped MnFe₂O₄ nanocrystals: A novel water splitting photocatalyst. Chem A Eurpean J 2016;22:15639–44. https://doi.org/10.1002/chem.201603419.

[203] Kim JS, Kim B, Kim H, Kang K. Recent progress on multimetal oxide catalysts for the oxygen evolution reaction. Adv Energy Mater 2018;8:1702774. https://doi.org/10.1002/aenm.201702774.

[204] Han L, Dong S, Wang E. Transition-metal (Co, Ni, and Fe)-based electrocatalysts for the water oxidation reaction. Adv Mater 2016;28:9266–91. https://doi.org/10.1002/adma.201602270.

[205] Zhang W, Cui L, Liu J. Recent advances in cobalt-based electrocatalysts for hydrogen and oxygen evolution reactions. J Alloys Compd 2020;821:153542. https://doi.org/10.1016/j.jallcom.2019.153542.

[206] Xue BW, Zhang CH, Wang YZ, Xie WW, Li NW, Yu L. Recent progress of Ni-Fe layered double hydroxide and beyond towards electrochemical water splitting. Nanoscale Adv 2020;2:5555–66. https://doi.org/10.1039/d0na00727g.

[207] Suen NT, Hung SF, Quan Q, Zhang N, Xu YJ, Chen HM. Electrocatalysis for the oxygen evolution reaction: Recent development and future perspectives. Chem Soc Rev 2017;46:337–65. https://doi.org/10.1039/c6cs00328a.

[208] Qiao J, Song F, Du Han, Yuan J, Shen J, et al. Mesoporous spinel NiFe oxide cubes as advanced electrocatalysts for oxygen evolution. Int J Hydrogen Energy 2019;44(31):16368–77.

[209] Li M, Xiong Y, Liu X, Bo X, Zhang Y, Han Ce, et al. Facile synthesis of electrospun MFe₂O₄ (M = Co, Ni, Cu, Mn) spinel nanofibers with excellent electro-catalytic properties for oxygen evolution and hydrogen peroxide reduction. Nanoscale 2015;7(19):8920–30.

[210] Yang H, Han X, Douka AI, Huang L, Gong L, Xia C, et al. Advanced oxygen electrocatalysis in energy conversion and storage. Adv Funtional Mater 2021;31(12): 2007602.

[211] Zeng J, Song T, Lv M, Wang T, Qin J, Zeng H. Plasmonic photocatalyst Au/g-C₃N₄/NiFe₂O₄ nanocomposites for enhanced visible-light-driven photocatalytic hydrogen evolution. RSC Adv 2016;6:54964–75. https://doi.org/10.1039/c6ra08356k.

[212] Liu Y, Li J, Li F, Li W, Yang H, Zhang X, et al. A facile preparation of CoFe₂O₄ nanoparticles on polyaniline-functionalised carbon nanotubes as enhanced catalysts for the oxygen evolution reaction. J Mater Chem A 2016;4(12):4472–8.

[213] Li M, Lu M, Yang J, Xiao J, Han L, Zhang Y, et al. Facile design of ultrafine CuFe₂O₄ nanocrystallines coupled porous carbon nanowires: Highly effective electrocatalysts for hydrogen peroxide reduction and the oxygen evolution reaction. J Alloy Compd 2019;809:151766.

[214] Wang YZ, Yang M, Ding YM, Li NW, Yu L. Recent advances in complex hollow electrocatalysts for water splitting. Adv Funct Mater 2022;32:2108681. https://doi.org/10.1002/adfm.202108681.

[215] Yang M, Zhang CH, Li NW, Luan D, Yu L, Lou XW. Design and synthesis of hollow nanostructures for electrochemical water splitting. Adv Sci 2022;9:2105135. https://doi.org/10.1002/advs.20210513.

[216] Feng C, Faheem MB, Fu J, Xiao Y, Li C, Li Y. Fe-based electrocatalysts for oxygen evolution reaction: Progress and perspectives. ACS Catal 2020;10:4019–47. https://doi.org/10.1021/acscatal.9b05445.

[217] Vij V, Sultan S, Harzandi AM, Meena A, Tiwari JN, Lee W-G, et al. Nickel-based electrocatalysts for energy-related applications: Oxygen reduction, oxygen evolution, and hydrogen evolution reactions. ACS Catal 2017;7(10):7196–225.

[218] Trotochaud L, Young SL, Ranney JK, Boettcher SW. Nickel-iron oxyhydroxide oxygen-evolution electrocatalysts: The role of intentional and incidental iron incorporation. J Am Chem Soc 2014;136:6744–53. https://doi.org/10.1021/ja502379c.

[219] Zhu S, Lei J, Qin Y, Zhang L, Lu L. Spinel oxide CoFe₂O₄ grown on Ni foam as an efficient electrocatalyst for oxygen evolution reaction. RSC Adv 2019;9: 13269–74. https://doi.org/10.1039/c9ra01802f.

[220] Zhang Z, Zhang J, Wang T, Li Z, Yang G, Bian H, et al. Durable oxygen evolution reaction of one dimensional spinel CoFe₂O₄ nanofibers fabricated by electrospinning. RSC Adv 2018;8(10):5338–43.

[221] Hong D, Yamada Y, Nagatomi T, Takai Y, Fukuzumi S. Catalysis of nickel ferrite for photocatalytic water oxidation using [Ru(bpy)₂]²⁺ and S₂O₈²⁻. J Am Chem Soc 2012;134:19572–5. https://doi.org/10.1021/ja309771h.

[222] Chandrasekaran S, Bowen C, Zhang P, Li Z, Yuan Q, Ren X, et al. Spinel photocatalysts for environmental remediation, hydrogen generation, CO₂ reduction and photoelectrochemical water splitting. J Mater Chem A 2018;6(24):11078–104.

[223] Soto-arreola A, Huerta-flores AM, Mora-Hernández JM, Torres-martínez LM. Comparative study of the photocatalytic activity for hydrogen evolution of MFe₂O₄ (M = Cu, Ni) prepared by three different methods. Journal Photochem Photobiol A: Chem 2018;357:20–9. https://doi.org/10.1016/j.jphotochem.2018.02.016.

[224] Soto-arreola A, Huerta-flores AM, Mora-Hernández JM, Torres-martínez LM. Improved photocatalytic activity for water splitting over MFe₂O₄–ZnO (M = Cu and Ni) type-ll heterostructures. Journal Photochem Photobiol A: Chem 2018;364:433–42. https://doi.org/10.1016/j.jphotochem.2018.06.033.

[225] Wang A, Yang H, Song T, Sun Q, Liu H, Wang T, et al. Plasmon mediated Fe-O in octahedral site of cuprospinel by Cu NPs for photocatalytic hydrogen evolution. Nanoscale 2017;9:15760–5. https://doi.org/10.1039/C7NR06217F.

[226] Cheng R, Fan X, Wang M, Li M, Tian J, Zhang L. Facile construction of CuFe₂O₄/g-C₃N₄ photocatalyst for enhanced visible-light hydrogen evolution. RSC Adv 2016;6:18990–5. https://doi.org/10.1039/C5RA27221A.

[227] Das S, Patnaik S, Parida K. Dynamic charge transfer through Fermi level equilibration in the p-CuFe₂O₄/n-NiAl LDH interface towards photocatalytic application. Catal Sci Technol 2020;10:6285–98. https://doi.org/10.1039/d0cy00980f.

[228] Liu Y, Niu Z, Lu Y, Zhang L, Yan K. Facile synthesis of CuFe₂O₂ crystals efficient for water oxidation and H₂O₂ reduction. J Alloys Compd 2017;735:654–9. https://doi.org/10.1016/j.jallcom.2017.11.181.

[229] Galindo R, Mazario E, Gutiérrez S, Morales MP, Herrasti P. Electrochemical synthesis of NiFe₂O₄ nanoparticles: Characterization and their catalytic applications. J Alloys Compd 2012;536S:S241–4. https://doi.org/10.1016/j.jallcom.2011.12.061.

[230] Mishra S, Kumar P, Samanta SK. Microwave catalytic degradation of antibiotic molecules by 2D sheets of spinel nickel ferrite. Ind Eng Chem Res 2020;59: 15839–47. https://doi.org/10.1021/acs.iecr.0c02352.

[231] He J, Yang S, Riisager A. Magnetic nickel ferrite nanoparticles as highly durable catalysts for catalytic transfer hydrogenation of bio-based aldehydes. Catal Sci Technol 2018;8:790–7. https://doi.org/10.1039/c7cy02197f.

[232] Ueda K, Ang CA, Ito Y, Ohyama J, Satsuma A. NiFe₂O₄ as an active component of a platinum group metal-free automotive three-way catalyst. Catal Sci Technol 2016;6:5797–800. https://doi.org/10.1039/c6cy00795c.

[233] Khalaf MM, Abd El-Lateef HM, Alnajjar AO, Mohamed IMA. A facile chemical synthesis of CuₓNi₍₁₋ₓ₎Fe₂O₄ nanoparticles as a nonprecious ferrite material for electrocatalytic oxidation of acetaldehyde. Sci Rep 2020;10:2761. https://doi.org/10.1038/s41598-020-59655-3.

[234] Agú UA, Mendieta SN, Gerbaldo MV, Crivello ME, Casuscelli SG. Highly active heterogeneous fenton-like system based on cobalt ferrite. Ind Eng Chem Res 2020;59:1702–11. https://doi.org/10.1021/acs.iecr.9b04042.

[235] Moura MN, Barrada RV, Almeida JR, Moreira TFM, Schettino MA, Freitas JCC, et al. Synthesis, characterization and photocatalytic properties of nanostructured CoFe₂O₄ recycled from spent Li-ion batteries. Chemosphere 2017;182:339–47.

[236] Carraro F, Vozniuk O, Calvillo L, Nodari L, La Fontaine C, Cavani F, et al. In operando XAS investigation of reduction and oxidation processes in cobalt and iron mixed spinels during the chemical loop reforming of ethanol. J Mater Chem A 2017;5(39):20808–17.

[237] Chuah G, Jaenicke S, Zhu Y, Liu S. Meerwein-Ponndorf-Verley reduction over heterogeneous catalysts. Curr Org Chem 2006;10:1639–54. https://doi.org/10.2174/138527206778249621.

[238] Ueda K, Ohyama J, Satsuma A. Investigation of reaction mechanism of NO-C₃H₆-CO-O₂ reaction over NiFe₂O₄ catalyst. ACS Omega 2017;2:3135–43. https://doi.org/10.1021/acsomega.7b00165.

[239] Sun W, Qiao K, Liu JY, Cao LM, Gong XQ, Yang J. Pt-doped NiFe₂O₄ spinel as a highly efficient catalyst for H₂ selective catalytic reduction of NO at room temperature. ACS Comb Sci 2016;18:195–202. https://doi.org/10.1021/acscombsci.5b00193.

[240] Chen L, Luo T, Yang S, Xu J, Liu Z, Wu F. Efficient metoprolol degradation by heterogeneous copper ferrite/sulfite reaction. Environ Chem Lett 2018;3:3–7. https://doi.org/10.1007/s10311-017-0696-1.

[241] Hariganesh S, Vadivel S, paul B, Kumaravel M, Balasubramanian N, Rajendran S, et al. Metal organic framework derived magnetically recoverable CuFe₂O₄ porous cubes for efficient photocatalytic application. Inorg Chem Commun 2021;125:108405.

[242] Dou R, Cheng H, Ma J, Komarneni S. Manganese doped magnetic cobalt ferrite nanoparticles for dye degradation via a novel heterogeneous chemical catalysis. Mater Chem Phys 2020;240:122181. https://doi.org/10.1016/j.matchemphys.2019.122181.

[243] Ortiz-Quiñonez J-L, Pal U, Salazar-Villanueva M. Structural, magnetic, and catalytic evaluation of spinel Co, Ni, and Co–Ni ferrite nanoparticles fabricated by low-temperature solution combustion process. ACS Omega 2018;3:14986–5001. https://doi.org/10.1021/acsomega.8b02229.

[244] Ortiz-Quiñonez J-L, Pal U. Borohydride-assisted surface activation of Co₃O₄/CoFe₂O₄ composite and its catalytic activity for 4-nitrophenol reduction. ACS Omega 2019;4:10129–39. https://doi.org/10.1021/acsomega.9b00118.

[245] Huang S, Xu Y, Liu Q, Zhou T, Zhao Y, Jing L, et al. Enhancing reactive oxygen species generation and photocatalytic performance via adding oxygen reduction reaction catalysts into the photocatalysts. Appl Catal B: Environ 2017;218:174–85.

[246] Bai S, Shen X, Zhong X, Liu Y, Zhu G, Xu X, et al. One-pot solvothermal preparation of magnetic reduced graphene oxide-ferrite hybrids for organic dye removal. Carbon 2012;50(6):2337–46.

[247] Furman OS, Teel AL, Watts RJ. Mechanism of base activation of persulfate. Environ Sci Technol 2010;44:6423–8. https://doi.org/10.1021/es1013714.

[248] White JL, Baruch MF, Pander JE, Hu Y, Fortmeyer IC, Park JE, et al. Light-driven heterogeneous reduction of carbon dioxide: Photocatalysts and photoelectrodes. Chem Rev 2015;115(23):12888–935.

[249] Guil-López R, Mota N, Llorente J, Millán E, Pawelec B, Fierro JLG, et al. Methanol synthesis from CO_2: A review of the latest developments in heterogeneous catalysis. Materials (Basel) 2019;12:3902. https://doi.org/10.3390/ma122333902.

[250] Li K, An X, Park KH, Khraisheh M, Tang J. A critical review of CO_2 photoconversion: Catalysts and reactors. Catal Today 2014;224:3–12. https://doi.org/10.1016/j.cattod.2013.12.006.

[251] Wu YA, McNulty I, Liu C, Lau KC, Liu Qi, Paulikas AP, et al. Facet-dependent active sites of a single Cu_2O particle photocatalyst for CO_2 reduction to methanol. Nat Energy 2019;4(11):957–68.

[252] Morris AJ, Meyer GJ, Fujita E. Molecular approaches to the photocatalytic reduction of carbon dioxide for solar fuels. Acc Chem Res 2009;42:1983–94. https://doi.org/10.1021/ar9001679.

[253] Long D, Li X, Yin Z, Fan S, Wang P, Xu F, et al. Novel Co_3O_4@$CoFe_2O_4$ double-shelled nanoboxes derived from Metal-Organic Framework for CO_2 reduction. J Alloy Compd 2021;854:156942.

[254] Uddin MR, Khan MR, Rahman MW, Yousuf A, Cheng CK. Photocatalytic reduction of CO_2 into methanol over $CuFe_2O_4$/TiO_2 under visible light irradiation. React Kinet Mech Catal 2015;116:589–604. https://doi.org/10.1007/s11144-015-0911-7.

[255] Rezaul Karim KM, Ong HR, Abdullah H, Yousuf A, Cheng CK, Rahman Khan MM. Photoelectrochemical reduction of carbon dioxide to methanol on p-type $CuFe_2O_4$ under visible light irradiation. Int J Hydrogen Energy 2018;43:18185–93. https://doi.org/10.1016/j.ijhydene.2018.07.174.

[256] Park RH, Pawara AU, Pal U, Zhang T, Kang YS. Enhanced solar photoreduction of CO_2 to liquid fuel over rGO grafted NiO-CeO_2 heterostructure nanocomposite. Nano Energy 2021;79:105483. https://doi.org/10.1016/j.nanoen.2020.105483.

[257] Yeh T, Cihlár J, Chang C, Cheng C, Teng H. Roles of graphene oxide in photocatalytic water splitting. Mater Today 2013;16:78–84. https://doi.org/10.1016/j.mattod.2013.03.006.

[258] Wu J, Huang Y, Ye W, Li Y. CO_2 Reduction: From the electrochemical to photochemical approach. Adv Sci 2017;4:1700194. https://doi.org/10.1002/advs.201700194.

[259] Liang L, Lei F, Gao S, Sun Y, Jiao X, Wu Ju, et al. Single unit cell bismuth tungstate layers realizing robust solar CO_2 reduction to methanol. Angew Chemie - Int Ed 2015;54(47):13971–4.

[260] Dimitrakis DA, Syrigou M, Lorentzoua S, Kostoglou M, Konstandopoulos AG. On kinetic modelling for solar redox thermochemical H_2O and CO_2 splitting over $NiFe_2O_4$ for H_2, CO and syngas production. Phys Chem Chem Phys 2017;19:26776–86. https://doi.org/10.1039/C7CP04002D.

[261] Takalkar G, Bhosale RR, Almomani F. Sol-gel synthesized $Ni_xFe_{3-x}O_4$ for thermochemical conversion of CO_2. Appl Surf Sci 2019;489:693–700. https://doi.org/10.1016/j.apsusc.2019.05.285.

[262] Chiang C, Lin K, Hsu P, Lin Y. Synthesis and characterization of magnetic zinc and manganese ferrite catalysts for decomposition of carbon dioxide into methane. Int J Hydrogen Energy 2017;42:22123–37. https://doi.org/10.1016/j.ijhydene.2017.06.033.

[263] Takalkar G, Bhosale RR, Almomani F, Khraisheh M. Thermocatalytic splitting of CO_2 using sol-gel synthesized Co-ferrite redox materials. Fuel 2019;257:115965. https://doi.org/10.1016/j.fuel.2019.115965.

[264] Qiu Yu, Ma Li, Zeng D, Li M, Cui D, Lv Y, et al. Efficient CO_2 to CO conversion at moderate temperatures enabled by the cobalt and copper co-doped ferrite oxygen carrier. J Energy Chem 2020;46:123–32.

[265] Goeppert A, Czaun M, Jones JP, Surya Prakash GK, Olah GA. Recycling of carbon dioxide to methanol and derived products-closing the loop. Chem Soc Rev 2014;43:7995–8048. https://doi.org/10.1039/c4cs00122b.

[266] Jiang X, Nie X, Guo X, Song C, Chen JG. Recent advances in carbon dioxide hydrogenation to methanol via heterogeneous catalysis. Chem Rev 2020;120:7984–8034. https://doi.org/10.1021/acs.chemrev.9b00723.

[267] LS ultracapacitor. http://lsmaterials.co.kr/ [accessed: 2022-05-01].

[268] Zhang LL, Zhao XS. Carbon-based materials as supercapacitor electrodes. Chem Soc Rev 2009;38:2520–31. https://doi.org/10.1039/b813846j.

[269] Panda PK, Grigoriev A, Mishra YK, Ahuja R. Progress in supercapacitors: Roles of two dimensional nanotubular materials. Nanoscale Adv 2020;2:70–108. https://doi.org/10.1039/c9na00307j.

[270] Simon P, Gogotsi Y. Materials for electrochemical capacitors. Nat Mater 2008;7:845–54. https://doi.org/10.1038/nmat2297.

[271] Bryan AM, Santino LM, Lu Y, Acharya S, Arcy JMD. Conducting polymers for pseudocapacitive energy storage. Chem Mater 2016;28:5989–98. https://doi.org/10.1021/acs.chemmater.6b01762.

[272] Liu Y, Yu F, Wang XW, Wen ZB, Zhu YS, Wu YP. Nanostructured oxides as cathode materials for supercapacitors. In: Kenneth I. Ozoemena SC, editor. Nanomaterials in Advanced Batteries and Supercapacitors. 1st ed., Switzerland: Springer; 2016. https://doi.org/10.1007/978-3-319-26082-2_7.

[273] Wu Z, Zhu Y, Ji X, Banks CE. Transition Metal Oxides as Supercapacitor Materials. In: Kenneth I. Ozoemena SC, editor. Nanomaterials in Advanced Batteries and Supercapacitors. 1st ed., Switzerland: 2016. https://doi.org/10.1007/978-3-319-26082-2_9.

[274] Zhang Y, Li L, Su H, Huang W, Dong X. Binary metal oxide: Advanced energy storage materials in supercapacitors. J Mater Chem A 2015;3:43–59. https://doi.org/10.1039/c4ta04996a.

[275] Saha S, Roy A, Ray A, Das T, Nandi M, Ghosh B, et al. Effect of particle morphology on the electrochemical performance of hydrothermally synthesized $NiMn_2O_4$. Electrochim Acta 2020;353:136515.

[276] Wang Z, Zhang X, Li Y, Liu Z, Hao Z. Synthesis of graphene-$NiFe_2O_4$ nanocomposites and their electrochemical capacitive behavior. J Mater Chem A 2013;1:6393–9. https://doi.org/10.1039/c3ta10433h.

[277] Senthilkumar B, Sankar KV, Sanjeeviraja C, Selvan RK. Synthesis and physico-chemical property evaluation of PANI – $NiFe_2O_4$ nanocomposite as electrodes for supercapacitors. J Alloys Compd 2013;553:350–7. https://doi.org/10.1016/j.jallcom.2012.11.122.

[278] Ishaq S, Moussa M, Kanwal F, Ehsan M, Saleem M, Van TN, et al. Facile synthesis of ternary graphene nanocomposites with doped metal oxide and conductive polymers as electrode materials for high performance supercapacitors. Sci Rep 2019;9:5974. https://doi.org/10.1038/s41598-019-41939-y.

[279] Moysiadou A, Lee S, Hsu CS, Chen HM, Hu X. Mechanism of oxygen evolution catalyzed by cobalt oxyhydroxide: Cobalt superoxide species as a key intermediate and dioxygen release as a rate-determining step. J Am Chem Soc 2020;142:11901–14. https://doi.org/10.1021/jacs.0c04867.

[280] Vignesh V, Subramani K, Sathish M, Navamathavan R. Electrochemical investigation of manganese ferrites prepared via a facile synthesis route for supercapacitor applications. Colloids Surfaces A 2018;538:668–77. https://doi.org/10.1016/j.colsurfa.2017.11.045.

[281] Xiong P, Hu C, Fan Y, Zhang W, Zhu J, Wang X. Ternary manganese ferrite/ graphene/polyaniline nanostructure with enhanced electrochemical capacitance performance. J Power Sources 2014;266:384–92. https://doi.org/10.1016/j.jpowsour.2014.05.048.

[282] Deng W, Ji X, Chen Q, Banks CE. Electrochemical capacitors utilising transition metal oxides: An update of recent developments. RSC Adv 2011;1:1171–8. https://doi.org/10.1039/c1ra00664a.

[283] Wu Z, Zhu Y, Ji X. $NiCo_2O_4$-based materials for electrochemical supercapacitors. J Mater Chem A 2014;2:14759–72. https://doi.org/10.1039/c4ta02390k.

[284] Liu Y, Zhang Y, Wu XW, Zhu YS, Wu YP. Features of design and fabrication of metal oxide–based supercapacitors. In: Dubal DP, Gomez-Romero P, editors. Metal Oxides in Supercapacitors. 1st ed.,. Amsterdam: Elsevier; 2017. https://doi.org/10.1016/B978-0-12-810464-4.00002-4.

[285] Largeot C, Portet C, Chmiola J, Taberna PL, Gogotsi Y, Simon P. Relation between the ion size and pore size for an electric double-layer capacitor. J Am Chem Soc 2008;130:2730–1. https://doi.org/10.1021/ja7106178.

[286] Agyemang FO, Kim H. Electrospun $ZnFe_2O_4$-based nanofiber composites with enhanced supercapacitive properties. Mater Sci Eng B 2016;211:141–8. https://doi.org/10.1016/j.mseb.2016.06.011.

[287] Wang Q, Gao H, Qin X, Dai J, Li W. Fabrication of $NiFe_2O_4$@$CoFe_2O_4$ core-shell nanofibers for high-performance supercapacitors. Mater Res Express 2020;7(1):015020.

[288] Choi HS, Park CR. Theoretical guidelines to designing high performance energy storage device based on hybridization of lithium-ion battery and supercapacitor. J Power Sources 2014;259:1–14. https://doi.org/10.1016/j.jpowsour.2014.02.001.

[289] Nishihara H, Kyotani T. Templated nanocarbons for energy storage. Adv Mater 2012;24:4466. https://doi.org/10.1002/adma.201201715.

[290] Zhang J, Zhao XS. On the configuration of supercapacitors for maximizing electrochemical performance. ChemSusChem 2012;5:818–41. https://doi.org/10.1002/cssc.201100571.

[291] Pandolfo AG, Hollenkamp AF. Carbon properties and their role in supercapacitors. J Power Sources 2006;157:11–27. https://doi.org/10.1016/j.jpowsour.2006.02.065.

[292] AL-Rubaye S, Rajagopalan R, Subramaniyam C, Tai Z, Xian J, Wang X, et al. NiFe$_2$O$_4$ nanoparticles coated on 3D graphene capsule as electrode for advanced energy storage applications. Dalt Trans 2018;47(39):14052–9.

[293] Zhang S, Pan N. Supercapacitors Performance Evaluation. Supercapacitors performance evaluation Adv Energy Mater 2015;5(6):1401401.

[294] Simon P, Gogotsi Y. Perspectives for electrochemical capacitors and related devices. Nat Mater 2020;19:1151–63. https://doi.org/10.1038/s41563-020-0747-z.

[295] Brousse T, Crosnier O, Bélanger D, Long JW. Capacitive and pseudocapacitive electrodes for electrochemical capacitors and hybrid devices. In: Dubal DP, Gomez-Romero P, editors. Metal Oxides in Supercapacitors. 1st ed.,. Amsterdam: Elsevier; 2017. https://doi.org/10.1016/B978-0-12-810464-4.00001-2.

[296] Huang Y, Zeng Y, Yu M, Liu P, Tong Y, Cheng F, et al. Recent smart methods for achieving high-energy asymmetric supercapacitors. Small Methods 2018;2(2):1700230.

[297] Stoller MD, Ruoff RS. Best practice methods for determining an electrode material's performance for ultracapacitors. Energy Environ Sci 2010;3:1294–301. https://doi.org/10.1039/c0ee00074d.

[298] Ishaque M, Islam MU, Khan MA, Rahman IZ, Genson A, Hampshire S. Structural, electrical and dielectric properties of yttrium substituted nickel ferrites. Phys B: Phys Condens Matter 2010;405:1532–40. https://doi.org/10.1016/j.physb.2009.12.035.

[299] Tang Z, Tang C, Gong H. A high energy density asymmetric supercapacitor from nano-architectured Ni(OH)$_2$/carbon nanotube electrodes. Adv Funct Mater 2012;22:1272–8. https://doi.org/10.1002/adfm.201102796.

[300] Liang X, Chen K, Xue D. A flexible and ultrahigh energy density capacitor via enhancing surface/interface of carbon cloth supported colloids. Adv Energy Mater 2018;8:1703329. https://doi.org/10.1002/aenm.201703329.

[301] Deng DH, Pang H, Du JM, Deng JW, Li SJ, Chen J, et al. Fabrication of cobalt ferrite nanostructures and comparison of their electrochemical properties. Cryst Res Technol 2012;47(10):1032–8.

[302] Zhang W, Quan Bo, Lee C, Park S-K, Li X, Choi E, et al. One-step facile solvothermal synthesis of copper ferrite-graphene composite as a high-performance supercapacitor material. ACS Appl Mater Interfaces 2015;7(4):2404–14.

[303] Wang R, Li Q, Cheng L, Li H, Wang B, Zhao XS, et al. Electrochemical properties of manganese ferrite-based supercapacitors in aqueous electrolyte: The effect of ionic radius. Colloids Surfaces A: Physicochem Eng Asp 2014;457:94–9.

[304] Fei M, Zhang R, Li L, Li J, Ma Z, Zhang K, et al. Epitaxial growth of MnFe$_2$O$_4$ nanosheets arrays for supercapacitor. Electrochim Acta 2021;368:137586.

[305] Nilmoung S, Kidkhunthod P, Maensiri S. The structural and electrochemical properties of CNF/MnFe$_2$O$_4$ composite nanostructures for supercapacitors. Mater Chem Phys 2018;220:190–200. https://doi.org/10.1016/j.matchemphys.2018.08.084.

[306] Sankar KV, Selvan RK. The ternary MnFe$_2$O$_4$/graphene/polyaniline hybrid composite as negative electrode for supercapacitors. J Power Sources 2015;275:399–407. https://doi.org/10.1016/j.jpowsour.2014.10.183.

[307] Maiti S, Pramanik A, Mahanty S. Interconnected network of MnO$_2$ nanowires with a 'cocoon' like morphology: Redox couple mediated performance enhancement in symmetric aqueous supercapacitor. ACS Appl Mater Interfaces 2014;6:10754–62. https://doi.org/10.1021/am502638d.

[308] Moitra D, Anand C, Ghosh BK, Chandel M, Ghosh NN. One-dimensional BiFeO$_3$ nanowire-reduced graphene oxide nanocomposite as excellent supercapacitor electrode material. ACS Appl Energy Mater 2018;1:464–74. https://doi.org/10.1021/acsaem.7b00097.

[309] Pinjari RV, Delcey MG, Guo M, Odelius M, Lundberg M. Restricted active space calculations of L-edge X-ray absorption spectra: From molecular orbitals to multiplet states. J Chem Phys 2014;141(12):124116.

[310] Spessard GO, Miessler GL. Organometallic Chemistry. 2nd ed. Oxford: Oxford University Press; 2010.

[311] Jin Y-H, Seo S-D, Shim H-W, Park K-S, Kim D-W. Synthesis of core/shell spinel ferrite/carbon nanoparticles with enhanced cycling stability for lithium ion battery anodes. Nanotechnology 2012;23(12):125402.

[312] Yang C, Shi M, Tian Y, Song X, Zhao L, Liu J, et al. Sustainable energy system utilizing high-voltage-stable and energy-dense supercapacitors based on porous Fe$_2$O$_3$@graphene electrode in ionic liquid electrolyte. Energy Technol 2018;6(12):2399–407.

[313] Ghadimi LS, Arsalani N, Tabrizi AG, Mohammadi A, Ahadzadeh I. Novel nanocomposite of MnFe$_2$O$_4$ and nitrogen-doped carbon from polyaniline carbonization as electrode material for symmetric ultra-stable supercapacitor. Electrochim Acta 2018;282:116–27. https://doi.org/10.1016/j.electacta.2018.05.160.

[314] Yan J, Wang Q, Wei T, Fan Z. Recent advances in design and fabrication of electrochemical supercapacitors with high energy densities. Adv Energy Mater 2014;4:1300816. https://doi.org/10.1002/aenm.201300816.

[315] Soam A, Kumar R, Sahoo PK, Mahender C, Kumar B, Arya N, et al. Synthesis of nickel ferrite nanoparticles supported on graphene nanosheets as composite electrodes for high performance supercapacitor. ChemistrySelect 2019;4(34):9952–8.

[316] Cai W, Lai T, Dai W, Ye J. A facile approach to fabricate flexible all-solid-state supercapacitors based on MnFe$_2$O$_4$/graphene hybrids. J Power Sources 2014;255:170–8. https://doi.org/10.1016/j.jpowsour.2014.01.027.

[317] Thu TV, Van Nguyen To, Le XD, Le TS, Van Thuy Vu, Huy TQ, et al. Graphene-MnFe$_2$O$_4$-polypyrrole ternary hybrids with synergistic effect for supercapacitor electrode. Electrochim Acta 2019;314:151–60.

[318] Su L, Lei S, Liu Li, Liu L, Zhang Y, Shi S, et al. Sprinkling MnFe$_2$O$_4$ quantum dots on nitrogen-doped graphene sheets: The formation mechanism and application for high-performance supercapacitor electrodes. J Mater Chem A 2018;6(21):9997–10007.

[319] Goljanian Tabrizi A, Arsalani N, Mohammadi A, Namazi H, Ghadimi LS, Ahadzadeh I. Facile synthesis of a MnFe$_2$O$_4$/rGO nanocomposite for an ultra-stable symmetric supercapacitor. New J Chem 2017;41:4974–84. https://doi.org/10.1039/c6nj04093d.

[320] Hwang JY, El-Kady MF, Wang Y, Wang L, Shao Y, Marsh K, et al. Direct preparation and processing of graphene/RuO$_2$ nanocomposite electrodes for high-performance capacitive energy storage. Nano Energy 2015;18:57–70.

[321] Gao H, Xiao F, Ching CB, Duan H. High-performance asymmetric supercapacitor based on graphene hydrogel and nanostructured MnO$_2$. ACS Appl Mater Interfaces 2012;4:2801–10. https://doi.org/10.1021/am300455d.

[322] Majumdar D, Thandavarayan M, Jiang Z. A review on recent progress in ruthenium oxide-based composites for supercapacitor applications. ChemElectroChem 2019;6:4343–72. https://doi.org/10.1002/celc.201900668.

[323] Xi J, Javed MS, Asim S, Idrees M, Shah SSA, Assiri MA, et al. High-performance flexible supercapatteries enabled by binder-free two-dimensional mesoporous ultrathin nickel-ferrite nanosheets. Mater Chem Front 2021;5(8):3436–47.

[324] Lalwani S, Munjal M, Singh G, Sharma RK. Layered nanoblades of iron cobaltite for high performance asymmetric supercapacitors. Appl Surf Sci 2019;476:1025–34. https://doi.org/10.1016/j.apsusc.2019.01.184.

[325] Rekhila G, Bessekhouad Y, Trari M. Visible light hydrogen production on the novel ferrite NiFe$_2$O$_4$. Int J Hydrogen Energy 2013;38:6335–43. https://doi.org/10.1016/j.ijhydene.2013.03.087.

[326] Sharifi S, Rahimi K, Yazdani A. Highly improved supercapacitance properties of MnFe$_2$O$_4$ nanoparticles by MoS$_2$ nanosheets. Sci Rep 2021;11:8378. https://doi.org/10.1038/s41598-021-87823-6.

[327] Taffa DH, Dillert R, Ulpe AC, Bauerfeind KCL, Bredow T, Bahnemann DW, et al. Photoelectrochemical and theoretical investigations of spinel type ferrites (M$_x$Fe$_{3-x}$O$_4$) for water splitting: A mini-review. J Photonics Energy 2017;7(1):012009.

[328] Zhao J, Cheng Y, Yan X, Sun D, Zhub F, Xue Q. Magnetic and electrochemical properties of CuFe$_2$O$_4$ hollow fibers fabricated by simple electrospinning and direct annealing. CrystEngComm 2012;14:5879–85. https://doi.org/10.1039/c2ce25684c.

[329] Wan F, Zhu J, Huang S, Niu Z. High voltage electrolytes for aqueous energy storage devices. Batter Supercaps 2020;3:323–30. https://doi.org/10.1002/batt.201900229.

[330] An C, Li W, Wang M, Deng Q, Wang Y. High energy density aqueous asymmetric supercapacitors based on MnO$_2$@C branch dendrite nanoarchitectures. Electrochim Acta 2018;283:603–10. https://doi.org/10.1016/j.electacta.2018.07.006.

[331] Wu X, Yang H, Yu M, Liu J, Li S. Design principles of high-voltage aqueous supercapacitors. Mater Today Energy 2021;21:100739.

[332] Zuo W, Xie C, Xu P, Li Y, Liu J. A Novel phase-transformation activation process toward Ni–Mn–O nanoprism arrays for 2.4 V ultrahigh-voltage aqueous supercapacitors. Adv Mater 2017;29(36):1703463.

[333] Jabeen N, Hussain A, Xia Q, Sun S, Zhu J, Xia H. High-performance 2.6 V aqueous asymmetric supercapacitors based on in situ formed Na$_{0.5}$MnO$_2$ nanosheet assembled nanowall arrays. Adv Mater 2017;29(32):1700804.

[334] Qu Q, Yang S, Feng X. 2D sandwich-like sheets of iron oxide grown on graphene as high energy anode material for supercapacitors. Adv Mater 2011;23: 5574–80. https://doi.org/10.1002/adma.201103042.

[335] Akinwolemiwa B, Chen GZ. Fundamental consideration for electrochemical engineering of supercapattery. J Braz Chem Soc 2018;29:960–72. https://doi.org/10.21577/0103-5053.20180010.

[336] Balasubramaniam S, Mohanty A, Balasingam SK, Kim SJ, Ramadoss A. Comprehensive insight into the mechanism, material selection and performance evaluation of supercapatteries. Nano-Micro Lett 2020;12:85. https://doi.org/10.1007/s40820-020-0413-7.

[337] Yu L, Chen GZ. Supercapatteries as high-performance electrochemical energy storage devices. Electrochem Energy Rev 2020;3:271–85. https://doi.org/10.1007/s41918-020-00063-6.

[338] Xia L, Yu L, Hu D, Chen GZ. Electrolytes for electrochemical energy storage. Mater Chem Front 2017;1:584–618. https://doi.org/10.1039/C6QM00169F.

[339] Chen GZ. Supercapacitor and supercapattery as emerging electrochemical energy stores. Int Mater Rev 2017;62:173–202. https://doi.org/10.1080/09506608.2016.1240914.

[340] Akinwolemiwa B, Wei C, Chen GZ. Mechanisms and designs of asymmetrical electrochemical capacitors. Electrochim Acta 2017;247:344–57. https://doi.org/10.1016/j.electacta.2017.06.088.

[341] Yu L, Chen GZ. Redox electrode materials for supercapatteries. J Power Sources 2016;326:604–12. https://doi.org/10.1016/j.jpowsour.2016.04.095.

[342] Guan L, Yu L, Chen GZ. Capacitive and non-capacitive faradaic charge storage. Electrochim Acta 2016;206:464–78. https://doi.org/10.1016/j.jpowsour.2016.04.095.

[343] Bandgar SB, Vadiyar MM, Jambhale CL, Ye Z, Kim J-H, Kolekar SS. Construction of dual metal ferrite-based core-shell nanostructures as low-cost multimetal electrode for boosting energy density of flexible asymmetric supercapattery. J Energy Storage 2021;36:102379. https://doi.org/10.1016/j.est.2021.102379.

[344] Hu L, Xue L, Fu J, Xiao P, Zhai T, Li H. A versatile capacity balancer for asymmetric supercapacitors. Adv Energy Mater 2020;10:2001608. https://doi.org/10.1002/aenm.202001608.

[345] Frackowiak E, Fic K, Meller M, Lota G. Electrochemistry serving people and Nature: High-energy ecocapacitors based on redox-active electrolytes. ChemSusChem 2012;5:1181–5. https://doi.org/10.1002/cssc.201200227.

[346] Hu L, Zhai T, Li H, Wang Y. Redox-mediator-enhanced electrochemical capacitors: Recent advances and future perspectives. ChemSusChem 2019;12:1118–32. https://doi.org/10.1002/cssc.201802450.

[347] Lalwani S, Joshi A, Singh G, Sharma RK. Sulphur doped iron cobalt oxide nanocaterpillars: An electrode for supercapattery with ultrahigh energy density and oxygen evolution reaction. Electrochim Acta 2019;328:135076. https://doi.org/10.1016/j.electacta.2019.135076.

[348] Athika M, Prasath A, Sharma AS, Devi VS, Duraisamy E, Elumalai P. Ni/NiFe$_2$O$_4$@carbon nanocomposite involving synergistic effect for high-energy density and high-power density supercapattery. Mater Res Express 2019;6:095503. https://doi.org/10.1088/2053-1591/ab2c59.

[349] Augustyn V, Simon P, Dunn B. Pseudocapacitive oxide materials for high-rate electrochemical energy storage. Energy Environ Sci 2014;7:1597–614. https://doi.org/10.1039/c3ee44164d.

[350] Brousse T, Taberna P-L, Crosnier O, Dugas R, Guillemet P, Scudeller Y, et al. Long-term cycling behavior of asymmetric activated carbon/MnO$_2$ aqueous electrochemical supercapacitor. J Power Sources 2007;173(1):633–41.

[351] Qin T, Xu Z, Wang Z, Peng S, He D. 2.5 V salt-in-water supercapacitors based on alkali type double salt/carbon composite anode. J Mater Chem A 2019;7(45): 26011–9.

[352] Jana M, Saha S, Samanta P, Murmu NC, Kim NH, Kuila T, et al. Growth of Ni-Co binary hydroxide on reduced graphene oxide surface by a successive ionic layer adsorption and reaction (SILAR) method for high performance asymmetric supercapacitor electrode. Mater Chem A 2016;4:2188–97. https://doi.org/10.1039/C5TA10297A.